MEMS MULTI-DOF WEAKLY COUPLED RESONATOR BASED ON MODE LOCALIZATION FOR MASS CHANGE SENSING APPLICATIONS

by

Yuan Wang

UNIVERSITY OF LIEGE

FACULTY OF APPLIED SCIENCE

Electrical Engineering and Computer Science

EMMI Research Group

In Partial Fulfillment of the requirements for the degree of
Doctor of Philosophy

2019

UNIVERSITY OF LIEGE

ABSTRACT

FACULTY OF APPLIED SCIENCE

Electrical Engineering and Computer Science

Doctor of Philosophy

MEMS MULTI-DOF WEAKLY COUPLED RESONATOR BASED ON MODE LOCALIZATION FOR MASS CHANGE SENSING APPLICATIONS

by *Yuan Wang*

The interest in MEMS (Micro-electro-mechanical-system) resonant devices has been rapidly growing over the past decades. They have become one of the major building blocks among all MEMS devices. MEMS resonators are mainly employed for sensing applications. By varying inherent physical properties of MEMS resonators, such as the effective mass and stiffness, the corresponding resonance frequency of the resonator will be altered and hence the shifted frequency will be considered as a sensing output metric. Stiffness resonator sensors have been used for accelerometers, atomic force microscopy, sensing physical forces and pressure sensors. Concurrently, for biological and chemical sensing applications, resonator mass sensors have proven a potential method for label-free sensing purpose. A novel sensing approach has been propounded recently, namely, utilizing an output metric which is based on mode shape variations in a linear array of several coupled resonators. In this approach, the changes of the mode shape are due to a phenomenon called mode localization. This has already demonstrated remarkable results for applications in mass and stiffness sensing.

This thesis comprehensively explores the potential of a 3-DOF mode localized weakly coupled resonator. A novel reversible method which exploits the usage of nanoparticles as well quantified mass changes is described. The mass sensitivity of the coupled resonator can be characterized accordingly. It has been demonstrated that a) the

resonance amplitude ratio as a sensing metric can improve the coupled resonator sensitivity. To be more specific, it yields a sensitivity in terms of mass perturbations around two times larger than the amplitude changes. Further, it yields around two orders of magnitude enhancement than the resonance frequency shifts. b) Nanoparticles as mass perturbations to characterize the MEMS mass sensors is an effective and cost-effective technique. Owing to the reversibility and flexibility of nanoparticles, the efficiency of characterizing mass sensitivity of a MEMS sensor is greatly improved. These techniques can contribute to the development of MEMS mass resonant sensor in general.

Further investigations of the capability for 3-DOF coupled resonators have been carried out. A novel mass to stiffness transduction mechanism has been proposed. Hereby, a commercial QCM mass sensor is combined with a 3-DOF mode localized coupled resonator stiffness sensor. This approach can solve the problem that typical micromachined resonators suffer from performance degradation when operated in high damping environments such as air or liquids which results in a low quality factor. Consequently, this contributes an important step towards a practical biochemical sensor that can exploit the advantages of mode localized coupled resonators but works directly in contact with a liquid.

In addition to aforementioned points, this thesis describes several simulation models for the 3-DOF mode localized weakly coupled resonators. MATLAB, SIMULINK, COMSOL and equivalent circuit models are presented, which agree well with practical experiments. Next, multiple device layouts of 3-DOF coupled resonator dedicated for biosensing purposes have been designed. Furthermore, a biochemical surface functionalization process is investigated, which is evolved subsequently to a general operation protocol.

Finally, a 2-DOF mode localized weakly coupled BAW disk resonator is studied, along with the interface electronic circuit and associated instrumentation. This research has the potential to put forward an alternation route for high Q coupled resonators that can operate in a highly damped environment, with the ultimate objective to result in a highly sensitive biosensor.

DECLARATION OF AUTHORSHIP

I, *Yuan Wang*, declare that the thesis entitled MEMS Multi-DOF Weakly Coupled Resonator Based on Mode Localization for Mass Change Sensing Applications and the work presented in the thesis are both my own, and have been generated by me as the result of my own original research. I confirm that:

- This work was done wholly or mainly while in candidature for a research degree at this university;
- Where any part of this thesis has previously been submitted for a degree or any other qualification at this University or any other institution, this has been clearly stated;
- Where I have consulted the published work of others, this is always clearly attributed;
- Where I have quoted from the work of others, the source is always given. With the exception of such quotations, this thesis is entirely my own work;
- I have acknowledged all main sources of help;
- Where the thesis is based on work done by myself jointly with others, I have made clear exactly what was done by others and what I have contributed myself;
- Parts of this work have been published as: references [107, 108].

Signed:...

Date:...

ACKNOWLEDGEMENTS

"Great Rome was not built in one day." Adhere to such belief, I have started my journey of Ph.D. The voyage is not so much as a trip, but an adventure, eventually an odyssey. A thorny path that less travelled, a maze that I desperately to escape. Fortunately, whenever I lost the direction in the veiled sea, my course is charted by Professor Michael Kraft, who I foremost to thank, words are barely enough to express the gratitude. As an obtuse apprentice, Professor Michael Kraft never lost his patience to me. He is a respectful scientist and an eminent mentor, his insight and diligence inspiring me and his edification will be engraved on my mind.

"If you want to go fast, go alone; if you want to go far, go together." Regrettably, I am not a fast walker, yet I am lucky to have faithful friends. I would like to represent my heartfelt gratitude to Dr. Chen Wang, Mathieu Baijot & Delphine Cerica. Your help are imponderable to my researches. Mathieu Baijot & Delphine Cerica are like the hospitable host, my life in Belgium is wherefore delightful. I admire Mathieu Bejot's engineering skill and I esteem Delphine Cerica's talent of mathematic. Nevertheless Chen Wang is a younger brother to me, I look upon him as a teacher. Indeed, I dare to assert that he will be an outstanding scientist in the future. I would also like to thank Dr. Chun Zhao, who provides essential advices to me. He stands for a successful young scientist and he is a paragon. I cannot begin to thank adequately those who helped me. They are uniformly kind and generous. Professor Tristan Gilet and Professor Jean-Michel Redouté, thank you for your guidance with my teaching assistant work. Thanks to Mr. Thierry Legros, your supports with the electronics accelerate my progress. Countless thanks to Microsys laboratory, Dr. Serguei Stoukatch, Mr. Francois Dupont, Mr. Samuel Dricot and everyone, your kindness surely be appreciated. I am truly grateful to Montefiore Institute, University of Liege. The opportunity as a teaching assistant is the most precious experience I ever had.

"Behind every successful man, there is a great woman." Shamefully, I am definitely yet to success. However, an ironic truth is, I somehow been granted an extraordinary lady. My wife, Wenling Wang, has made enormous sacrifice for me. She devotes to accompany me in a foreign country which is far from her deeply cared motherland. She is sharing every burden of mine, even I am working on this hundreds of pages inky embarrassments. Generally, my wife can always distract me with her botanical lessons or simply warning me to close the window tight so that her beloved plants could endure the winter. I am especially indebted to her and her pure soul.

Above all, and as always, my profoundest thanks to my parents. I am proud to be your son. Your selfless contributions, your unconditional supports, your warmest love and your unremitting encouragements are the reason that I can sit here， organizing my manuscript and fulfill my dreams.

TABLE OF CONTENT

DECLARATION OF AUTHORSHIP iii

ACKNOWLEDGEMENTS iv

TABLE OF CONTENT v

LIST OF FIGURES ix

LIST OF TABLES xvii

LIST OF ABBREVIATIONS xix

Chapter 1 1

Introduction 1

1.1 Background 1

1.2 Dissertation Outline 3

Chapter 2 5

MEMS Resonator Review 5

2.1 MEMS Resonator Concept 5

2.2 MEMS Resonator Structure 6

2.2.1 Clamped-Free Structure: Cantilever 6

2.2.2 Clamped-Clamped Structure: Mass Spring Damper System 10

2.2.3 Multi-DOF Coupled Resonators 16

2.2.4 Multi-DOF Mode Localized Weakly Coupled Resonators 21

2.2.5 Multi-DOF Mode Localized Weakly Coupled Resonators: Vibration Amplitude Ratio as An Output Metric 28

2.2.6 Multi-DOF Mode Localized Weakly Coupled Resonators: Mode Aliasing 31

2.3 The Advantages and Disadvantages 32

2.4 Chapter Summary 33

Chapter 3 35

MEMS 3-DOF Mode Localized Weakly Coupled Resonator 35

3.1 Theoretical Analysis of a 3-DOF Mode Localized Electrostatic Weakly Coupled Resonator 35

3.1.1 Fundamentals 35

3.1.2 Derivations of Output Metrics: Stiffness Perturbations 46

3.1.3 Derivations of Output Metrics: Mass Perturbations 51

3.2 Mode Aliasing in a 3-DOF Mode Localized Electrostatic Weakly Coupled Resonator 54

3.3 Transduction Techniques of a 3-DOF Mode Localized Electrostatic Weakly Coupled Resonator 58

3.3.1 Actuation 58

3.3.2 Sensing Element 61

3.3.3 Pull-in Effect 65

3.4 Chapter Summary 67

Chapter 4 68

Simulation Models of Multi-DOF Mode Localized Weakly Coupled Resonators 68

4.1 Simulations of a 3-DOF Mode Localized Weakly Coupled Resonator 68

4.1.1 Equivalent Electronic Circuit Model of a 3-DOF Mode Localized Weakly Coupled Resonator 68

4.1.2 MATLAB & Simulink Model of a 3-DOF Mode Localized Weakly Coupled Resonator 74

4.1.3 COMSOL Simulation Model of a 3-DOF Mode Localized Weakly Coupled Resonator 81

4.2 Simulations of QCM Mass Sensing System 82

4.2.1 Equivalent Electronic Circuit Model of a QCM Mass Sensor 82

4.2.2 MATLAB & Simulink Model of a QCM Mass Sensor Incorporated With a 3-DOF Weakly Coupled Resonator Stiffness Sensor 84

4.3 Simulations of 2-DOF Coupled BAW Disk Resonator 86

4.3.1 Equivalent Electronic Circuit Model of a 2-DOF Mode Localized Coupled BAW Disk Resonator 88

4.3.2 MATLAB Model of a 2-DOF Mode Localized Coupled BAW Disk Resonator 89

4.3.3 COMSOL Simulation Model of a 2-DOF Mode Localized Coupled BAW Disk Resonator 91

4.4 Chapter Summary 94

Chapter 5 95

Fabrications of Multi-DOF Mode Localized Weakly Coupled Resonators......95
5.1 Fabrication of 3-DOF Mode Localized Weakly Coupled Resonator................95
5.1.1 Fabrication of 3-DOF Mode Localized Weakly Coupled Resonator: SOI Based Process that Exploits Two Steps of Release 95
5.1.2 Fabrication of 3-DOF Mode Localized Weakly Coupled Resonator: Dry Release Process with Dicing Free Technique for SOI Devices..........................100
5.1.3 Fabrication of 3-DOF Mode Localized Weakly Coupled Resonator: SOI Based Process with Dicing Free Technique that Exploits a Carrier Wafer........105
5.2 Fabrications of 2-DOF Mode Localized Coupled BAW Disk Resonator........108
5.2.1 Fabrication of 2-DOF Mode Localized Coupled BAW Disk Resonator: SOI Based Process with Dicing Free Technique that Exploits a Carrier Wafer........108
5.3 Chapter Summary..111
Chapter 6 112
Interface Circuit Designs and Experimental Materials..................................112
6.1 Interface Circuit Designs for 3-DOF Mode Localized Weakly Coupled Resonator...112
6.1.1 Signal Pick-up Circuit for 3-DOF Mode Localized Weakly Coupled Resonator 112
6.1.2 Peak Detector Circuit for QCM & 3-DOF Mode Localized Weakly Coupled Resonator Hybrid System...115
6.2 Interface Circuit Designs for 2-DOF Mode Localized Coupled BAW Disk Resonator...117
6.3 Experiment Materials for Mass Sensing Characterizations 121
6.3.1 Preparations of Magnetic Nanoparticles..124
6.3.2 Reversibility of Magnetic Nanoparticles as Mass Perturbations..............127
6.3.3 Dispensing of Magnetic Nanoparticles..129
6.4 Surface Functionalization of Multi-DOF Mode Localized Coupled Resonators 131
6.5 Chapter Summary..136
Chapter 7 138
Experiments 138
7.1 Experiments...138

7.1.1 A Mass Sensor Based on 3-DOF Mode Localized Coupled Resonator under Atmospheric Pressure 138

7.1.2 A Novel QCM Mass Sensing System Incorporated with a 3-DOF Mode Localized Coupled Resonator Stiffness Sensor 144

7.1.3 Investigations of a 3-DOF Mode Localized Coupled Resonator under Small Stiffness Perturbations 153

7.2 Chapter Summary 160

Chapter 8 162

Future Works 162

8.1 3-DOF Mode Localized Weakly Coupled Resonator for Multi-Mass Detection 162

8.1.1 Theoretical Analysis 162

8.1.2 Simulations 164

8.2 3-DOF Mode Localized Weakly Coupled Resonator with Embedded Micro-channel 168

8.3 Research Questions and Future Directions 169

8.4 Chapter Summary 170

Chapter 9 172

Conclusions 172

9.1 Research Contributions and Novelties 172

9.2 Practical Works 173

Appendix A 175

Interface Circuit PCBs 175

Appendix B 177

Bonding and Packaging 177

Appendix C 179

Publication List 179

References 181

LIST OF FIGURES

Chapter 2

Figure 2. 1: Normalized system response of a 1-DOF MEMS resonator. a) MEMS stiffness sensor. b) MEMS mass sensor....6
Figure 2. 2: A typical cantilever design. a) Cross section view, the cantilever is comprised of a mechanical beam. An external force in longitudinal direction can deflect the beam. b) 3D model with a load stimuli....7
Figure 2. 3: 1) A capacitive driving atomic force microscopy [42]: A thin film capacitor is integrated beneath the cantilever beam. The AFM cantilever can be actuated by introducing a potential difference V across the thin film capacitor. The thin film capacitor is consisted of a deposited metal layer and separated by an insulator with a relative permittivity ε. The separation distance is D. The voltage V across the thin film capacitor causes deflections that alter the capacitor dimensions, separation distance and dielectric properties, hence resulting in the actuation of the cantilever beam. 2) Two typical methods to extract the mechanical deflections of a cantilever beam are exhibited [43]. (a) Optical beam deflection sensing: the beam angular changes are measured by the shifts of the reflected laser spot incorporated with a position detector. (b) Pizeoresistive beam deflection sensing: The beam deflection causes the resistivity changes of the doped silicon, where the changes are also proportional to the voltages measured by the Wheatstone Bridge....9
Figure 2. 4: MEMS resonant cantilever biosensor. a) Dynamic mode. b) Static mode. 10
Figure 2. 5: A basic equivalent model of 1-DOF mass spring damper system. a) Simplified mass spring damper model. b) Clamped-Clamped model....11
Figure 2. 6: 1-DOF MEMS resonator system response: a) Step response. b) Impulse response. c) Frequency domain response. d) Bode plot....14
Figure 2. 7: 1-DOF MEMS resonator biosensor. a) Proof mass surface cleaning. b) Surface functionalization. c) Forming bio-affinity counterpart layer. d) Deposition of sample solution, target molecules are bonded with selective counterpart....15
Figure 2. 8: A 2-DOF coupled resonator mechanical model....16
Figure 2. 9: Multi-DOF cantilever array with mechanical coupling [21, 60, 63]. 17
Figure 2. 10: Mechanical Coupling. a) Straight beam coupling. b) Folded beam coupling....19
Figure 2. 11：A 2-DOF electrostatic coupled resonator....20
Figure 2. 12: A 2-DOF electrostatic coupled resonator with tunable coupling strength [66]. Each resonator has a relatively large proof mass which is suspended by four supporting beams. The supporting beams can be perturbed via capacitive perturbation plate. The coupled resonator is driven by one group of capacitive comb fingers while another group of comb fingers is used for sensing....21
Figure 2. 13: FEM simulation model of a 2-DOF mechanical coupled resonator. a) Natural resonance frequency. b) Mode localization effect with 500ng mass perturbation on the left resonator, consequently the left resonator vibration amplitude is dramatically changed but

the right one is less affected. The system resonance frequency is also shifted. 22
Figure 2. 14: 2-DOF mechanical coupled resonator vibration modes. a) In-phase mode. b) Out-of-phase mode. 24
Figure 2. 15: Loci veering of a 2-DOF mode localized mechanical coupled resonator. a) Mass perturbations. b) Stiffness perturbations. 25
Figure 2. 16: Loci veering of a 2-DOF mode localized mechanical coupled resonator with different coupling strength. 26
Figure 2. 17: 2-DOF mode localized electrostatic weakly coupled resonators [71]. a) Two double ended tuning forks (DETF) resonators with both ends anchored and they are coupled via electrostatic coupling, as shown in the dash box. Two adjacent electrodes serve as drive and sense electrodes, respectively. b) Two double free-free beam resonators are coupled via electrostatic coupling, as shown in the dash box. The double free-free beam resonator is suspended by tether supporting spring. Two adjacent electrodes serve as drive and sense electrodes, respectively. 28
Figure 2. 18: Amplitude ratios of a 2-DOF mode localized mechanical coupled resonator. a) Mass perturbations. b) Stiffness perturbations. 29
Figure 2. 19: Sensitivity comparisons of three different output metrics. 30
Figure 2. 20: Demonstration of mode aliasing phenomena..31

Chapter 3

Figure 3. 1: 3-DOF coupled resonator lumped parameter system model...............................36
Figure 3. 2: A 3-DOF mode localized electrostatic weakly coupled resonator system behavior. a) Eigenvalue loci veering curve. b) Amplitude ratio versus stiffness perturbations. 38
Figure 3. 3: A 3-DOF weakly coupled resonator compared with a 2-DOF weakly coupled resonator. a) Eigenvalue loci veering curve. b) Amplitude ratio versus stiffness perturbations...39
Figure 3. 4: Investigations of middle resonator stiffness variations. a) Eigenvalue loci veering curve with different value of K_2. b) Amplitude ratio versus stiffness perturbations with different value of K_2. 40
Figure 3. 5: A 3-DOF mode localized electrostatic weakly coupled resonator in response to stiffness perturbations. a) Eigenvalue loci veering curve with different value of K_c. b) Amplitude ratio versus stiffness perturbations with different value of K_c. 42
Figure 3. 6: A 3-DOF mode localized electrostatic weakly coupled resonator in response to mass perturbations. a) Eigenvalue loci veering curve. b) Amplitude ratio versus mass perturbations..44
Figure 3. 7: A 3-DOF weakly coupled resonator compared with a 2-DOF weakly coupled resonator. a) Eigenvalue loci veering curve. b) Amplitude ratio versus mass perturbations. 45
Figure 3. 8: A 3-DOF weakly coupled resonator normalized sensitivity comparisons in three different output metrics. 46
Figure 3. 9: A 3-DOF weakly coupled resonator lump parameter model and system block

diagram. 47
Figure 3. 10: 3-DOF weakly coupled resonator vibration modes. a) c) e) Three identical resonators coupled via mechanical springs. b) d) f) Left and right resonators are identical, middle resonator supporting spring stiffness $K2 \geq 2K1 = 2K3$. a) & b) All three resonators are vibrating in-phase. c) & d) Left and right resonators are vibrating out-of-phase while middle resonator maintains stationary. e) & f) Each resonator is vibrating out-of-phase with adjacent one, left and right resonators are vibrating in-phase however both of them are out-of-phase with middle resonator. 49
Figure 3. 11: Mode aliasing with different values of coupling strength Kc. 56
Figure 3. 12: Mode aliasing with different values of quality factor Q (different damping conditions)...57
Figure 3. 13: Capacitive actuation in a 3-DOF coupled resonator system. 59
Figure 3. 14: Integrated capacitive sensing element. 62
Figure 3. 15: Differential capacitive sensing...64
Figure 3. 16: Pull-in phenomenon. a) The equilibrium point stiffness as a function of displacement. b) The applied voltage versus the relative displacement. 67

Chapter 4

Figure 4. 1: Electronic equivalent circuit model in corresponding to a lumped model of 1-DOF MEMS resonator. 69
Figure 4. 2: Equivalent RLC circuit of a 3-DOF coupled resonator system. 70
Figure 4. 3: SPICE simulation model of a 3-DOF coupled resonator. 71
Figure 4. 4: Equivalent RLC circuit simulated 3-DOF coupled resonator system responses (strong coupling). a) Resonator1. b) Resonator 3. 72
Figure 4. 5: Equivalent RLC circuit simulation model output metric sensitivities comparison (strong coupling). 72
Figure 4. 6: Equivalent RLC circuit simulated 3-DOF coupled resonator system responses (weak coupling). a) Resonator1. b) Resonator 3. 74
Figure 4. 7: Equivalent RLC circuit simulation model output metric sensitivities comparison (weak coupling)..74
Figure 4. 8: Simulink system level simulation of a 3-DOF coupled resonator. 76
Figure 4. 9: MATLAB & Simulink simulated frequency responses with given stiffness perturbations. a) Resonator 1. b) Resonator 3. 77
Figure 4. 10: MATLAB & Simulink model output metric sensitivities comparison (stiffness perturbations). 77
Figure 4. 11: MATLAB & Simulink simulated frequency responses with given mass perturbations. a) Resonator 1. b) Resonator 3. 78
Figure 4. 12: MATLAB & Simulink model output metric sensitivities comparison (mass perturbations). 78
Figure 4. 13: MATLAB & Simulink simulated frequency responses with given stiffness perturbations under atmospheric pressure. a) Resonator 1. b) Resonator 3. 79
Figure 4. 14: MATLAB & Simulink model output metric sensitivities comparison under

atmospheric pressure (stiffness perturbations). 79
Figure 4. 15: MATLAB & Simulink simulated frequency responses with given mass perturbations under atmospheric pressure. a) Resonator 1. b) Resonator 3. 80
Figure 4. 16: MATLAB & Simulink model output metric sensitivities comparison under atmospheric pressure (mass perturbations). 80
Figure 4. 17: COMSOL simulated vibration modes of a 3-DOF coupled resonator. a) In-phase mode. b) Out-of-phase mode...82
Figure 4. 18: COMSOL simulated vibration amplitudes with a given excitation force on resonator1..82
Figure 4. 19: SPICE equivalent RLC circuit model. a) Actual model set-up. b) Frequency responses with mass perturbations. 83
Figure 4. 20: Simulated QCM mass sensor frequency responses with consecutive mass perturbations under atmospheric pressure. a) MATLAB & Simulink model. b) Equivalent RLC circuit model...84
Figure 4. 21: MATLAB & Simulink system level modeling. 85
Figure 4. 22: QCM incorporated with 3-DOF coupled resonator MATLAB & Simulink model. a) QCM mass sensor in air, the output signals are converted to DC voltages via peak detector. The converted DC voltages are used as electrostatic forces to generate stiffness perturbations for resonator3 in a 3-DOF weakly coupled resonator which operates in vacuum. b) The frequency responses of resonator1 in the hybrid system. c) The frequency responses of resonator3 in the hybrid system...85
Figure 4. 23: MATLAB & Simulink simulated QCM combined with 3-DOF coupled resonator hybrid system normalized sensitivities comparison..86
Figure 4. 24: 2-DOF coupled BAW disk resonator lumped parameter model. 87
Figure 4. 25: SPICE simulation model of a 2-DOF coupled BAW disk resonator. 89
Figure 4. 26: SPICE simulated frequency responses with given mass perturbations. a) Resonator 1. b) Resonator 2..89
Figure 4. 27: MATLAB simulated frequency responses of a 2-DOF coupled BAW disk resonator under atmospheric pressure. a) Resonator 1. b) Resonator 2. 90
Figure 4. 28: MATLAB simulated 2-DOF coupled BAW disk resonator normalized sensitivities comparison...91
Figure 4. 29: COMSOL simulated vibration modes of a 2-DOF coupled BAW disk resonator. a) In-phase mode. b) Out-of-phase mode..92
Figure 4. 30: COMSOL model of a 2-DOF mode localized coupled BAW disk resonator with an added mass perturbation on the right disk proof mass. a) In-phase mode. b) Out-of-phase mode...93
Figure 4. 31: 2-DOF coupled BAW disk resonator COMSOL simulated vibration amplitudes with a given excitation force on resonator 1. a) Without mass perturbation. b) With mass perturbation. 94

Chapter 5

Figure 5. 1: Device layouts of the 3-DOF coupled resonator. a) With tether structure. b) Without

tether structure..98
Figure 5. 2: Fabrication flow of SOI based process that exploits two steps of release. a) Spincoating photoresist layer. b) DRIE dry etching. c) DRIE overetching (dry release). d) Remove photoresist layer. e) HF wet etching fully release. 99
Figure 5. 3: Microscope view of fabricated 3-DOF coupled resonator devices. (SOI based process that exploits two steps of release) 100
Figure 5. 4: Modified layout (dicing free): Device layouts of the 3-DOF coupled resonator. a) Front side device layer. b) Bottom side release trenches. c) Overlapped view of one block unit on the wafer, consisted of two 3-DOF coupled resonator devices. 101
Figure 5. 5: Fabrication flow of dry release process with dicing free technique. 102
Figure 5. 6: Close-up view of the fabricated 3-DOF coupled resonator (dry release with dicing free technique)..103
Figure 5. 7: Failure of floating structures after releasing. 104
Figure 5. 8: 3-DOF coupled resonator structure modification: extended frame. 104
Figure 5. 9: Modified layout (dicing free with removed proof mass substrate): Device layouts of the 3-DOF coupled resonator. a) Front side device layer. b) Backside layer. c) Overlapped view..106
Figure 5. 10: Fabrication flow of SOI based process with dicing free technique that exploits a carrier wafer. 107
Figure 5. 11: Microscope view of failed device structure due to overetch (dicing free technique with a carrier wafer). 108
Figure 5. 12: Device layouts of the 2-DOF coupled BAW disk resonators. a) Disk radius 100 um. b) Disk radius 250 um. c) Disk radius 500 um. d) Disk radius 750 um. 110
Figure 5. 13: Microscope view of fabricated 2-DOF coupled BAW disk resonator devices. a) Disk radius 100 um. b) Disk radius 250 um. c) Disk radius 500 um. d) Disk radius 750 um. 111

Chapter 6

Figure 6. 1: Schematic of the I/V converters and amplification stages. 114
Figure 6. 2: 3-DOF coupled resonator measurement platform. 114
Figure 6. 3: Fabricated PCB interface circuit for a 3-DOF mode localized weakly coupled resonator. 115
Figure 6. 4: Peak detector circuit. a) Typical peak detector design. b) Modified high speed design 116
Figure 6. 5: Actual circuit of the high speed peak detector. a) Prototype board. b) Proposed PCB layout design. 117
Figure 6. 6: RLC equivalent circuit model of a 750um radius 2-DOF coupled BAW disk resonator. a) Absence of parasitic feedthrough capacitance. b) Presence of parasitic feedthrough capacitance. 118
Figure 6. 7: Feedthrough cancellation method. a) Tunable capacitance compensation technique. b) Dummy MEMS compensation technique. 119
Figure 6. 8: 2-DOF coupled BAW disk resonator measurement platform. 120

Figure 6. 9: Fabricated PCB interface circuit for a 2-DOF mode localized coupled BAW disk resonator. 121
Figure 6. 10: Magnetic nanoparticles. a) Structure diagram. b) TEM image of magnetic nanoparticles cluster [110]. c) TEM image of a single magnetic nanoparticle [110]. ...123
Figure 6. 11: Commercialized magnetic nanoparticles. 124
Figure 6. 12: Magnetic nanoparticles pre-treatment. a) Transporting the magnetic nanoparticles from original container. b) Eppendorf tube temporary storage. c) Using magnet to attract floating nanoparticles. d) Separation of carrier liquid. e) Fully remove the liquid, only solid nanoparticle clusters exist. f) Reinjecting 70% ethanol. g) Shaking the Eppendorf tube to make the nanoparticles evenly distributed in 70% ethanol solution. h) Taking the desired quantity of diluted nanoparticle solution, relocating in a shallow well plate, preparing to be dispensed. 126
Figure 6. 13: Magnetic nanoparticles removal. a) Dispensed magnetic nanoparticles on packaged multi-DOF coupled resonator device. b) Flip-over the packaged device and approaching the liquid surface. c) Dispensed surface contacts the liquid. d) Using a magnet to attract the dispensed nanoparticles. e) Waiting humid evaporation. f) Oven dryer program. 129
Figure 6. 14: Dispensing of magnetic nanoparticles. a) Calibration of positioning system. b) Set-up the coordinates to the filled well. c) Loading-up magnetic nanoparticle solution in the capillary. d) Depositing magnetic nanoparticle solution onto resonator proof mass surface. 130
Figure 6. 15: Microdispenser system. a) Computation of dispensed weight of magnetic nanoparticles, where h is the change of liquid level. b) SonoPlot GIX Microplotter system. 130
Figure 6. 16: Flow diagram of APTES & GA treatment for silicon surface functionalization. a) Original silicon surface (SiO_2 layer) cleaning via oxygen plasma or piranha solution. b) Hydroxyl groups are formed up after cleaning. c) 2% v/v APTES solution treatment, silane layer is formed. d) GA linker solution treatment. e) Functionalized silicon surface immobilizing bioreceptor (counterpart) of target analyte, here for example, specific antibodies. f) Adding sample solution, target analyte, here is antigen, are binding with antibodies. g) Additional sandwich assay procedure, using fluorescence labelled antibodies to confirm the antigen/antibody binding. 134

Chapter 7

Figure 7. 1: a) Microplotter capillary tip above resonator1 of 3-DOF coupled resonator chip. b) Magnetic nanoparticles attached to resonator1. c) Magnetic nanoparticles had been washed away. 139
Figure 7. 2: Frequency response of 3-DOF coupled resonator system after three consecutive mass perturbations. a) Frequency response of resonator1. b) Frequency response of resonator3. c) Simulated frequency response of resonator1. d) Simulated frequency response of resonator3. 140
Figure 7. 3: Frequency response of 3-DOF coupled resonator system. a) Frequency response

of Resonator1without perturbation/after rinsing. b) Frequency response of Resonator3 without perturbation/ after rinsing. 141
Figure 7. 4: Theoretical (simulated) and experimental sensitivities of 3-DOF coupled resonator system. 142
Figure 7. 5: Simulation model of a 3-DOF coupled resonator operating in three different environments: a) Responses of resonator 1. b) Responses of resonator 2....146
Figure 7. 6: Schematic of a QCM device has a resonant frequency of 5MHz, AT-cut and wrapped over electrodes....148
Figure 7. 7: Oscilloscope captured signal of an unperturbed QCM device, the QCM device has a resonant frequency of 5 MHz. 148
Figure 7. 8: Oscilloscope captured signal of an unperturbed QCM device connected with a high speed peak detector. 149
Figure 7. 9: QCM incorporated with a 3-DOF coupled resonator sensing system. 150
Figure 7. 10: (a) QCM holder platform, (b) Dispensed magnetic nanoparticles on QCM....150
Figure 7. 11: Simulation for the frequency response of QCM incorporated with 3-DOF coupled resonator mass sensing system. a) Resonator1. b) Resonator3. 151
Figure 7. 12: The measured frequency response of 3-DOF coupled resonator system. (a) Resonator1. (b) Resonator3....151
Figure 7. 13: Theoretical and experimental sensitivities of QCM incorporated with 3-DOF coupled resonator mass sensing system. 152
Figure 7. 14: System sensitivity comparison. 152
Figure 7. 15: Extracted noise floor of the 3-DOF coupled resonator. a) Resonator1. b) Resonator3. 154
Figure 7. 16: Simulated 3-DOF coupled resonator responses with noise equivalent stiffness perturbation. a) Resonator1. b) Resonator3. 155
Figure 7. 17: Small stiffness perturbation experiments with DC perturbation voltage from 0.02V to 0.1V. a) Resonator1. b) Resonator3....156
Figure 7. 18: Curve fitting technique for small stiffness perturbation experiments: a) Original data of resonator1 and polynomial fitting. b) Fitted curve of resonator1. c) Original data of resonator3 and polynomial fitting. d) Fitted curve of resonator3. 157
Figure 7. 19: Output metrics of 3-DOF coupled resonator with small stiffness perturbations. a) Resonant frequency shift. b) Amplitude ratio. c) Comparison of the two output metrics. 158
Figure 7. 20: Output metrics of 3-DOF coupled resonator with small stiffness perturbations. a) Vibration amplitude changes. b) Compared with resonant frequency shifts. 160

Chapter 8

Figure 8. 1: Theoretical analysis of a 3-DOF mode localized coupled resonator for multi-mass detection. a) Mode frequencies versus two independent mass perturbations on resonator 2 and resonator 3 respectively. b) Amplitude ratio (resonator1/resonator3) versus mass perturbations of resonator3. c) Amplitude ratio (resonator2/resonator3) versus mass perturbations of resonator2. 164

Figure 8. 2: Simulated responses of multi-mass detection (only resonator3 has mass perturbations): a) Resonator1. b) Resonator2. c) Resonator3. d) Amplitude ratio change of resonator1/resonator3. e) Amplitude ratio change of resonator2/resonator3. 165
Figure 8. 3: Simulated responses of multi-mass detection (both resonator2 & resonator3 have independent mass perturbations): a) Resonator1. b) Resonator2. c) Resonator3. d) Amplitude ratio change of resonator1/resonator3. e) Amplitude ratio change of resonator2/resonator3. The label named multi indicates multi-mass perturbations. 166
Figure 8. 4: COMSOL simulation of a 3-DOF coupled resonator for multi-mass detection. a), c), e) Only resonator3 has mass perturbation; b), d), f) Both resonator2 and resonator3 have mass perturbations. 167
Figure 8. 5: 3-DOF coupled resonator as a multi-analyte biosensor. 168
Figure 8. 6: A resonator with embedded micro-channels (EMC)..169

LIST OF TABLES

Chapter 2

Table 2. 1: MEMS resonators pros and cons...33

Chapter 3

Table 3. 1: System parameters of eigenvalue loci veering curve model for a 3-DOF mode localized electrostatic weakly coupled resonator (with stiffness perturbations). 37
Table 3. 2: Stiffness perturbation sensitivity comparisons under the condition of extreme values. 51
Table 3. 3: Mass perturbation sensitivity comparisons under the condition of extreme values. 54
Table 3. 4: A comparison of MEMS actuation methods..58
Table 3. 5: Comparisons of MEMS sensing techniques...62

Chapter 4

Table 4. 1: Parameter definitions of equivalent RLC circuit simulation model. 71
Table 4. 2: MATLAB & Simulink simulation model parameters. 76
Table 4. 3: Equivalent RLC circuit parameter definitions..83
Table 4. 4: Parameter definitions of equivalent RLC circuit model for a 2-DOF coupled BAW disk resonator. 88
Table 4. 5: Parameters of MATLAB simulation model for a 2-DOF coupled BAW disk resonator. 90

Chapter 5

Table 5. 1: Dimension parameters of fabricated 3-DOF coupled resonator device.................96
Table 5. 2: Dimension parameters of fabricated 2-DOF coupled BAW disk resonators.......109

Chapter 6

Table 6. 1: Comparison of the 2-DOF coupled BAW disk resonator sensing electrode schemes. 118
Table 6. 2: Comparison of mass/stiffness perturbation features in terms of feasibilities. 122
Table 6. 3: Strategies of silicon surface functionalization...131

Table 6. 4: Silicon surface silanization. Colored sections indicate the possibility to be adopted for multi-DOF coupled resonators as biosensors. 132
Table 6. 5: Chemical productions used for silicon surface functionalization........................135

Chapter 7

Table 7. 1: Calculated mass sensitivity...142
Table 7. 2: A summary of MEMS resonant mass sensors. It is needed to be concerned, the mass sensitivities in the table are based on resonant frequency shift. Mode localization metric (AR) had been proved theoretically and experimentally, which improved the normalized sensitivity for orders of magnitudes compared with resonant frequency shift. Hence the 3-DOF coupled resonator that exploits mode localization effect can yield higher sensitivity and possess common mode rejection ability. 143
Table 7. 3: 5 MHz QCM device parameter values. 147
Table 7. 4: Hybrid system and conventional QCM mass sensor sensitivity comparison. 153

LIST OF ABBREVIATIONS

Abbreviations of device

MEMS:	Micro-electro-mechanical systems
DOF:	Degree of freedom
CR:	Coupled resonator
QCM:	Quartz crystal microbalance
BAW:	Bulk acoustic wave
FEM:	Finite element modelling
AFM:	Atomic force microscopy
Q-factor:	Quality factor
AR:	Amplitude Ratio
SNR:	Signal to noise ratio
EMC:	Embedded micro-channel

Abbreviations of fabrication

SOI:	Silicon on insulator
DRIE:	Deep reactive ion etching
HF:	hydrofluoric acid
VPE:	Vapor phase etcher

Abbreviations of interface circuit

PCB:	Printed circuit board
SMD:	Surface mounted devices
TIA:	Transimpedance amplifier
INS:	Instrumentation amplifier
CMRR:	Common mode rejection ratio

Abbreviations of surface functionalization

APTES:	(3-Aminopropyl)triethoxysilane
GA:	Glutaraldehyde
APMS:	2-Acrylamido-2-methylpropane sulfonic acid
BSA:	Bovine serum albumin
PBS:	Phosphate buffer saline
CRP:	C-reactive protein
PSA:	Prostate-specific antigen

Chapter 1

Introduction

1.1 Background

Micro-electro-mechanical systems (MEMS), also known as micromachines or microsystems, are increasingly the objects of cutting-edge research. Their multidisciplinary applications have attracted substantial scientific interest. Their microscopic size and capacity to implement mechanics on a micro scale overcome the problems of bulky machinery. Batch manufacturing, compatibility with conventional metal-oxide semiconductors, and their integrity allow MEMS to be used in a wide range of applications. The early prototype resonant gate transistor [1] have evolved into silicon-based micro-mechanical transducers [2]. Notable new fabrication flows, device designs, and integration processes have led to great success for MEMS in the 1990s. Commercialized MEMS have had a large impact on society. MEMS-based products range from navigation equipment, military weaponry, and aerospace facilities, to more everyday appliances, such as inkjet printers [3], projectors [4, 5], and smartphones.

Interest in MEMS resonators has grown rapidly in recent decades. They have become one of the major building blocks of all MEMS devices. As a complementary solution of integrated circuits, MEMS resonators are used in applications such as switches, oscillators, and filters [6-9]. Additionally, MEMS resonators are employed in sensing applications. Varying the inherent physical properties of MEMS resonators, such as the effective mass and stiffness, alters the corresponding resonance frequency of the resonator. This shifted frequency is considered an output metric [10]. Stiffness

resonator sensors have been applied in atomic force microscopy [11]. Physical forces (for instance, magnetic and electrostatic forces) can also be measured by stiffness resonator sensors [12, 13]. In addition, MEMS resonators are also found in inertial sensors (accelerometers and gyroscopes) [14, 15]. Such accelerometers can achieve relatively wider bandwidth and significantly improve the resolution [16]. These accelerometers can be further adapted with an electrostatic force feedback system, namely electromechanical sigma-delta modulators [17]. Additionally, MEMS resonant membranes have demonstrated their effectiveness as pressure sensors [18]. For biological and chemical sensing applications, mass resonator sensors have already been proven as a potential label-free technique [19, 20].

As a further development from single degree-of-freedom (1-DOF) MEMS resonator sensors, multi-DOF resonator sensors have recently gained considerable attention. 2-DOF resonator sensors have already demonstrated remarkable results for applications in mass and stiffness sensing [21, 22]. Research has indicated that in comparison with conventional 1-DOF resonator sensors with frequency shift as the sensing output metric, approximately two orders of magnitude enhancement in sensitivity can be achieved by utilizing the mode localization effect in a 2-DOF coupled resonator sensor system. With particular emphasis of the principle [23], the mode localization effect is based on external perturbation energy that is confined at a particular area in a weakly coupled periodic vibration system. This leads to variations in the mode shape of such a system.

Recently, a novel sensing method has been proposed, which uses the ratio of the resonant amplitudes of the resonators as an output metric. Such an approach can concurrently achieve a high sensitivity and a high common mode rejection. Accordingly, a 3-DOF weakly coupled resonator system [24, 25] utilizing mode localization has improved stiffness change sensitivity by approximately three orders of magnitude compared to a conventional 1-DOF MEMS resonator of similar geometry when operated in vacuum. Furthermore, the 3-DOF weakly coupled resonator has been investigated with a similar experimental frame but under the condition of atmospheric pressure [26]. With the same stiffness perturbation, the change of the resonator

amplitude ratio is significantly higher than that of the resonant frequency shift, indicating the resonator amplitude ratio is an output metric with higher sensitivity in respect to external perturbations. A 4-DOF coupled resonant accelerometer has been developed, which has attained superior sensitivity and resolution over that of the conventional accelerometers [27].

1.2 Dissertation Outline

This dissertation investigates multi degree-of-freedom (DOF) mode localized weakly coupled resonators in mass and biological sensors. It is organized as follows.

Chapter 2 begins with a review of MEMS resonant devices, covering the fundamentals, design concepts, and performance metrics. The focus moves from 1-DOF to multi-DOF resonant devices that are used as either stiffness or mass sensors. Particular emphasis is given to multi-DOF mode localized coupled resonators, and the chapter closes with a discussion of the advantages and disadvantages of multi-DOF coupled resonant devices.

Chapter 3 provides a comprehensive theoretical analysis of a 3-DOF mode localized weakly coupled resonator. Sub-technical levels such as actuation, coupling, and sensing are illustrated. The vibration mode behavior and system responses are examined.

Chapter 4 introduces various simulation models for a 3-DOF mode localized weakly coupled resonator. The theoretical analysis in the previous chapter is verified with Simulink, finite element modelling (FEM), and equivalent electronic circuit models. System-level simulations are conducted with environmental variables such as noise, temperature, and pressure. Additionally, simulation models based on a quartz crystal microbalance (QCM) and its hybrid system and a 2-DOF weakly coupled bulk acoustic wave (BAW) resonant device are also included. These results are compared with the data obtained from the experiment.

Chapter 5 presents the layouts of 3-DOF weakly coupled resonator devices for

biosensing and the layouts of 2-DOF weakly coupled BAW resonators, along with two different dicing-free fabrication flows. The chapter ends by presenting the fabricated multi-DOF weakly coupled resonators.

Chapter 6 introduces the interface circuit designs for the 3-DOF weakly coupled resonator, the QCM incorporated with a 3-DOF weakly coupled resonator, and the 2-DOF weakly coupled BAW resonator. The chapter also introduces the experiment materials and platforms: (1) the preparation of magnetic nanoparticles, (2) the standard operation protocol for dispensing nanoparticles on multi-DOF resonant devices, (3) the reversibility of nanoparticles as mass perturbations, and (4) the protocol of the surface functionalization process.

Chapter 7 presents the experimental results for the 3-DOF mode localized weakly coupled resonator as a mass sensor, the QCM mass sensor incorporated with a 3-DOF mode localized weakly coupled resonator stiffness sensor, and the 3-DOF mode localized weakly coupled resonator as a stiffness change sensor with small stiffness perturbations (under laboratory conditions).

Chapter 8 explores the possibilities for future work. A novel multi-mass detection scheme of the 3-DOF mode localized weakly coupled resonator is proposed, along with theoretical analysis and simulation models. In addition, a novel structural modification is suggested; namely, a 3-DOF mode localized weakly coupled resonator integrated with an embedded micro-channel.

Chapter 9 concludes the dissertation.

Chapter 2

MEMS Resonator Review

2.1 MEMS Resonator Concept

Aside from MEMS resonant oscillators employed in timing devices, MEMS resonant transducers have drawn a great amount of attention in recent years. The central principle of a MEMS resonant transducer is its intrinsic vibration frequency. Given a periodic stimulus, the MEMS resonator begins to vibrate within a certain frequency range. The vibrating amplitude will increase and eventually reach a maximum when the vibration frequency is identical to the intrinsic natural frequency (the natural frequency is constrained by the resonator design). Subsequently, the vibration amplitude will decrease to the baseline value. By properly tuning the physical properties of the MEMS resonator, such as the effective mass and stiffness, the corresponding intrinsic natural frequency of the resonator, or simply resonance frequency, will be altered, and the shifted frequency value can be used to determine the device sensitivity. A typical linear MEMS resonator operating in response to either stiffness or mass perturbations is shown in Figure 2.1. Research outcomes based on 1-DOF MEMS resonator stiffness sensors are applied for measuring small physical forces, such as inertial force [28], magnetic force [29], and pressure force [30]. Single-DOF resonator mass sensors are suitable for biosensing applications [31].

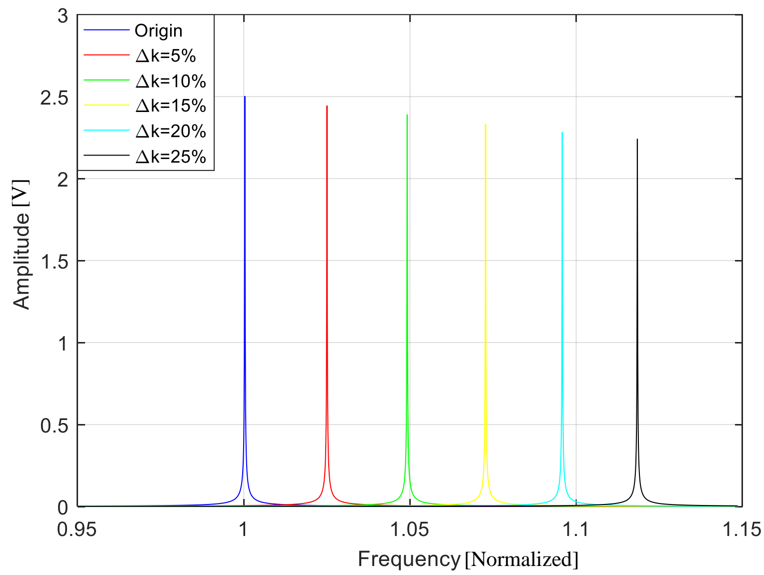

a)

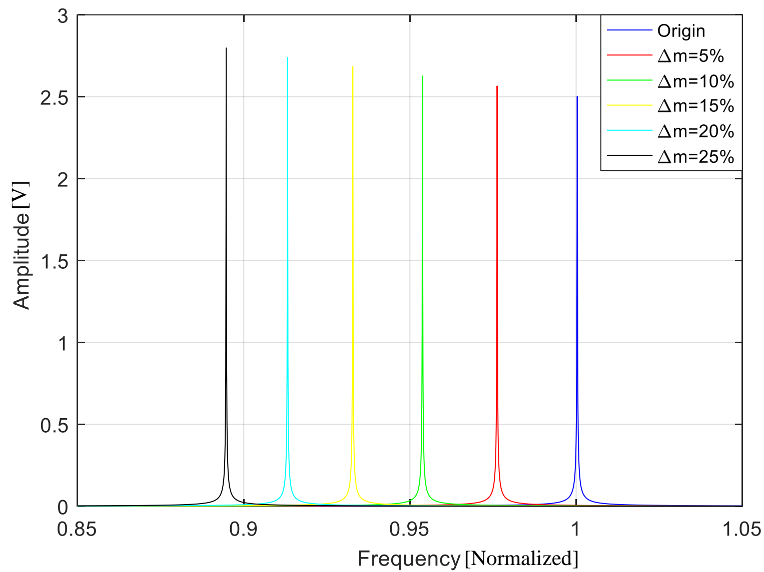

b)

Figure 2. 1: Normalized system response of a 1-DOF MEMS resonator. a) MEMS stiffness sensor. b) MEMS mass sensor.

2.2 MEMS Resonator Structure

2.2.1 Clamped-Free Structure: Cantilever

Adopted from macro-mechanical applications, cantilevers are one of the most widely used structures in MEMS resonator designs. Cantilevers share similar behavior

to springboards. The transduction mechanism of MEMS cantilevers utilizes deformation in response to external stimulus, ideally only bending vertically. Such deformation requires flexibility or elasticity so that the bending of the cantilever can be measured. Figure 2.2 shows a schematic of a typical cantilever and its 3D model.

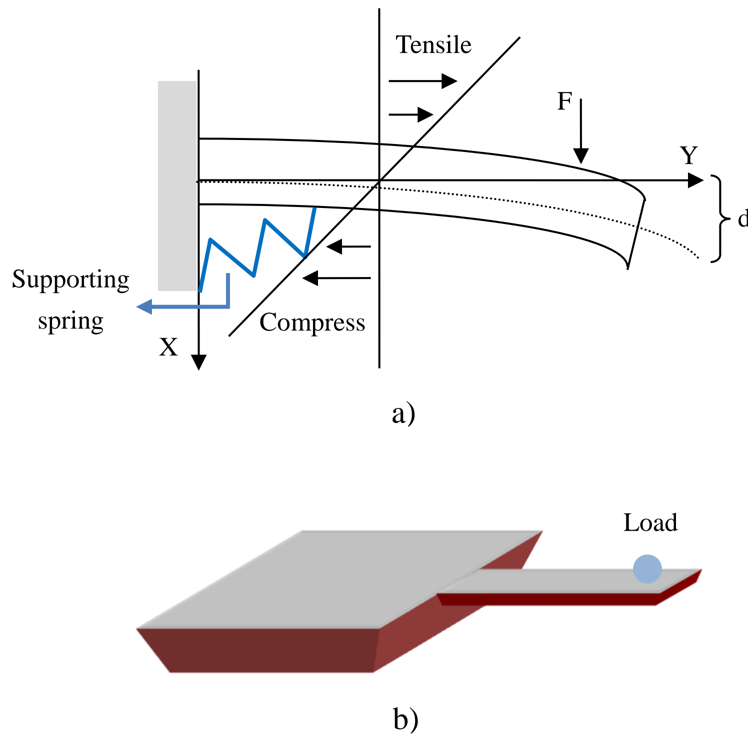

Figure 2. 2: A typical cantilever design. a) Cross section view, the cantilever is comprised of a mechanical beam. An external force in longitudinal direction can deflect the beam. b) 3D model with a load stimuli.

The main advantage of the cantilever structure is the predictable vibration mode, whereby it flexes rather than extends. The cantilever displacement can be derived as [32, 33]:

$$EI\frac{\partial^2 x(Y)}{\partial Y^2} = M(Y) \tag{2.1}$$

$$I = \frac{ab^3}{12} \tag{2.2}$$

where I is the second moment of inertia, a is the transverse length, b is the

longitudinal thickness of the cantilever cross section, $x(Y)$ is the displacement along the cantilever beam, $M(Y)$ is the bending moment at the same location, E is Young's modulus, which depends on the device material, and L is the cantilever beam length. By applying boundary conditions to the anchor where the rotation and movement are constrained, the displacement at location Y in response to a force F can be deduced:

$$x(Y) = \frac{F}{EI}\left(\frac{LY^2}{2} - \frac{Y^3}{6}\right) \tag{2.3}$$

The angle due to the bending action can be expressed:

$$\theta(Y) = \frac{\partial x(Y)}{\partial Y} = \frac{F}{EI}\left(LY - \frac{Y^2}{2}\right) \tag{2.4}$$

The effective spring constant for the cantilever can be solved by Hooke's Law $F = kx$:

$$k(L) = \frac{3EI}{L^3} \tag{2.5}$$

MEMS cantilevers benefit from a relatively simple structure and batch fabrication process, which can be implemented by either bulk micromachining or surface micromachining. MEMS cantilevers benefit from a relatively simple structure and batch fabrication process, which can be implemented by either bulk micromachining or surface micromachining. In addition, MEMS cantilevers can be employed as sensitive force sensors and biosensors. Small device dimensions render the ability to integrate with interface circuitry, which attains a miniature system. Despite the noticeable advantages, MEMS cantilevers are commonly confined to high-frequency regimes. The resonance frequency is determined by the effective mass of the cantilever and the spring constant. The small and stiff cantilever beam pushes the resonance frequency to a higher region (in kHz to MHz range). Correspondingly, such a property leads to complexity of interface circuit design.

MEMS cantilevers are actuated via diverse approaches, including thermal [34],

piezoelectric [11], and capacitive [35] actuations. General pick-off techniques include optical [36, 37], capacitive [38] and piezoresistive [39-41]. Figure 2.3 demonstrates a typical capacitive actuation principle and two pick-off systems [42, 43].

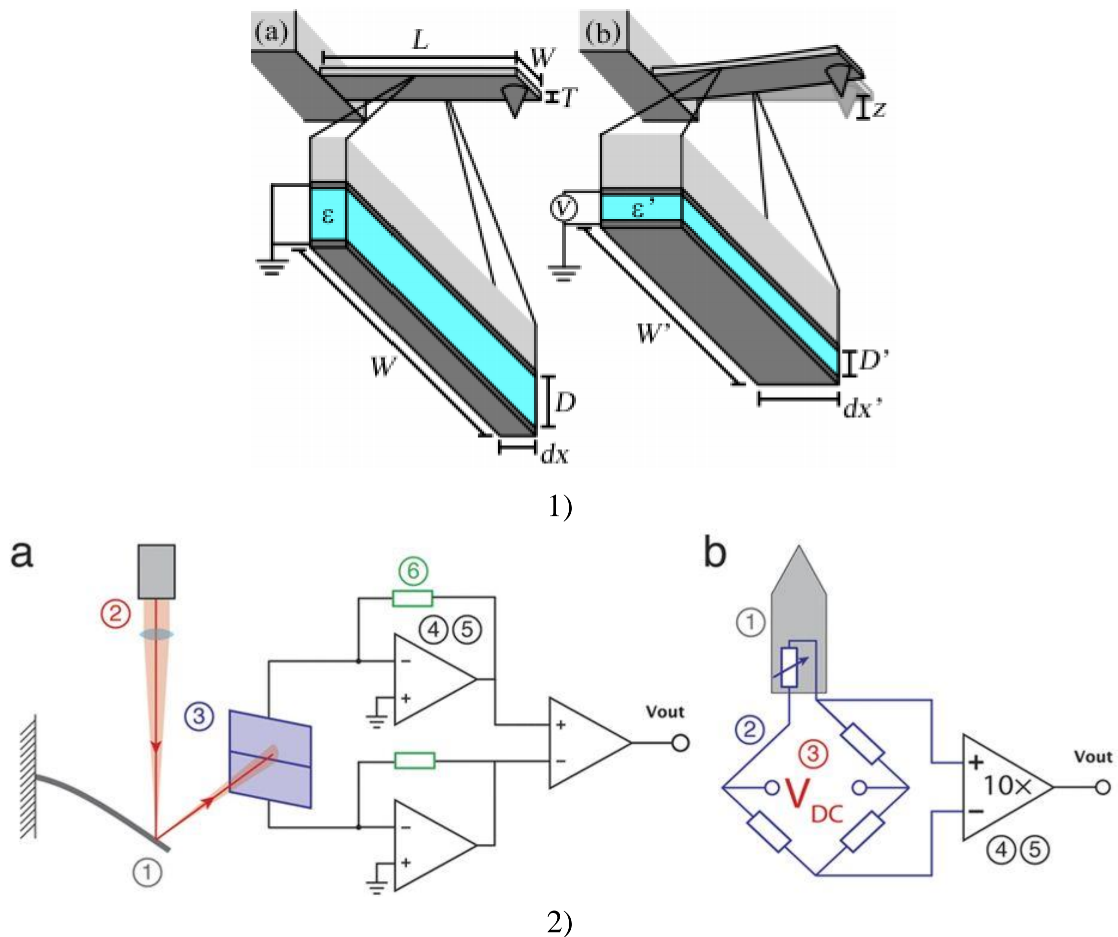

Figure 2. 3: 1) A capacitive driving atomic force microscopy [42]: A thin film capacitor is integrated beneath the cantilever beam. The AFM cantilever can be actuated by introducing a potential difference V across the thin film capacitor. The thin film capacitor is consisted of a deposited metal layer and separated by an insulator with a relative permittivity ε. The separation distance is D. The voltage V across the thin film capacitor causes deflections that alter the capacitor dimensions, separation distance and dielectric properties, hence resulting in the actuation of the cantilever beam. 2) Two typical methods to extract the mechanical deflections of a cantilever beam are exhibited [43]. (a) Optical beam deflection sensing: the beam angular changes are measured by the shifts of the reflected laser spot incorporated with a position detector. (b) Pizeoresistive beam deflection sensing: The beam deflection causes the resistivity changes of the doped silicon, where the changes are also proportional to the voltages measured by the Wheatstone Bridge.

Among the versatile applications of MEMS cantilevers, AFM has achieved great success [44, 45]. Nevertheless, much recent research has focused on MEMS cantilevers in biosensors. MEMS cantilever biosensors can operate in either dynamic or static modes. In the dynamic mode, properties such as resonance frequency and amplitude before and after the external mass perturbation are captured and compared. In contrast, in the static mode, only the displacement of the cantilever beam after the external mass perturbation is measured. With the adoption of proper surface functionalizations, MEMS cantilevers can be used for a variety of biosensing purposes [46-49]. Figure 2.4 shows an example of a MEMS cantilever biosensor.

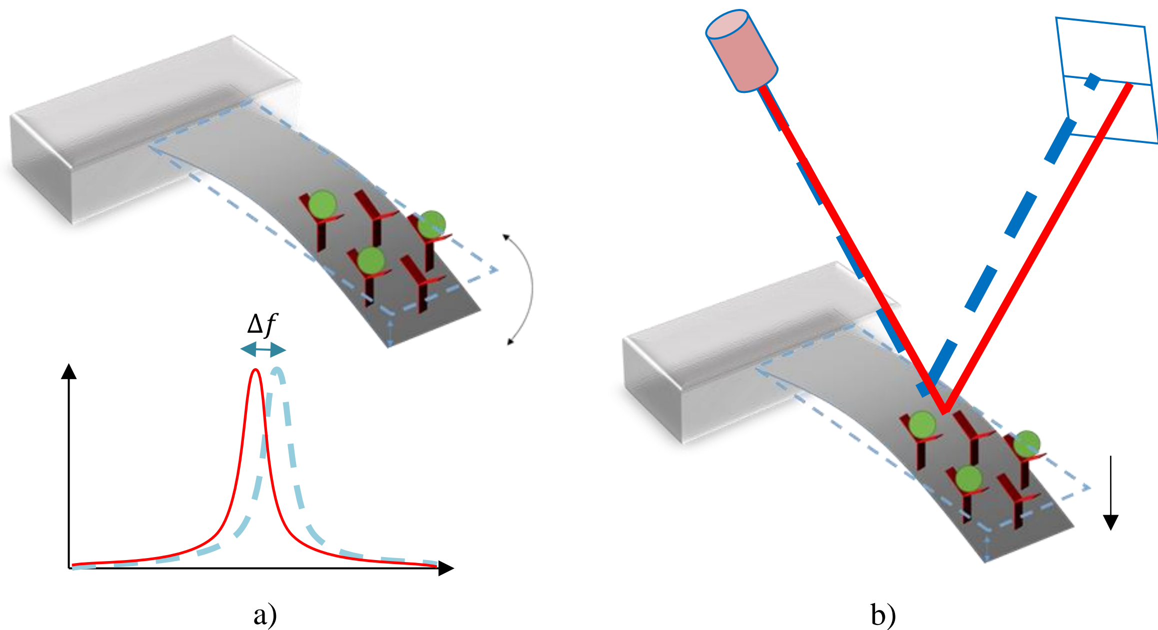

Figure 2. 4: MEMS resonant cantilever biosensor. a) Dynamic mode. b) Static mode.

2.2.2 Clamped-Clamped Structure: Mass Spring Damper System

Another widely investigated MEMS resonator structure is the mass-spring-damper system. This structure can be briefly described as a block of proof mass that has been confined to in-plane vibration. Figure 2.5 (a) exhibits a simple 1-DOF mass-spring-damper model. However, the proof mass in the model is likely to have unwanted out-of-plane movement due to insufficiently fixed boundaries. An improved model is shown in Figure 2.5 (b). Single-DOF clamped-clamped MEMS resonators have a

variety of proof mass designs. Typically, the shapes of the proof mass include circle [50], square [51], rectangle [52], and ring [53]. The supporting spring designs are also vital for a practical 1-DOF resonator. The supporting spring guides the vibration direction of the proof mass and prevents interference from out-of-plane displacement. The designs of both the supporting spring and the proof mass are critical to the production of the final resonator, as they determine the natural behavior of the resonant device. Most importantly, the supporting spring constant and the proof mass weight have a direct impact on the functionality of the resonant device. For instance, they are correlated with the sensitivity and resolution of the designed resonator.

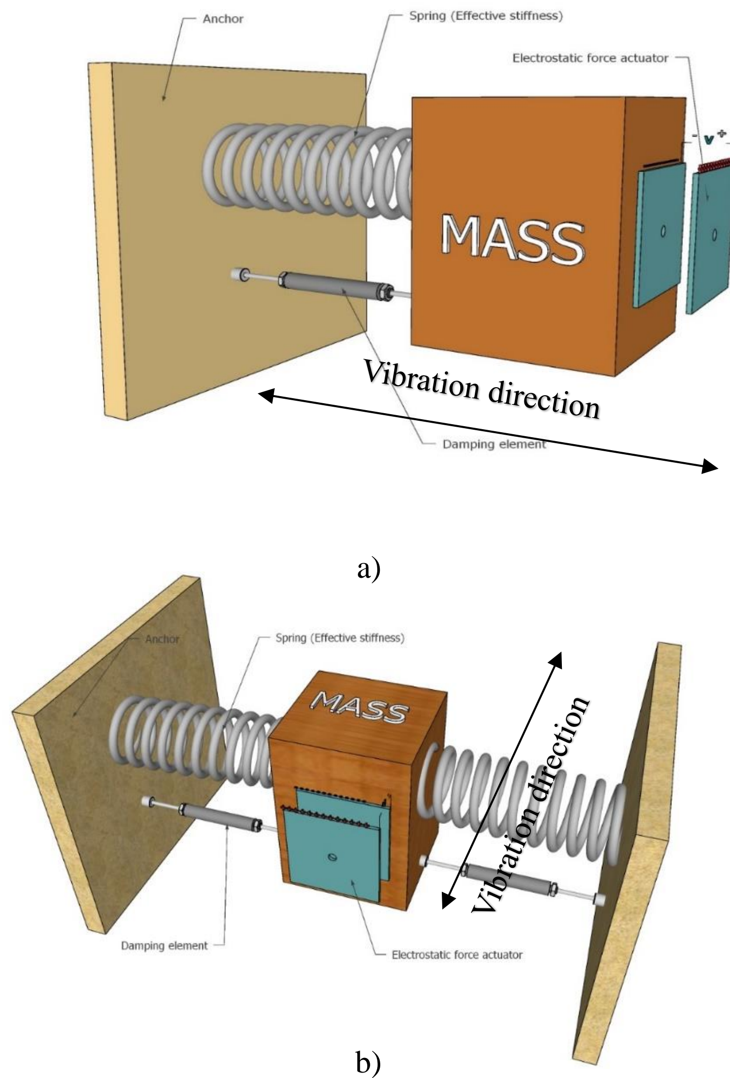

Figure 2. 5: A basic equivalent model of 1-DOF mass spring damper system. a) Simplified mass spring damper model. b) Clamped-Clamped model.

To predict the vibrational behavior of a practical 1-DOF MEMS resonator, an equation of motion is needed. This equation provides a theoretical analysis of the resonance frequency, vibration displacement, and system response of the resonator. Consider a 1-DOF MEMS resonator based on the concept in Figure 2.5 (b), the total supporting spring constant with an effective stiffness value *K*, the proof mass with a weight M, and the damping element with a damping coefficient b. Accordingly, the mass-spring-damper system will start to vibrate with an external stimulus force *F*, and the proof mass will undergo a position shift with a displacement value *X*, which exists on the same plane as the external excitation force. The equation of motion for this 1-DOF mass-spring-damper can be expressed as:

$$M\ddot{X}(t) + b\dot{X}(t) + KX(t) = F(t) \tag{2.6}$$

The equation of motion is an intuitional expression of relation between the acceleration, velocity, and displacement of the proof mass in response to an external excitation force. To obtain the resonance frequency, the equation of motion must be transferred into the frequency domain via Laplace transforms, where *M* and *K* are determined by the dimensions and materials of the resonator. Consider an ideal case in which the mass-spring-damper system is not affect by the damping element and the system is self-actuated without an external force. The equation of motion in the frequency domain can be expressed as:

$$Ms^2X(s) + KX(s) = 0 \tag{2.7}$$

where $s = j\omega$,

$$-M{\omega_0}^2X(s) + KX(s) = 0 \tag{2.8}$$

$$\omega_0 = \sqrt{\frac{K}{M}} \quad \& \quad f_0 = \frac{1}{2\pi}\sqrt{\frac{K}{M}} \tag{2.9}$$

The displacement of proof mass induced by an external force can be deduced from:

$$X(s) = \frac{F(s)}{Ms^2 + bs + K} \tag{2.10}$$

The quality factor is correlated with the effective stiffness and mass of the resonator, as well as the damping coefficient:

$$Q = \frac{\sqrt{MK}}{b} \tag{2.11}$$

Therefore, the displacement can be reorganized as:

$$X(s) = \frac{\frac{F(s)}{M}}{s^2 + \frac{s\omega_0}{Q} + \omega_0{}^2} \equiv H(s)F(s) \tag{2.12}$$

$$H(w) = \frac{1}{M}\frac{1}{\omega_0{}^2 - w^2 + j\omega\omega_0/Q} \equiv H_{real}(\omega) + jH_{im}(\omega) \tag{2.13}$$

The displacement of proof mass can be altered by either tuning the value K or M, simultaneously changing the resonance frequency ω_0. Thus, the 1-DOF MEMS resonator can be used as a sensor for detecting small mass perturbations; for example, small particles docking on the surface of proof mass. Similarly, the resonator can be used as a sensor to measure small physical forces that influence the effective spring stiffness. A system-response model in both time and frequency domains is shown in Figure 2.6.

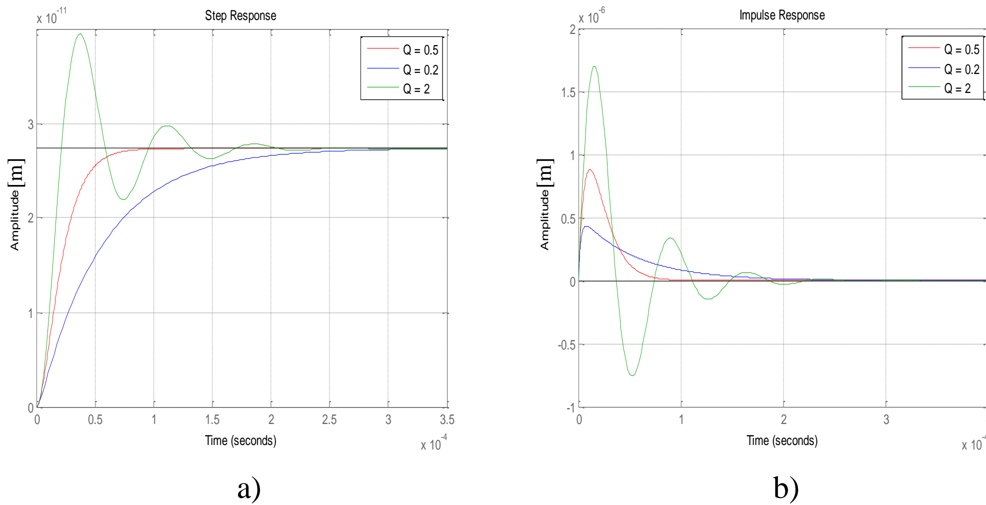

a) b)

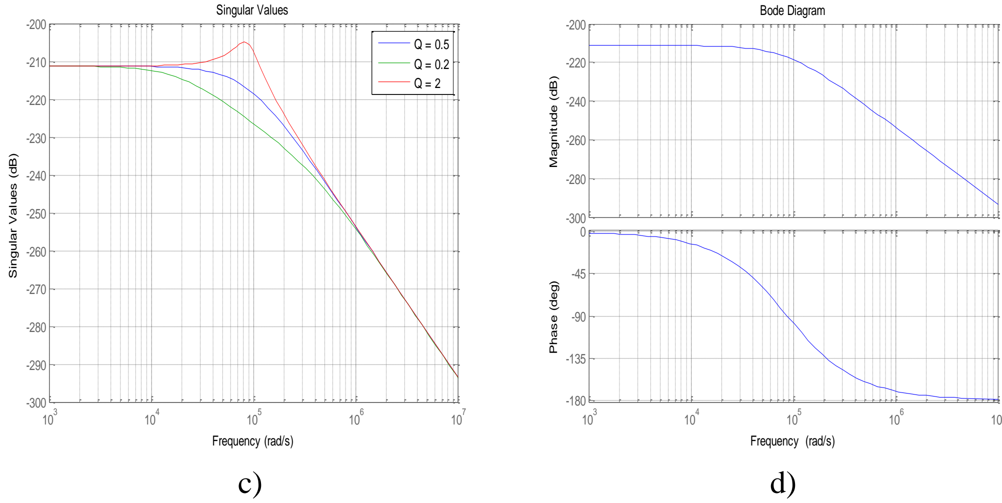

c) d)

Figure 2. 6: 1-DOF MEMS resonator system response: a) Step response. b) Impulse response. c) Frequency domain response. d) Bode plot.

Clamped-clamped 1-DOF MEMS resonators are widely used for sensing tiny physical forces, such as inertial force. A 1-DOF MEMS resonator gyroscope can achieve a quality factor of a few ten thousands [54], while a more complex design could achieve a quality factor of 5.1×10^5 with a 74.9 s decaying time constant [55]. Furthermore, MEMS resonators are suitable for measuring accelerations [56].

One-DOF MEMS resonators can also be found in biosensors, such as the measurements of microdroplets [57], the biotin-streptavidin interaction [58], and glucose molecules [59]. Figure 2.7 shows the principle of a 1-DOF MEMS resonator biosensor.

To define the sensitivity of 1-DOF MEMS resonators and help characterize such devices, a normalized figure of merit is required. The general output metrics are resonance frequency and the relative resonance frequency shift due to external perturbations. As in the principle of clamped-clamped 1-DOF MEMS resonators, either induced stiffness or mass variations can be measured as a result of resonance frequency shifts. Accordingly, the final expression of normalized sensitivity can be written as [21, 25]

$$S_{1-DOF}^{Mass} = \left| \frac{f}{\partial f_0} \times \frac{\partial M}{M} \right| \approx \frac{1}{2} \tag{2.14}$$

$$S_{1-DOF}^{Stiff} = \left|\frac{f}{\partial f_0} \times \frac{\partial K}{K}\right| \approx \frac{1}{2} \tag{2.15}$$

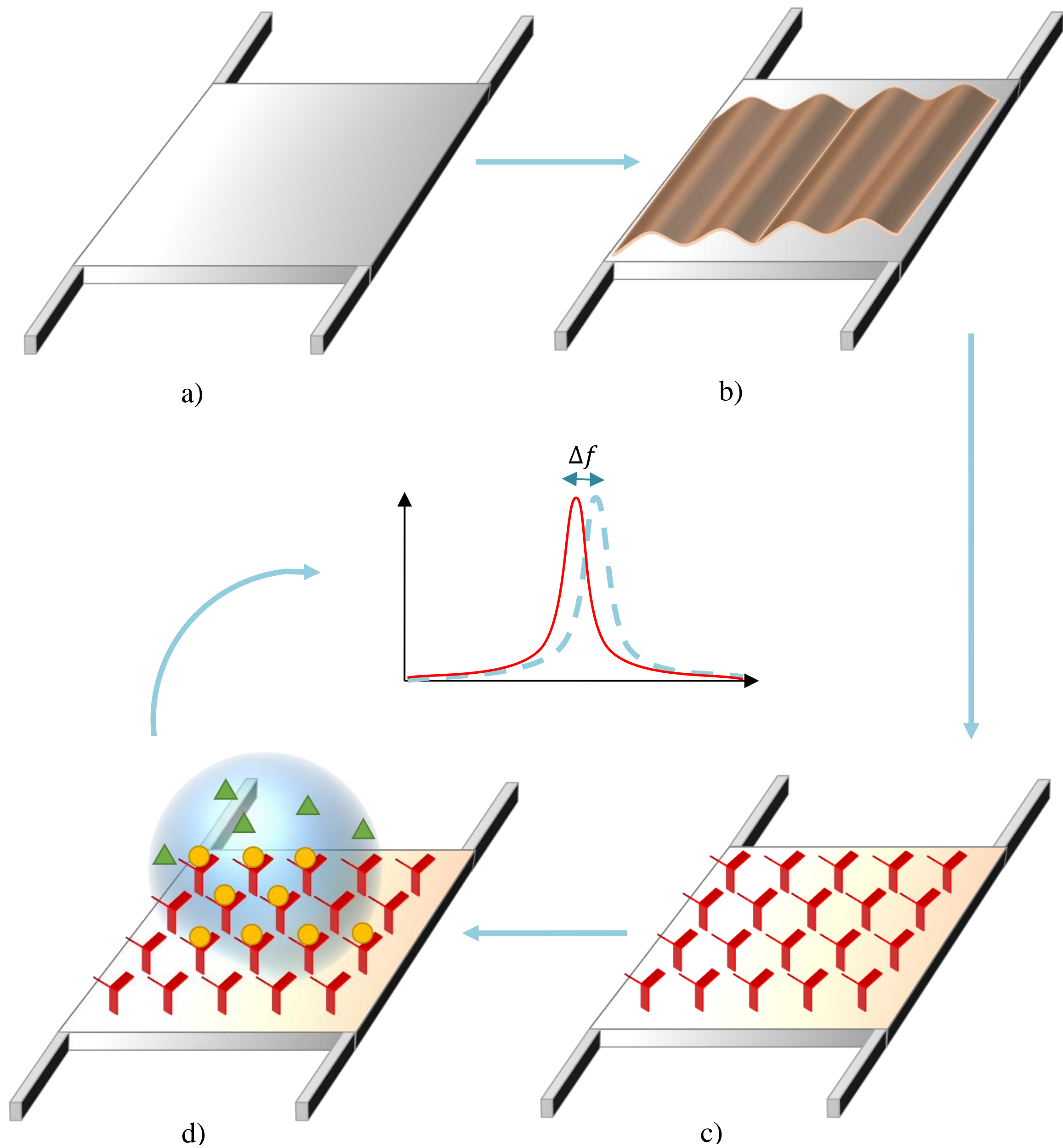

Figure 2. 7: 1-DOF MEMS resonator biosensor. a) Proof mass surface cleaning. b) Surface functionalization. c) Forming bio-affinity counterpart layer. d) Deposition of sample solution, target molecules are bonded with selective counterpart.

2.2.3 Multi-DOF Coupled Resonators

Demand for novel miniature devices continues to grow, and 1-DOF MEMS resonators have played a role in such devices thanks to their batch fabrication capability and superior functionality as transducers. Despite the progress so far, researchers are pursuing improvements and optimizations. However, there is an obstacle in the way of further extending the capabilities of 1-DOF resonators. Limited by the fabrication process and materials, the development of MEMS resonators require system- and structure-wise innovation. A natural solution is to increase the degree of freedom. This can realize specific vibration modes among multiple resonators in an interrelated oscillating system. A multi-DOF resonant system consists of two or more resonators, and adjacent resonators are connected through a coupling element. Figure 2.8 presents a fundamental 2-DOF resonator model.

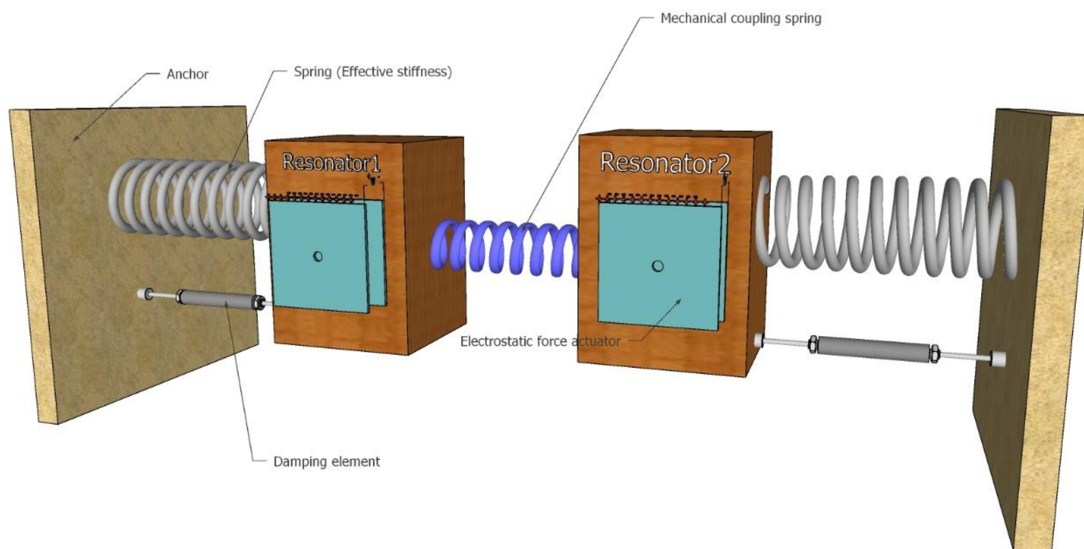

Figure 2. 8: A 2-DOF coupled resonator mechanical model.

The coupling element in the multi-DOF system determines the behavior of the device. To form correlated resonator pairs, the coupling element can take the form of a mechanical cell or a physical phenomenon that exploits the electrostatic force. The mechanical coupling may already exist as the cantilever anchor or may be designed as an independent component in the multi-DOF system. For instance, a multi-DOF MEMS

cantilever array has been proposed that utilizes four cantilevers coupled to a shuttle [60]. The coupled multi-DOF cantilever array can detect biochemical mixtures and has achieved a viable label-free technique. Moreover, a 3-DOF coupled cantilever array has been proposed that can verify two types of mass changes simultaneously [61]. The unique vibration modes among the three coupled cantilevers are used as fingerprints whereby different mass perturbations can be distinguished. Another research trend of MEMS cantilever arrays explores the possibility of asymmetrical structures, including several different cantilever designs [62]. Figure 2.9 illustrates a series of multi-DOF MEMS cantilever arrays [21, 60, 63].

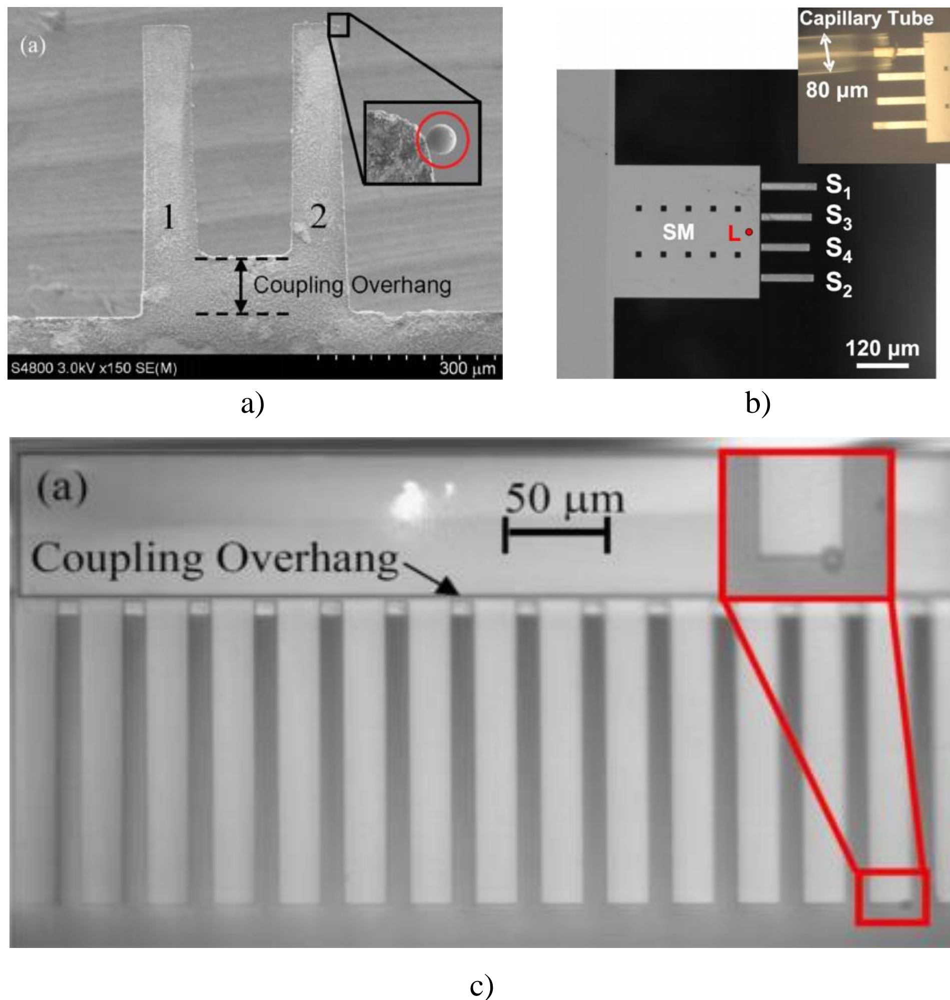

Figure 2. 9: Multi-DOF cantilever array with mechanical coupling [21, 60, 63].

As well as the cantilever array, the clamped-clamped mass-spring-damper can also be coupled through a mechanical beam. A mechanically coupled resonant

accelerometer, for example, has shown great improvement over the conventional 1-DOF device [64]. A multi-DOF coupled resonator gyroscope [22, 65], on the other hand, has proven that the coupled resonator system can improve the overall sensing performance.

Another widely applied coupling element is electrostatic coupling. Electrostatic coupling can be perfectly equivalent to mechanical coupling, with the extra capability of tunable coupling strength. To explain the principle, a comparison will be made that shows both mechanical and electrostatic coupling can achieve the same effective coupling strength. Figure 2.10 shows two possible designs of mechanical coupling elements. The straight coupling beam can be considered as a clamped-clamped guided beam structure; hence, the effective coupling stiffness is expressed as:

$$k_{scb} = \frac{12EI}{h^3} = \frac{EtW^3}{h^3} \tag{2.16}$$

where $I = \frac{\mathrm{tW}^3}{12}$, h and t are the cross-section width and thickness, and W is the straight beam transverse length.

The folded coupling beam achieves a relatively weaker coupling strength but maintains the properties of the coupled system. To determine the effective stiffness of the folded coupling beam, a simplified method is implemented in which the folded beam is equivalent to two straight beams in series. However, this simplification is only valid for a folded coupling beam with a short transverse length. By revising the stiffness equation for the straight coupling beam, the stiffness of the folded coupling beam can be calculated:

$$k_{vertical} = \frac{12EI}{L^3} = \frac{Eth^3}{L^3} \tag{2.17}$$

The small transverse beam connecting two vertical beams can be ignored, as it is far smaller in reality. Therefore, one folded coupling beam can be treated as two straight beams in series:

$$k_{fcb} = (\frac{1}{k_{vertical}} + \frac{1}{k_{vertical}})^{-1} = \frac{Eth^3}{2L^3} \quad (2.18)$$

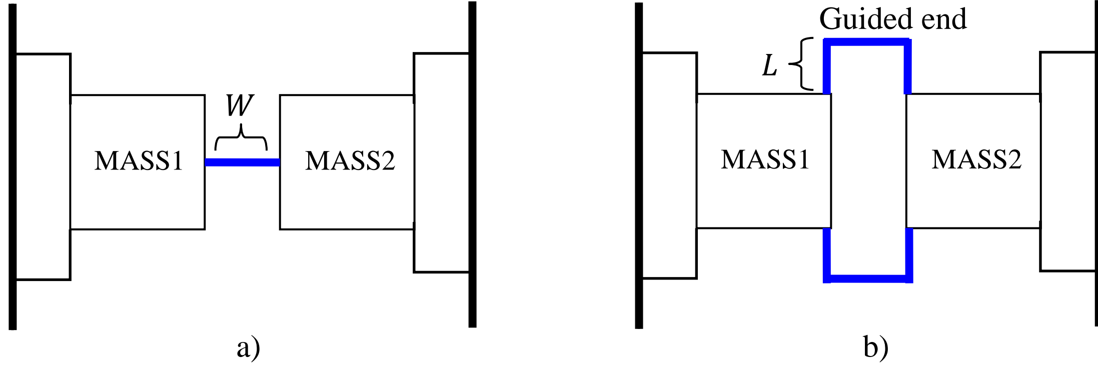

Figure 2. 10: Mechanical Coupling. a) Straight beam coupling. b) Folded beam coupling

Unlike mechanical coupling, the electrostatic coupling is less intuitive. The fundamental principle can be established on two identical and parallel capacitive plates, between which a given DC potential difference exists. The stored charges in the gap interact and induce an electric field. The displacements of the two plates will result in potential energy generation, expressed in a form of physical force and further computed as an effective spring stiffness. Figure 2.11 shows an electrostatic coupling between two resonator proof masses. Assume a stimulus is applied, and the 2-DOF resonator starts to vibrate with a displacement value x, the original separated gap between the two proof masses d, the DC potential difference V, and the parallel cross-section area A. The effective electrostatic coupling stiffness can be calculated as:

$$E = \frac{1}{2}CV^2 - CV^2 = -\frac{1}{2}CV^2 \quad (2.19)$$

where $C = \varepsilon A/(d - x)$, ε is the permittivity of the medium in the gap, most commonly air.

$$F_{es} = \frac{\partial E}{\partial x} = \frac{1}{2}\frac{\partial C}{\partial x}V^2 = \frac{\varepsilon A V^2}{2d^2}\left(1 + 2\frac{x}{d} + 3\frac{x^2}{d^2} + 4\frac{x^3}{d^3}\right) \approx \frac{\varepsilon A V^2}{2d^2}(1 + 2\frac{x}{d}) \tag{2.20}$$

By using Hooke's Law, the electrostatic coupling stiffness is:

$$k_{es} = \frac{\partial F_{es}}{\partial x} \approx -\frac{\varepsilon A V^2}{d^3} \tag{2.21}$$

Unlike mechanical coupling stiffness, electrostatic coupling stiffness is always negative. The negative coupling stiffness will result in only a "pull" physical force; however, the mechanical coupling stiffness has both "push" and "pull" states. The direct effect of such a situation is the vibration mode exchange, details of which will be given in later sections. The main advantage of electrostatic coupling is that the coupling strength can be altered by tuning the DC potential difference.

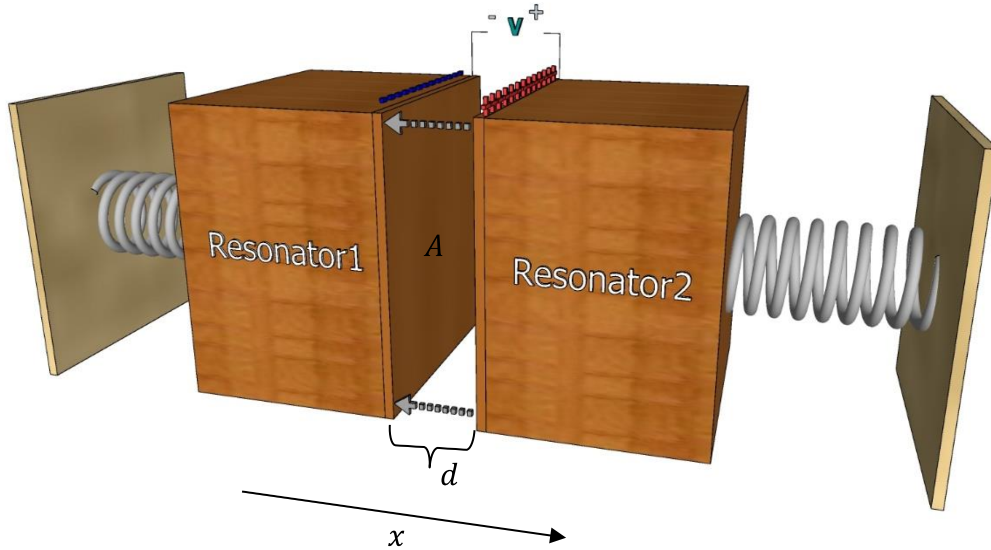

Figure 2. 11： A 2-DOF electrostatic coupled resonator.

Multi-DOF electrostatic coupled resonator systems have shown great potential in sensing applications, with tunable coupling strength, enhanced sensitivity, and sensor system flexibility. Figure 2.12 demonstrates a 2-DOF electrostatic coupled resonator [66]. Following the principle of multi-DOF electrostatic coupled resonators, a mode

localization transduction mechanism is proposed. This novel mode localized multi-DOF weakly coupled resonator system is the topic of this dissertation.

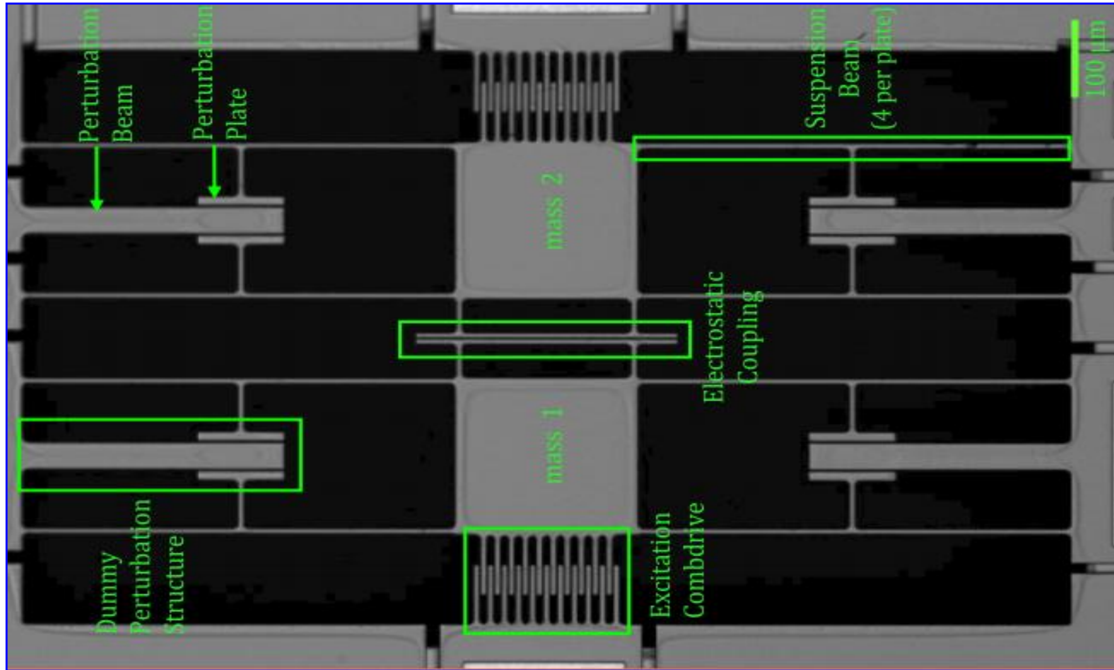

Figure 2. 12: A 2-DOF electrostatic coupled resonator with tunable coupling strength [66]. Each resonator has a relatively large proof mass which is suspended by four supporting beams. The supporting beams can be perturbed via capacitive perturbation plate. The coupled resonator is driven by one group of capacitive comb fingers while another group of comb fingers is used for sensing.

2.2.4 Multi-DOF Mode Localized Weakly Coupled Resonators

To increase the functionality of multi-DOF coupled resonators, a novel transduction output metric that is more efficient than structure- and material-based optimizations is proposed. In what follows, a new output metric is developed from the theory of mode localization. As well as conventional frequency shift monitoring, mode localization based technology exploits the resonant amplitude change in response to perturbation.

Mode localization was first introduced in 1958, with the original theory proposed by Anderson [23] in solid-state physics. Since then, mode localization has been widely investigated and adopted in different disciplines. Mechanical vibration structures are one of the applied field. Especially for a periodic vibrating mechanical structure [67], mode localization will result in energy confinement [68]. To be more specific, as the 2-

DOF electrostatic coupled resonator described above is periodically vibrating, a perturbation either affects the effective stiffness or mass given to one of the two identical resonators. Naturally, the injected perturbation energy should propagate evenly through the coupled system. However, mode localization spatially confines the energy in a small region, which will dramatically change the relative vibration mode. The FEM model given in Figure 2.13 demonstrates the influence of mode localization.

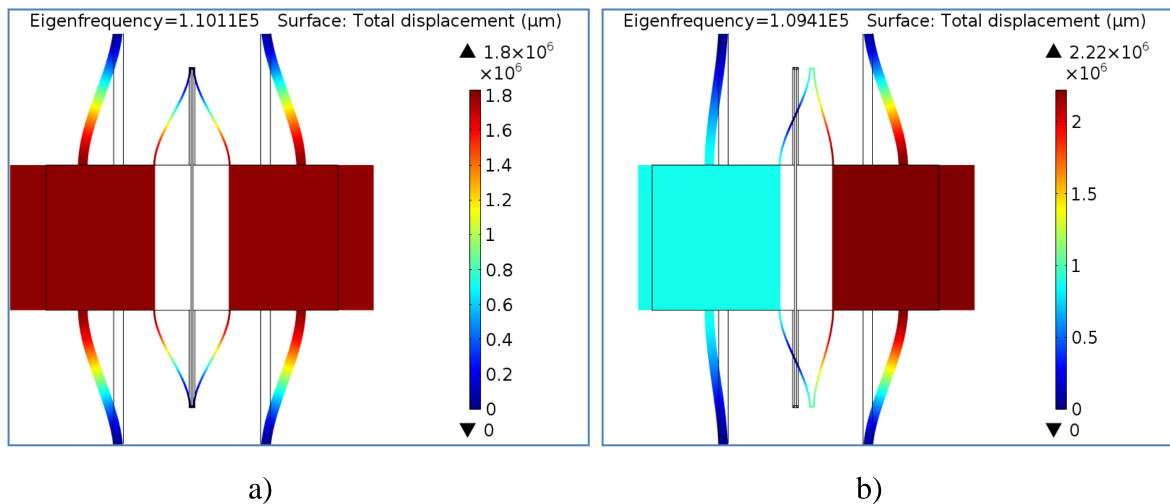

a) b)

Figure 2. 13: FEM simulation model of a 2-DOF mechanical coupled resonator. a) Natural resonance frequency. b) Mode localization effect with 500ng mass perturbation on the left resonator, consequently the left resonator vibration amplitude is dramatically changed but the right one is less affected. The system resonance frequency is also shifted.

Another interesting point from the simulation above is the comparison of resonance frequency shift and vibration amplitude change. The relative resonance frequency shift is 0.64%; however, the amplitude change is 23.3%. The amplitude change induced by mode localization is weighted more in respect to the original state. To delve deeper into this idea, consider the following theoretical analysis of a 2-DOF mode localized coupled resonator. Assume the two resonators are identical: both have effective mass value $M_1 = M_2 = M$, supporting spring constant $K_1 = K_2 = K$, damping coefficient $b_1 = b_2 = b$ and the coupling stiffness Kc. The equation of motion for the coupled resonator system can be expressed:

$$M_1\ddot{X}_1(t) + b_1\dot{X}_1(t) + K_1X_1(t) + K_c[X_1(t) - X_2(t)] = 0 \quad (2.22)$$

$$M_2\ddot{X}_2(t) + b_2\dot{X}_2(t) + K_2X_2(t) + K_c[X_2(t) - X_1(t)] = 0 \quad (2.23)$$

where X_1 and X_2 are the vibration amplitude of resonator 1 and resonator 2. The damping terms are ignored for simplification, and the system is presumed to be purely symmetric. The equations can be solved using an eigenstate method with the assistance of a matrix. Accordingly, equations 2.22 and 2.23 are revised:

$$\lambda \begin{bmatrix} M_1 & 0 \\ 0 & M_2 \end{bmatrix} \begin{bmatrix} u_1 \\ u_2 \end{bmatrix} = \begin{bmatrix} K_1 + K_c & -K_c \\ -K_c & K_2 + K_c \end{bmatrix} \begin{bmatrix} u_1 \\ u_2 \end{bmatrix} \quad (2.24)$$

$$\lambda M_{matrix} u = K_{matrix} u \quad (2.25)$$

where u and λ are the eigenvectors and eigenvalues. These two parameters are correlated with the coupled resonator system behavior:

$$X = ue^{j\omega t} = \begin{bmatrix} u_1 \\ u_2 \end{bmatrix} e^{j\omega t} \quad \& \quad \ddot{X} = -\omega^2 u e^{j\omega t} = -\omega^2 X \quad (2.26)$$

$$\lambda = -\omega^2 \quad (2.27)$$

The coupled resonator vibration amplitude is determined by the eigenvectors, and the vibration mode frequency is determined by the eigenvalues. Owing to the two equations of motion and matrix computations, the solutions consist of two groups of eigenvectors and eigenvalues. More specifically, one eigenvalue corresponds to one vibration mode resonance frequency, and the two resonators in the coupled system each have a vibration amplitude u_1 and u_2 in respect to the mode frequency. The final expression of the solutions are:

$${\omega_1}^2 = \frac{K}{M} \quad \& \quad {\omega_2}^2 = \frac{K + 2K_c}{M} \quad (2.28)$$

Before examining the solutions further, the electrostatic coupling and mechanical coupling mode exchange mystery can now be solved. By inspecting the two computed

mode frequencies, one has a term of coupling spring stiffness K_c. If the 2-DOF coupled resonator has a mechanical coupling, K_c is positive and hence the second mode frequency will be higher than the first. However, if an electrostatic coupling is used, K_c will be negative and the second mode frequency will be smaller than the first, which results in a vibration mode exchange. To return to the matrix solutions, the two groups of vibration amplitude are (under the condition of mechanical coupling):

$$u_{\omega 1} = \begin{bmatrix} 1 \\ 1 \end{bmatrix} \quad \& \quad u_{\omega 2} = \begin{bmatrix} 1 \\ -1 \end{bmatrix} \tag{2.29}$$

The two resonators with the first vibration mode are in the *in-phase* mode because they vibrate in the same direction. In the second vibration mode, on the contrary, the two resonators vibrate in opposite directions, and hence they are in the *out-of-phase* mode. Figure 2.14 shows the vibration modes of a 2-DOF mechanical coupled resonator.

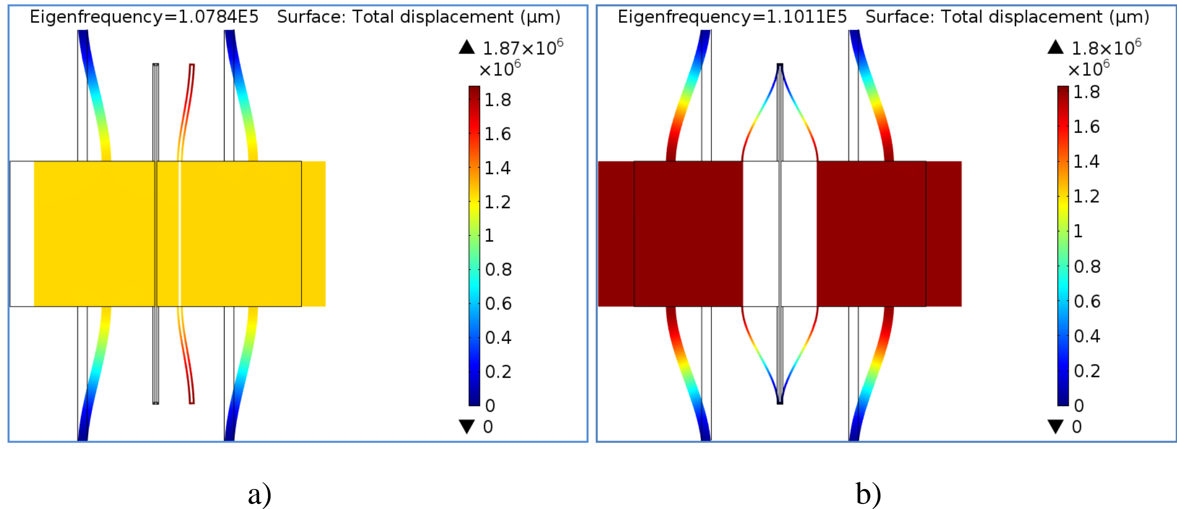

Figure 2. 14: 2-DOF mechanical coupled resonator vibration modes. a) In-phase mode. b) Out-of-phase mode.

Another characterization of multi-DOF mode localized coupled resonators is the eigenvalues loci curve veering [69-72]. The eigenvalues obtained from the system matrix can be plotted as a function of external perturbations; for instance, added masses or effective spring stiffness alterations. Accordingly, the two vibration modes, in-phase and out-of-phase, each have a curve plotted against the perturbations:

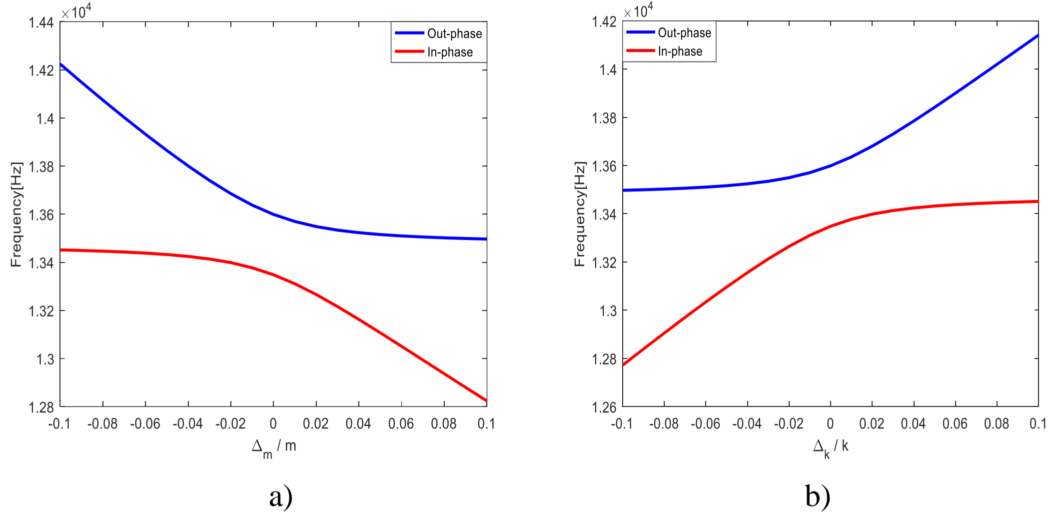

Figure 2. 15: Loci veering of a 2-DOF mode localized mechanical coupled resonator. a) Mass perturbations. b) Stiffness perturbations.

The in-phase and out-of-phase eigenvalue curves are symmetrical, and the trends of the curves are likely to intersect. However, the two curves cannot cross. The gap between the curves is determined by the coupling strength K_c. For a clearer interpretation of loci veering and the veering zone, Figure 2.16 illustrates the loci veering with different coupling strengths.

The following conclusion can be drawn after observing the loci veering diagram: The weaker the coupling strength in coupled resonator systems, the closer the gap in the loci veering zone. Accordingly, coupled resonator systems can directly benefit from extending the linear response range when the weak coupling condition is satisfied. A narrow veering zone enhances the sensitivity of mode localized behavior. Following this principle, electrostatic coupling can achieve relatively lower coupling strength by simply tuning the DC potential difference, whereas mechanical coupling has limited flexibility in mode localized weakly coupled resonator systems.

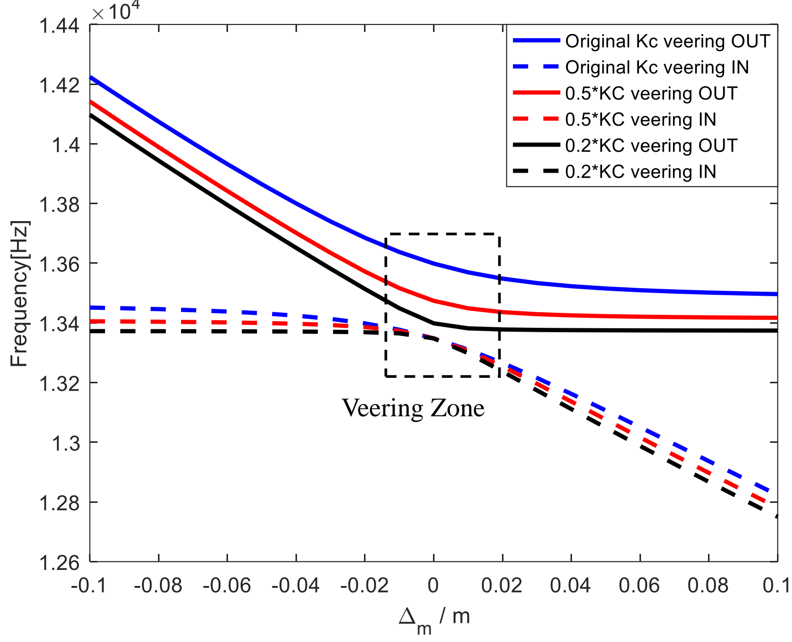

Figure 2. 16: Loci veering of a 2-DOF mode localized mechanical coupled resonator with different coupling strength.

As the output metric comparison from previous section, where the mode localized coupled resonator exploits vibration amplitude changes and mode frequency shifts as sensing outputs, the vibration amplitude changes yield higher sensitivity. The eigenvector solutions from the system matrix stand for the vibration amplitudes and the final sensitivity can be derived as follows:

$$\begin{bmatrix} M_1 & 0 \\ 0 & M_2 \end{bmatrix} \begin{bmatrix} \ddot{X}_1 \\ \ddot{X}_2 \end{bmatrix} + \begin{bmatrix} K_1 + K_c + \Delta K & -K_c \\ -K_c & K_2 + K_c \end{bmatrix} \begin{bmatrix} X_1 \\ X_2 \end{bmatrix} = 0 \tag{2.30}$$

$$\begin{bmatrix} M_1 + \Delta M & 0 \\ 0 & M_2 \end{bmatrix} \begin{bmatrix} \ddot{X}_1 \\ \ddot{X}_2 \end{bmatrix} + \begin{bmatrix} K_1 + K_c & -K_c \\ -K_c & K_2 + K_c \end{bmatrix} \begin{bmatrix} X_1 \\ X_2 \end{bmatrix} = 0 \tag{2.31}$$

where ΔK is the stiffness perturbation that can be applied on either resonator in the coupled system and ΔM is the mass perturbation. The deduced eigenvector solution groups corresponding to the in-phase mode with eigenvalue λ_{w1} and out-of-phase mode with eigenvalue λ_{w2}, respectively [25, 71]:

$$\left|\frac{u_{\omega i}-u_{\omega 0i}}{u_{\omega 0i}}\right| \approx \left|\frac{K}{4K_c}\times\frac{\Delta K}{K}\right| \qquad i=1,2 \tag{2.32}$$

$$\left|\frac{u_{\omega i}-u_{\omega 0i}}{u_{\omega 0i}}\right| \approx \left|\frac{K}{4K_c}\times\frac{\Delta M}{M}\right| \qquad i=1,2 \tag{2.33}$$

where $u_{\omega 0i}$ are the original eigenvectors corresponding to either one of the two vibration modes with its unperturbed resonance frequency. $u_{\omega i}$ are the shifted eigenvectors in response to the external stimulus. The expression of normalized eigenvector shift sensitivity can be written:

$$S^{Mass}_{\substack{2-DOF \\ eigenvector}} = \left|\frac{u}{\partial u}\times\frac{\partial M}{M}\right| \approx \frac{K}{4K_c} \tag{2.34}$$

$$S^{Stiff}_{\substack{2-DOF \\ eigenvector}} = \left|\frac{u}{\partial u}\times\frac{\partial K}{K}\right| \approx \frac{K}{4K_c} \tag{2.35}$$

The relative normalized resonance frequency shift sensitivity can also be obtained:

$$S^{Mass}_{\substack{2-DOF \\ freqshift}} = \left|\frac{f}{\partial f}\times\frac{\partial M}{M}\right| \approx \frac{1}{2} \tag{2.36}$$

$$S^{Stiff}_{\substack{2-DOF \\ freqshift}} = \left|\frac{f}{\partial f}\times\frac{\partial K}{K}\right| \approx \frac{1}{2} \tag{2.37}$$

Evidently, eigenvector shift as an output metric possesses higher normalized sensitivity. By carefully designing the supporting spring stiffness K and the coupling strength K_c, the overall normalized eigenvector shift sensitivity can be optimized. However, the supporting spring stiffness can hardly be adjusted in practice since it is fixed by the original design. A simple approach is to decrease the coupling strength. Thus, electrostatic coupling is the most suitable candidate for this task. In addition, a tunable coupling strength also provides adjustable sensitivity, which offers flexibility in a variety of applications.

A 2-DOF mode localized electrostatic weakly coupled resonator has been proven

to have two to three orders of magnitude higher sensitivity than 1-DOF frequency shift based resonator devices [21, 73]. Figure 2.17 illustrates two 2-DOF mode localized electrostatic weakly coupled resonators [71].

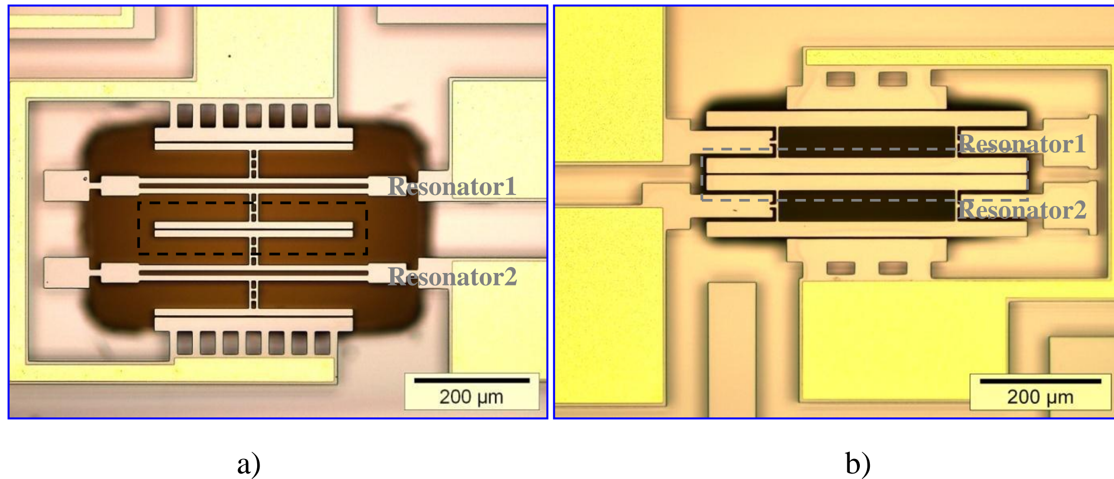

a) b)

Figure 2. 17: 2-DOF mode localized electrostatic weakly coupled resonators [71]. a) Two double ended tuning forks (DETF) resonators with both ends anchored and they are coupled via electrostatic coupling, as shown in the dash box. Two adjacent electrodes serve as drive and sense electrodes, respectively. b) Two double free-free beam resonators are coupled via electrostatic coupling, as shown in the dash box. The double free-free beam resonator is suspended by tether supporting spring. Two adjacent electrodes serve as drive and sense electrodes, respectively.

Moreover, multi-DOF mode localized weakly coupled resonators have the capability of inherent common mode noise rejection. The instability of the ambient environment, such as temperature and pressure, will cause resonance frequency shifts or vibration amplitude changes even without any perturbations. The mode localized weakly coupled resonators have experimentally proven that the eigenvector shifts are less influenced by environmental factors, and hence the system has improved common mode rejection [74].

2.2.5 Multi-DOF Mode Localized Weakly Coupled Resonators: Vibration Amplitude Ratio as An Output Metric

Delving deeper into the potential of multi-DOF mode localized weakly coupled resonators, a new theory has been proposed that utilizes resonator vibration amplitude

ratio as an output metric. Originally proposed by Gil-Santos [75], amplitude ratio theory uses the vibration amplitude of a specific resonator in one vibration mode (e.g., the in-phase mode in the coupled system) divided by another vibration amplitude in a different mode (e.g., the out-of-phase mode). However, such a technique has an intrinsic defect: it requires a full frequency sweep to extract all the vibration modes and shapes in a wide range of bandwidths. Consequently, this drawback impinges on the device functionality, as it cannot realize a real-time transducer. Recently, Chun Zhao [76] has adopted a similar concept but has ingeniously surmounted the difficulty by using the quotient of vibration amplitudes that belong to each resonator in the coupled system within the same vibration mode. The real-time transduction can thereby be implemented. Fundamentally, the theoretical analysis of amplitude ratio shares the same principle as the eigenvector and eigenvalue computations. To be more specific, the amplitude ratios can be expressed by revising equation 2.29:

$$AR_{\omega 1} = 1 \qquad \& \qquad AR_{\omega 2} = -1 \tag{2.38}$$

The same 2-DOF mode localized coupled resonator simulation model is employed in this section. The calculated amplitude ratios are plotted as a function of either mass perturbations or stiffness perturbations, as demonstrated in Figure 2.18.

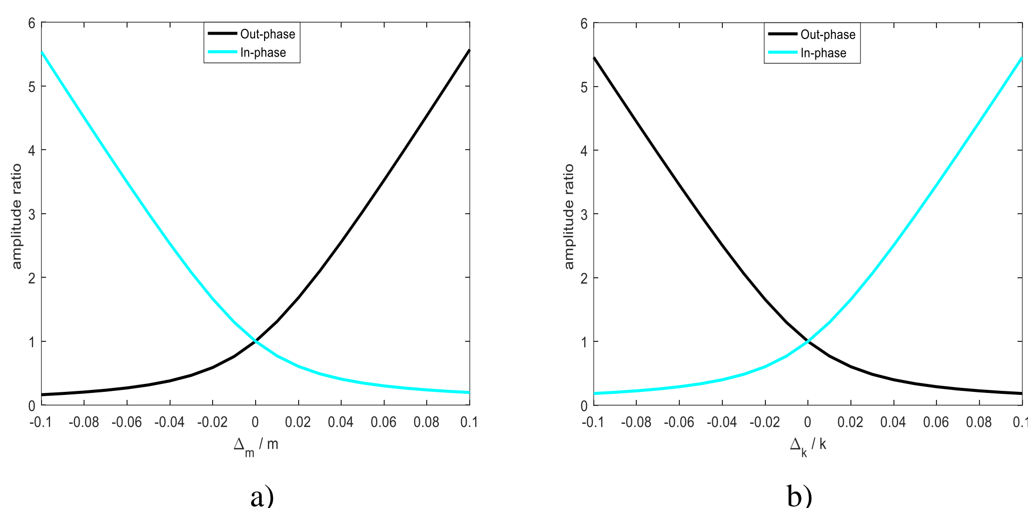

Figure 2. 18: Amplitude ratios of a 2-DOF mode localized mechanical coupled resonator. a) Mass perturbations. b) Stiffness perturbations.

A comparison is conducted of the three output metrics: resonance frequency shift, eigenvector shift, and amplitude ratio change. By plotting the sensitivity curves with the same perturbations, and additionally rescaling the sensitivity as normalized change in percentage, the comparison is fair and reasonable. The normalized sensitivity of the amplitude ratio change is one to two orders of magnitude greater than the eigenvector shift, and the normalized sensitivity of the eigenvector shift is approximately two to three orders magnitude greater than the resonance frequency shift.

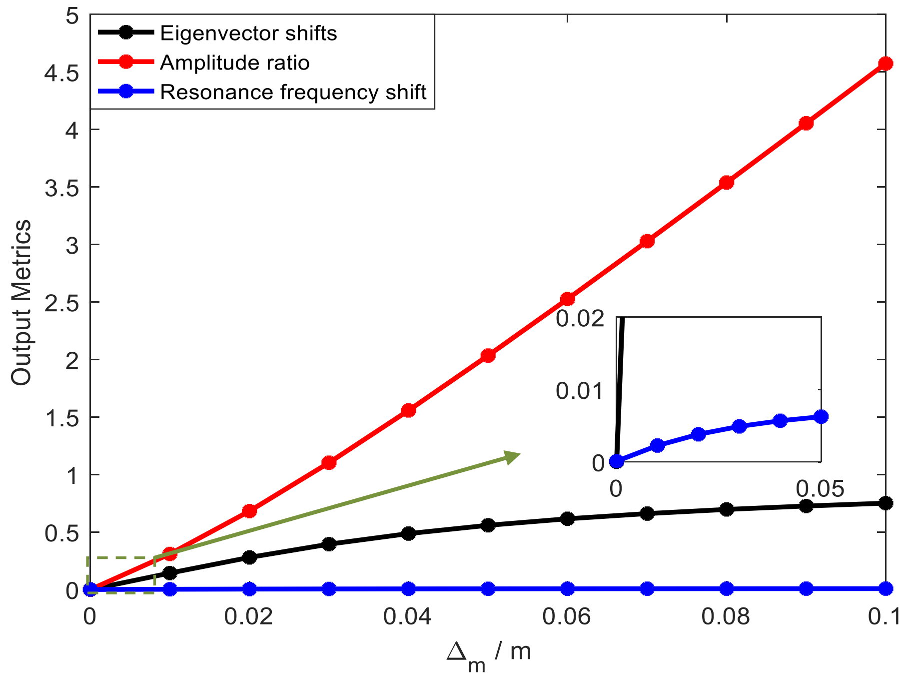

Figure 2. 19: Sensitivity comparisons of three different output metrics.

In addition to its superior sensitivity, the amplitude ratio as an output metric also possesses the capability of common mode noise suppression. Since the quotient of the two vibration amplitudes is adopted, the affections of ambient common mode noises induced system variations are less weighted. Further common mode rejection ability is granted by the transduction signal read-out stage; namely, a differential pick-off interface circuit. More details will be covered in later chapters.

2.2.6 Multi-DOF Mode Localized Weakly Coupled Resonators: Mode Aliasing

As explained in previous sections, weaker coupling strength results in higher sensitivity. However, coupling strength cannot decrease indefinitely. Not only is it constrained by the physical properties of the coupling element, but it is also limited by the system bandwidths. Figure 2.20 shows the consequences of extremely weak coupling in a 2-DOF mode localized mechanical coupled resonator model.

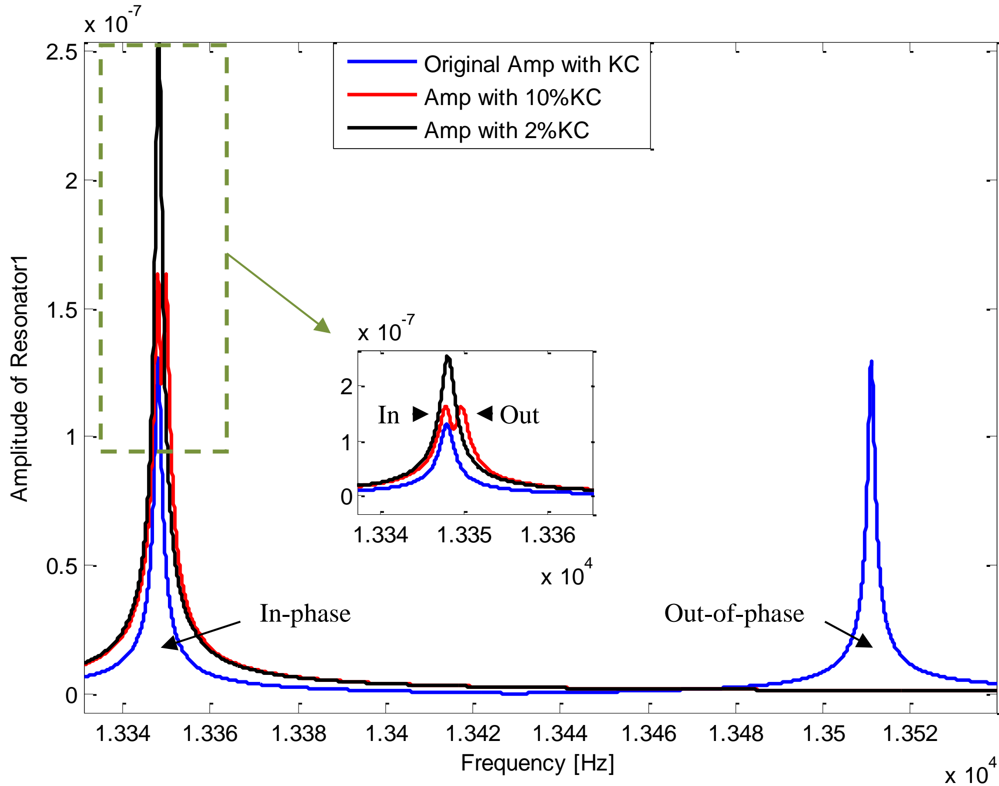

Figure 2. 20: Demonstration of mode aliasing phenomena.

The vibration modes have certain bandwidths, and the gap frequency between the two modes shrinks as the coupling strength decreases. Eventually, the two vibration modes overlap and only one mode is left. This phenomenon is called mode aliasing. However, mode aliasing is not a fatal problem for mode localized weakly coupled resonators. It can be avoided by carefully defining the mode bandwidth and its related cut-off frequency [77]:

$$f_{outphase} - f_{inphase} \geq 2 \times f_{cut-off} \qquad (2.39)$$

The out-of-phase and in-phase resonance frequencies indicate the centre frequencies, where the cut-off frequencies are the two 3 dB points adjacent to the related vibration mode centre frequency. In addition, a mode localized coupled resonator with a low system quality factor and a relatively heavy damping element will lead to mode aliasing. Such influences will be discussed in the following chapters.

2.3 The Advantages and Disadvantages

The development of MEMS resonator technologies has been rapid and encouraging; however, certain drawbacks cannot be denied. Despite the superior functionality of multi-DOF coupled resonator systems, several compromises must be made. Table 2.1 below summarized the pros and cons of the MEMS resonators that have been introduced so far. Efforts to compensate for those disadvantages will be discussed in this dissertation.

Resonator type	***Pros***	***Cons***
1-DOF resonators	• Simple structure, fast design, easy to fabricate. • Frequency shift as an output metric. • Output can be extracted via different facilities: electrically or optically. • High fabrication yield rate, easier to be commercialized. • Relative simple chip wire bonding and packaging.	• Relative lower sensitivity. • Ambient environment noises can heavily affect the performance. • Cannot perform multiple sensing tasks.

Multi-DOF coupled resonators	• Improved normalized sensitivity. • Use vibration modes and mode frequencies to perform multiple targets sensing or mixture targets discriminations. • Can adopt differential pick-off method to suppress noises. • Electrostatic coupling can realize system flexibility for a variety of applications.	• Complex device structure design. • Relative low fabrication yield rate. • Electrostatic coupling requires high DC voltage. • Relative higher power consumption. • Still mainly remain in labs.
Multi-DOF mode localized weakly coupled resonators	• Extremely high normalized sensitivity. • Use eigenvector shifts or vibration amplitude ratios as output metric. • Inherent common mode rejection capability. • Tunable electrostatic coupling can realize controllable system sensitivity. • Potentials and opportunities that still waiting to be discovered.	• Complex interface circuit design, especially in high frequency devices. • Suffering from fabrication tolerances. • Electrostatic coupling requires high DC voltage. • Operating in low Q environment will dramatically affect the performance and make it difficult for biosensing.

Table 2. 1: MEMS resonators pros and cons.

2.4 Chapter Summary

This chapter covers the fundamentals of conventional 1-DOF resonators and reviewes two basic device structures: cantilevers and mass-spring-dampers.

Furthermore, the chapter introduces multi-DOF coupled resonators, in which the coupling element is either mechanical or electrostatic. A novel sensing metric is described that exploits the mode localization effect, and 2-DOF electrostatic weakly coupled resonators utilizing mode localization is demonstrated. The chapter also includes system characterizations such as normalized sensitivity and mode aliasing. Finally, a comparison is conducted of different types of MEMS resonators.

Chapter 3

MEMS 3-DOF Mode Localized Weakly Coupled Resonator

3.1 Theoretical Analysis of a 3-DOF Mode Localized Electrostatic Weakly Coupled Resonator

3.1.1 Fundamentals

Intuitively, increasing the degrees of freedom in a coupled resonator system should raise its performance (e.g., sensitivity). Although this worked well for 2-DOF coupled resonators, it has limitations for 3-DOF coupled resonator systems. Specifically, as shown in chapter 2, a 2-DOF mode localized weakly coupled resonator improves sensitivity by more than two orders of magnitude over a 1-DOF resonator. Research has been conducted to extend the principle to 3-DOF systems to produce extremely sensitive and high-performance transducers. However, the results have not been as expected; the sensitivity enhancement has been limited [78]. Nonetheless, increasing the degrees of freedom of coupled resonator systems is a worthwhile research topic. Chun Zhao has theoretically proved that by increasing the supporting-spring stiffness of the middle resonator in a 3-DOF coupled resonator system while keeping the first and third resonators the same, the overall sensitivity can be vastly improved [79]. In what follows, a computational method based on matrices and equations of motion is

used to develop a 3-DOF mode localized weakly coupled resonator system.

The 3-DOF mode localized weakly coupled resonator can be equivalent to a lumped mass-spring-damper system. A physical model of such a device is exhibited to correlate the relative parameters. Figure 3.1 demonstrates the operation principle of a 3-DOF coupled resonator.

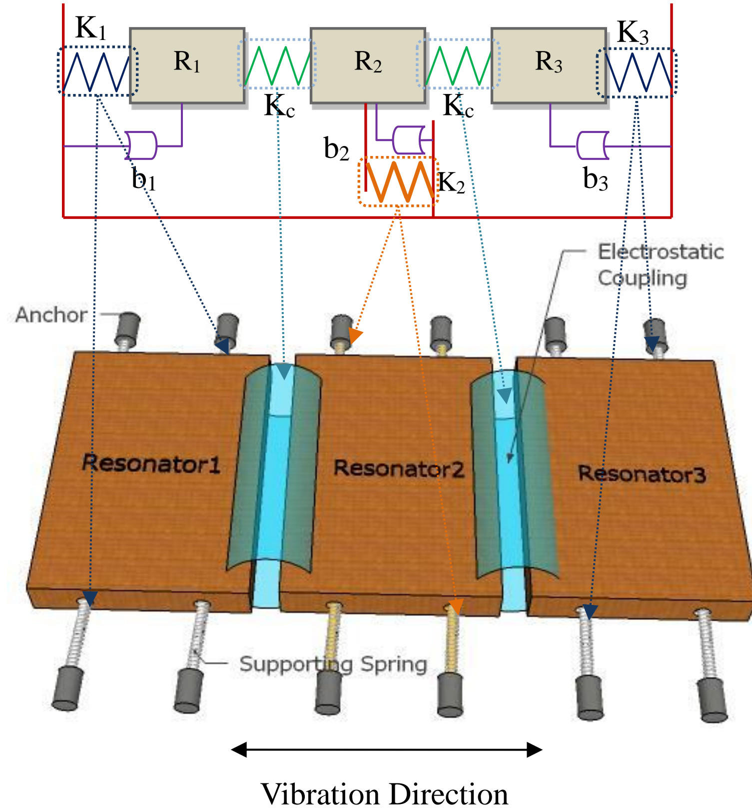

Figure 3. 1: 3-DOF coupled resonator lumped parameter system model.

Regarding to the lumped parameter model of Figure 3.1, assuming the proof mass value of each resonator R1 = R2 = R3 = M, the effective supporting spring stiffness of the first and third resonators K1 = K3 = K, the middle resonator 2 has a unique effective stiffness value with K2 ≠ K, consider a stiffness perturbation is added to resonator 3, thus the effective stiffness of resonator 3 becomes K3 = K + ΔK. The damping coefficients b1, b2, b3 are identical. The motion of the three resonators in the time domain can be expressed as:

$$M\ddot{X}1(t) + b1\dot{X}1(t) + (K_1 + Kc)X1(t) - KcX2(t) = F1\,(t) \qquad (3.1)$$

$$M\ddot{X}2(t) + b2\dot{X}2(t) + (K_2 + 2Kc)X2(t) - Kc(X1(t) + X3(t)) = F2(t) \quad (3.2)$$

$$M\ddot{X}3(t) + b3\dot{X}3(t) + (K_3 + \Delta K + Kc)X3(t) - KcX2(t) = F3(t) \quad (3.3)$$

The equations of motion of a 3-DOF resonator can be re-written in a matrix form and hence can be solved using an eigenstates computation method. The damping coefficients b1, b2, and b3 are disregarded in the following equation. This allows the derivation of expressions for the vibration amplitudes, amplitude ratios, and mode frequencies of the 3-DOF coupled resonator system. The coupled system with a stiffness perturbation on resonator 3 can be expressed as:

$$\lambda_n \begin{bmatrix} M & 0 & 0 \\ 0 & M & 0 \\ 0 & 0 & M \end{bmatrix} \begin{bmatrix} u_{\lambda_n 1} \\ u_{\lambda_n 2} \\ u_{\lambda_n 3} \end{bmatrix} = \begin{bmatrix} K_1 + Kc & -Kc & 0 \\ -Kc & K_2 + 2Kc & -Kc \\ 0 & -Kc & K_3 + \Delta K + Kc \end{bmatrix} \begin{bmatrix} u_{\lambda_n 1} \\ u_{\lambda_n 2} \\ u_{\lambda_n 3} \end{bmatrix} \quad (3.4)$$

where $\lambda_n = -\omega_n{}^2$; n = 1, 2, 3; and the eigenvalue λ_n represents the corresponding mode frequency ($\omega_n = -\sqrt{\lambda_n}$). The vibration amplitudes are correlated with the eigenvectors, and thus the amplitude ratio can be calculated from the parameters $[u_{\lambda_n 1}\, u_{\lambda_n 2}\, u_{\lambda_n 3}]^T$. An eigenvalue loci veering curve can be plotted by adopting proper values for the 3-DOF coupled resonator system parameters. As listed in Table 3.1, the values are chosen to reflect realistic system behavior, and they are verified with experimental data in the following chapters.

Parameters	M	K_1 & K_3	K_2	Kc
Value	6.94ug	48.815N/m	285.212N/m	-0.926N/m

Table 3. 1: System parameters of eigenvalue loci veering curve model for a 3-DOF mode localized electrostatic weakly coupled resonator (with stiffness perturbations).

The eigenvalue loci veering curve and the amplitude ratio versus the stiffness

perturbations are illustrated in Figure 3.2 (a) and (b), respectively.

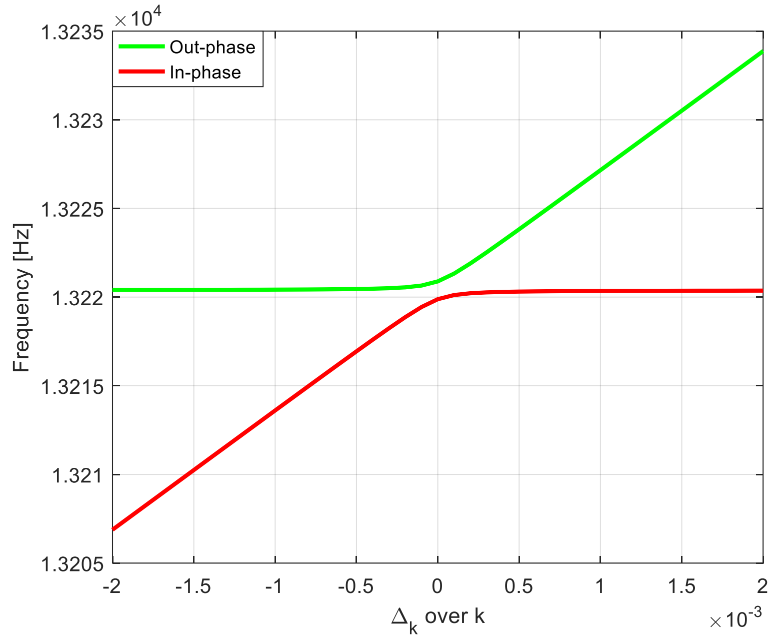

a)

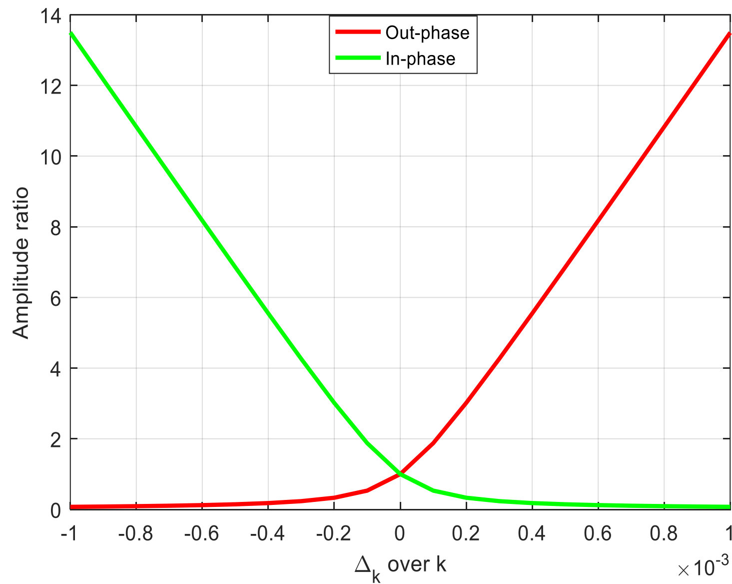

b)

Figure 3. 2: A 3-DOF mode localized electrostatic weakly coupled resonator system behavior. a) Eigenvalue loci veering curve. b) Amplitude ratio versus stiffness perturbations.

To provide convincing evidence that such a 3-DOF coupled resonator design can considerably improve sensitivity, the system behavior diagrams in Figure 3.2 show a comparison with a 2-DOF electrostatic weakly coupled resonator that possess the same

system parameter values as listed in Table 3.1.

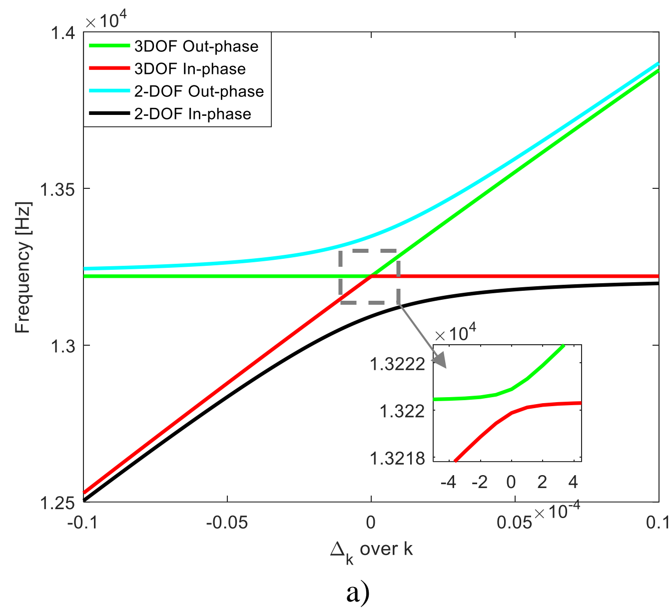

a)

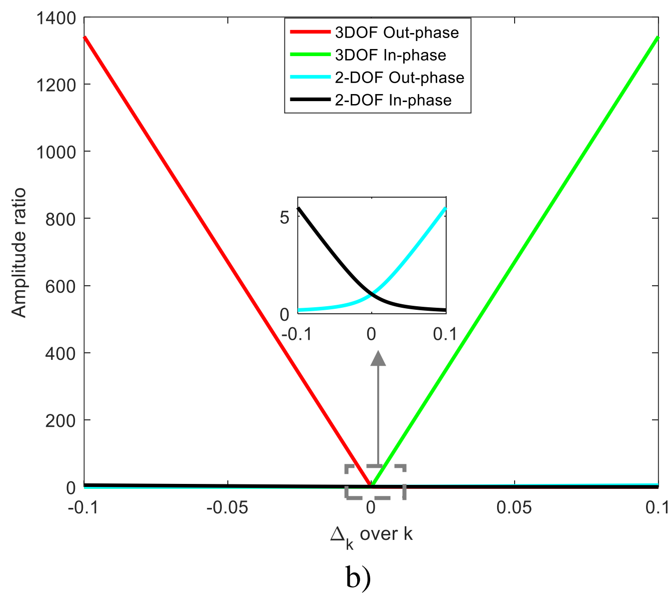

b)

Figure 3. 3: A 3-DOF weakly coupled resonator compared with a 2-DOF weakly coupled resonator. a) Eigenvalue loci veering curve. b) Amplitude ratio versus stiffness perturbations.

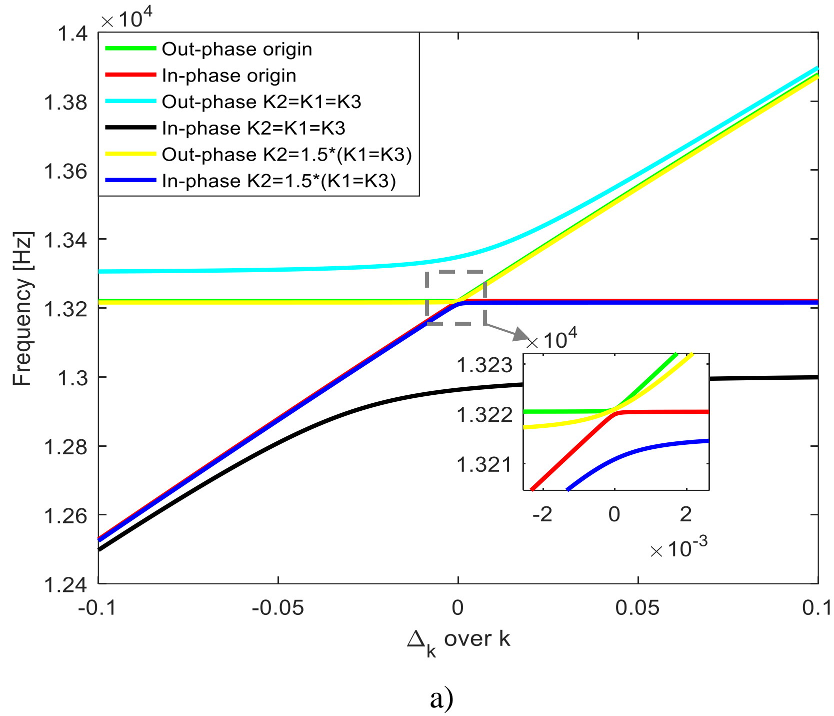

a)

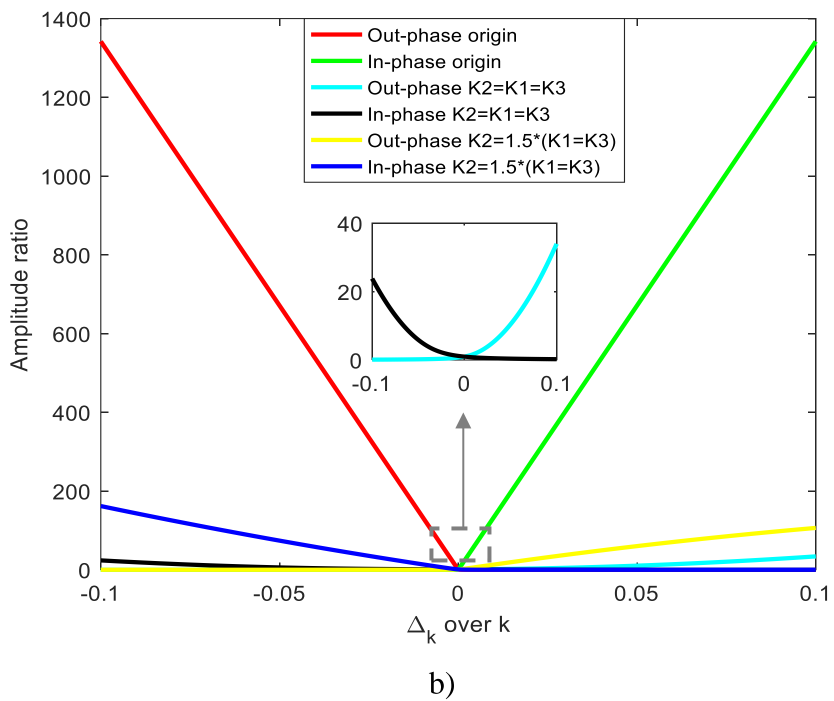

b)

Figure 3. 4: Investigations of middle resonator stiffness variations. a) Eigenvalue loci veering curve with different value of K_2. b) Amplitude ratio versus stiffness perturbations with different value of K_2.

The ideal stiffness perturbation sensitivity in respect to the amplitude ratio has been increased by more than two orders of magnitude. However, there is little difference in

the resonant frequency shifts of the 2-DOF and 3-DOF coupled resonators. This is mainly due to the constant value of nominalized resonance frequency shift sensitivity from equation 2.37. However, the linear region of the eigenvalue loci veering curve for the 3-DOF coupled resonator is larger than that of the 2-DOF coupled resonator.

Investigations for the supporting spring stiffness of the middle resonator is carried out, as shown in Figure 3.4. In summary, the system performance is improved by increasing the supporting-spring stiffness of the middle resonator in a 3-DOF coupled system. This result is consistent with the theory proposed by Chun Zhao [79]. The middle resonator stiffness should be sufficiently strong but not exceed the limitation of a movable structure. Thus, to attain relatively high sensitivity and preserve the properties of the coupled system, the middle resonator stiffness should satisfy:

$$K_2 \geq 2K_1 = 2K_3 \tag{3.5}$$

As introduced in chapter 2, the coupling strength is an essential element in 2-DOF coupled resonators. The overall system functionality is affected by the coupling spring stiffness. This idea can be further extended to 3-DOF coupled resonators. The coupling strength is another factor that determines the coupled system sensitivity. For a basic overview, the eigenvalue loci veering curve and amplitude ratio versus stiffness perturbations with different coupling strengths K_c are plotted in Figure 3.5 (a) and (b), respectively.

A conclusion can be drawn: in a 3-DOF coupled resonator system, both middle resonator supporting-spring stiffness K_2 and coupling strength K_c influence the final performance. However, K_2 is a fixed parameter constrained by the design and fabrication. The parameter K_c, in contrast, is tunable, owing to the electrostatic coupling. The next section will examine mathematical expressions that denote the relationship between the resonant mode frequencies or vibration amplitude ratios and the related system parameters.

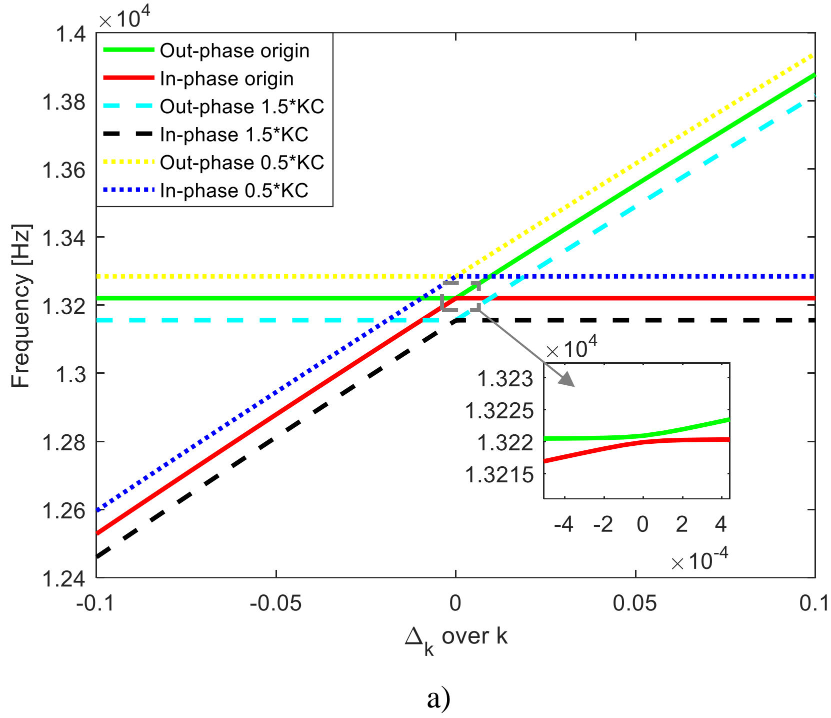

a)

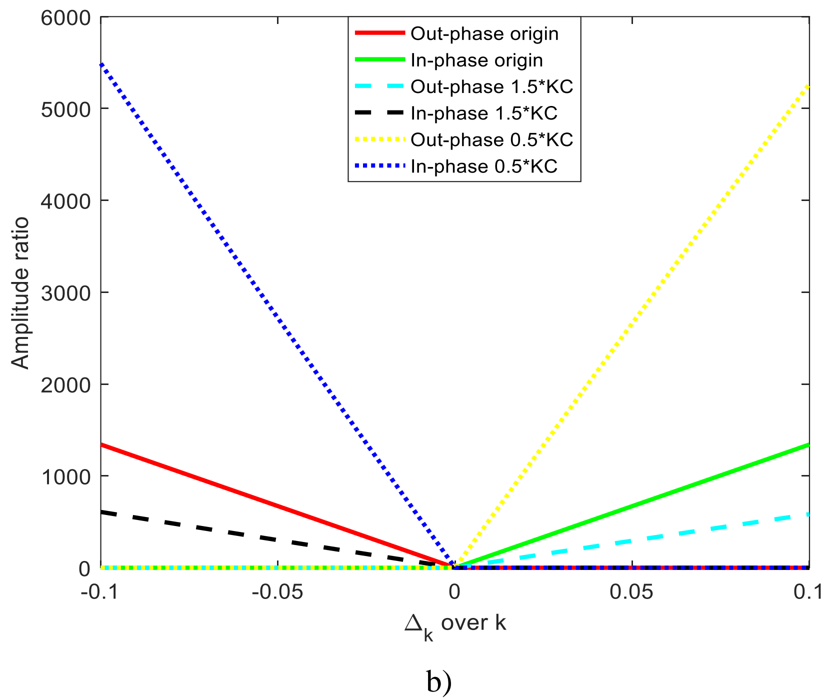

b)

Figure 3. 5: A 3-DOF mode localized electrostatic weakly coupled resonator in response to stiffness perturbations. a) Eigenvalue loci veering curve with different value of K_c. b) Amplitude ratio versus stiffness perturbations with different value of K_c.

Similar analysis methodology is applied to the theoretical computation of mass perturbations for the 3-DOF weakly coupled resonator. In this case, R1 = R2 = M, K1 = K3 = K, with K2 ≠ K, the damping coefficients b1, b2, b3 are identical. The perturbed

resonator3 is assumed to have an added mass R3 = M + ΔM. Thus,

$$M\ddot{X}1(t) + b1\dot{X}1(t) + (K_1 + Kc)X1(t) - KcX2(t) = F1\ (t) \quad (3.6)$$

$$M\ddot{X}2(t) + b2\dot{X}2(t) + (K_2 + 2Kc)X2(t) - Kc(X1(t) + X3(t)) = F2(t) \quad (3.7)$$

$$(M + \Delta M)\ddot{X}3(t) + b3\dot{X}3(t) + (K_3 + Kc)X3(t) - KcX2(t) = F3(t) \quad (3.8)$$

By rewriting the system equation of motion in a matrix form, the damping coefficients b1, b2, and b3 are disregarded, and hence the coupled system with added mass on resonator 3 can be expressed as:

$$\lambda_n \begin{bmatrix} M & 0 & 0 \\ 0 & M & 0 \\ 0 & 0 & M + \Delta M \end{bmatrix} \begin{bmatrix} u_{\lambda_n 1} \\ u_{\lambda_n 2} \\ u_{\lambda_n 3} \end{bmatrix} = \begin{bmatrix} K_1 + Kc & -Kc & 0 \\ -Kc & K_2 + 2Kc & -Kc \\ 0 & -Kc & K_3 + Kc \end{bmatrix} \begin{bmatrix} u_{\lambda_n 1} \\ u_{\lambda_n 2} \\ u_{\lambda_n 3} \end{bmatrix} \quad (3.9)$$

The same system parameters from Table 3.1 are adopted in what follows. The plotted eigenvalue loci veering curve and the amplitude ratio versus the mass perturbations are illustrated in Figure 3.6 (a) and (b), respectively.

Figure 3.7 compares the theoretical computations of a 3-DOF coupled resonator with a 2-DOF electrostatic weakly coupled resonator that possess the same system parameter values as listed in Table 3.1. Accordingly, the simulated mass perturbation sensitivity is significantly improved by adopting such a 3-DOF weakly coupled resonator design, as shown in Figure 3.7.

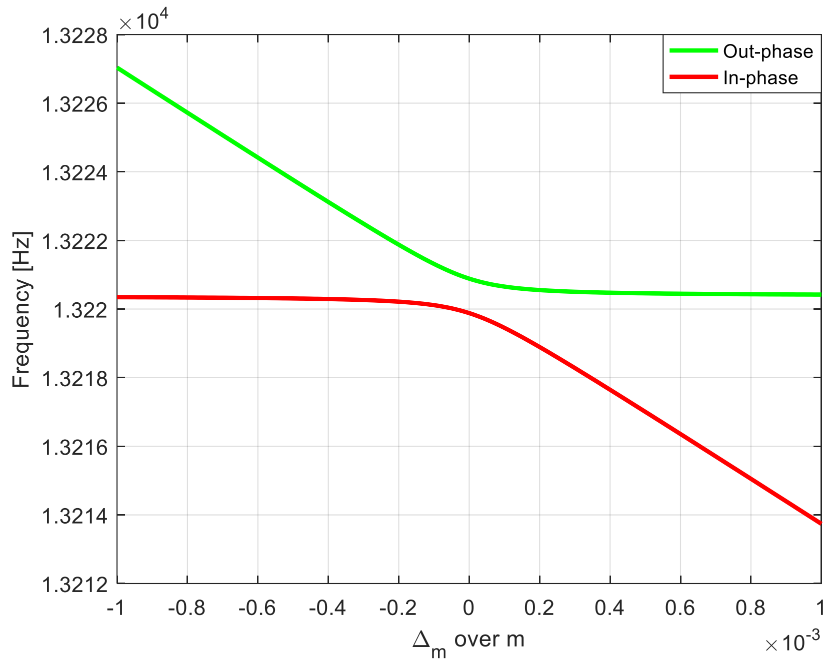

a)

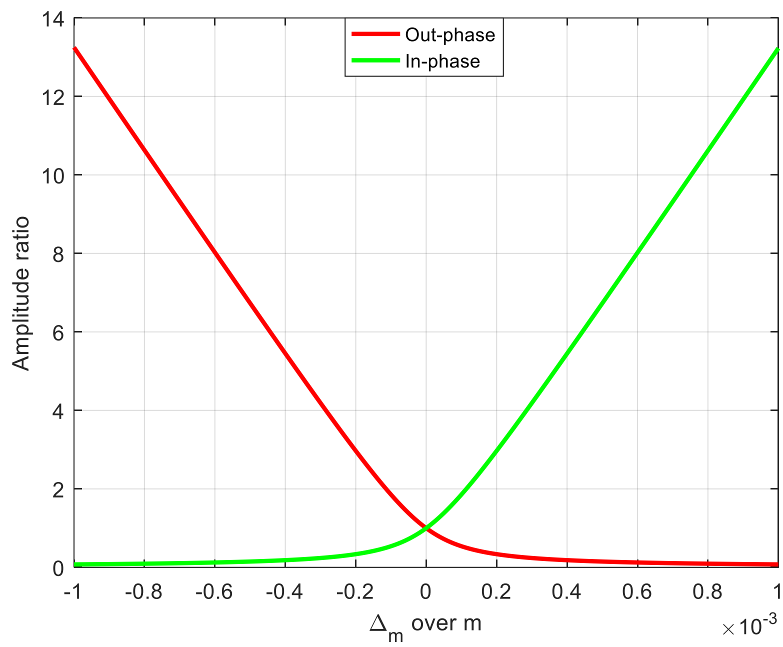

b)

Figure 3. 6: A 3-DOF mode localized electrostatic weakly coupled resonator in response to mass perturbations. a) Eigenvalue loci veering curve. b) Amplitude ratio versus mass perturbations.

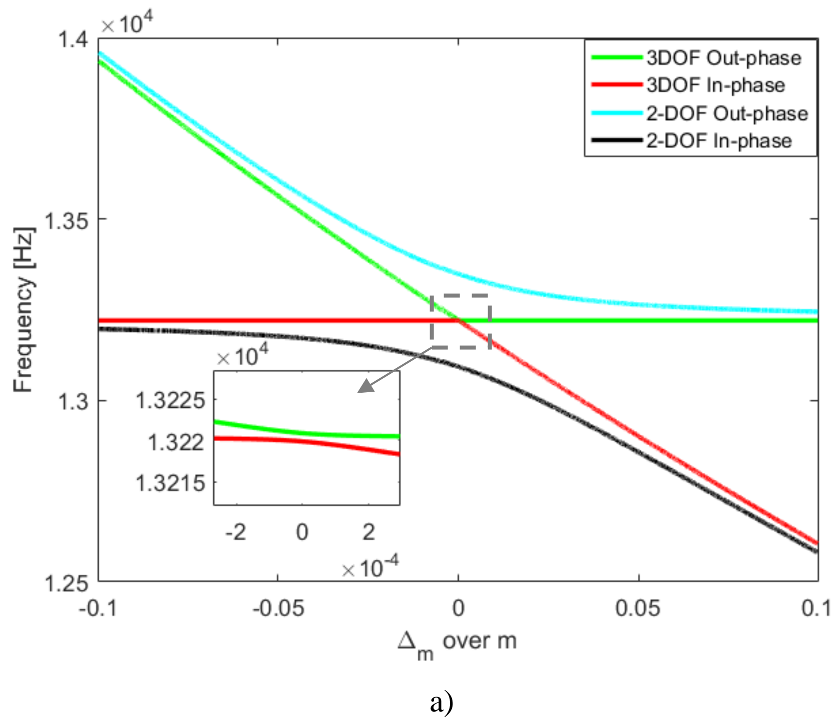

a)

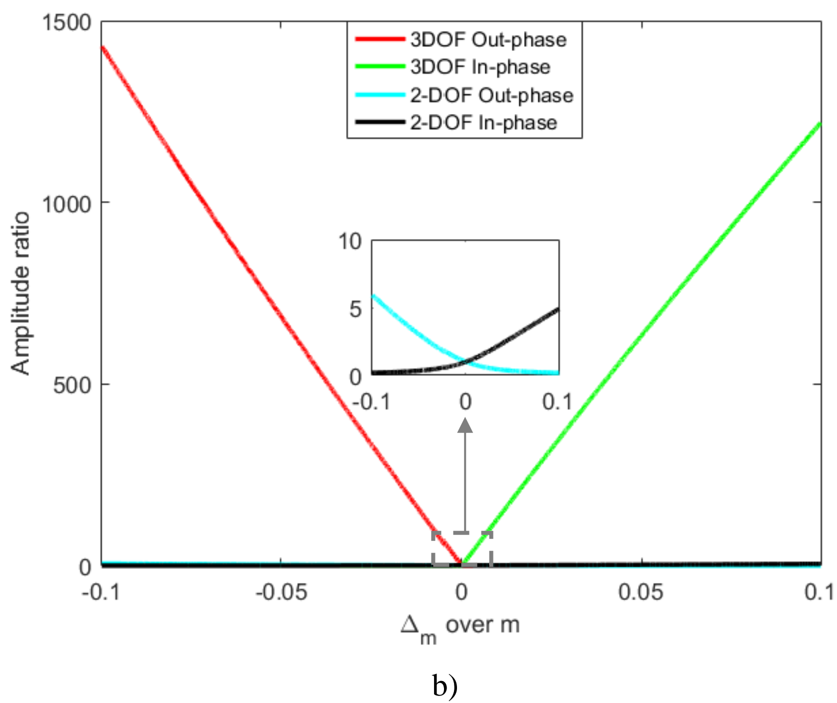

b)

Figure 3. 7: A 3-DOF weakly coupled resonator compared with a 2-DOF weakly coupled resonator. a) Eigenvalue loci veering curve. b) Amplitude ratio versus mass perturbations.

Finally, a comparison of the three different output metrics is conducted. In a 3-DOF weakly coupled resonator system, the amplitude ratio yields the highest normalized

sensitivity compared to eigenvector shifts and resonance frequency shifts, as illustrated in Figure 3.8.

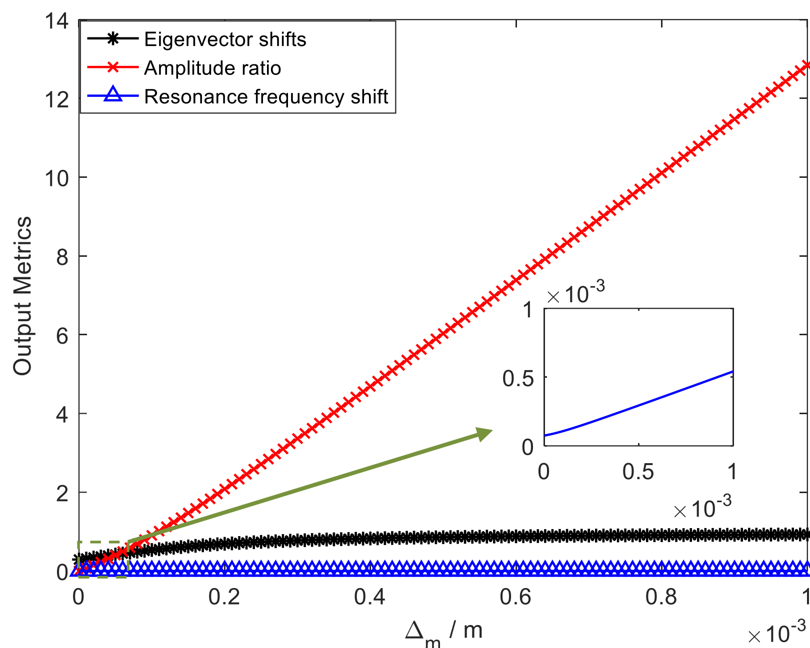

Figure 3. 8: A 3-DOF weakly coupled resonator normalized sensitivity comparisons in three different output metrics.

3.1.2 Derivations of Output Metrics: Stiffness Perturbations

This subsection presents a mathematical derivation method that provides a theoretical basis for the output metrics and offers an intuitive view of the relationships of the system parameters in a 3-DOF coupled resonator, such as coupling strength and supporting-spring stiffness. Starting with Chun Zhao's proposition, a transfer function based computational approach is adopted. As described in previous research [24, 25, 77], such a method can allow for an analysis of nonlinearity, noise, and system response to excitation force. To provide an intuitional understanding of the transfer functions for a 3-DOF weakly coupled resonator system, a lumped parameter model in conjunction with a system block diagram are utilized. The equations of motion can thereby be deduced and subsequently revised in the form of transfer functions.

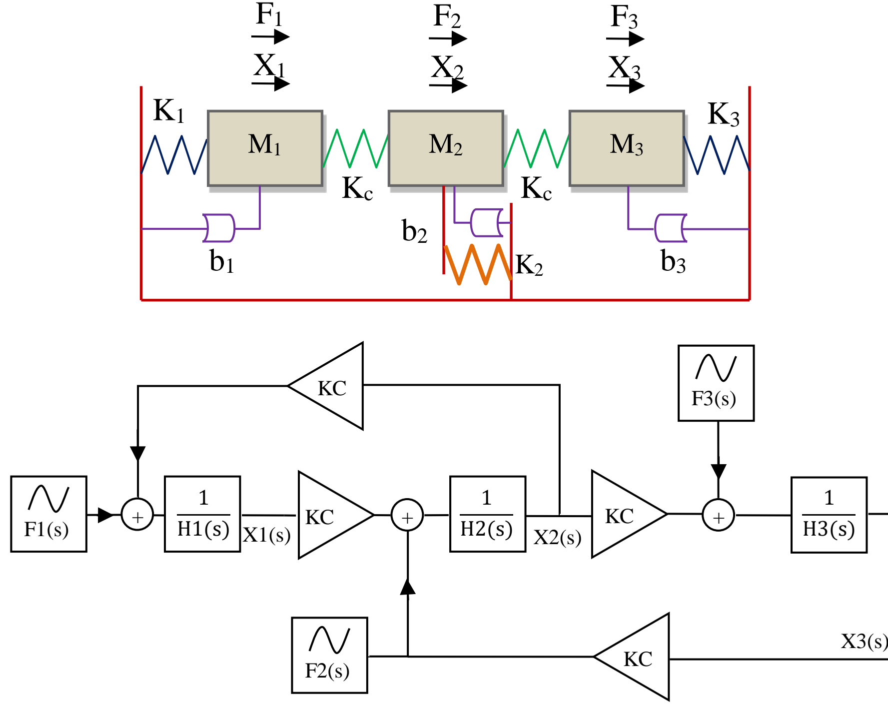

Figure 3. 9: A 3-DOF weakly coupled resonator lump parameter model and system block diagram.

By applying Laplace transform to the system equations of motion:

$$M_1s^2X_1(s) + b_1X_1(s) + K_1X_1(s) + Kc[X_1(s) - X_2(s)] = F_1(s) \quad (3.10)$$

$$M_2s^2X_2(s) + b_2X_2(s) + (K_2+2Kc)X_2(s) - Kc[X_3(s) + X_1(s)] = F_2(s) \quad (3.11)$$

$$M_3s^2X_3(s) + b_3X_3(s) + (K_3 + \Delta K)X_3(s) + Kc[X_3(s) - X_2(s)] = F_3(s) \quad (3.12)$$

A symmetrical condition is assumed, where $M_1 = M_2 = M_3 = M$, $K_1 = K_3 = K$, $K_2 \geq 2K$, a stiffness perturbation ΔK is applied to resonator 3. The damping coefficients b1 = b2 = b3= b. Only resonator 1 in the coupled system is given an actuation force hence $F_1 = F, F_2 = F_3 = 0$. Accordingly, the revised system transfer functions are:

$$H_1(s) = Ms^2 + bs + K + Kc \quad (3.13)$$

$$H_2(s) = Ms^2 + bs + K_2 + 2Kc \quad (3.14)$$

$$H_3(s) = Ms^2 + bs + K + \Delta K + \ Kc \tag{3.15}$$

By combining equations 3.13–3.15 with equations 3.10–3.12, the relationship between the input actuation force and the output resonator displacement can be obtained [25]:

$$\frac{H_2(s)H_3(s) - Kc^2}{H_1(s)H_2(s)H_3(s) - [H_1(s)+H_3(s)]Kc^2} = \frac{X_1(s)}{F(s)} \tag{3.16}$$

$$\frac{Kc^2}{H_1(s)H_2(s)H_3(s) - [H_1(s)+H_3(s)]Kc^2} = \frac{X_3(s)}{F(s)} \tag{3.17}$$

A weak coupling condition is satisfied with $Kc \leq K/10$ and $s = jw$. The resonance mode frequencies can be found by disregarding the damping elements. Solving equations 3.16 and 3.17 will give:

$$\omega_{inphase} = \sqrt{\frac{1}{M}(K + Kc + \frac{1}{2}(\Delta K - \frac{2K}{\gamma} - \sqrt{\Delta K^2 + (\frac{2K}{\gamma})^2)}} \tag{3.18}$$

$$\omega_{outphase} = \sqrt{\frac{1}{M}(K + Kc + \frac{1}{2}(\Delta K - \frac{2K}{\gamma} + \sqrt{\Delta K^2 + (\frac{2K}{\gamma})^2)}} \tag{3.19}$$

$$\gamma = \frac{K(K_2 - K + Kc)}{Kc^2} \tag{3.20}$$

In practice, there are three resonance mode frequencies, each corresponding to one dedicated vibration mode. This can also be proved with the eigenstate matrix calculation (the three eigenvalues), which has been covered in the previous section. However, only two vibration modes are used for sensing applications due to operation frequency, vibration amplitude, and overall functionality. More specifically, Figure 3.10 shows a COMSOL model of a 3-DOF weakly coupled resonator, including the three

vibration modes.

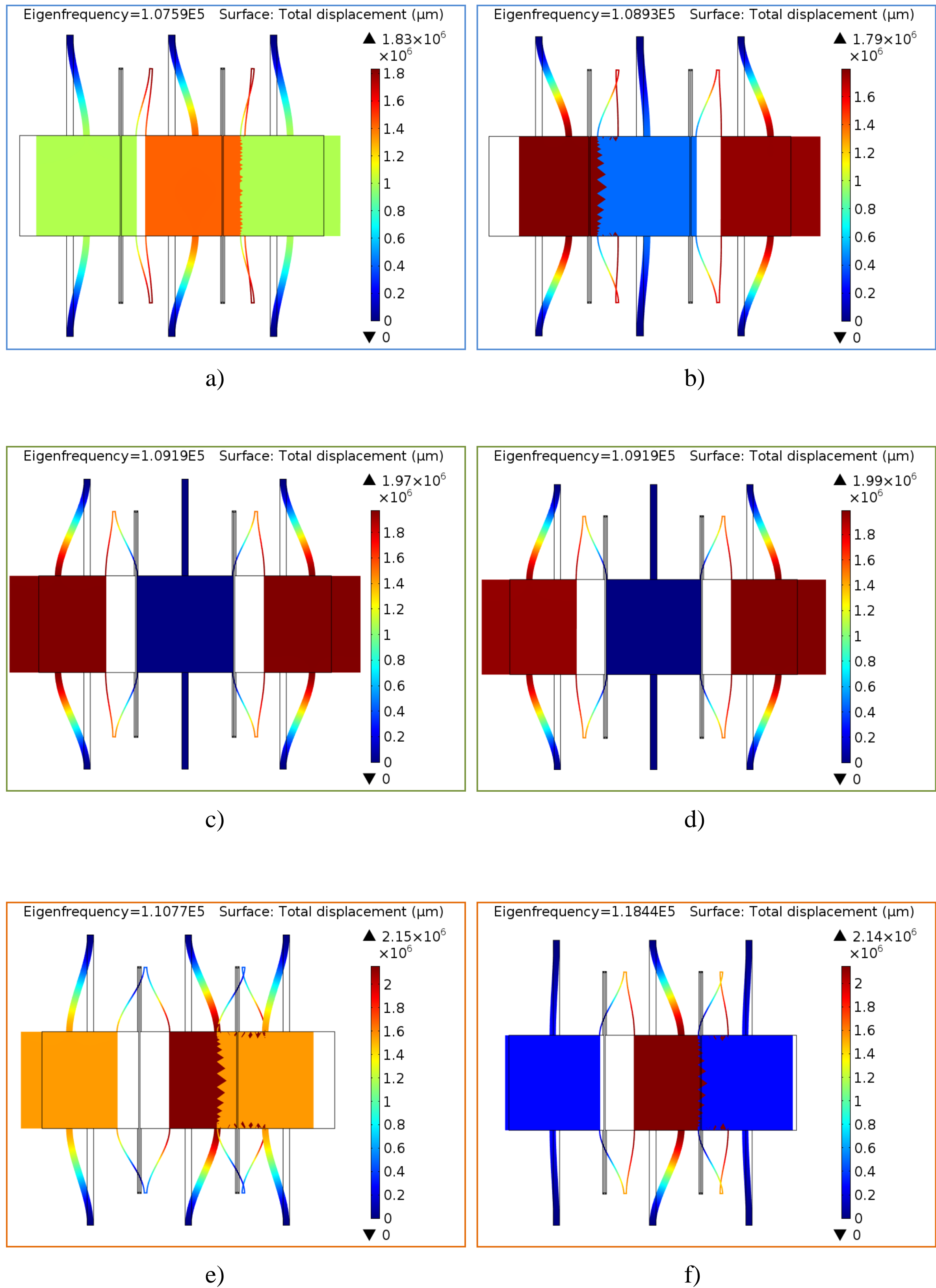

Figure 3. 10: 3-DOF weakly coupled resonator vibration modes. a) c) e) Three identical resonators coupled via mechanical springs. b) d) f) Left and right resonators are

identical, middle resonator supporting spring stiffness $K_2 \geq 2K_1 = 2K_3$. a) & b) All three resonators are vibrating in-phase. c) & d) Left and right resonators are vibrating out-of-phase while middle resonator maintains stationary. e) & f) Each resonator is vibrating out-of-phase with adjacent one, left and right resonators are vibrating in-phase however both of them are out-of-phase with middle resonator.

By increasing the supporting-spring stiffness of the middle resonator, the third vibration mode with the highest resonance frequency is dramatically changed in comparison with the symmetrical case. The vibration amplitudes of the left and right resonators are considerably reduced. Another influence is the resonance frequency: the gap frequency between the third and second modes is increased, but the gap between the first and second modes is reduced. In contrast, the symmetrical case has three vibration mode frequencies with nearly the same gap values.

In sensing applications, to maximize the signal to noise ratio (SNR) and the overall sensitivity, the displacements of the left and right resonators should be sufficiently large. As for the vibration mode frequency, the third mode resonance frequency is relatively higher than that of the previous two. The increased frequency sweeping range will increase the transduction processing time. The third vibration mode is accordingly treated as an invalid mode and hence can be disregarded.

After the vibration modes have been selected and the corresponding resonance frequencies have been derived from equations 3.18 and 3.19, the next step is to define the amplitude ratios in accordance with the system transfer functions by solving equations 3.13–3.17:

$$AR_{inphase} = \frac{\gamma\left(\frac{\Delta K}{K}\right) + \sqrt{(\gamma\frac{\Delta K}{K})^2 + 4}}{2} \tag{3.21}$$

$$AR_{outphase} = \frac{\gamma\left(\frac{\Delta K}{K}\right) - \sqrt{(\gamma\frac{\Delta K}{K})^2 + 4}}{2} \tag{3.22}$$

To obtain valid solutions, the stiffness perturbation should be constrained as $\Delta K \ll K + K_c$. A general definition of weak coupling in such a 3-DOF coupled resonator

system can also be given:

$$|K_c| < 0.1K \leq 0.05\, K_2 \tag{3.23}$$

The relevance for all stiffness related parameters can be expressed as:

$$|\Delta K| < |K_c| < 0.1K \leq 0.05\, K_2 \tag{3.24}$$

The normalized amplitude ratio sensitivity can hence be written:

$$S_{\substack{3-DOF \\ AR}}^{Stiff} = \left|\frac{AR}{\partial AR} \times \frac{\partial K}{K}\right| \approx \frac{K(K_2 - K + Kc)}{Kc^2} \tag{3.25}$$

An extreme case is used, which will give an intuitive and quantified sensitivity comparison of a 3-DOF coupled resonator, a 2-DOF coupled resonator, and a 1-DOF resonator. Using equations 2.32 and 3.25 and assuming $K = 10K_c$ and $K_2 = 2K$, the comparison results are summarized in Table 3.2.

Type	3-DOF	2-DOF	1-DOF
Nor.S	110	2.5	0.5
Multiple	44		5

Table 3. 2: Stiffness perturbation sensitivity comparisons under the condition of extreme values.

The sensitivity of the 3-DOF weakly coupled resonator is 44 times that of the 2-DOF one. However, this conclusion is based on extreme values, which eventually yield the lowest normalized sensitivity. By carefully specifying the supporting stiffness K, the middle resonator stiffness K_2, and the coupling strength K_c, the sensitivity can be greatly enhanced.

3.1.3 Derivations of Output Metrics: Mass Perturbations

A mathematical computational method is adopted to derive the 3-DOF weakly coupled resonator output metrics in response to mass perturbations. Disregarding

damping, the equations of motion for the resonator system with a mass perturbation on resonator 3 can be defined as:

$$-M_1 w^2 X_1(s) = -(K_1 + Kc)X_1(s) + KcX_2(s) \tag{3.26}$$

$$-M_2 w^2 X_2(s) = -(K_2 + 2Kc)X_2(s) + KcX_1(s) + KcX_3(s) \tag{3.27}$$

$$-M_3(1 + \delta M_3) w^2 X_3(s) = -(K_3 + Kc)X_3(s) + KcX_2(s) \tag{3.28}$$

A symmetrical condition is assumed, where $M_1 = M_2 = M_3 = M$, $K_1 = K_3 = K$, $K_2 \geq 2K$, the mass perturbations on resonator 3 satisfy: $\Delta M > 0$, $\delta M_3 = \delta M = {}^{\Delta M}/_{M_3} = {}^{\Delta M}/_{M} > 0$. The amplitude ratios in the coupled system are defined as: $\tau_1 \equiv {}^{X_2}/_{X_1}$ & $\tau_2 \equiv {}^{X_2}/_{X_3}$ & $AR = {}^{X_1}/_{X_3} = {}^{\tau_2}/_{\tau_1}$. Using algebra method to equation 3.26-3.28:

$$\tau_2 = (1 + \delta M)\tau_1 - \frac{K + Kc}{Kc}\delta M \tag{3.29}$$

$$AR = 1 + (1 - \frac{K + Kc}{Kc\tau_1})\delta M \tag{3.30}$$

To obtain the final expression of AR, the solution of τ_1 should be extracted. By applying the algebraic method, the roots can be obtained:

$$\tau_1^{(1,2)} = \frac{K + Kc}{Kc(1 + \delta M)}[\frac{1}{\gamma} + (1 + \frac{1}{\gamma})]\frac{\delta M}{2} \mp \sqrt{\left(1 - \frac{1}{\gamma}\right)^2 (\frac{\delta M}{2})^2 + \frac{1 + \delta M}{\gamma^2}} \tag{3.31}$$

$$\gamma = \frac{(K + Kc)(K_2 - K + Kc)}{Kc^2} \tag{3.32}$$

Accordingly, inserting equation 3.31 into equation 3.30 will give the in-phase and out-phase amplitude ratios respectively.

$$AR_{inphase} = (1-\gamma)\frac{\delta M}{2} + \sqrt{(1-\gamma)^2(\frac{\delta M}{2})^2 + 1 + \delta M} \qquad (3.33)$$

$$AR_{outphase} = (1-\gamma)\frac{\delta M}{2} - \sqrt{(1-\gamma)^2(\frac{\delta M}{2})^2 + 1 + \delta M} \qquad (3.34)$$

Similar algebra method is used to derive the resonance mode frequencies:

$$w_{inphase} = \sqrt{\frac{K+Kc}{M(1+\delta M)}}\sqrt{\left(1-\frac{1}{\gamma}\right) + \left(1-\frac{1}{\gamma}\right)\frac{\delta M}{2} - \sqrt{\left(1-\frac{1}{\gamma}\right)^2 (\frac{\delta M}{2})^2 + \frac{1+\delta M}{\gamma^2}}} \qquad (3.35)$$

$$w_{outphase} = \sqrt{\frac{K+Kc}{M(1+\delta M)}}\sqrt{\left(1-\frac{1}{\gamma}\right) + \left(1-\frac{1}{\gamma}\right)\frac{\delta M}{2} + \sqrt{\left(1-\frac{1}{\gamma}\right)^2 (\frac{\delta M}{2})^2 + \frac{1+\delta M}{\gamma^2}}} \qquad (3.36)$$

As shown in Figure 3.10, only the first and second vibration modes are used in view of the relatively large vibration amplitudes and rational resonance mode frequencies. The same principle is adopted in mass perturbation characterizations. Furthermore, the weak coupling condition in the previous section is valid here, as $|K_c| < 0.1K \leq 0.05\, K_2$. The normalized sensitivity in terms of amplitude ratio can be deduced:

$$S_{\substack{3-DOF \\ AR}}^{MASS} = \left|\frac{AR}{\partial AR} \times \frac{\partial M}{M}\right| = \frac{(1-\gamma)}{2} \pm \frac{(1-\gamma)^2\delta M + 1}{2\sqrt{(1-\gamma)^2(\frac{\delta M}{2})^2 + 1 + \delta M}} \qquad (3.37)$$

$$\left|S_{\substack{3-DOF\\AR}}^{MASS}\right| \approx \frac{(K+Kc)(K_2-K+Kc)}{Kc^2} \tag{3.38}$$

An extreme case is used again to compare the mass sensitivities. Using equations 2.32 and 3.38 and assuming $K = 10K_c$ and $K_2 = 2K$, the results are summarized in Table 3.3.

<table>
<tr><th>Type</th><th colspan="2">3-DOF</th><th colspan="2">2-DOF</th><th colspan="2">1-DOF</th></tr>
<tr><td>Nor.S</td><td colspan="2">121</td><td colspan="2">2.5</td><td colspan="2">0.5</td></tr>
<tr><td>Multiple</td><td colspan="3">48</td><td colspan="3">5</td></tr>
</table>

Table 3. 3: Mass perturbation sensitivity comparisons under the condition of extreme values.

Again, this conclusion is drawn from extreme values, and consequently it yields the lowest normalized sensitivity. The system parameters such as supporting stiffness K, middle resonator stiffness K_2, and coupling strength K_c are correlated with the final mass perturbation sensitivity. According to equation 3.32, optimizing the system parameters can result in dramatic sensitivity enhancement.

3.2 Mode Aliasing in a 3-DOF Mode Localized Electrostatic Weakly Coupled Resonator

As mentioned in chapter 2, the mode aliasing phenomenon causes an overlap in the coupled resonator vibration modes, which inhibits the mode localized sensing mechanism. A general definition of an anti-mode aliasing condition is expressed in equation 2.39; however, it is based on the final system response rather than the initial coupled resonator design. In what follows, the anti-mode aliasing condition will be revised in terms of the parameters of a 3-DOF weakly coupled resonator system. In accordance with the derived expressions from the previous section, both stiffness and

mass perturbations are correlated with the anti-mode aliasing condition. Assuming a given stiffness perturbation and inserting equations 3.18 and 3.19 into equation 2.39 [25]:

$$\begin{gathered} 2\pi(f_{outphase} - f_{inphase}) \geq 4\pi f_{cut-off} \\ \Rightarrow w_{outphase} - w_{inphase} \geq 2w_{3dB} \\ \Rightarrow \Delta w \geq 2w_{3dB} \end{gathered} \tag{3.39}$$

$$\Delta w \approx \sqrt{\frac{K}{M}} \sqrt{(\frac{\Delta K}{2K})^2 + \frac{1}{{\gamma_K}^2}} \tag{3.40}$$

$$\gamma_K = \frac{K(K_2 - K + Kc)}{Kc^2} \tag{3.41}$$

The cut-off 3dB bandwidth can be expressed as a function of the system quality factor Q, hence:

$$w_{3dB} = \frac{w_0}{Q} = \frac{1}{Q}\sqrt{\frac{K}{M}} \tag{3.42}$$

Combine equation 3.39, 3.40 and 3.42 will give:

$$(\frac{\Delta K}{2K})^2 + \frac{1}{{\gamma_K}^2} \geq (\frac{2}{Q})^2 \tag{3.43}$$

$$\frac{\Delta K}{K} < -2\sqrt{(\frac{2}{Q})^2 - \frac{1}{{\gamma_K}^2}} \tag{3.44}$$

Evidently, the stiffness perturbation ΔK and its normalized term $\Delta K/K$ are determined by the vibration modes Q-factor and the system stiffness sensitivity γ_K. More importantly, the dynamic range of a 3-DOF mode localized weakly coupled resonator is determined. The mode aliasing phenomenon, on the other hand, can be avoided by limiting the input stiffness perturbation, tuning the coupling strength Kc or adjusting the system quality factor Q (either the environment or the design).

Figure 3.11 shows the influence of mode aliasing with different coupling strength K_c in a 3-DOF mode localized weakly coupled resonator system.

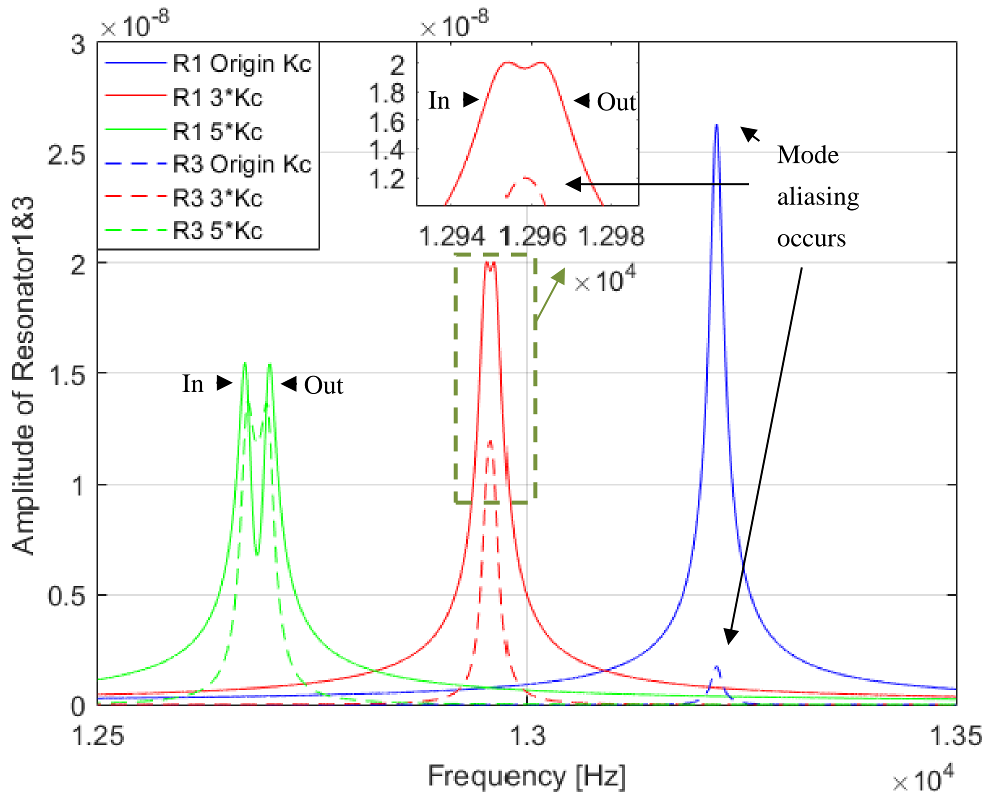

Figure 3. 11: Mode aliasing with different values of coupling strength Kc.

Ideally, a relatively strong coupling strength could effectively suppress mode aliasing. However, the stiffness perturbation sensitivity from equation 3.41 indicates that the coupling strength is an inverse function of sensitivity. Simply increasing the coupling strength will yield lower sensitivity. Although maximizing sensitivity is the ultimate goal in designing sensor devices, in some cases, especially where the Q-factor is unchangeable and mode aliasing is inevitable, there must be compromise among the system parameters such as Kc, K_2, and K. The Q-factor, however, is a major determinant of the anti-mode aliasing condition, and it is closely correlated with the sensor system functionality.

Figure 3.12 shows the results of another study of mode aliasing with different Q-factors.

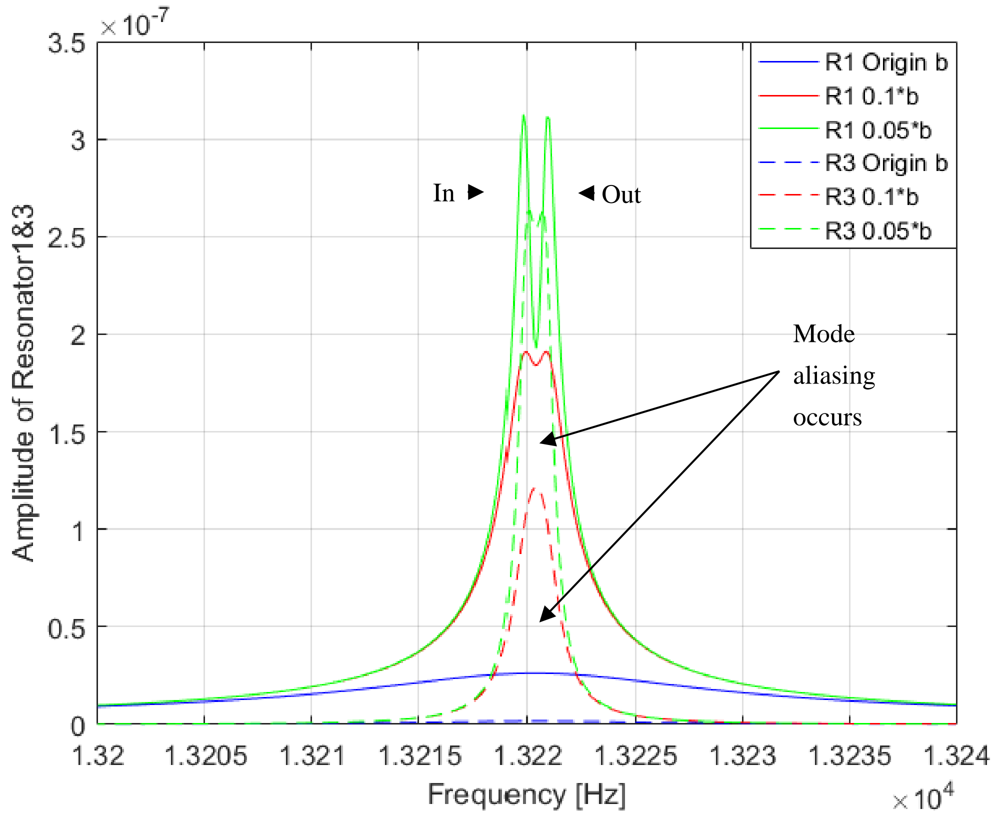

Figure 3. 12: Mode aliasing with different values of quality factor Q (different damping conditions).

Next, the anti-mode aliasing condition for mass perturbations can be computed with a similar pattern. Substituting equation 3.35 and 3.36 into equation 3.39:

$$\frac{1}{\sqrt{1+\Delta M/_{M}}}\sqrt{(\frac{\Delta M}{2M})^2+\frac{1}{{\gamma_m}^2}}>\frac{2}{Q} \tag{3.45}$$

$$\overset{\Delta M=0}{\Longrightarrow} \quad \frac{1}{\gamma_m}>\frac{2}{Q} \tag{3.46}$$

$$\gamma_m=\frac{(K+Kc)(K_2-K+Kc)}{Kc^2} \tag{3.47}$$

In conclusion, the mode aliasing effect restricts the lower limit of coupling strength in a coupled resonator system. Due to the Q-factor correlation, the anti-mode aliasing

condition also gives guidelines for the design of coupled resonators and the preferred operating environment. Eventually, the upper limit of the device sensitivity is constrained by mode aliasing.

3.3 Transduction Techniques of a 3-DOF Mode Localized Electrostatic Weakly Coupled Resonator

3.3.1 Actuation

Actuators are essential elements for MEMS devices, especially MEMS resonators that work in a dynamic mode with an excitation force. A brief comparison of commonly applied actuation technologies is provided in Table 3.4.

Type of actuation	*Pros*	*Cons*
Thermal	• Simple to implement. • Generate large force.	• Slow response time. • Large power consumption. • Thermal noise.
Piezoelectric	• No dc power consumption. • Fast response time.	• Small displacements. • Require large voltage.
Capacitive	• Easy to manufacture. • No dc power consumption. • Relative large displacements. • Low noise.	• Nonlinearity. • Feedthrough current.

Table 3. 4: A comparison of MEMS actuation methods.

To achieve a cost-effective and flexible design, simplicity of fabrication, and relatively good excitation force with reasonable displacements, capacitive actuation is selected for the 3-DOF mode localized weakly coupled resonator system. The principle of capacitive actuation is similar to the electrostatic coupling introduced in chapter 2. Capacitive actuation utilizes a parallel plate structure with an actuation voltage to form

an electric field that attracts electric charges, thus inducing an electrostatic force. The magnitude of the generated electrostatic force depends on the actuation voltage and the parallel plate geometry. In the 3-DOF coupled resonator system, the capacitive actuation structure is formed by an actuation port and the proof mass of either the left or right resonator. Figure 3.13 shows the schematic of capacitive actuation in a 3-DOF coupled resonator system.

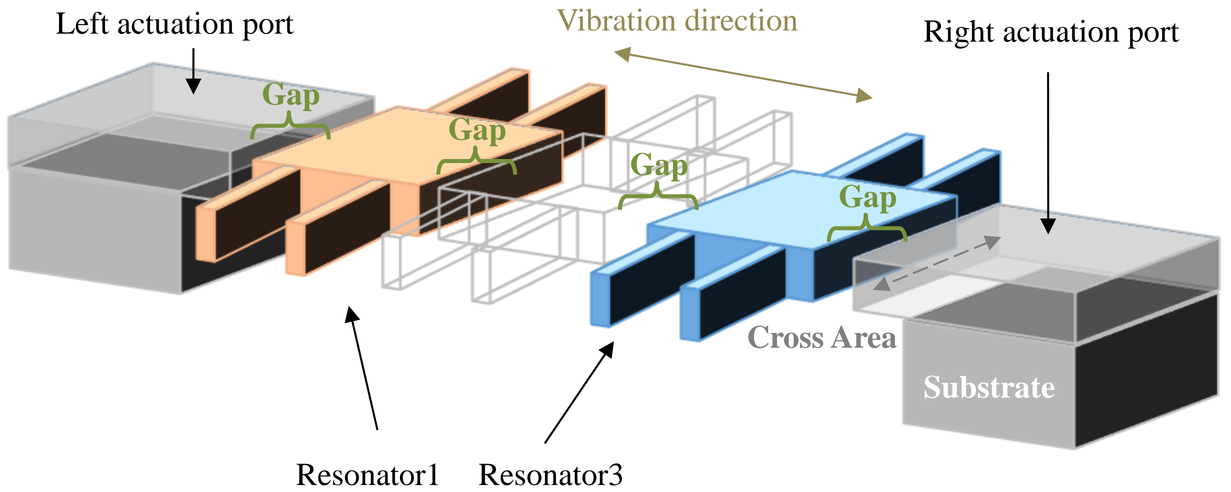

Figure 3. 13: Capacitive actuation in a 3-DOF coupled resonator system.

The boundary of the actuation port and the cross-section of the proof mass of resonator1 and resonator 3 form a parallel plate structure. The effective area of the parallel plate is defined by the thickness and width of the proof mass. Thus, the equations that were used to deduce electrostatic coupling can be adopted here. The actuation force is equivalent to the generated electrostatic force and hence can be computed using equations 2.19 and 2.20:

$$F_{actuation} = \frac{1}{2}\frac{\partial C}{\partial x}V^2 \tag{3.48}$$

where V is the potential difference between the actuation port and proof mass, d is the original gap value, x is the displacement due to proof mass vibration, and C is the capacitance formed by the structure. With capacitive actuation, there is no DC power consumption, and thus only an AC voltage is applied on the actuation port. However,

in the 3-DOF coupled resonator system, a DC voltage is required to maintain sufficient coupling strength to establish electrostatic coupling. Hence, assuming resonator 1 and resonator 3 are given the same DC voltage and the middle resonator is grounded, the desired coupling stiffness can be calculated by equation 2.21:

$$K_C^{3-DOF} = -\frac{\varepsilon A {V_{DC}}^2}{d^3} \tag{3.49}$$

With an AC actuation voltage of frequency f and amplitude v, $V_{AC} = vsin2\pi ft$; after the DC coupling voltage is applied, the final potential difference is $V = V_{AC} - V_{DC}$. Equation 3.48 can be rewritten as:

$$\begin{aligned} F_{actuation} &= \frac{1}{2}\frac{\partial C}{\partial x}(V_{AC} - V_{DC})^2 = \frac{1}{2}\frac{\partial C}{\partial x}(vsin2\pi ft - V_{DC})^2 \\ &= \frac{1}{2}\frac{\partial C}{\partial x}\left[(vsin2\pi ft)^2 + {V_{DC}}^2 - 2vsin2\pi ftV_{DC}\right] \\ &= \frac{1}{2}\frac{\partial C}{\partial x}\left[v^2(\frac{1 - cos4\pi ft}{2}) + {V_{DC}}^2 - 2vsin2\pi ftV_{DC}\right] \end{aligned} \tag{3.50}$$

The constant term in equation 3.50 expresses a DC component of the actuation force. The doubled frequency term, however, can be disregarded if the voltage is $|V_{AC}| \ll |V_{DC}|$. In general, the mixed term with the original frequency component is considered as the true actuation force. The DC constant term, on the other hand, generates an initial force that sets up the quiescent position of the resonator proof mass. Following from this, equation 3.50 can be further revised by using a Taylor series on the variable capacitance term:

$$\frac{\partial C}{\partial x} = -\frac{\varepsilon A}{d^2} + \frac{2\varepsilon Ax}{d^3} - \frac{3\varepsilon Ax^2}{d^4} + \frac{4\varepsilon Ax^3}{d^5} \tag{3.51}$$

$$F_{actuation} = \left[\left(\frac{{V_{DC}}^2}{2} + \frac{v^2}{4}\right) - vsin2\pi ftV_{DC}\right]\frac{\partial C}{\partial x} \tag{3.52}$$

$$= -\frac{\varepsilon A}{d^2}\left(\frac{V_{DC}{}^2}{2} + \frac{v^2}{4} - vsin2\pi ftV_{DC}\right)$$

$$+\left(\frac{V_{DC}{}^2}{2} + \frac{v^2}{4} - vsin2\pi ftV_{DC}\right)\left(\frac{2\varepsilon Ax}{d^3} - \frac{3\varepsilon Ax^2}{d^4} + \frac{4\varepsilon Ax^3}{d^5}\right)$$

$$\approx -\frac{V_{DC}{}^2}{2}\frac{\varepsilon A}{d^2} + V_{AC}V_{DC}\frac{\varepsilon A}{d^2}$$

After the dimensions and geometry of the coupled resonator device are finalized, the effective actuation force of the capacitive actuator is determined by three parameters: excitation voltage V_{AC}, coupling voltage V_{DC}, and the induced displacement x. Careful selection of the voltage values can generate a desired actuation force with predictable displacements. In contrast, if V_{DC} is too large, a pull-in phenomenon (details are introduced in the following section) will occur, causing the coupled resonator system to fail; a relatively large V_{AC} could allow for unwanted influences and trigger system instability.

3.3.2 Sensing Element

As well as actuators, the sensing element is another vital component of MEMS resonator sensors. The sensing element picks up target activities and then transport to the final readout stage. A comparison of the most commonly adopted sensing technologies is provided in Table 3.5.

Sensing element	***Pros***	***Cons***
Piezoresistive	• Easy to implement. • Inherent shielding.	• Noisy. • Large temperature dependency. • Large power consumption.
Piezoelectric	• Self-generating. • No bias voltage or current.	• Cannot use in static measurements. • Materials are difficult to process.

Capacitive	• Low power consumption. • Good noise performance.	• Parasitic influences. • Hermetic packaging. • Complex circuitry. • Small comb finger gaps.

Table 3. 5: Comparisons of MEMS sensing techniques.

For the purpose of small signal pick up, less noise affections, greater SNR and adaptability with capacitive actuation and electrostatic coupling, capacitive sensing is applied to the 3-DOF mode localized weakly coupled resonator. The working principle of integrated capacitive sensing elements is shown in Figure 3.14.

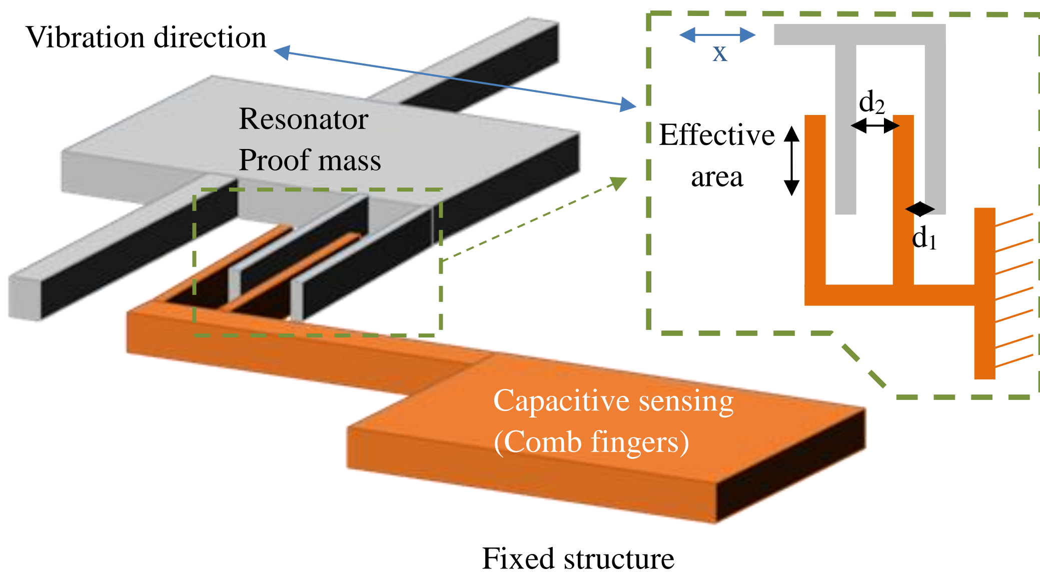

Figure 3. 14: Integrated capacitive sensing element.

The capacitive sensing element consists of one movable part and one stationary part. The sensing plate is designed to be close to one of the parts but distant from the other. This is because the displacement of the proof mass is relatively small in practice, and to successfully extract the generated motional current, an initial small gap is necessary. When a DC voltage is applied to the resonator but maintains the capacitive comb finger structure unchanged, a DC potential difference is formed. When the resonator is excited and starts to vibrate, the displacement of the movable plate induces the effective capacitance variations that result in generated motional current. Assuming

the gaps satisfy $d_1 \ll d_2$, the capacitance in respect to d_2 can be disregarded. The effective capacitance is determined by the overlap area A between the movable and stationary plates. Accordingly, the motional current can be expressed as:

$$i_{motion} = -\frac{\partial Q}{\partial t} = -\frac{\partial (CV)}{\partial t} = -(C\frac{\partial V}{\partial t} + V\frac{\partial C}{\partial t}) \tag{3.53}$$

There are two components in the motional current equation. The variable capacitance term expresses the valid motional current that is picked up by the capacitive sensing element. The variable voltage term, however, denotes an AC voltage across fixed capacitance and results in feedthrough current. In the 3-DOF mode localized weakly coupled resonator, a DC voltage is applied on the left and right resonators because of electrostatic coupling and capacitive actuation. The DC voltage also serves as the voltage source in the capacitive sensing element. Supposing the movable plates have a displacement value x and substituting equation 3.51 into equation 3.53, the motional current equation can be rewritten as:

$$\begin{aligned} i_{motion} &= -V_{DC}\frac{\partial C}{\partial t} = -V_{DC}\frac{\partial C}{\partial x}\frac{\partial x}{\partial t} \\ &= -V_{DC}\left(-\frac{\varepsilon A}{{d_1}^2} + \frac{2\varepsilon Ax}{{d_1}^3} - \frac{3\varepsilon Ax^2}{{d_1}^4} + \frac{4\varepsilon Ax^3}{{d_1}^5}\right)\frac{\partial x}{\partial t} \\ &\approx V_{DC}\frac{\varepsilon A}{{d_1}^2}\frac{\partial x}{\partial t} \end{aligned} \tag{3.54}$$

Further optimization of the sensing element can be achieved by utilizing a differential capacitive sensing technique. Another group of capacitive sensing elements is integrated on the resonator structure but with an opposite positional order. This can generate a motional current measurement with an inverted direction. The two measured motional currents are then fed to a differential device such as an instrumentation amplifier, and a differential algorithm between the two contrary motional current is executed. This technique eventually achieves a doubled motional current pick-up along with suppressed noise and reduced feedthrough current and parasitic capacitance

induced current [80]. The differential capacitive sensing configuration also results in enhanced common mode rejection capability and reduced nonlinearity [81]. Figure 3.15 demonstrates the setup of a basic differential capacitive sensing element.

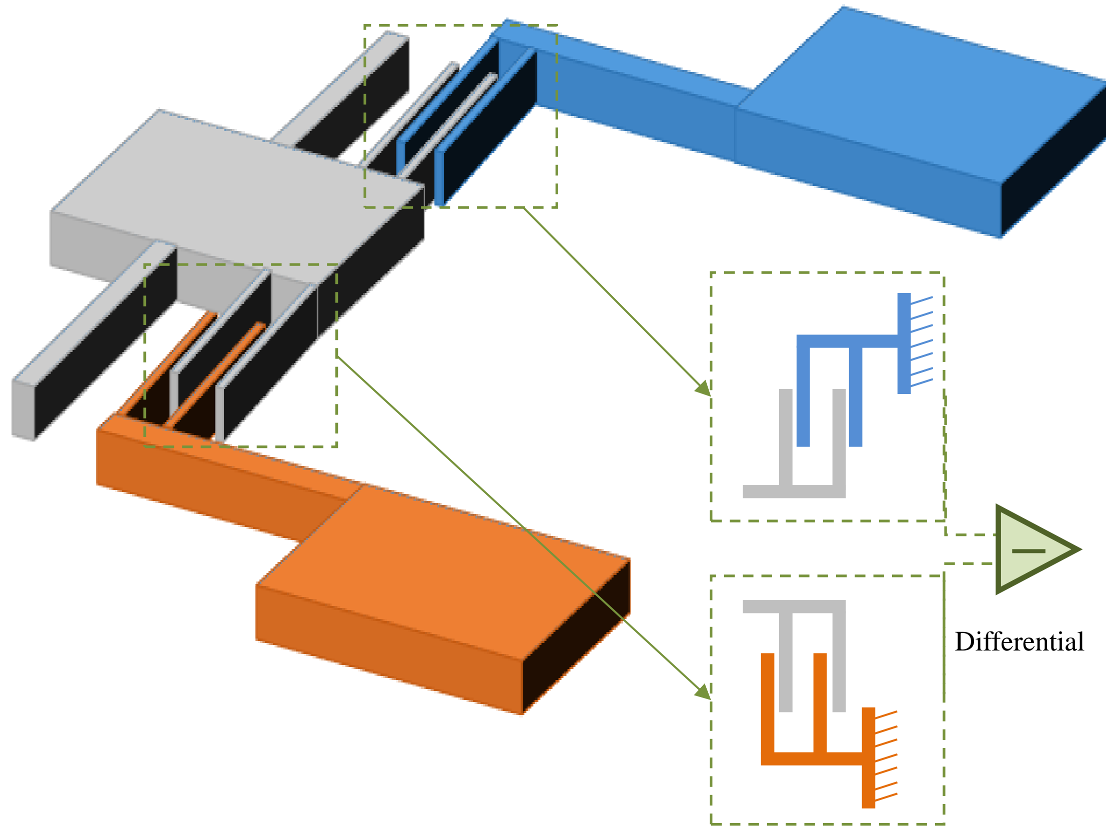

Figure 3. 15: Differential capacitive sensing.

If both motional current components consist of an effective sensing current, noise current, feedthrough current, and parasitic current, then the environment variables such as temperature and pressure will cause the alternations of all unwanted current sources. Accordingly, the differential motional current output can be expressed as:

$$i^{+}_{motion} = i_{sense} + i_{n}{}^{\Delta P}_{\Delta T} + i_{f}{}^{\Delta P}_{\Delta T} + i_{p}{}^{\Delta P}_{\Delta T} \tag{3.55}$$

$$i^{-}_{motion} = -i_{sense} + i_{n}{}^{\Delta P}_{\Delta T} + i_{f}{}^{\Delta P}_{\Delta T} + i_{p}{}^{\Delta P}_{\Delta T} \tag{3.56}$$

$$i_{diff} = i_{motion}^{+} - i_{motion}^{-} = 2i_{sense} \tag{3.57}$$

In conclusion, although differential capacitive sensing has increased the complexity and fragility of the device structure, with a proper design the enhanced motional current signal will effectively improve the device sensitivity, SNR, and noise signal rejection ability.

3.3.3 Pull-in Effect

As mentioned before, though capacitive transduction has many advantages, it has a serious problem: pull-in. The pull-in effect not only limits the total displacement of the proof mass but also affects the dynamic range and sensitivity. To analyze the pull-in effect, a state of equilibrium is assumed between the electrostatic force and the mechanical spring force. Hence, the total force existing on the parallel plate structure can be expressed as:

$$F_{total} = F_M + F_E = \frac{1}{2}\frac{\partial C}{\partial x}V^2 - Kx = 0 \tag{3.58}$$

where K is the effective spring stiffness, d is the original gap in the parallel plate structure, and x is the displacement. The equilibrium point stiffness can thus be derived as:

$$\frac{\partial F_{total}}{\partial x} = \frac{\varepsilon A V^2}{(d-x)^3} - K \tag{3.59}$$

$$V^2 = 2Kx\frac{(d-x)^2}{\varepsilon A} = \frac{2Kd^3}{\varepsilon A}\frac{x}{d}(1-\frac{x}{d})^2 \tag{3.60}$$

Accordingly, the relationship between the equilibrium point stiffness K, the displacement x, and the applied voltage V can be plotted as in Figure 3.16 (a) and (b). At the equilibrium point where the equilibrium stiffness is zero, the ratio of x/d is

around 0.3. Thus, the pull-in displacement is determined as:

$$x_{pull-in} \approx {}^{d}/_{3} \tag{3.61}$$

Inserting equation 3.56 back into equation 3.55, the pull-in voltage can also be deduced:

$$V_{pull-in} = \sqrt{\frac{8}{27}\frac{Kd^3}{\varepsilon A}} \tag{3.62}$$

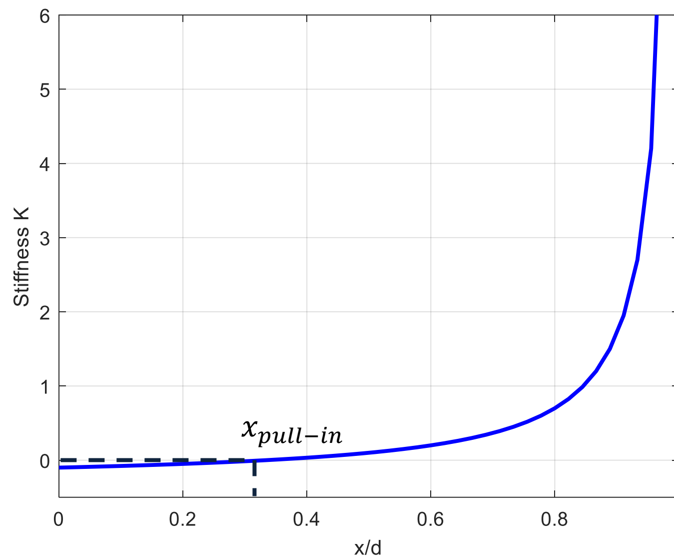

a)

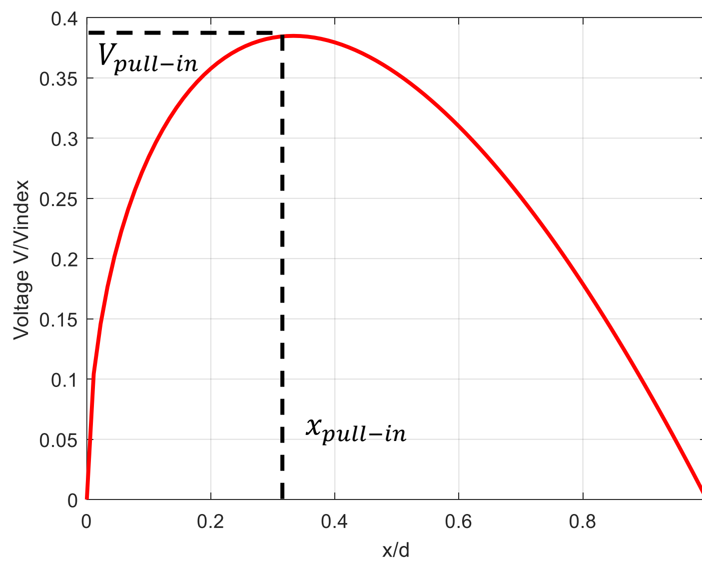

b)

Figure 3. 16: Pull-in phenomenon. a) The equilibrium point stiffness as a function of displacement. b) The applied voltage versus the relative displacement.

The system is unstable when the displacement is above the pull-in threshold. If the pull-in occurs, the mechanical spring force cannot compensate for the generated electrostatic force. Consequently, the parallel plate structure will be over-pulled and snap. Thus, proper design of capacitive actuation and sensing must include the coordination of the relationship between the pull-in displacement and pull-in voltage. The pull-in effect constrains the minimum gap between the parallel plate structures. The displacement in response to the excitation force, however, has to be carefully reviewed, as relatively small displacements will result in unsatisfactory SNR and sensitivity; conversely, large displacements will cause the problem of the pull-in effect.

3.4 Chapter Summary

This chapter provides a comprehensive theoretical analysis of a 3-DOF mode localized weakly coupled resonator. It discusses theoretical characterizations such as vibration modes, veering curves, and sensitivities in terms of frequency shift, eigenvector shift, and amplitude ratio. Additionally, it includes mathematical derivations for vibration mode frequencies and amplitude ratios. The chapter also examines system responses in respect to both stiffness perturbations and mass perturbations, and provides comparisons of actuation and sensing techniques, with a focus on capacitive actuation. Finally, this chapter investigates the anti-mode aliasing conditions and pull-in effects.

Chapter 4

Simulation Models of Multi-DOF Mode Localized Weakly Coupled Resonators

4.1 Simulations of a 3-DOF Mode Localized Weakly Coupled Resonator

4.1.1 Equivalent Electronic Circuit Model of a 3-DOF Mode Localized Weakly Coupled Resonator

Based on the fundamentals of the 3-DOF mode localized weakly coupled resonator, an equivalent electronic circuit model is adopted to mimic realistic system behaviors. Such modeling method offers simple, effective and rapid simulations that can be used for investigating linear responses of the 3-DOF coupled resonator. In addition, the equivalent electronic circuit model is capable of performing a sweep function to simulate multiple system responses in respect to different external perturbations. Further, it can include excitation force, noise and interface circuitry such as amplifiers. The flexibility and rapidity make equivalent electronic circuit a good simulation tool to study coupled resonators.

To correlate the electrical components with mechanical objects, an electrical transduction factor is needed. This is attained by revising equation 3.54 as:

$$i_{motion} = V_{DC}\frac{\partial C}{\partial x}\frac{\partial x}{\partial t} = \eta\dot{x} \tag{4.1}$$

Henceforth, the electrical transduction factor is defined as $\eta = V_{DC}\frac{\partial C}{\partial x}$. By substituting the motional current from equation 4.1 into the mechanical motion from equation 2.6 to obtain:

$$\frac{M}{\eta}\frac{\partial i_{motion}}{\partial t} + \frac{b}{\eta} i_{motion} + \frac{K}{\eta}\int i_{motion}\,dt = F \tag{4.2}$$

Assume an AC voltage is applied to actuate the system, the corresponding excitation force can hence be written as $F = \eta V_{AC}$, then substituting this expression into equation 4.2 to have:

$$\frac{M}{\eta^2}\frac{\partial i_{motion}}{\partial t} + \frac{b}{\eta^2} i_{motion} + \frac{K}{\eta^2}\int i_{motion}\,dt = V_{AC} \tag{4.3}$$

Accordingly, the constant term of each variable can be replaced by an electrical component. Consequently, it is adaptable to a series RLC electronic circuit:

$$L_e\frac{\partial i_{motion}}{\partial t} + R_e i_{motion} + \frac{1}{C_e}\int i_{motion}\,dt = V_{AC} \tag{4.4}$$

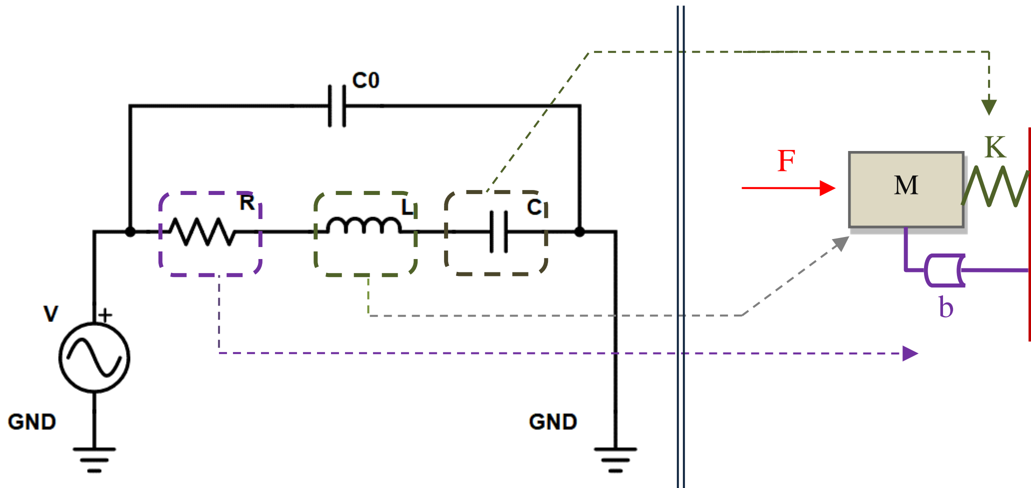

Figure 4. 1: Electronic equivalent circuit model in corresponding to a lumped model of 1-DOF MEMS resonator.

Diagram of a 1-DOF resonator in the form of equivalent electrical circuit model and lumped parameter model is demonstrated in Figure 4.1. To summarize, the equivalent electronic components are defined as:

$$L_e = {}^{M}/_{\eta^2} = {}^{K}/_{w^2\eta^2}$$
$$C_e = {}^{\eta^2}/_{w^2M} = {}^{\eta^2}/_{K} \quad (4.5)$$
$$R_e = {}^{b}/_{\eta^2} = {}^{\sqrt{KM}}/_{Q\eta^2} = {}^{wM}/_{Q\eta^2}$$

Once the equivalent RLC circuit for 1-DOF resonator is done, multi-DOF structure with coupling elements can be easily modeled by adopting this principle. As the stiffness term is equivalent to capacitance in RLC circuit, the coupling element is another stiffness component in the mechanically coupled system, hence it can be expressed as a unique capacitance in a multi-stage RLC circuit. A multi-stage RLC circuit model is proposed to represent the 3-DOF coupled resonator, as shown in Figure 4.2.

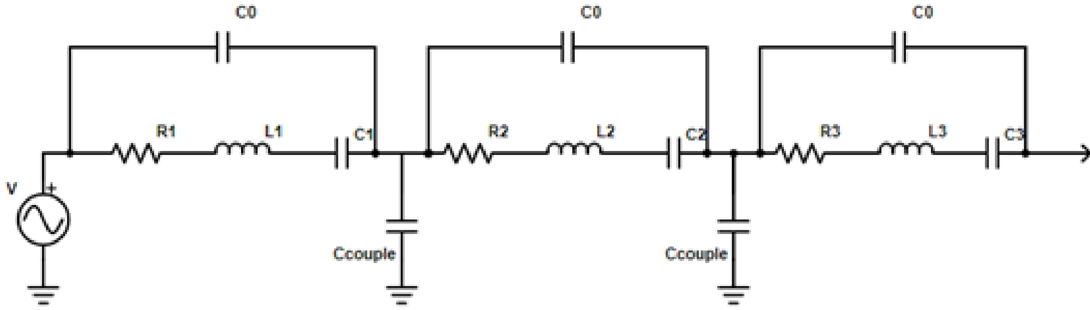

Figure 4. 2: Equivalent RLC circuit of a 3-DOF coupled resonator system.

The computed RLC circuit component values are listed in Table 4.1. To characterize the simulated system behavior, a group of stiffness perturbations are given to resonator3, which are in a form of capacitances. The established SPICE circuit simulation model is illustrated in Figure 4.3. The simulated system responses with stiffness perturbations for resonator 1 and resonator 3 are shown in Figure 4.4 (a) and (b), respectively.

Mechanical Parameter	***Component***	***Value***
$b1 = b2 = b3$	$R1 = R2 = R3$	$5.5 \times 10^6 \Omega$
Signal amplification	R_{TA}	$66 \times 10^6 \Omega$
$M1 = M2 = M3$	$L1 = L2 = L3$	$0.475 \times 10^6 H$

K1 = K3	C1 = C3	2.543×10^{-16}F
K2	C2	8.477×10^{-17}F
$K_{couple1} = K_{couple2}$	$C_{couple1} = C_{couple2}$	-1.907×10^{-15}F
Stiffness perturbation	C_{perb}	$[-4.2383331 \times^{-13}$ to $-6.3575001 \times^{-14}]$
Exitation force	$V_{actuation}$	15mV

Table 4. 1: Parameter definitions of equivalent RLC circuit simulation model.

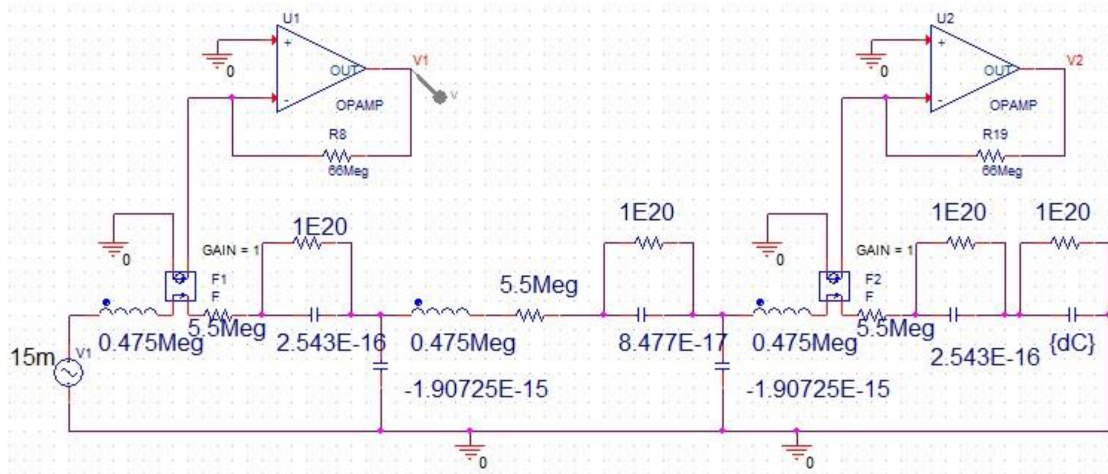

Figure 4. 3: SPICE simulation model of a 3-DOF coupled resonator.

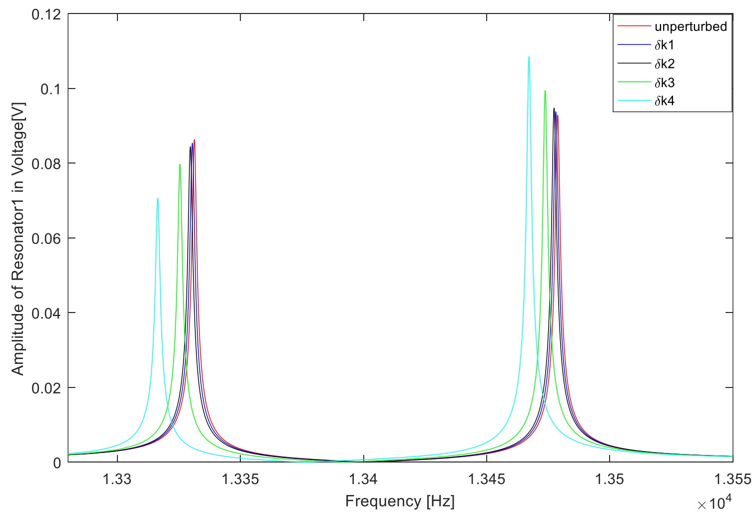

a)

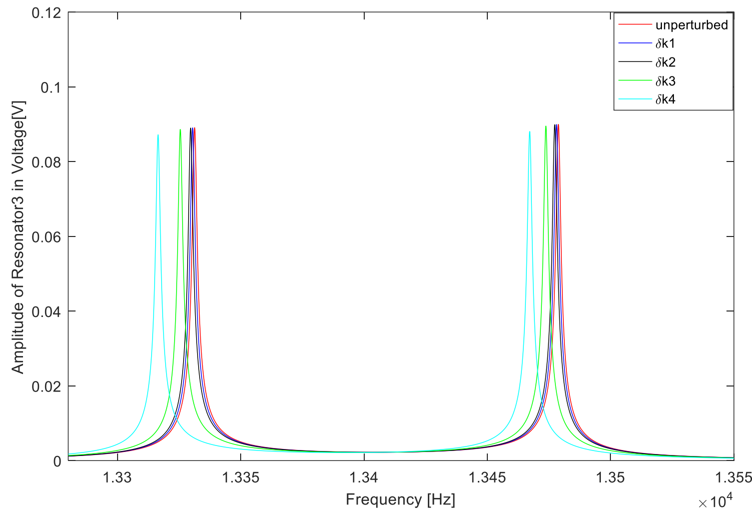

b)

Figure 4. 4: Equivalent RLC circuit simulated 3-DOF coupled resonator system responses (strong coupling). a) Resonator1. b) Resonator 3.

Accordingly, the sensitivities in term of resonance frequency shift, resonant amplitude change and resonance amplitude ratio change are able to plot in same scale by using normalization process. The two vibration modes: in-phase mode and out-of-phase mode are treated separately for the sensitivity characterization. The comparison of output metric sensitivities is depicted in Figure 4.5.

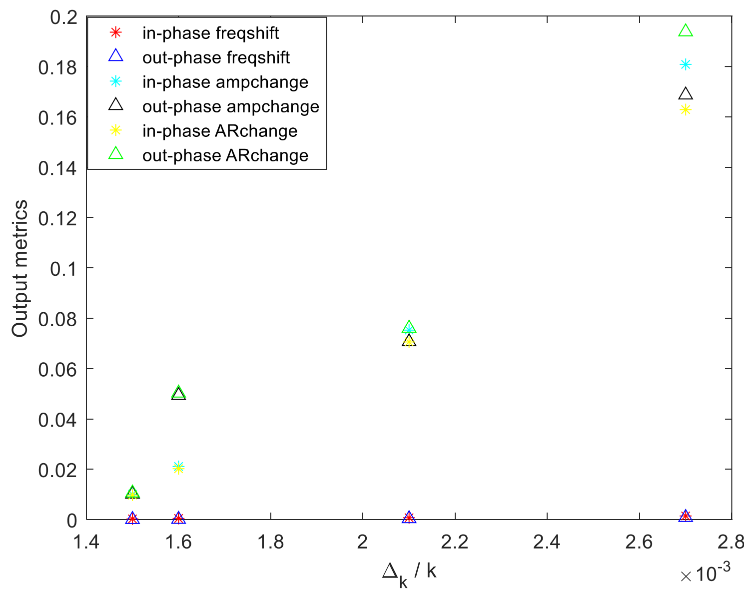

Figure 4. 5: Equivalent RLC circuit simulation model output metric sensitivities comparison (strong coupling).

It is can be seen, both amplitude change and amplitude ratio change yield one to two orders of sensitivity enhancements compared with resonance frequency shift. This is agreed well with the theoretical analysis. However, due to the simulation model was based on a relative large coupling strength, the discrimination of amplitude ratio change and amplitude change are not obvious. This is agreed with the computation from equation 3.20. A strong coupling can achieve good anti-mode aliasing, which results in clear separated mode curves with a relative large gap frequency. On the contrary, strong coupling heavily affects the final sensitivity in terms of amplitude ratio change. As shown in the simulation results, the sensitivity in terms of amplitude ratio change and amplitude change are tangled. Concurrently, another simulation model is implemented but alter the coupling strength to a much weaker level, the corresponding system responses and the comparison of output metric sensitivities are shown in Figure 4.6, Figure 4.7 respectively.

It is can be observed, after the coupling strength is adjusted to 5 times weaker than the first model, the final comparison denotes the sensitivity of vibration amplitude change is two orders higher than that of the resonance mode frequency shift. Moreover, the amplitude ratio change yields one to two orders of sensitivity enhancements compared with vibration amplitude change. The amplitude ratio sensitivity can be further improved by optimizing the system parameters such as coupling strength, middle resonator supporting beam stiffness and system Q factor, as discussed in the previous chapter.

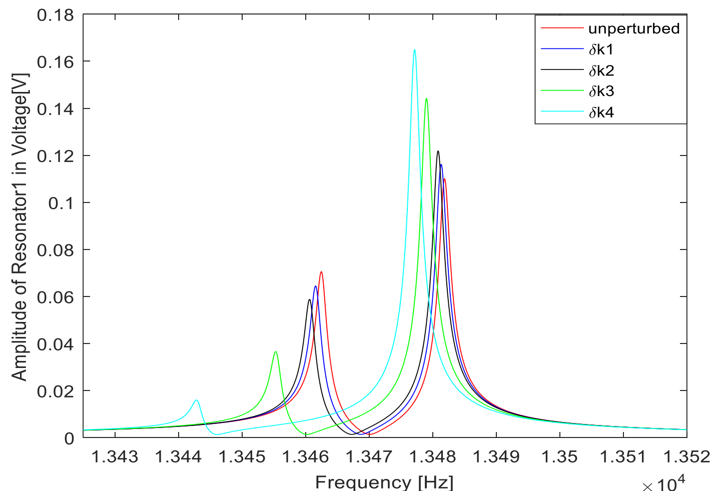

a)

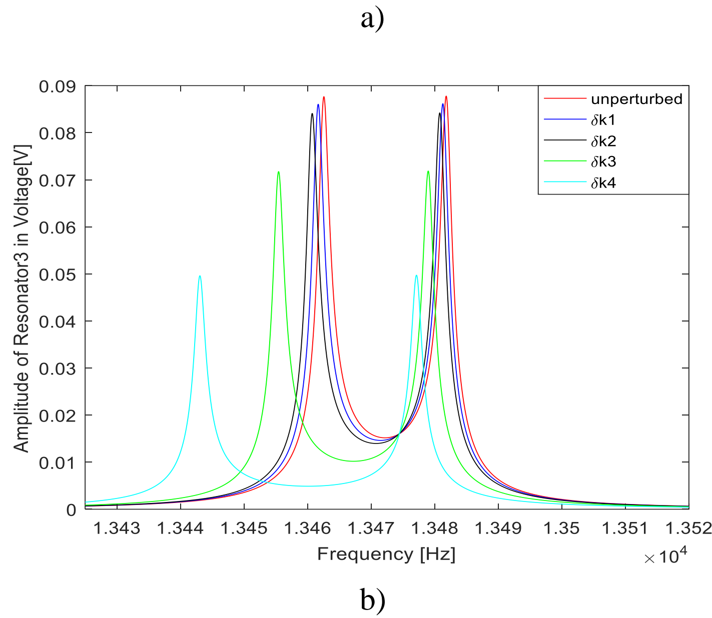

b)

Figure 4. 6: Equivalent RLC circuit simulated 3-DOF coupled resonator system responses (weak coupling). a) Resonator1. b) Resonator 3.

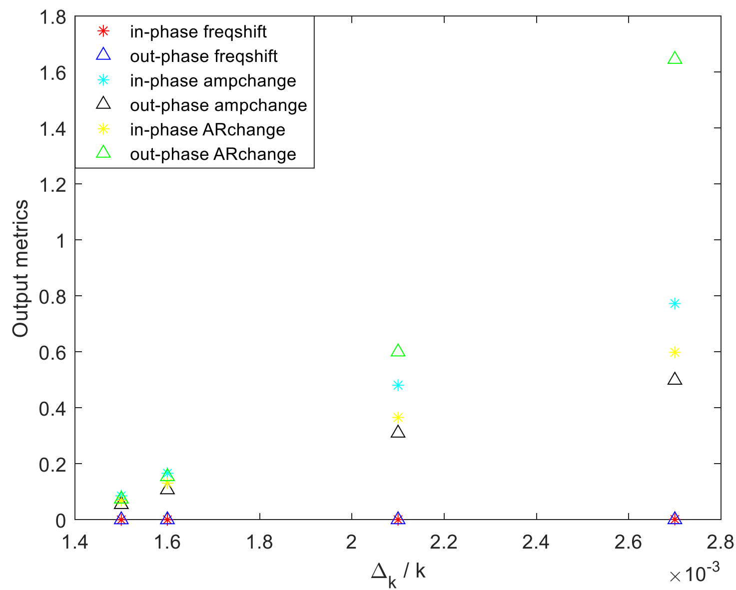

Figure 4. 7: Equivalent RLC circuit simulation model output metric sensitivities comparison (weak coupling).

4.1.2 MATLAB & Simulink Model of a 3-DOF Mode Localized Weakly Coupled Resonator

MATLAB in joint with Simulink simulations are benefitting from accurate, flexible

and system level modelling. Concurrently, it can attain complex simulations including non-linearity, different source of noises and environment variables. To perform theoretical analysis, MATLAB is the perfect tool to verify basic properties such as mode frequencies and eigenstates. However, merely MATLAB is difficult in system level simulations, thus Simulink is combined. Although the many advantages of MATLAB & Simulink simulation, the modeling speed and complexity (mathematical and logical block functions) are the main drawbacks.

In what follows, a series of MATLAB & Simulink models for a 3-DOF mode localized coupled resonator are presented. Starting with Table 4.2, which has listed the system parameters, followed by a demonstration of Simulink model in Figure 4.8.

System Parameters	***Values***
Actuation force	$1.45 \times 10^{-9}\mathrm{N}$
Resonator effective mass $\mathrm{M_1 = M_2 = M_3}$	$6.94 \times 10^{-9}\mathrm{kg}$
Resonator1 & resonator3 effective stiffness $\mathrm{K_1 = K_3}$	$48.815\mathrm{N/m}$
Resonator2 effective stiffness $\mathrm{K_2}$	$285.212\mathrm{N/m}$
Coupling strength (in stiffness) $\mathrm{K_c}$	$3.9255\mathrm{N/m}$
Sweeping frequency range & step	$[10000: 0.1: 16000]\mathrm{Hz}$
Actuation electrode effective area	$360 \times 10^{-6} \times 22 \times 10^{-6}\mathrm{um}^2$
Comb fingers effective area	$70 \times 10^{-6} \times 22 \times 10^{-6}\mathrm{um}^2$
Original gaps	$4.5\mathrm{um}$
Damping coefficient in vacuum $\mathrm{b_1 = b_2 = b_3}$	6.2×10^{-8}
Damping coefficient in air $\mathrm{b_1 = b_2 = b_3}$	6.6×10^{-6}

Mass perturbations	$[10:10:50]$ng
Stiffness perturbations	$-[0.083:0.083:0.415]$N/m

Table 4. 2: MATLAB & Simulink simulation model parameters.

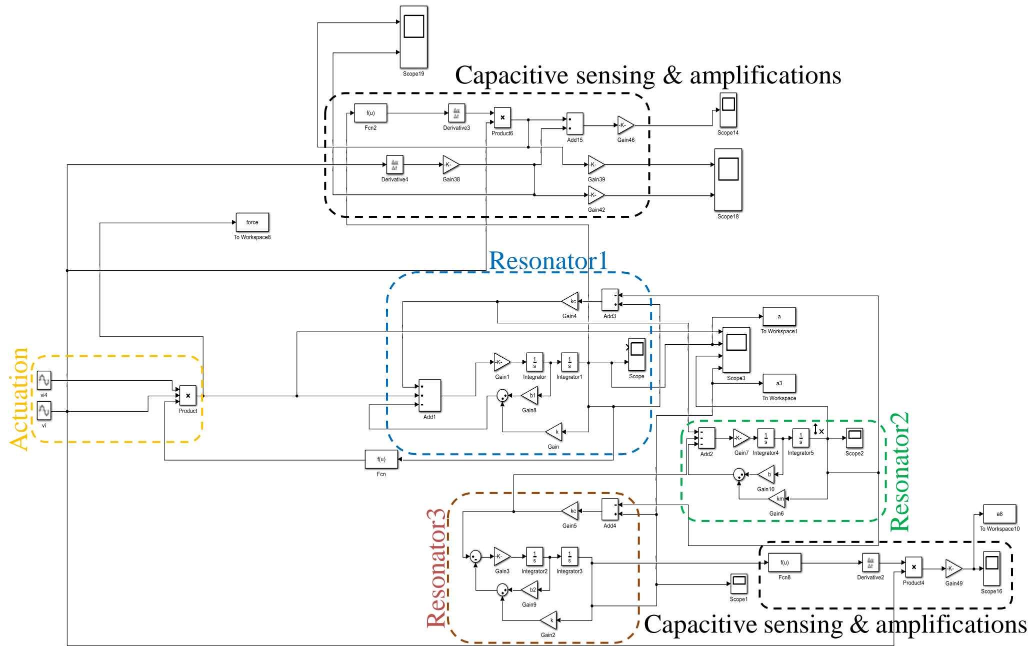

Figure 4. 8: Simulink system level simulation of a 3-DOF coupled resonator.

Two different types of perturbations are given to the established model: five consecutive mass perturbations are added on the effective mass of resonator3 and five consecutive stiffness perturbations are put on the effective stiffness of resonator3, respectively. Further, two scenarios of the environment condition are assumed: i) vacuum. ii) atmospheric pressure. The motional currents are obtained from vibration displacements of resonator1 & resonator3 via capacitive sensing principle. Henceforth, the motional currents are converted to voltage signals and amplified by external electrical facilities such as transimpedence amplifier. The noise sources are neglected in the simulations. Figure 4.9 a) and b) illustrate the simulated frequency responses of resonator1 and resonator3 under the condition of stiffness perturbations, respectively. The output metric sensitivities are deduced accordingly, followed by a normalized sensitivity comparison as shown in Figure 4.10.

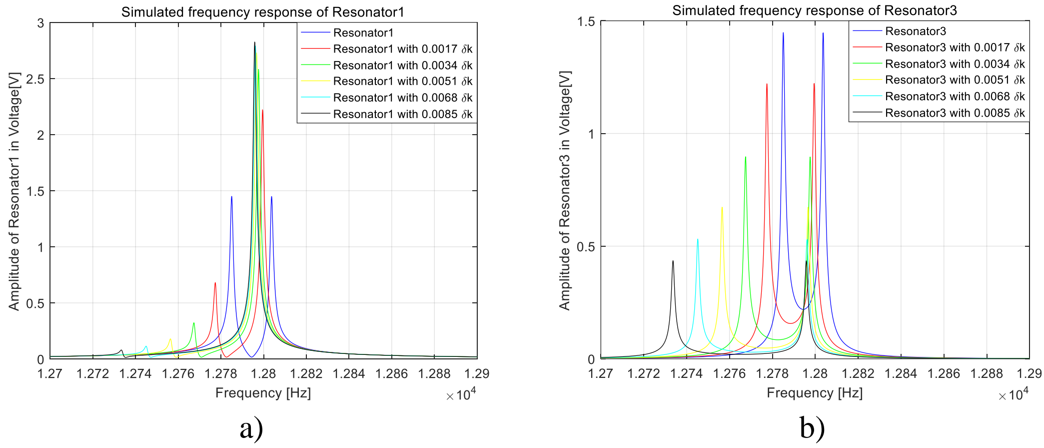

Figure 4. 9: MATLAB & Simulink simulated frequency responses with given stiffness perturbations. a) Resonator 1. b) Resonator 3.

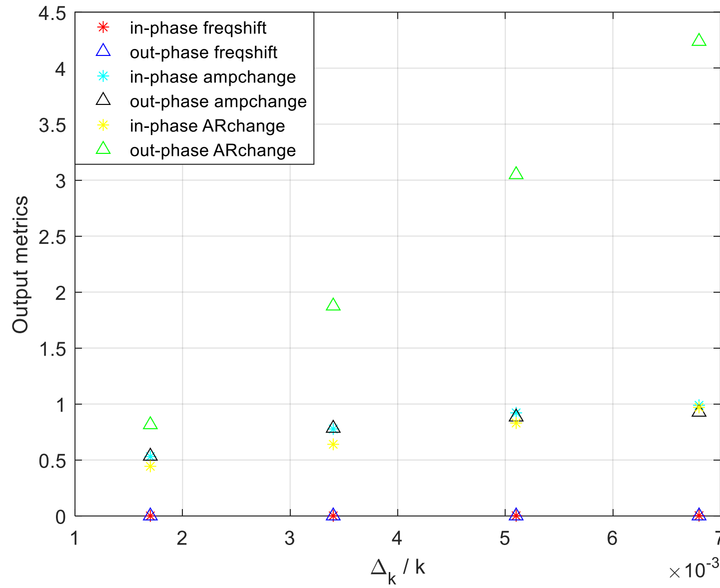

Figure 4. 10: MATLAB & Simulink model output metric sensitivities comparison (stiffness perturbations).

Similarly, the simulated frequency responses of resonator1 and resonator3 under the condition of mass perturbations are exhibited in Figure 4.11 a) and b), accompanied with output metric sensitivities comparison in Figure 4.12.

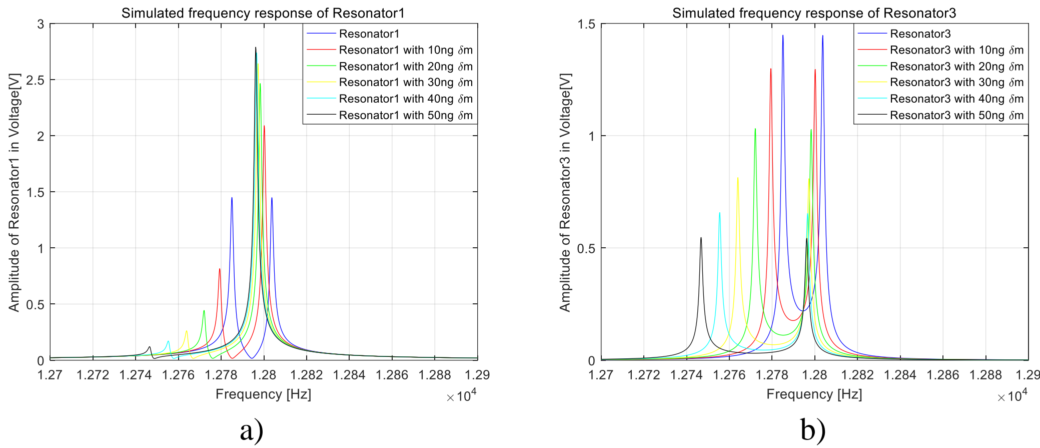

Figure 4. 11: MATLAB & Simulink simulated frequency responses with given mass perturbations. a) Resonator 1. b) Resonator 3.

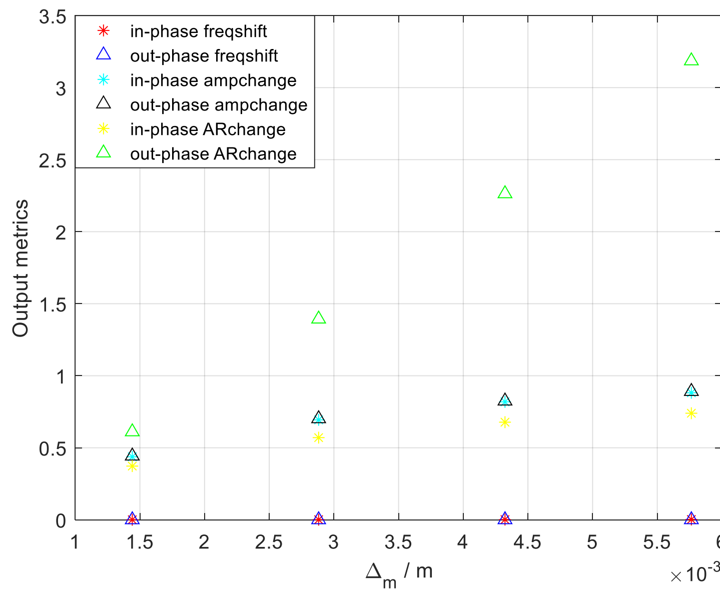

Figure 4. 12: MATLAB & Simulink model output metric sensitivities comparison (mass perturbations).

As can be observed, both perturbation cases have proved that the amplitude ratio change as an output metric yields one to two orders of sensitivity enhancements compared with vibration amplitude change. On the other hand, the vibration amplitude change yields at least two orders of sensitivity improvements than that of the resonance frequency shift. The simulation models are in a good agreement with the theoretical analysis in chapter 3.

Next, the simulation models are altered to atmospheric pressure condition. The simulated results are depicted in the following. Figure 4.13 a) and b) illustrate the

simulated frequency responses of resonator1 and resonator3 with stiffness perturbations under atmospheric pressure condition, respectively. The output metric sensitivities are deduced accordingly, followed by a normalized sensitivity comparison as shown in Figure 4.14.

Then, the mass perturbations are given, whereby the simulated frequency responses of resonator1 and resonator3 are exhibited in Figure 4.15 a) and b), accompanied with output metric sensitivities comparison in Figure 4.16.

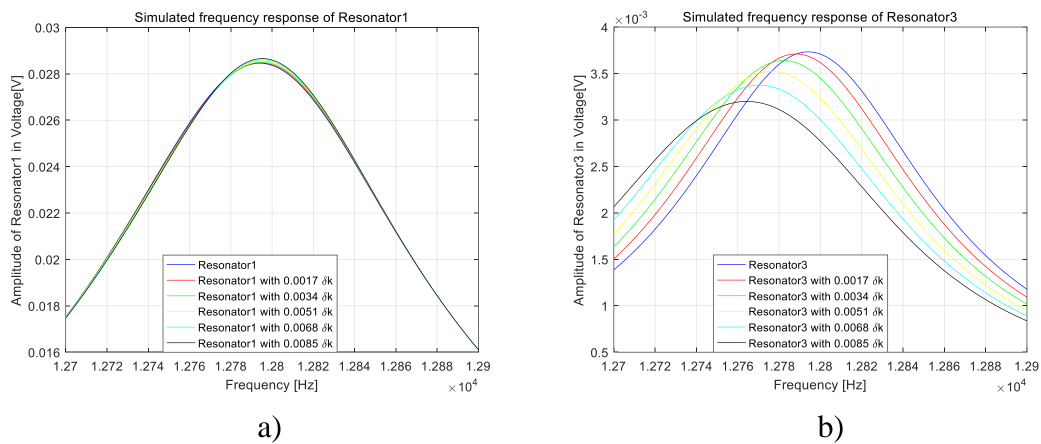

Figure 4. 13: MATLAB & Simulink simulated frequency responses with given stiffness perturbations under atmospheric pressure. a) Resonator 1. b) Resonator 3.

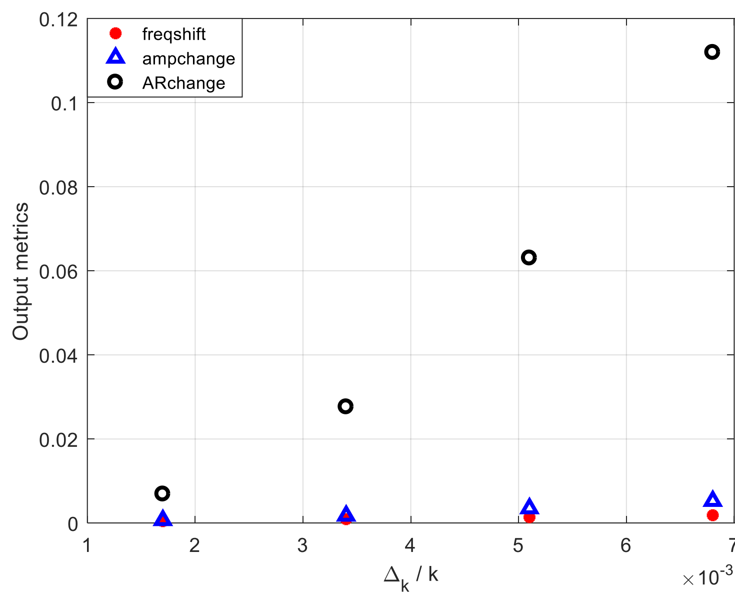

Figure 4. 14: MATLAB & Simulink model output metric sensitivities comparison under

atmospheric pressure (stiffness perturbations).

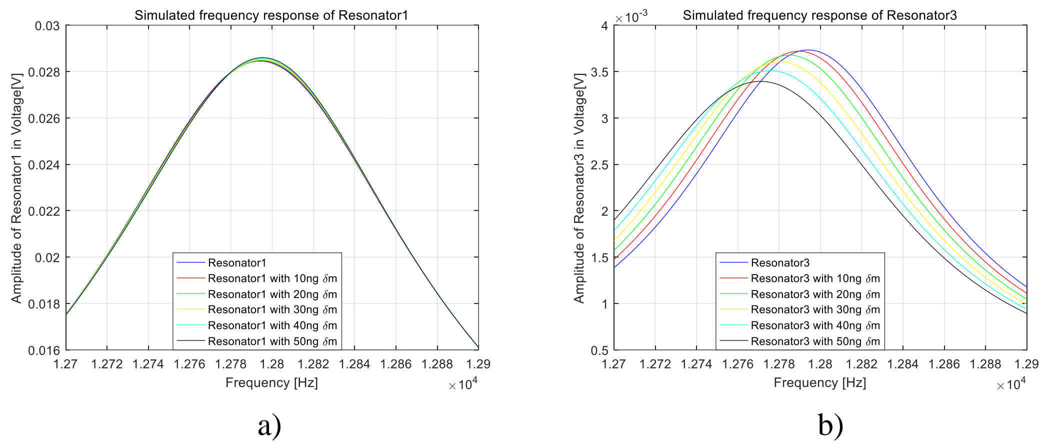

a) b)

Figure 4. 15: MATLAB & Simulink simulated frequency responses with given mass perturbations under atmospheric pressure. a) Resonator 1. b) Resonator 3.

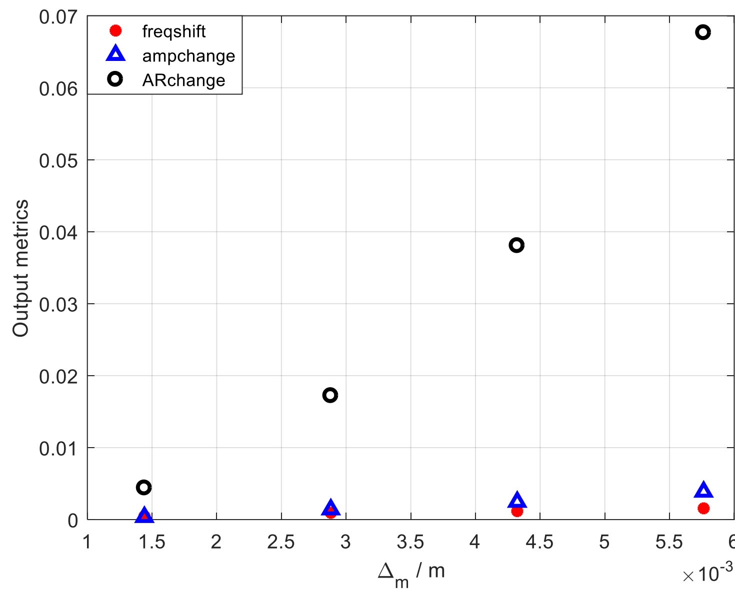

Figure 4. 16: MATLAB & Simulink model output metric sensitivities comparison under atmospheric pressure (mass perturbations).

Evidently, due to the simulation condition was under atmospheric pressure, mode aliasing effect heavily affected the system behavior. First and foremost, the vibration modes are overlapped, which results in only one peak. Consequently, the output metric cannot be defined according to the dedicated vibration mode. Hence, the output metric sensitives merely derived from the single mixed peak. It is can be seen, the normalized sensitivities deduced from amplitude change and amplitude ratio change are

dramatically reduced, whereas the frequency shift sensitivity remains the same. Another interesting point is the amplitude change sensitivity (assume the perturbation is given to resonator3), under low Q condition (in air), the superiority of amplitude ratio is doubtable when it is compared with amplitude change of resonator3. However, the amplitude ratio still maintain excellence in contrast to amplitude change of resonator1 (the actuation force is given to resonator1). In summary, even though the vibration modes are overlapped under atmospheric pressure, the 3-DOF coupled resonator still has the capability to be employed as a sensor device; in which the amplitude ratio as an output metric yields the highest sensitivity in comparison with amplitude change and resonance frequency shift.

4.1.3 COMSOL Simulation Model of a 3-DOF Mode Localized Weakly Coupled Resonator

COMSOL finite element method (FEM) provide intuitive simulations for periodic mechanical vibration structures. It is a perfect platform to study the MEMS coupled resonator mechanical structure properties. The characterization of vibration modes can be easily extracted as well as garnered the eigenfrequencies (natural resonance frequencies). However, the main drawback of COMSOL is the simulation speed. Complex structure for instance comb fingers with a fine mesh could bring failure to the software. In addition, multi-physics simulations such as involving damping, electrostatic force, currents and voltages are greatly increased the simulation difficulty.

In this section, starting with Figure 4.17, which shows the vibration modes of a 3-DOF mode localized weakly coupled resonator. Followed by Figure 4.18 that illustrates the corresponding frequency responses of resonator1 and resonator3, respectively.

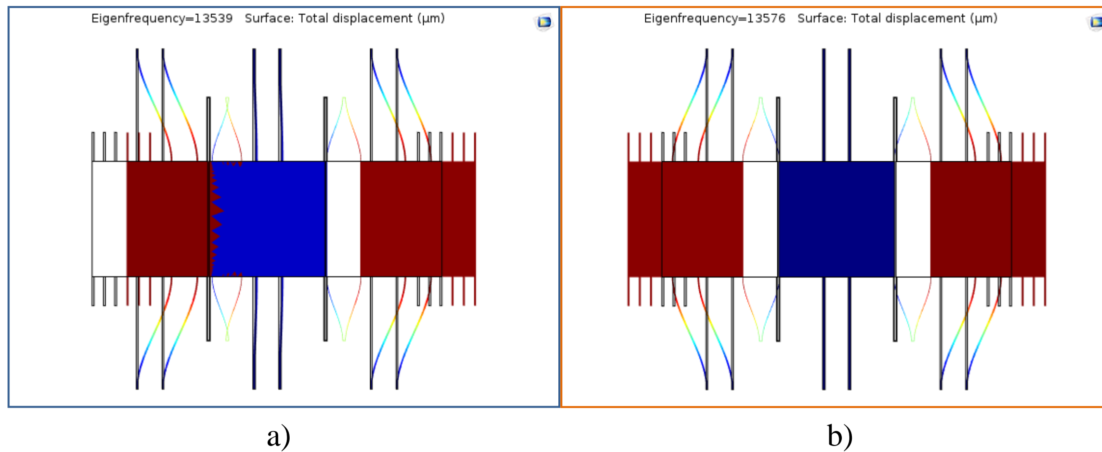

a) b)

Figure 4. 17: COMSOL simulated vibration modes of a 3-DOF coupled resonator. a) In-phase mode. b) Out-of-phase mode.

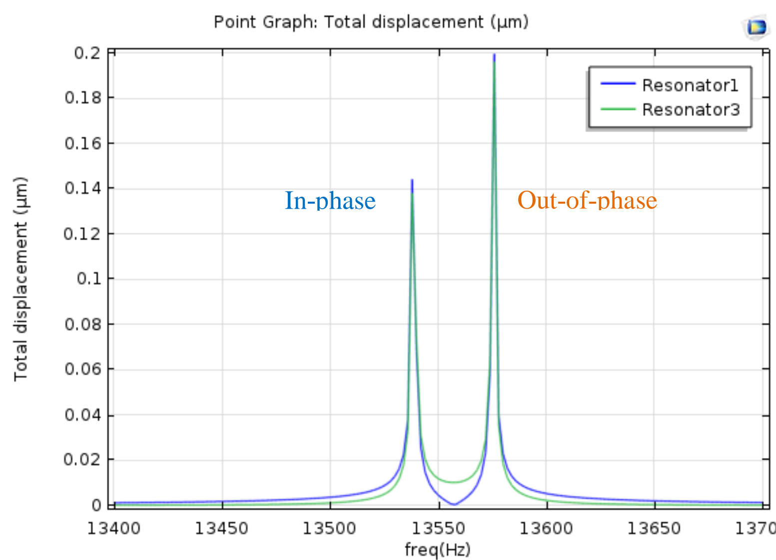

Figure 4. 18: COMSOL simulated vibration amplitudes with a given excitation force on resonator1.

4.2 Simulations of QCM Mass Sensing System

4.2.1 Equivalent Electronic Circuit Model of a QCM Mass Sensor

In order to overcome the losses of functionality in a 3-DOF coupled resonator due to damped environment applications, an alternative approach is proposed, which exploits a QCM mass sensor incorporated with 3-DOF weakly coupled resonator stiffness sensor to attain a hybrid transduction mechanism.

Similar as the electrical model of coupled resonators, a RLC circuit can also be

adopted to represent a QCM mass sensor. To be more specific, the Butterworth van Dyke electrical model [82, 83] is used. This RLC model can efficiently extract accurate resonant frequency of the QCM sensor, as well as predicting the QCM frequency responses in respect to mass perturbations. The SPICE model of the RLC circuit is represented in Figure 4.19 a), Figure 4.19 b) shows the frequency responses with mass perturbations and finally, the parameter definitions are listed in Table 4.3.

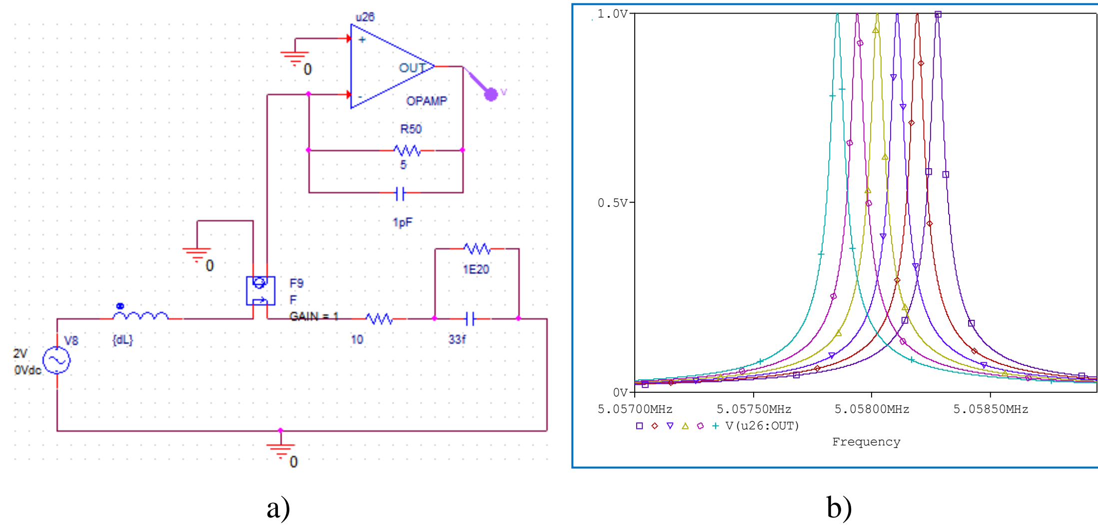

Figure 4. 19: SPICE equivalent RLC circuit model. a) Actual model set-up. b) Frequency responses with mass perturbations.

Component	***Defination***	***Value***
R	Dissipation of the oscillation energy (damping elements)	10Ω
R_{TA}	Signal amplification	5Ω
L	Effective mass	30mH
C	Stored energy (elasticity of the quartz structure)	33fF
C_{TA}	Signal amplification	5pF
L_{perb}	Mass perturbations	[0.001: 0.001: 0.005]mH
$V_{actuation}$	Excitation force	2V

Table 4. 3: Equivalent RLC circuit parameter definitions.

4.2.2 MATLAB & Simulink Model of a QCM Mass Sensor Incorporated With a 3-DOF Weakly Coupled Resonator Stiffness Sensor

The MATLAB & Simulink combined simulation can attain system level modeling which consists of QCM mass sensor in damped environment, peak detector, and 3-DOF weakly coupled resonator in vacuum. Starting with QCM mass sensor, the frequency responses with consecutive mass perturbations are shown in Figure 4.20.

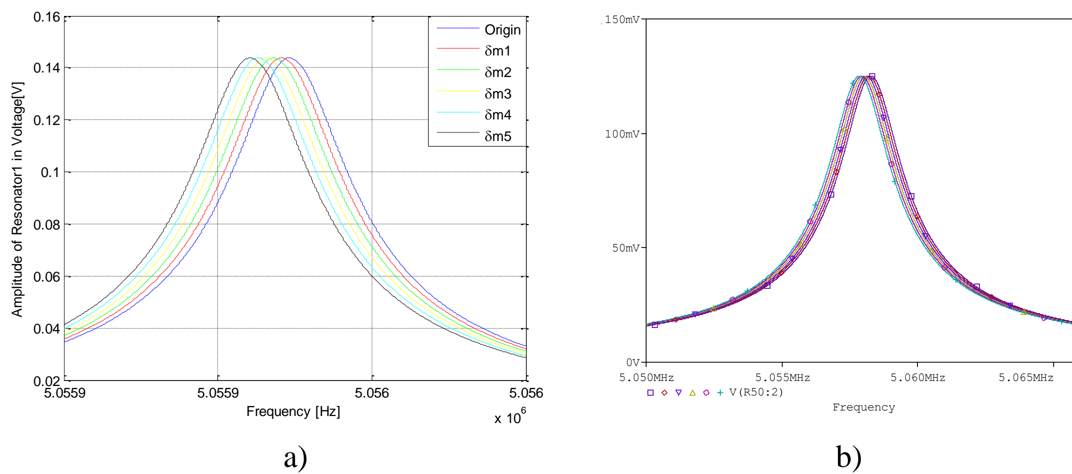

a) b)

Figure 4. 20: Simulated QCM mass sensor frequency responses with consecutive mass perturbations under atmospheric pressure. a) MATLAB & Simulink model. b) Equivalent RLC circuit model.

Next, the system level simulation is carried out. As illustrated in Figure 4.21, the QCM mass sensor is combined with a 3-DOF weakly coupled resonator, in which the 3-DOF coupled resonator model is the same as the MATLAB & Simulink model in the previous section. A peak detector stage is existed between the output of the QCM mass sensor and the input of 3-DOF coupled resonator stiffness perturbation port. The QCM mass sensor is actuated at the original resonance frequency, constantly. When an external mass perturbation is rendered, the output AC signal will be converted to a DC voltage signal via the peak detector and hence fed to the stiffness perturbation port of the 3-DOF coupled resonator. The 3-DOF coupled resonator on the other hand, is operating in *vacuum* condition. Consequently, the functionality of the weakly coupled resonator is preserved and the low-Q drawback is avoided. Simultaneously, the QCM is capable to perform direct liquid contact measurements, which denotes the hybrid

system has potential to be employed in heavy damped applications, such as liquid contact biosensors. The system model and the corresponding outputs are exhibited in Figure 4.21 and Figure 4.22, respectively.

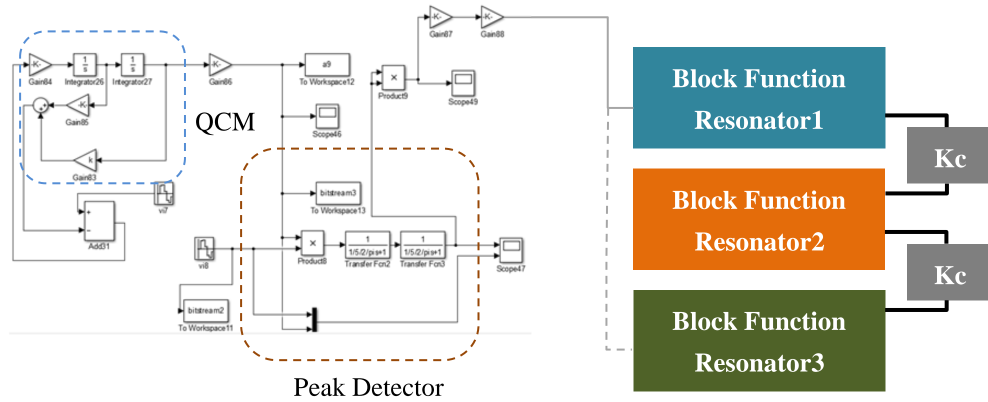

Figure 4. 21: MATLAB & Simulink system level modeling.

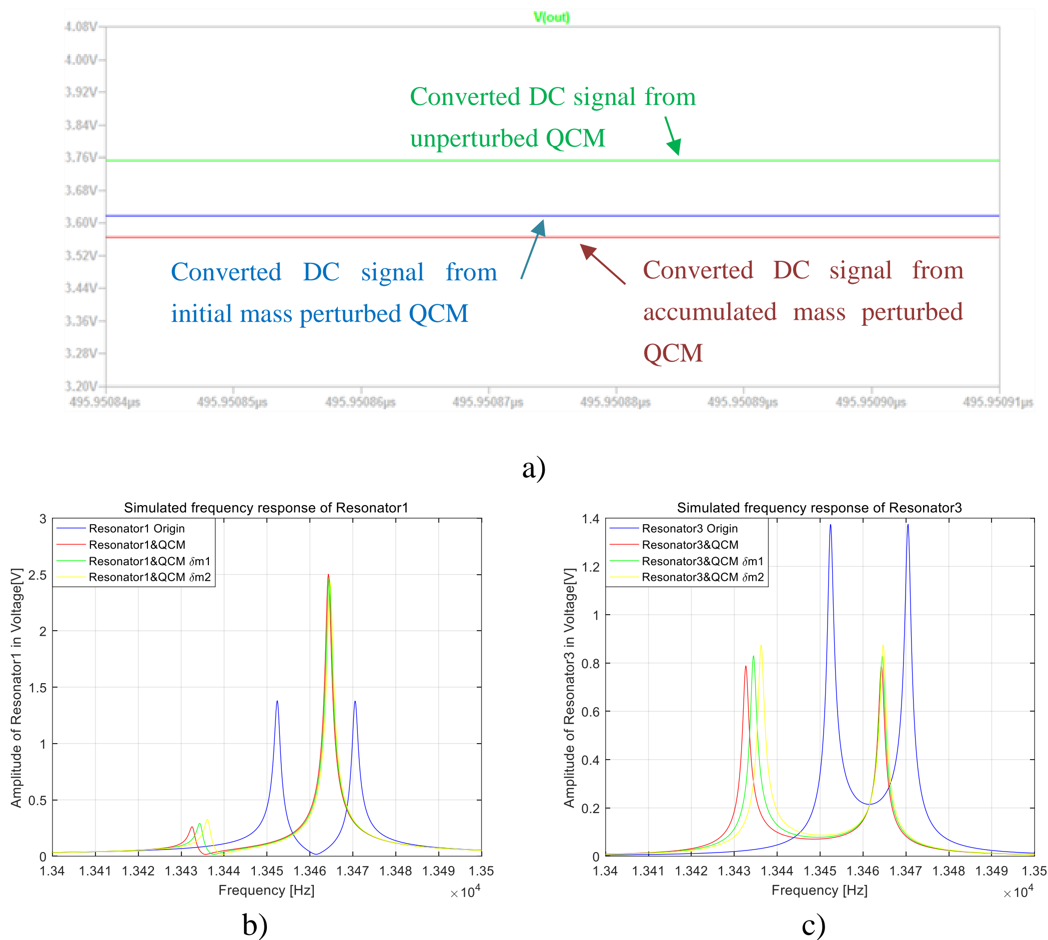

Figure 4. 22: QCM incorporated with 3-DOF coupled resonator MATLAB & Simulink model. a) QCM mass sensor in air, the output signals are converted to DC voltages via peak detector. The converted DC voltages are used as electrostatic forces to generate

stiffness perturbations for resonator3 in a 3-DOF weakly coupled resonator which operates in vacuum. b) The frequency responses of resonator1 in the hybrid system. c) The frequency responses of resonator3 in the hybrid system.

The output metrics in terms of resonance frequency shift, amplitude change and amplitude ratio can be adopted for the hybrid system. The normalized sensitivities comparison is shown in Figure 4.23.

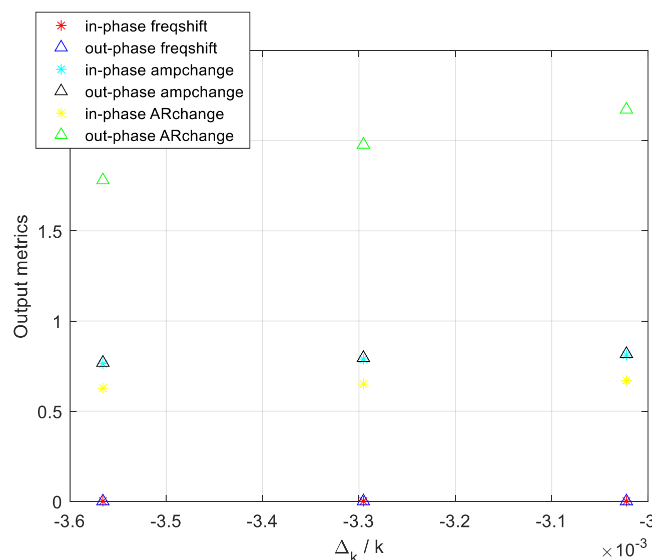

Figure 4. 23: MATLAB & Simulink simulated QCM combined with 3-DOF coupled resonator hybrid system normalized sensitivities comparison.

It is can be observed, as the theoretical analysis and simulations for the 3-DOF mode localized weakly coupled resonator under high Q condition (operate in vacuum), the amplitude ratio as an output metric yields one to two orders of sensitivity enhancements compared with amplitude change, and again, the resonance frequency shift yields the lowest normalized sensitivity. Accordingly, the advantages of the multi-DOF mode localized coupled resonator are preserved while an effective mass sensing approach can also be attained in damped condition. Further possibilities remains in the capability of direct liquid contact measurements by using this hybrid system.

4.3 Simulations of 2-DOF Coupled BAW Disk Resonator

The ongoing investigation focus on employing multi-DOF mode localized coupled

resonator in damped environment but maintaining its superior functionality. Based on structure wise modifications, Silicon disk Bulk Acoustic Wave (BAW) resonators are the suitable candidates which can operate in damped environment yet have a good system quality factor (Q-factor). By adopting the theory of coupled resonator and mode localization mechanism, a 2-DOF weakly coupled mode localized BAW disk resonator is proposed.

Silicon disk Bulk Acoustic Wave resonators are excited in either Extensional mode (Breath mode) [84, 85] or Wine-Glass mode [86, 87], they can achieve thousands of Q-factor in air. Generally, BAW resonant devices are operating in high frequency region(>1 MHz) [88, 89], the disk shape proof mass has intrinsic large surface area that is suitable for droplet deposition (adding masses), also they sharing similar fabrication process with other types of resonator, and IC-compatibility.

The 2-DOF weakly coupled mode localized BAW disk resonator can also be expressed as a mechanical lumped parameter model [90-92], as shown in Figure 4.24.

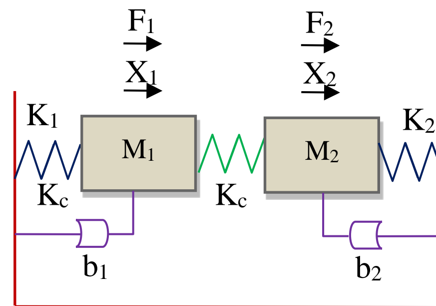

Figure 4. 24: 2-DOF coupled BAW disk resonator lumped parameter model.

The theoretical analysis of typical 2-DOF coupled resonator on the other hand, has already been introduced in chapter 2, as well as basic characterizations of mode localization behaviors in the 2-DOF coupled system. In what follows, different simulation models are represented, including equivalent RLC circuit model, MATLAB model and COMSOL model.

4.3.1 Equivalent Electronic Circuit Model of a 2-DOF Mode Localized Coupled BAW Disk Resonator

To establish an equivalent RLC circuit model, equation 4.5 is availed. The RLC circuit model is similar as it is for 3-DOF coupled resonator, but only has two stages. The computed electrical component values are listed in Table 4.4. To characterize the simulated system behavior, a group of mass perturbations are given to resonator 2, in a form of additional inductances. The actual SPICE model is illustrated in Figure 4.25. The equivalent RLC circuit simulated frequency responses of resonator 1 and resonator 2 with mass perturbations are shown in Figure 4.26 (a) and (b), respectively.

Mechanical Parameter	*Component*	*Value*
b1 = b2	R1 = R2	$2.1718 \times 10^{6}\Omega$
Signal amplification	R_{TA}	$230 \times 10^{6}\Omega$
M1 = M2	L1 = L2	888.2264H
K1 = K2	C1 = C2	4.036×10^{-18}F
K_{couple}	C_{couple}	9.086×10^{-15}F
Mass perturbation	L_{perb}	0.05% to 0.2%
Exitation force	$V_{actuation}$	220mV

Table 4. 4: Parameter definitions of equivalent RLC circuit model for a 2-DOF coupled BAW disk resonator.

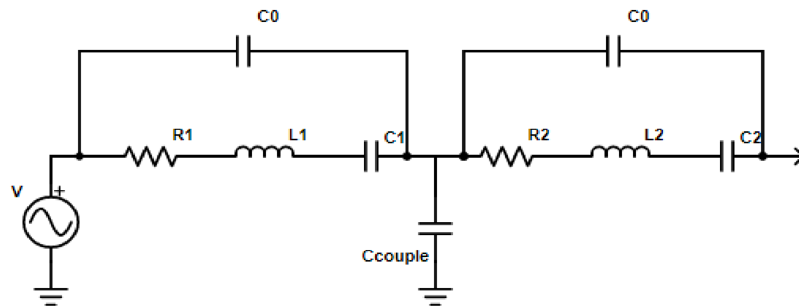

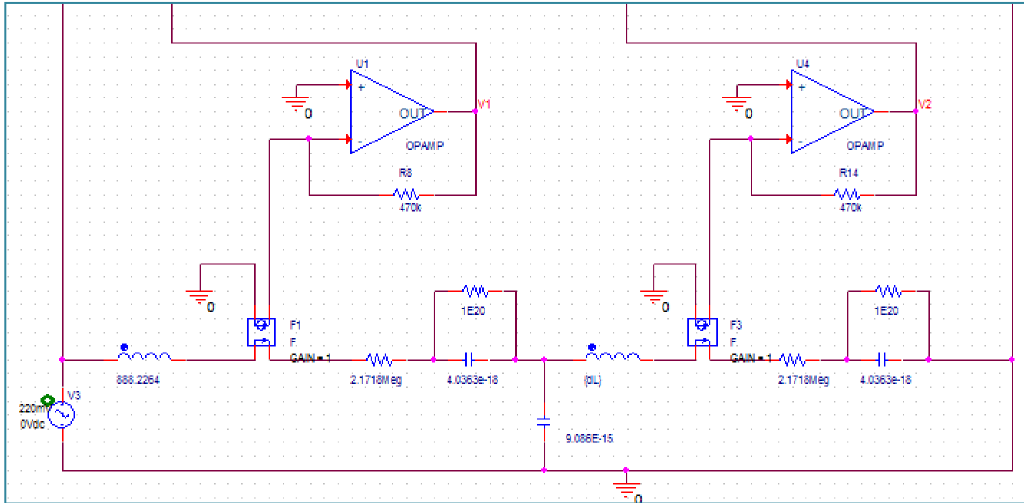

Figure 4. 25: SPICE simulation model of a 2-DOF coupled BAW disk resonator.

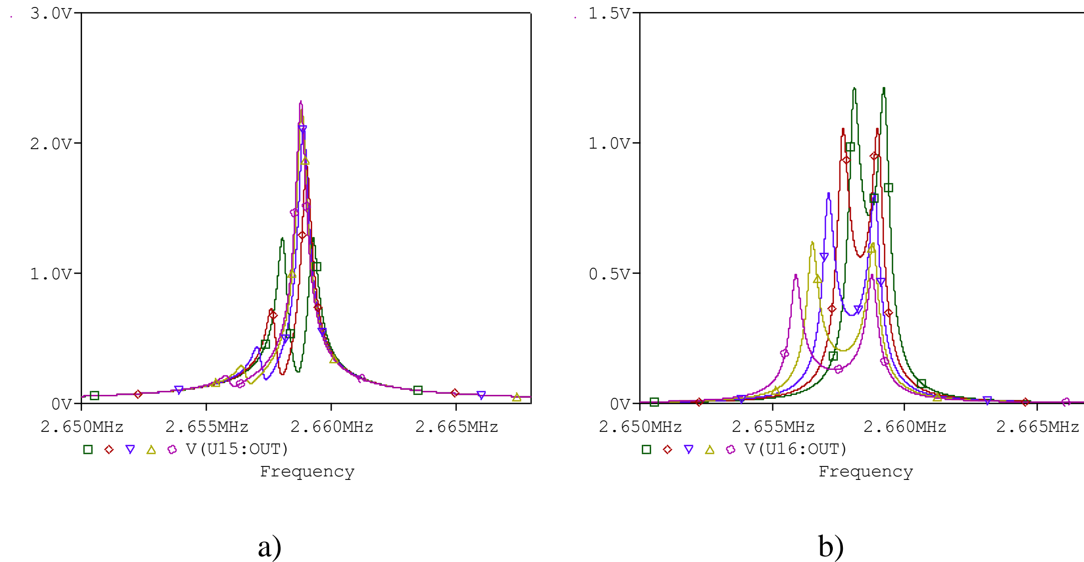

a) b)

Figure 4. 26: SPICE simulated frequency responses with given mass perturbations. a) Resonator 1. b) Resonator 2.

4.3.2 MATLAB Model of a 2-DOF Mode Localized Coupled BAW Disk Resonator

The abovementioned equivalent RLC circuit model can be verified by using MATLAB simulation model, in which the MATLAB model is based on the 2-DOF coupled BAW disk resonator system equations of motion. Firstly, Table 4.5 listed the parameters and corresponding values of the MATLAB model. Followed by the demonstrations of simulated frequency responses in Figure 4.27 a) and b). In the end,

the output metric sensitivities comparison is implemented in Figure 4.28.

System Parameters	***Values***
Actuation force	$2.21 \times 10^{-8}\mathrm{N}$
Resonator effective mass $M_1 = M_2$	$6.3451 \times 10^{-8}\mathrm{kg}$
Resonator1 & resonator3 effective stiffness $K_1 = K_2$	$1.7698 \times 10^{7}\mathrm{N/m}$
Coupling strength (in stiffness) K_c	$586.4\mathrm{N/m}$
Sweeping frequency range & step	$[2.655\mathrm{Meg}: 0.1: 2.661\mathrm{Meg}]\mathrm{Hz}$
Mass perturbations	$[635,1269,1904,2538]\mathrm{ng}$

Table 4. 5: Parameters of MATLAB simulation model for a 2-DOF coupled BAW disk resonator.

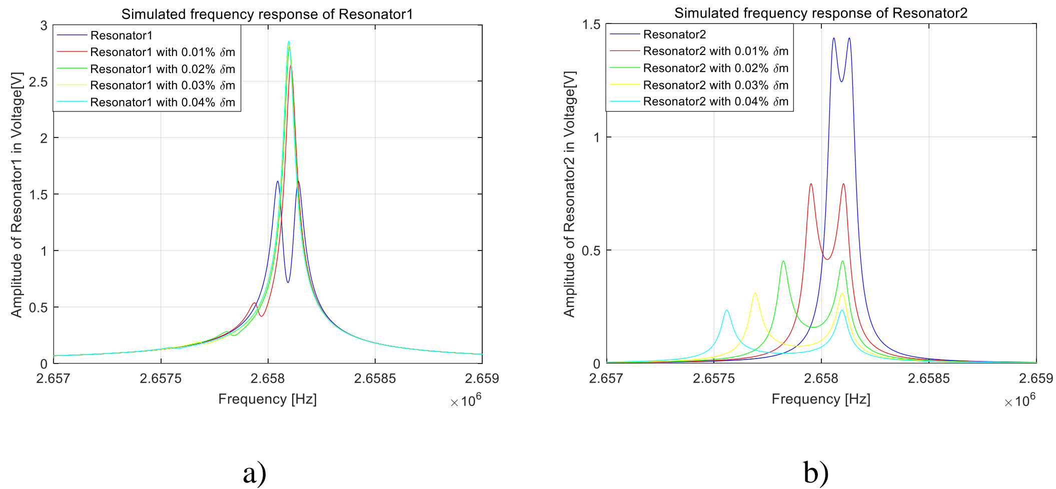

Figure 4. 27: MATLAB simulated frequency responses of a 2-DOF coupled BAW disk resonator under atmospheric pressure. a) Resonator 1. b) Resonator 2.

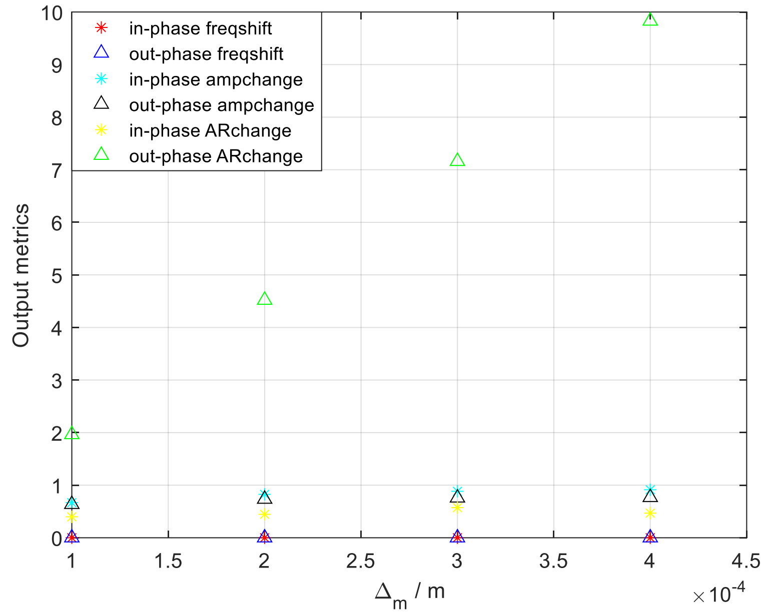

Figure 4. 28: MATLAB simulated 2-DOF coupled BAW disk resonator normalized sensitivities comparison.

Evidently, the notion of mode localization is well proved in the simulation model, in which the amplitude ratio change yields the highest normalized sensitivity. Even if the simulation condition is under atmospheric pressure, the 2-DOF coupled BAW disk resonator however, has demonstrated a Q-factor ~5000, which is a distinguished property for such BAW coupled resonator.

4.3.3 COMSOL Simulation Model of a 2-DOF Mode Localized Coupled BAW Disk Resonator

In order to investigate the mechanical vibration mode shapes and the corresponding mode frequencies, COMSOL FEM simulation models of the 2-DOF coupled BAW disk resonator system with mechanical beam coupling are established. The COMSOL model is constructed under the condition of atmospheric pressure, in which the Rayleigh damping parameters [93] are availed to represent the viscous losses.

Firstly, the eigenfrequency analysis is carried out. Similar as what has been done for the 3-DOF coupled resonator, eigenfrequency studies in COMSOL can attain an

accurate computation of mode frequencies and visualize the vibration mode shapes. Figure 4.29 a) and b) illustrate the in-phase and out-of-phase modes, respectively.

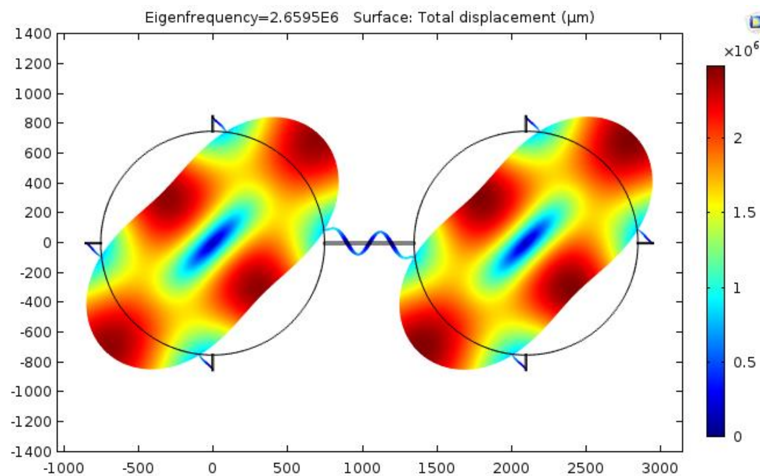

a)

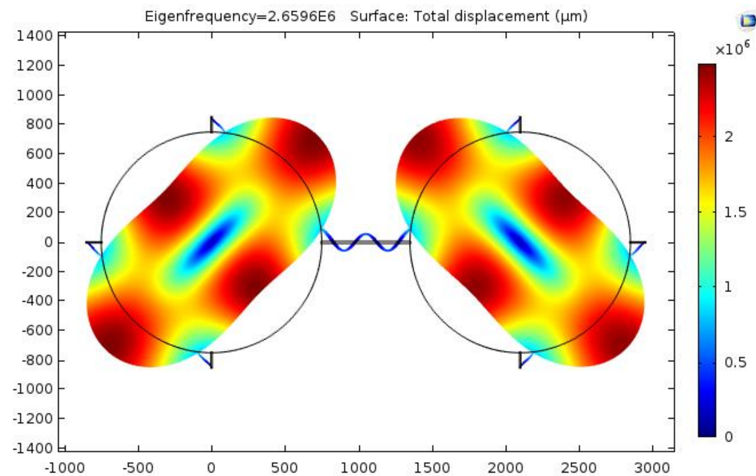

b)

Figure 4. 29: COMSOL simulated vibration modes of a 2-DOF coupled BAW disk resonator. a) In-phase mode. b) Out-of-phase mode.

A mass perturbation on resonator 2 is utilized to demonstrate the phenomenon of mode localization in the 2-DOF coupled BAW disk resonator system. It is can be seen from Figure 4.30, the balance of the coupled periodic vibration system is disrupted and the related vibration amplitude is dramatically altered, which denotes the effect of mode localization.

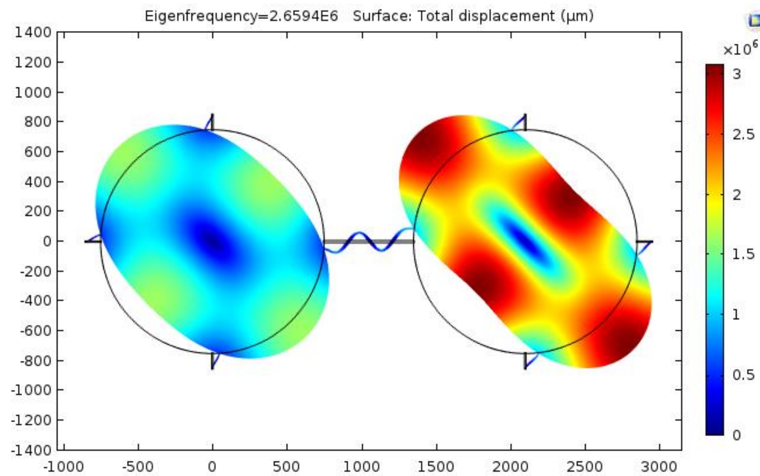

a)

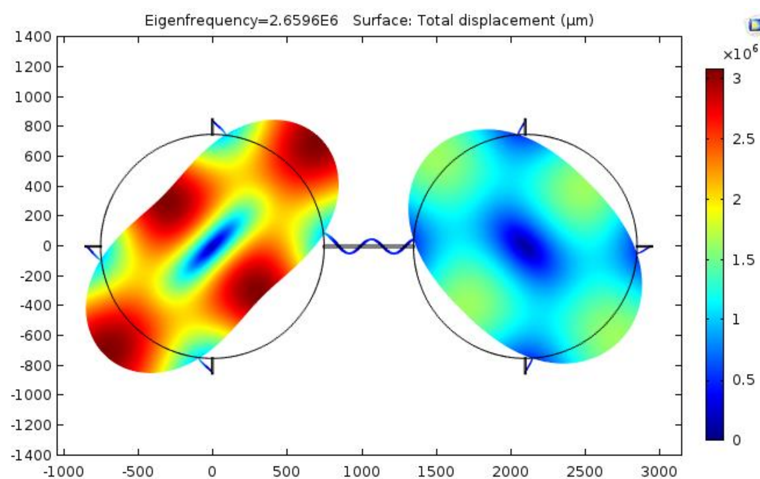

b)

Figure 4. 30: COMSOL model of a 2-DOF mode localized coupled BAW disk resonator with an added mass perturbation on the right disk proof mass. a) In-phase mode. b) Out-of-phase mode.

Subsequently, a frequency domain study in COMSOL is exploited to generate the frequency sweep function. Resonator 1 (left) is actuated via electrostatic force, the frequency responses of each disk resonator hence can be garnered, as demonstrated in Figure 4.31.

In conclusion, mode localization effects in the 2-DOF coupled wine-glass BAW disk resonator are successfully demonstrated by COMSOL FEM modeling, equivalent RLC circuit model and MATLAB model. The characterizations of such resonant device are comprehensively estimated, in which the simulation results render reliable information for the 2-DOF coupled BAW disk resonator system.

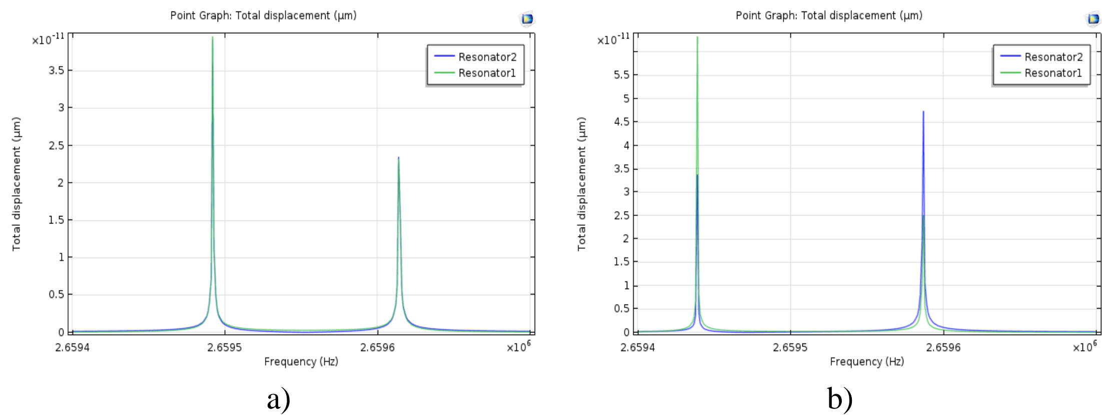

Figure 4. 31: 2-DOF coupled BAW disk resonator COMSOL simulated vibration amplitudes with a given excitation force on resonator 1. a) Without mass perturbation. b) With mass perturbation.

4.4 Chapter Summary

In this chapter, three different multi-DOF coupled resonator systems were simulated: i) a 3-DOF mode localized weakly coupled resonator for sensing either stiffness or mass perturbations, ii) a hybrid mass sensing system consisted of a QCM mass sensor & a 3-DOF mode localized weakly coupled resonator stiffness sensor, and iii) a 2-DOF mode localized coupled BAW disk resonator. Three modeling tools were employed for mechanical structure, device characterizations, vibration behaviors and system level simulations. All simulation results agreed well with the theoretical analysis, in addition, the predictions of system responses were reasonable. Further, mode localization effects were successfully simulated, different output metrics were investigated. Finally, comparisons of normalized sensitivities for different output metrics were performed and conclusion was drawn.

Chapter 5

Fabrications of Multi-DOF Mode Localized Weakly Coupled Resonators

---

5.1 Fabrication of 3-DOF Mode Localized Weakly Coupled Resonator

In this chapter, the aforementioned and simulated multi-DOF coupled resonators are realized via different fabrication flows: i) SOI based process that exploits two steps of release. ii) Dry release process with dicing free technique for SOI devices. iii) SOI based process with dicing free technique that exploits a carrier wafer. The geometric dimensions of each designed resonator are listed and the corresponding device layouts are demonstrated. The detailed fabrication processes are depicted with the assistance of 3D cross section view.

5.1.1 Fabrication of 3-DOF Mode Localized Weakly Coupled Resonator: SOI Based Process that Exploits Two Steps of Release

Silicon-on-insulator (SOI) technology benefiting from simple fabrication flow, in which a single mask is used for sculpting the device features and releasing. Deep reactive ion etching (DRIE) and hydrofluoric acid (HF) wet etching are the two main techniques to define the device structure layer and to release the suspended movable structures [94]. However, stiction is a crucial problem that is induced by HF wet etching [95]. To overcome this barrier, one-step dry release process has been proposed [96, 97], yet the notching effect overetches the moveable structures and results in structural

fragility. Accordingly, an improved fabrication flow is presented in [98] , which utilizes selective release process consisted of two steps: dry release and HF wet release.

To fabricate the 3-DOF coupled resonator, a single mask SOI process with two steps of release is adopted. The device structural dimensions are listed in Table 5.1.

Parameter	***Value***
Thickness of structural layer	$30\ \mu m$
Suspended beam length	$350\ \mu m$
Suspended beam width	$5\ \mu m$
Middle suspended beam width	$7.5\ \mu m$
Comb finger overlap	$70\ \mu$m
Comb finger length	$90\ \mu m$
Proof mass	$360^2\ \mu\text{m}^2$
Gaps between proof masses & Gaps between comb fingers & Gaps between proof mass and electrodes	$4.5\ \mu$m
Suspended structure thickness after overetch	$22\ \mu m$
Effective cross section area for electrostatic coupling and electrostatic actuation	$360 \times 22\ \mu\text{m}^2$
Effective cross section area for capacitive comb fingers	$70 \times 22\ \mu\text{m}^2$

Table 5. 1: Dimension parameters of fabricated 3-DOF coupled resonator device.

The mask layouts are drawn by L-Edit software, two different prototype designs of the 3-DOF coupled resonator are represented: one integrated with extra tether structures as bias voltage input to adjust the initial state of the device, one without the tether structure. The layouts are shown in Figure 5.1 a) and b) respectively.

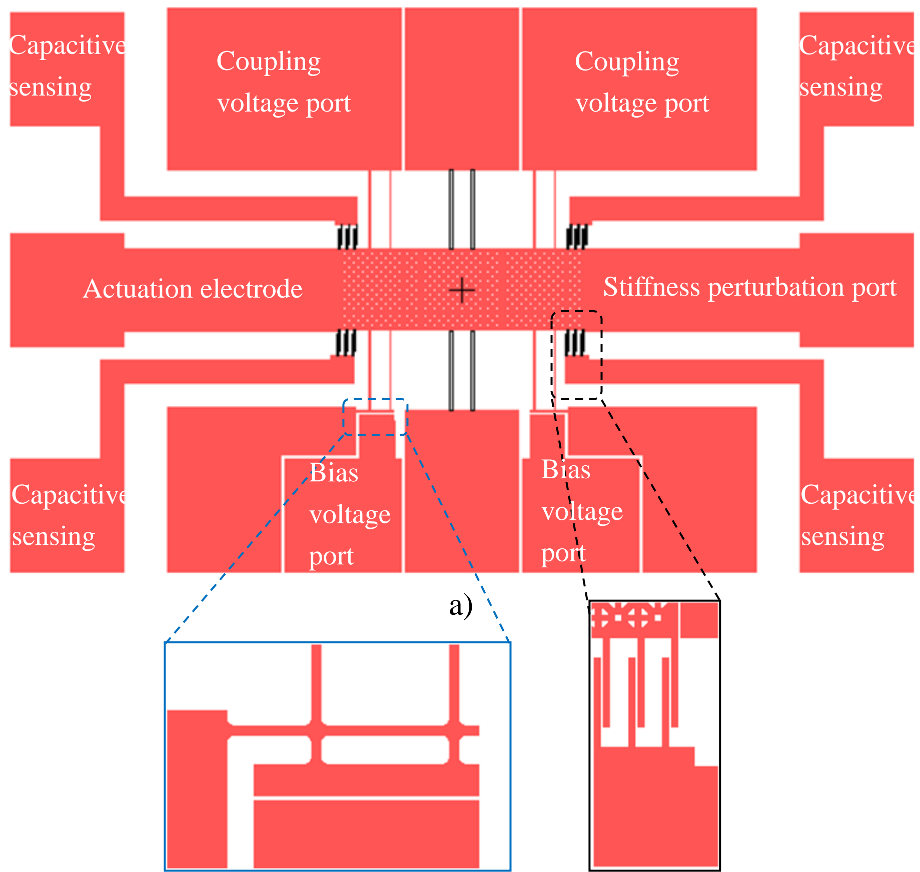

a)

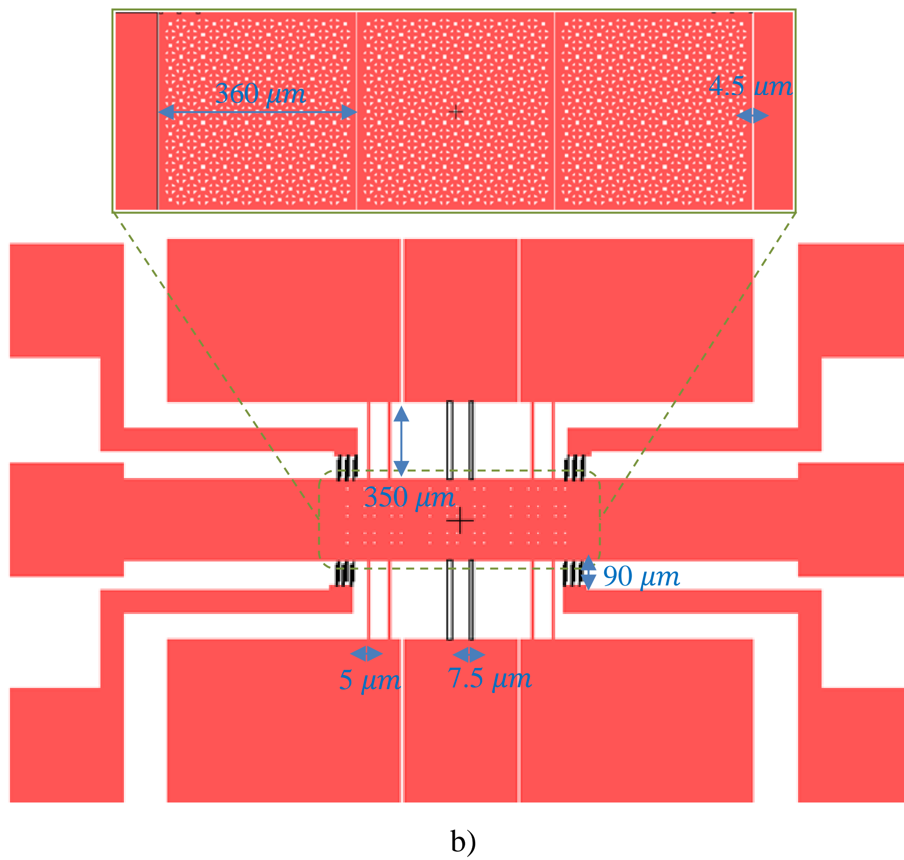

b)

Figure 5. 1: Device layouts of the 3-DOF coupled resonator. a) With tether structure. b) Without tether structure.

To interpret the fabrication flow, a procedure comprised of 5 steps is represented, 3D cross section view are introduced to assist the explanation:

a) Form the photoresist layer by spin-coating, then the photoresist is patterned according to the mask layout. (Figure 5.2 a)

b) The device layer is defined by deep reactive ion etching (DRIE). (Figure 5.2 b)

c) DRIE dry overetching process which exploits notching effect to undercut the main parts of the proof masses and comb fingers, the silicon dioxide layer beneath is also removed. However the overetch process is stopped to keep the edge part of the proof masses unreleased. Hence the movements that could damage the suspended beams and other fragile structures are confined. (Figure 5.2 c)

d) Remove the patterned photoresist layer, separate the fabricated devices by physical dicing. Due to the unreleased proof masses edge, the movements during dicing process are constrained, hence protects the device structure. (Figure 5.2 d)

e) Fully release the device by using HF wet etching. The residue of silicon dioxide layer under the edge of proof masses are removed. The movable structures are suspended and the released devices are put in carrier boxes for future packaging. (Figure 5.2 e)

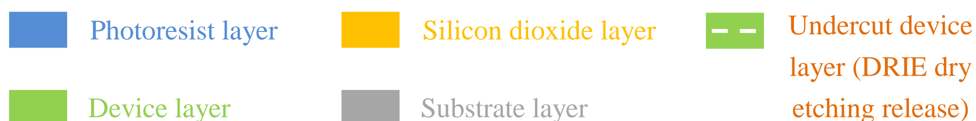

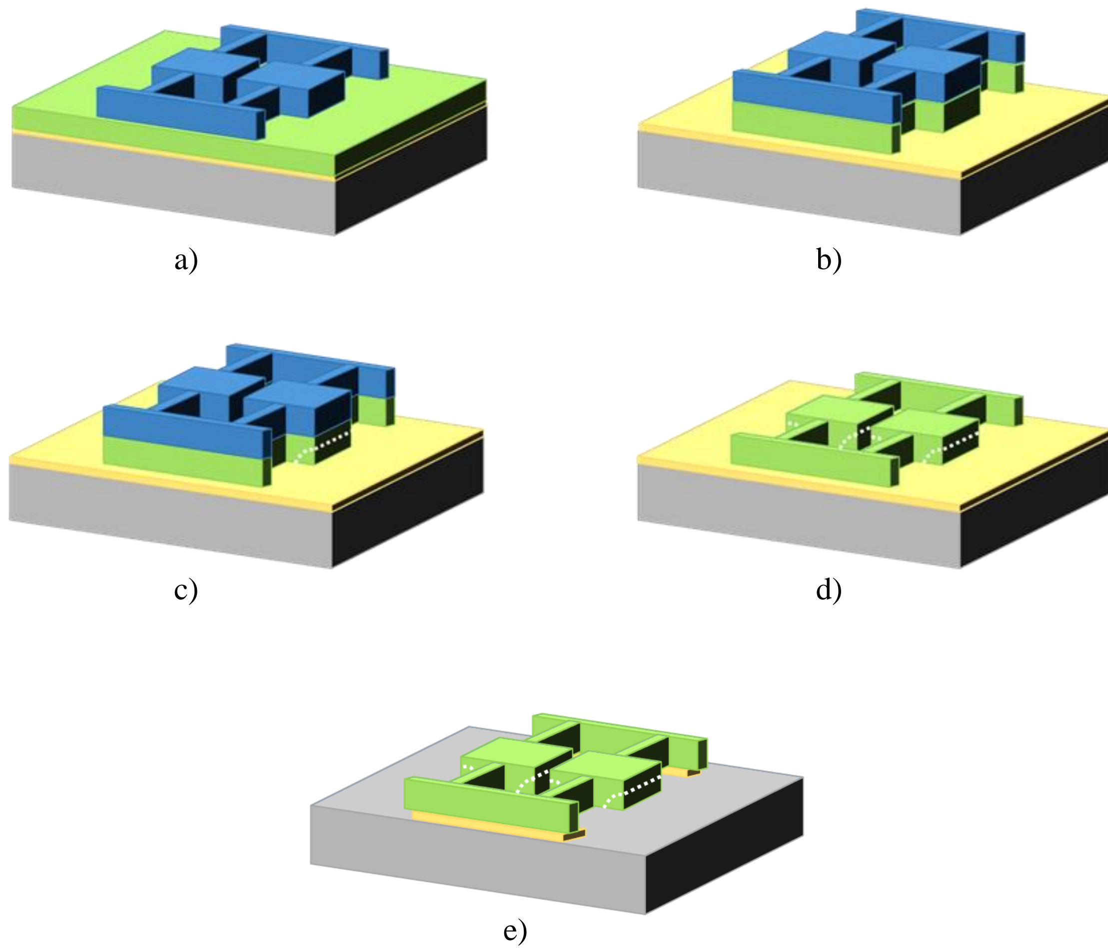

Figure 5. 2: Fabrication flow of SOI based process that exploits two steps of release. a) Spincoating photoresist layer. b) DRIE dry etching. c) DRIE overetching (dry release). d) Remove photoresist layer. e) HF wet etching fully release.

The fabricated 3-DOF coupled resonator devices are inspected under optical microscope, the captured images are demonstrated in Figure 5.3. All the images are acquired via Leica ZA6APO optical facilities.

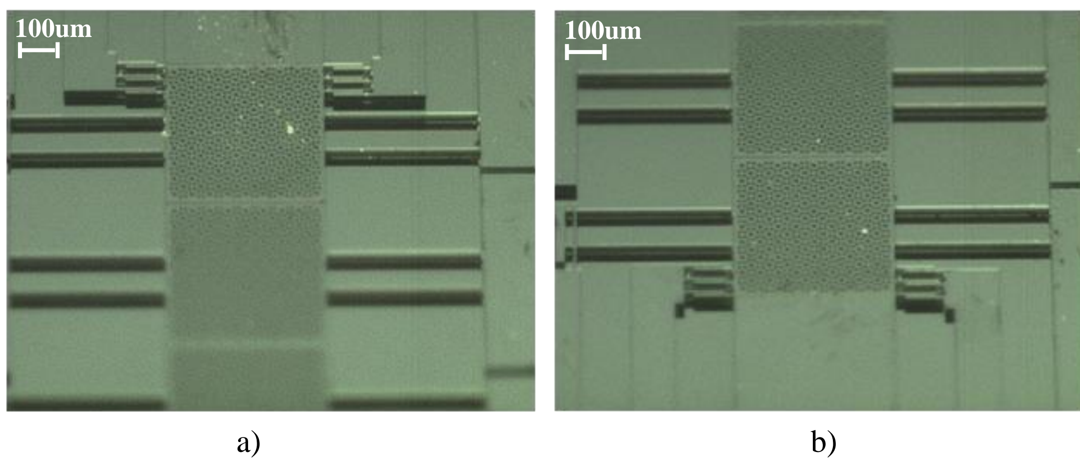

Figure 5. 3: Microscope view of fabricated 3-DOF coupled resonator devices. (SOI based process that exploits two steps of release)

5.1.2 Fabrication of 3-DOF Mode Localized Weakly Coupled Resonator: Dry Release Process with Dicing Free Technique for SOI Devices

The aforementioned two steps of release SOI process can attain single mask fabrication, however, the separation procedure by physical dicing significantly reduce the device yield rate. Even though the device structure is not fully released by dry etching process and protected by part of silicon dioxide layer, physical dicing force can still damage or destroy the device. In order to achieve better fabrication yield rate, a dicing free technique is adopted [99]. In this technique, two masks are required: front side device layer mask and bottom side release trenches mask. Accordingly, the mask layouts are shown in Figure 5.4 a), b) and c) respectively.

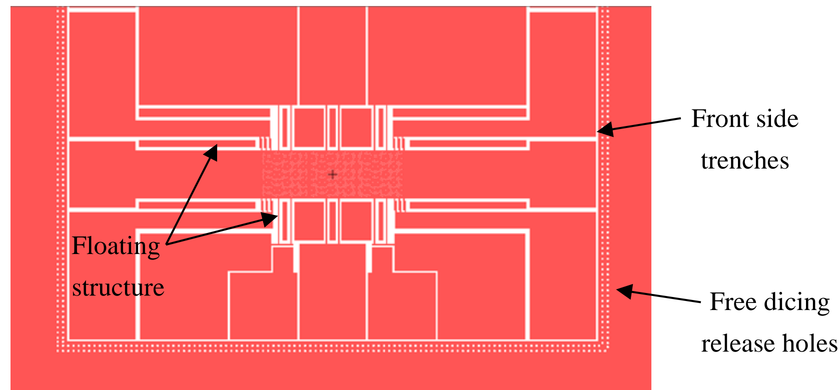

a)

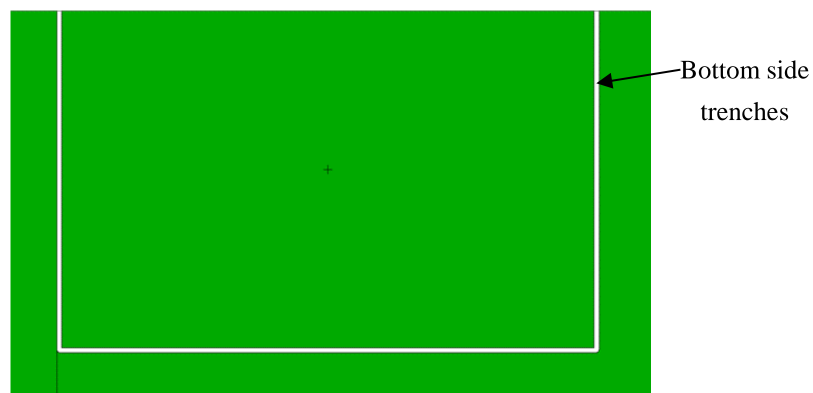

b)

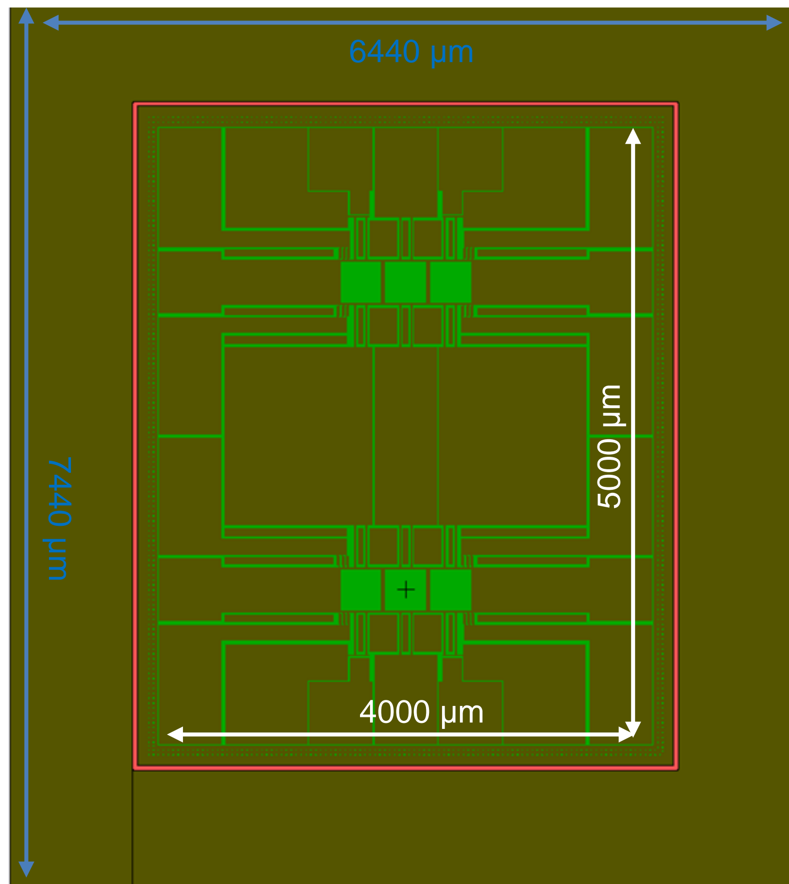

c)

Figure 5. 4: Modified layout (dicing free): Device layouts of the 3-DOF coupled resonator. a) Front side device layer. b) Bottom side release trenches. c) Overlapped view of one block unit on the wafer, consisted of two 3-DOF coupled resonator devices.

It is can be observed, there are floating structures exist in between each section of the resonator. The reason is to uniform the gaps between each part in the device structure, as well as decreasing the relative large gaps, for instance, the gap between the suspended beam of resonator1 and the suspended beam of resonator2. The floating structure can control the DRIE dry etching speed thus the slim structure such as comb fingers and long suspended beams are protected from overetching, concequently increases the final fabrication yield rate. There are 4 gap variations that been introduced to the front side layout: *20 um, 30 um, 40 um* and *50 um*. The gaps are distributed evenly, for example, the gap between the floating structure and the two adjacent supporting beams of resonator1 is the same as the gap between the supporting beams to the next floating structure.

The fabrication flow is explained by a procedure consisted of 7 steps, with the

assistance of 3D images in Figure 5.5:

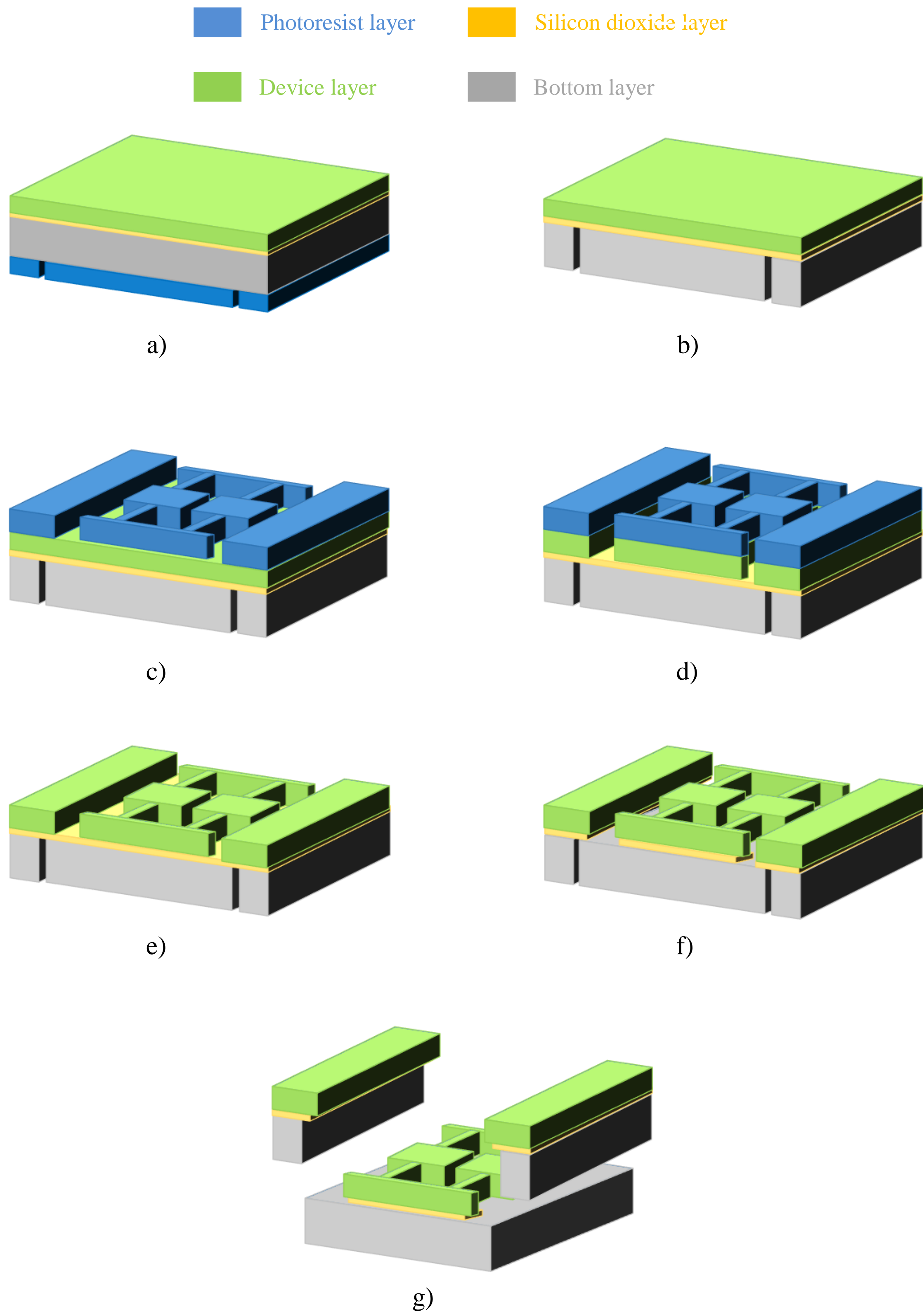

Figure 5. 5: Fabrication flow of dry release process with dicing free technique.

a) Forming photoresist layer on the bottom side.

b) DRIE to form the bottom side trenches and remove photoresist.

c) Forming photoresist on top layer and patterning the device features with front side mask.

d) DRIE to form the front side device features.

e) Removing the photoresist and preparing for releasing.

f) HF VPE dry releasing process. The movable structures are released first, followed by the release of grid.

g) Finalizing the release procedure, separating the individual unit.

The fabricated device is exhibited in Figure 5.6.

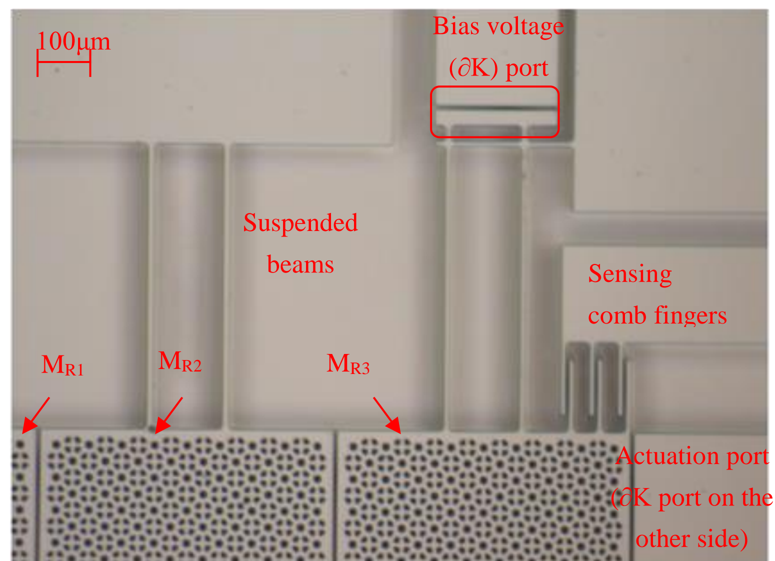

Figure 5. 6: Close-up view of the fabricated 3-DOF coupled resonator (dry release with dicing free technique).

Although the floating structures in the modified layout could effectively protect the fragile & slim parts, they have an intrinsic defect: the possibility of stuck in the device layer during release process. Figure 5.7 shows the floating structures that stuck in the gaps of the device layer.

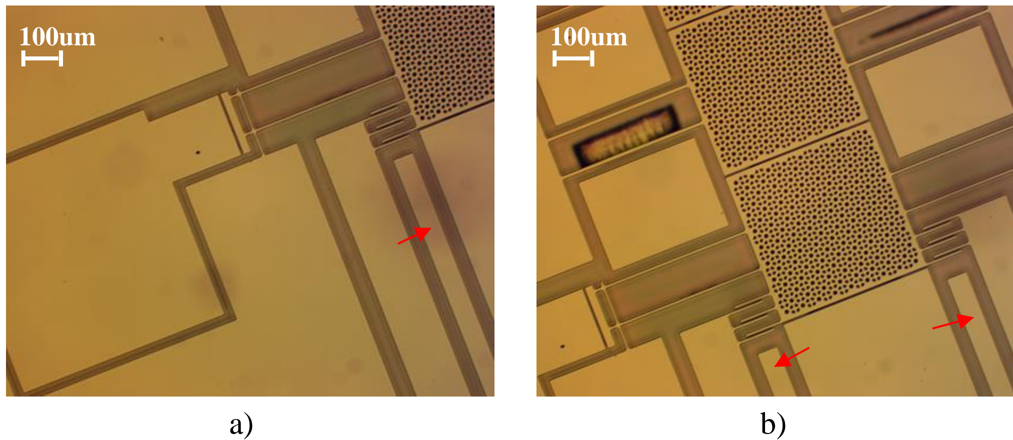

Figure 5. 7: Failure of floating structures after releasing.

By positioning the device layer facing down during the release process, the problem can be countered. The floating structures hence can drop out and separate from device layer under the force of gravity.

Apart from the adjustments in release process, another structure modification is proposed. As the layout shown in Figure 5.8, floating structures are removed, whereas the extended structure frames are introduced.

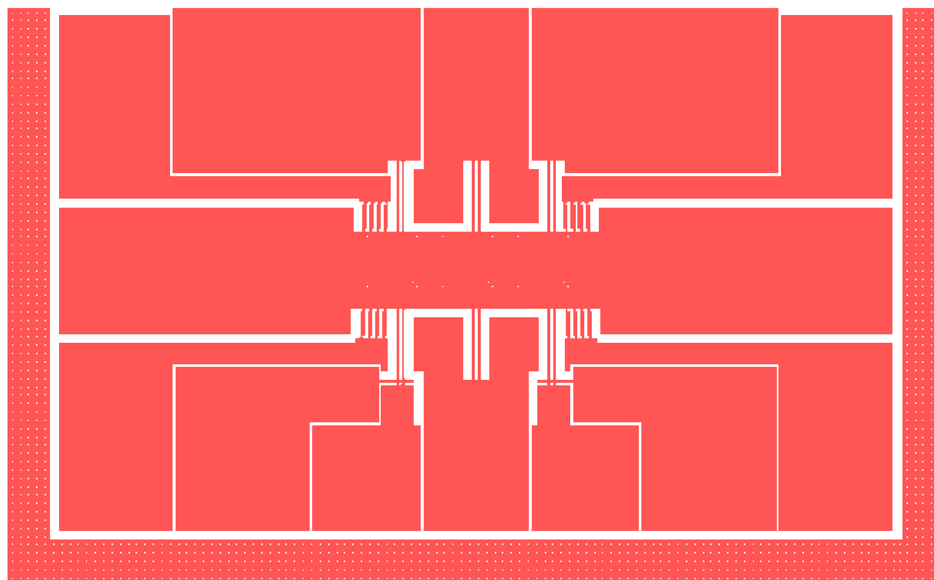

Figure 5. 8: 3-DOF coupled resonator structure modification: extended frame.

As can be seen, the large gap area between the middle resonator and the adjacent resonators are covered by extended frame. The capacitive comb fingers are increased to 4 pairs instead of 3, which results in better output signal strength and enhanced SNR.

The variations of gaps are limited to *19 um* and *49 um*, which can attain better structural uniformity and better release control.

5.1.3 Fabrication of 3-DOF Mode Localized Weakly Coupled Resonator: SOI Based Process with Dicing Free Technique that Exploits a Carrier Wafer

Alternatively, a different dicing free technique is adopted [100], which is suitable for fabricating the 3-DOF coupled resonator as a biosensor. Commonly, a large dispensing area is required for biosening applications. The biological samples are typically in liquid phase, a large dispensing area can maintain the sample droplet shape and provide enough space for molecules to bind onto the device surface. On the other hand, the aforementioned fabrication flows demand the etching holes to be integrated in the resonator proof mass, which result in the imperfection of biosensing purposes. The liquid sample could pass through the small etching holes on the proof mass and leak into the gap between the suspended structure and substrate. Consequently, there are possibilities of stiction during biosensing operations. To counter this problem, the substrate beneath the resonator proof mass is removed, the etching holes on the proof mass are also eliminated owing to double side DRIE process. In this technique, two masks are required: front side device layer mask and backside mask. Accordingly, the mask layouts are shown in Figure 5.9 a), b) and c) respectively.

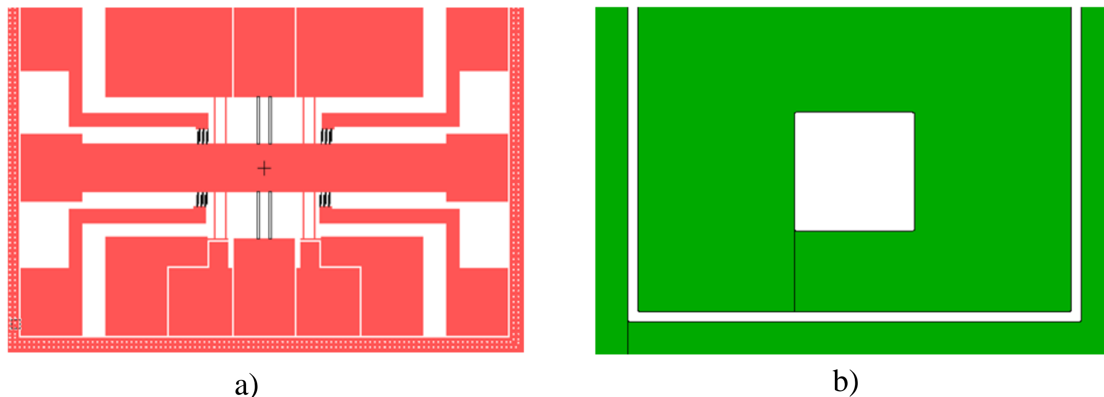

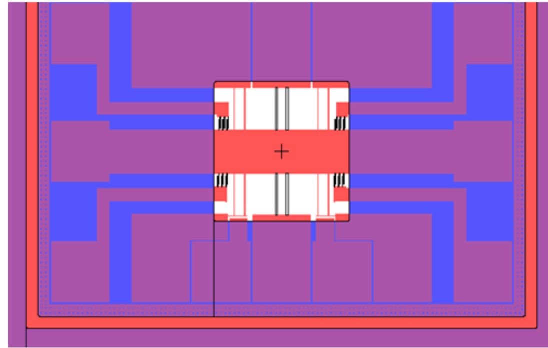

c)

Figure 5. 9: Modified layout (dicing free with removed proof mass substrate): Device layouts of the 3-DOF coupled resonator. a) Front side device layer. b) Backside layer. c) Overlapped view.

The fabrication flow is explained by a procedure consisted of 8 steps with the assistance of 3D images in Figure 5.10:

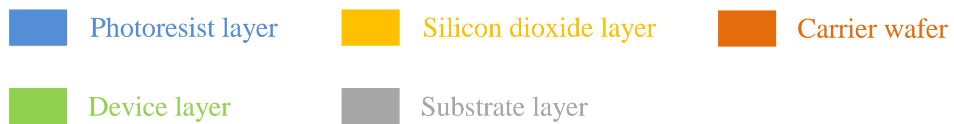

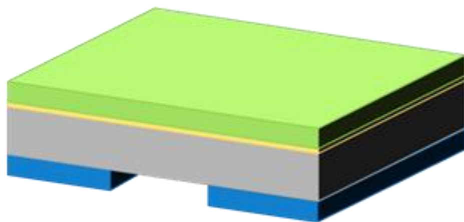

a)

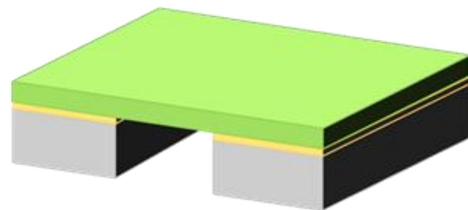

b)

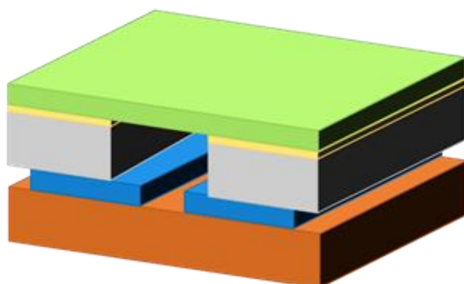

c)

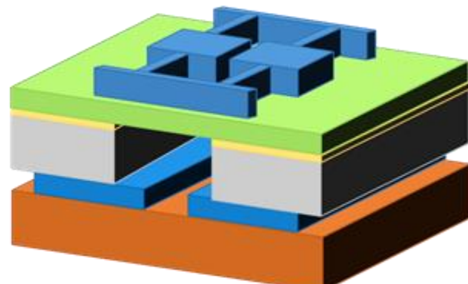

d)

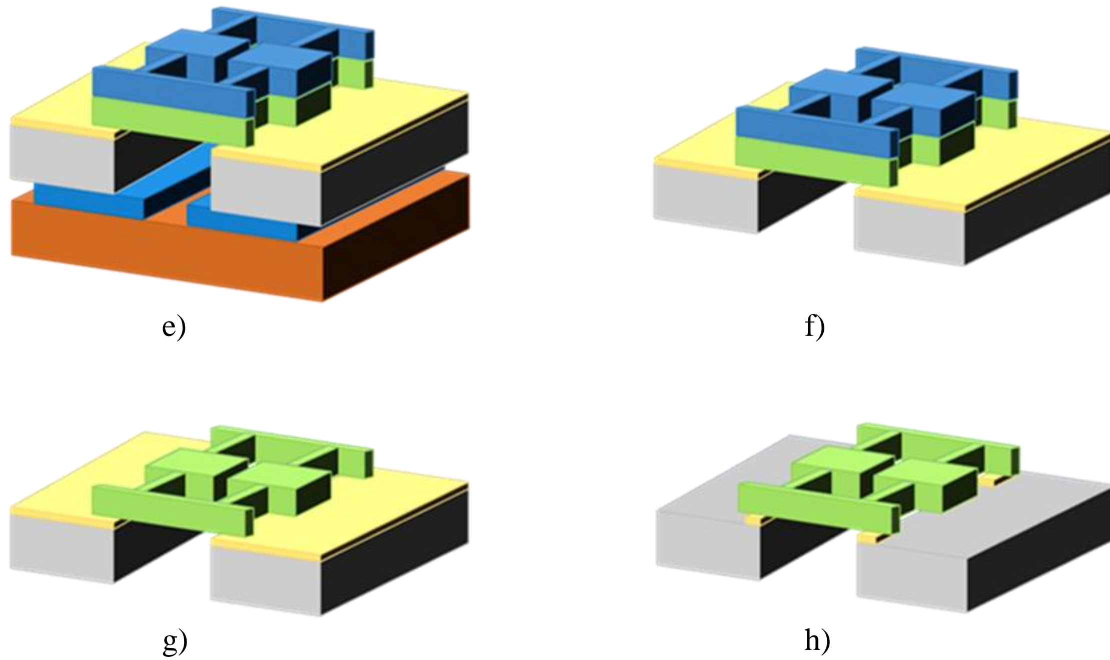

Figure 5. 10: Fabrication flow of SOI based process with dicing free technique that exploits a carrier wafer.

a) Forming photoresist layer on the bottom side.

b) DRIE to remove bottom side proof mass substrate.

c) Bonding with carrier wafer.

d) Forming photoresist on top layer and patterning the device features with front mask.

e) DRIE to form the front side device features.

f) Separating the carrier wafer.

g) Removing the front layer photoresist and preparing to release.

h) Releasing the units: HF solution wet release the movable structures.

However, a defect was found after this fabrication flow, where the structures with relative large structural gaps were overetched. The damages were mainly appeared at the middle resonator suspended beams and their surroundings. As demonstrated in Figure 5.11, slim structures such as suspended beams of side resonators were completely overetched, the suspended structures of middle resonator were barely survived. To solve this critical failure, the large gap areas should be minimized. Both structure modifications in Figure 5.4 and Figure 5.8 are competent, in addition, reducing the removed substrate areas and utilizing supporting anchors can effectively

control the influences of overetch.

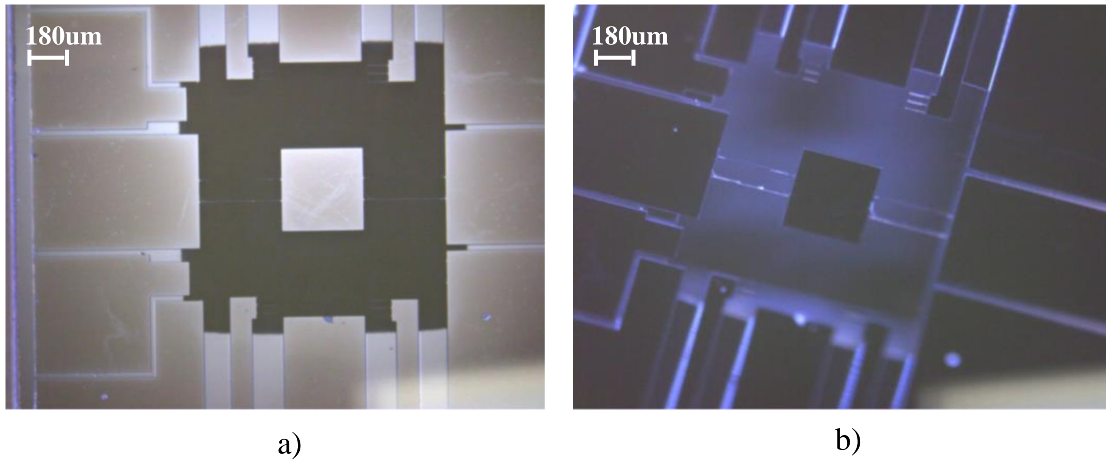

a) b)

Figure 5. 11: Microscope view of failed device structure due to overetch (dicing free technique with a carrier wafer).

5.2 Fabrications of 2-DOF Mode Localized Coupled BAW Disk Resonator

The 2-DOF coupled BAW disk resonator devices are fabricated by using the SOI based dicing free technique with a carrier wafer. Due to the large surface area of the proof mass in the disk resonator system and the purpose of biosensing applications, the substrates beneath proof masses are removed. Hence, the fabrication flow includes double side etching and dicing free technique is the appropriate one. Four designs are introduced in this section, including disk radius of *100um, 250um, 500um* and *750um*.

5.2.1 Fabrication of 2-DOF Mode Localized Coupled BAW Disk Resonator: SOI Based Process with Dicing Free Technique that Exploits a Carrier Wafer

The device structural dimensions of the 2-DOF coupled BAW disk resonators are listed in Table 5.2. The device layouts are exhibited in Figure 5.12.

Parameter	*Value*
Suspension beam lengths (R_100)	50 μm

Suspension beam lengths (R_250)	50 μm
Suspension beam lengths (R_500)	100 μm
Suspension beam lengths (R_750)	100 μm
Suspension beam width for all designs	10 μm
Gaps between resonator and electrodes for all designs	2 μm
Coupling beam length (R_100)	220 μm
Coupling beam width (R_100)	10 μm
Coupling beam length (R_250)	350 μm
Coupling beam width (R_250)	10 μm
Coupling beam length (R_500)	600 μm
Coupling beam width (R_500)	15 μm
Coupling beam length (R_750)	590 μm
Coupling beam width (R_750)	15 μm

Table 5. 2: Dimension parameters of fabricated 2-DOF coupled BAW disk resonators.

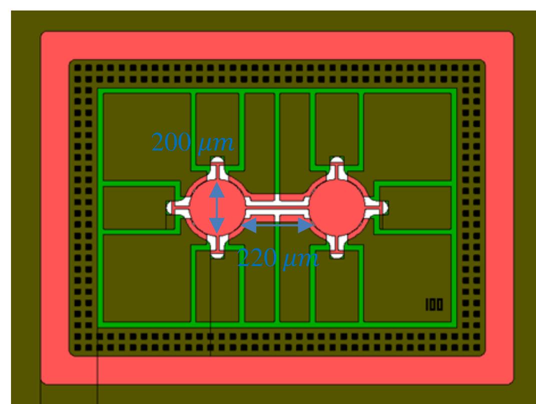

a)

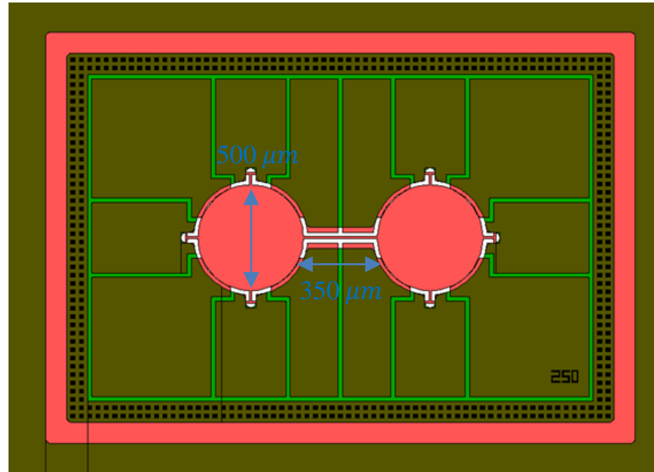

b)

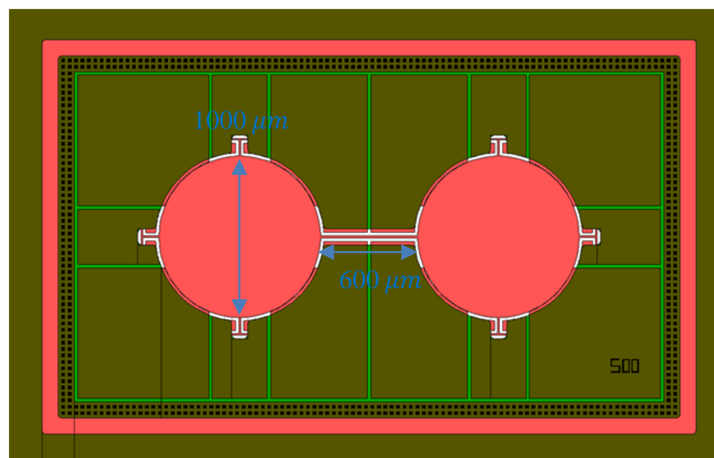

c)

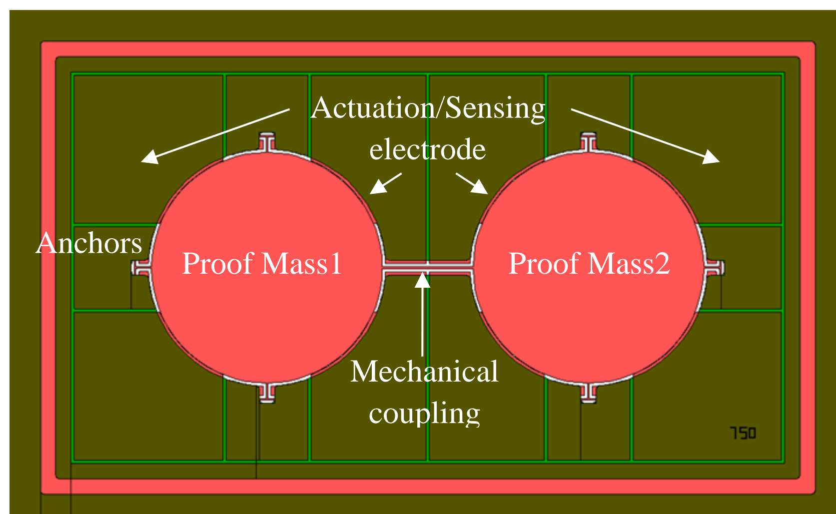

d)

Figure 5. 12: Device layouts of the 2-DOF coupled BAW disk resonators. a) Disk radius 100 um. b) Disk radius 250 um. c) Disk radius 500 um. d) Disk radius 750 um.

The fabrication flow is identical to the process that has been described in Figure 5.10. Accordingly, the actual fabricated devices are shown in Figure 5.13.

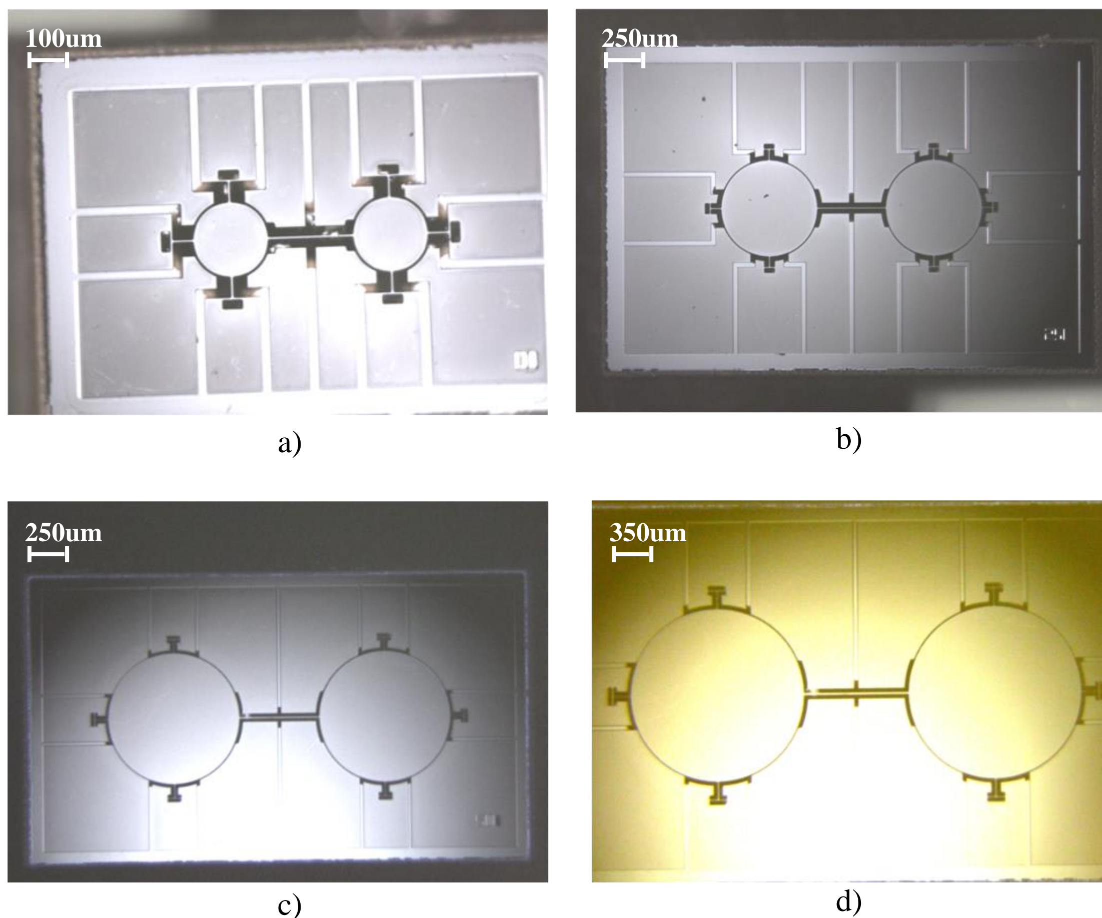

Figure 5. 13: Microscope view of fabricated 2-DOF coupled BAW disk resonator devices. a) Disk radius 100 um. b) Disk radius 250 um. c) Disk radius 500 um. d) Disk radius 750 um.

5.3 Chapter Summary

In this chapter, the fabrication flows of the 2-DOF mechanical coupled BAW disk resonators and the 3-DOF electrostatic coupled resonators were introduced. Three different fabrication processes were discriminated into dicing and dicing free techniques, in which the 3-DOF coupled resonators were fabricated by all the three processes. The 2-DOF coupled BAW disk resonators on the other hand, were fabricated by dicing free technique with a carrier wafer. Devices layouts were demonstrated and structural parameters were listed. The microscope view of actual fabricated devices were inspected, the possibilities of fabrication failure and corresponding solutions were summarized.

Chapter 6

Interface Circuit Designs and Experimental Materials

6.1 Interface Circuit Designs for 3-DOF Mode Localized Weakly Coupled Resonator

To measure the motional currents induced by periodic vibrations of the parallel plates, a proper interface circuit is required. An interface circuit integrates the functions of signal filtering, signal buffering, and signal amplification. The input signals are processed and then delivered to the output ports that communicate with an extended platform such as a precise measurement facility (e.g., a lock-in amplifier or network analyzer) or signal processing software on a PC. In short, an interface circuit assists the transducer device to measure physical quantities that are correlated with final output signals.

6.1.1 Signal Pick-up Circuit for 3-DOF Mode Localized Weakly Coupled Resonator

The capacitive sensing element of the 3-DOF coupled resonator system has already been introduced in chapter 3. Theoretically, the total generated motional current is expressed in equation 3.54 (multiplied by the number of comb finger pairs). To use a lock-in amplifier to measure the output signals from the 3-DOF coupled resonator system, the motional current signals have to be converted into voltage signals. This is

achieved using a transimpedance amplifier. To select the correct transimpedance amplifier among the many variations, two properties should be considered: amplifier noise level and the bandwidth of the amplifier. The motional currents are very weak, usually in the nanoampere to microampere range. The resonance frequency of such a device is approximately 20 kHz, which is not difficult for many types of transimpedance amplifiers to achieve. The gain value of a transimpedance amplifier, determined by the resistor value in the negative feedback loop, is also easy to control. Ideally, the generated motional currents in the range of tens to hundreds of nanoamperes should be converted and amplified to hundreds to thousands of millivolts. Hence, given its high gain bandwidth product, high speed, and low noise, the operational amplifier OPA657U (Texas Instruments) was chosen as the current-to-voltage converter and as the first stage of amplification for the interface circuit.

To obtain a stronger signal and suppress noise, a second stage of amplification is employed. Instrumentation amplifiers can achieve a controllable gain and perform signal subtraction. In the 3-DOF coupled resonator design, four groups of comb fingers forming two pairs of differential capacitive sensing elements, whereby four transimpedance amplifiers are used as I/V converters. Subsequently, two instrumentation amplifiers perform subtractions for each differential capacitive pair. The amplifier AD8429 (Analog Devices) was selected as the instrumentation amplifier in the interface circuit. This low-noise instrumentation amplifier has excellent common mode rejection ratio (CMRR) and relatively wide bandwidth. In addition, the second stage amplification can provide significant signal boosts so that the final output signal reaches hundreds to thousands of millivolts.

The schematic of the motional current converter and amplification circuit is shown in Figure 6.1. Figure 6.2 presents an overview of the 3-DOF coupled resonator measurement platform, which consists of the MEMS 3-DOF coupled resonator device, interface circuit, and data acquisition facilities.

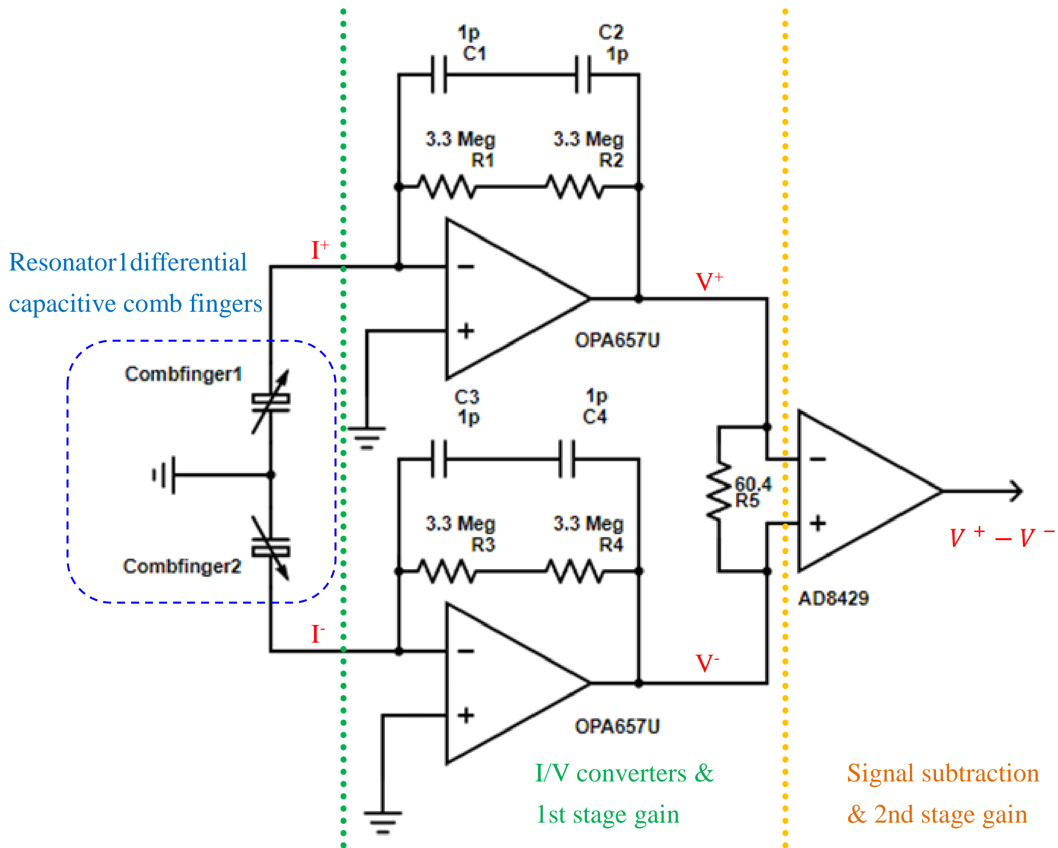

Figure 6. 1: Schematic of the I/V converters and amplification stages.

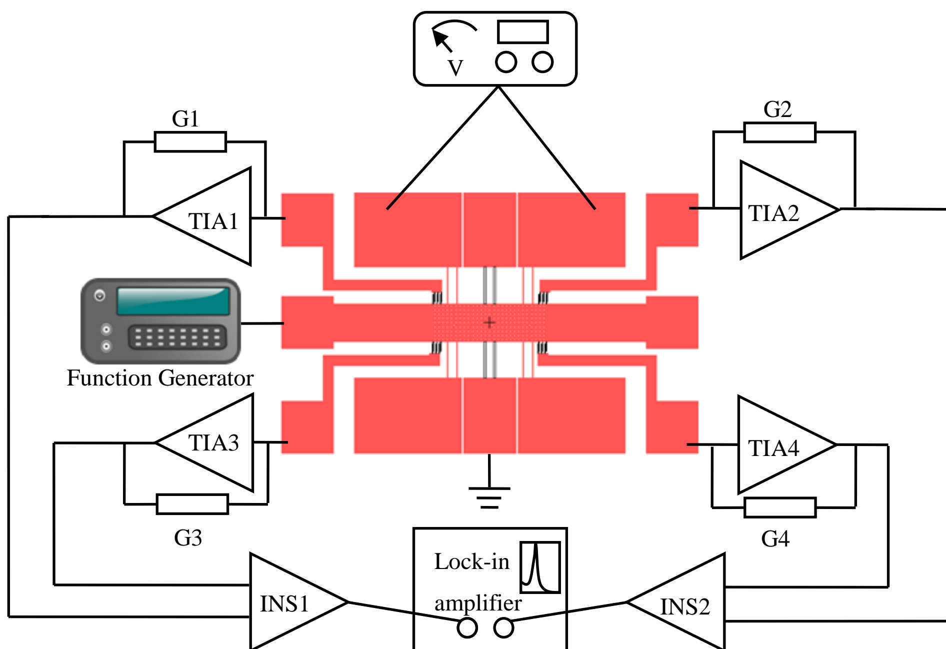

Figure 6. 2: 3-DOF coupled resonator measurement platform.

The interface circuit was fabricated on a printed circuit board (PCB). All the

electronic components were standard surface-mounted devices (SMD). The prototype PCB had a dimension of $75 \times 70\ \mathrm{mm}^2$. The fabricated PCB board is shown in Figure 6.3.

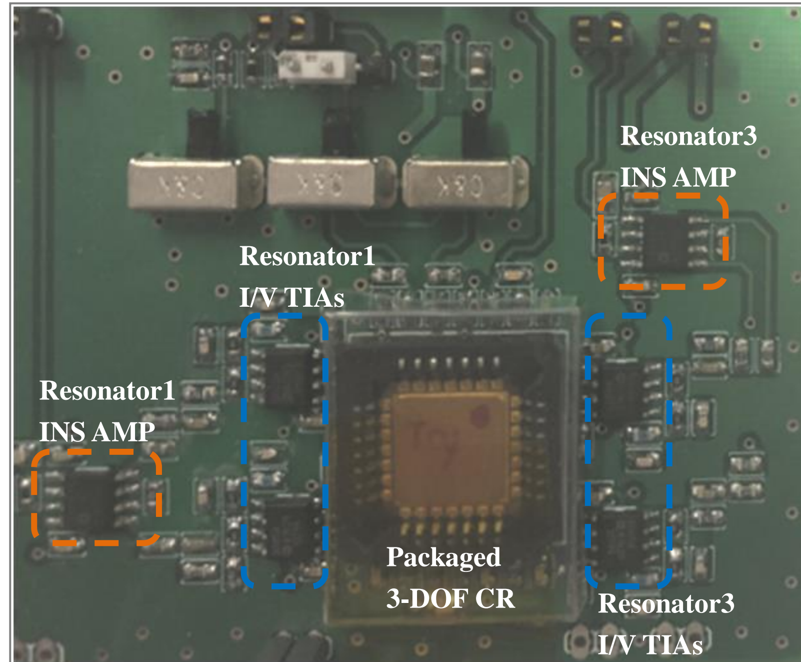

Figure 6. 3: Fabricated PCB interface circuit for a 3-DOF mode localized weakly coupled resonator.

6.1.2 Peak Detector Circuit for QCM & 3-DOF Mode Localized Weakly Coupled Resonator Hybrid System

As introduced in chapter 4, the QCM mass sensor is exploited as a sample contact platform, which can operate in damped environment. To establish the interaction between the QCM mass sensor and the 3-DOF coupled resonator stiffness sensor, the AC output signal from QCM is needed to be converted to a DC voltage and hence can be used as electrostatic force to induce the stiffness perturbation in the 3-DOF coupled resonator system.

Quartz crystal microbalance mass sensors come in a variety of dimensions and with a variety of electrode materials and generally operate in the MHz range. In this hybrid system, the QCM mass sensor (commercially available from thinkSRS) has a resonance

frequency of 5 MHz, has Cr/Au electrodes, and has a nominal blank diameter of 25.4 mm. A continuous AC stimulus generated from a function generator facility can maintain the QCM device vibrating at certain frequencies (initially at resonance frequency). To convert the high frequency AC output signal produced by the QCM, a high-speed peak detector is necessary. Figure 6.4 a) shows a typical peak detector design, which is intended for slow-speed signals. Figure 6.4 b) shows a modified peak detector design, which has improved tracking speed and hence can be used for the QCM output signal peak detecting task.

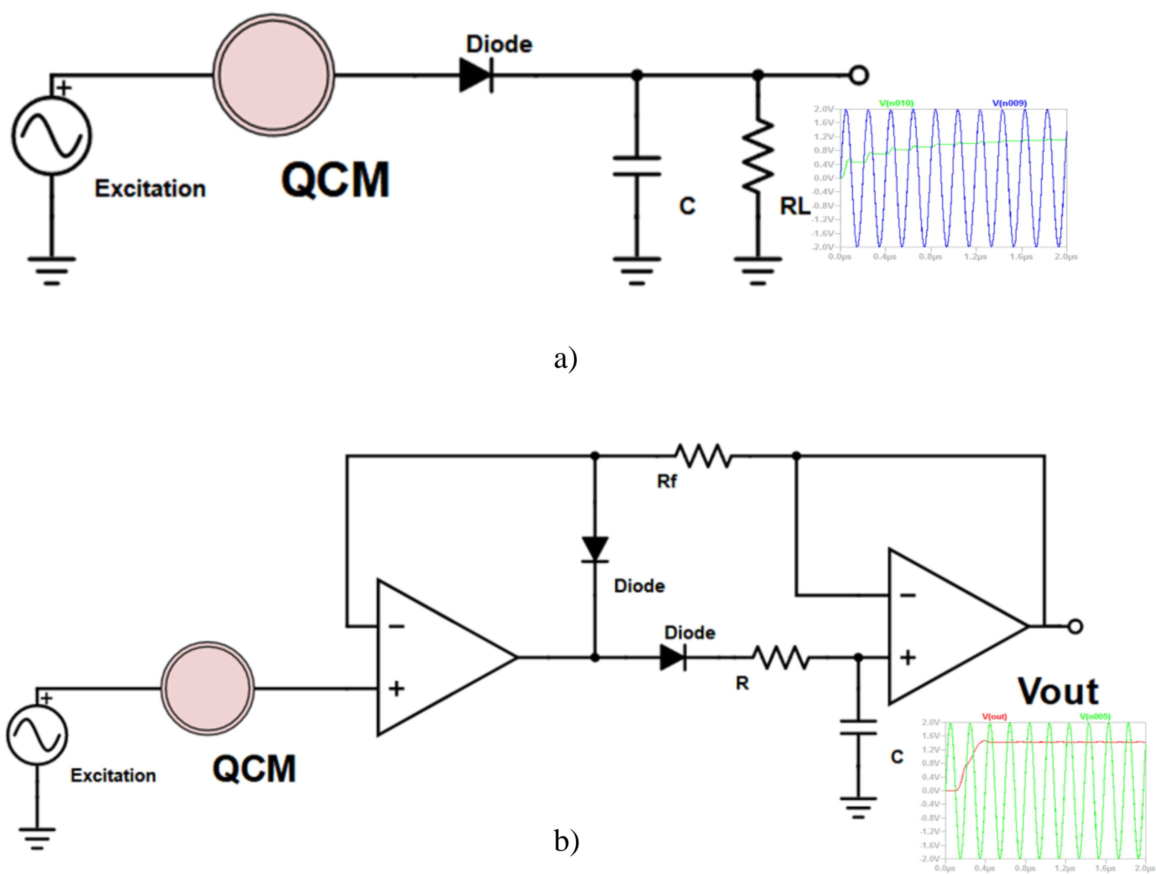

Figure 6. 4: Peak detector circuit. a) Typical peak detector design. b) Modified high speed design

Although a more advanced PCB layout was proposed, the electronic components were integrated in a prototype board (stripboard). For convenience, the experiments were conducted using this prototype board. As demonstrated in Figure 6.5, the QCM is clamped in a dedicated holder fabricated by 3D printing.

Figure 6. 5: Actual circuit of the high speed peak detector. a) Prototype board. b) Proposed PCB layout design.

6.2 Interface Circuit Designs for 2-DOF Mode Localized Coupled BAW Disk Resonator

There are several options for the interface circuit design for BAW disk resonators in terms of drive and sense schemes [101-103]. As mentioned previously, 2-DOF coupled BAW disk resonator devices are electrostatically actuated. The sensing elements, on the other hand, are capacitive. There are four electrodes surrounding each disk resonator, which can be configured either as an actuation electrode or a capacitive sensing electrode. A comparison of different configurations, in terms of vibration modes compatibility, interface circuit simplicity, noise rejection capability and parasitic feedthrough signal influences is summarized in Table 6.1.

Based on the experiment design and for packaging convenience, a 1-port capacitive sensing scheme was selected as the starting point. The main disadvantage of this method is noise–signal disturbance, especially feedthrough current interferences. Specifically, a dominant parasitic capacitance results in a relatively large feedthrough current at the operating frequency range, rendering impossible the detection of the motional current signal. An RLC equivalent circuit model can verify the weights of effective motional current and feedthrough current at the resonance frequency, as demonstrated in Figure 6.6.

	Breath mode compatibility	*Wine glass mode compatibility*	*Simplicity*	*Noise rejection*	*Feedthrough influences*
1-port capacitive					
2-port capacitive					
2-port differential capacitive					

Table 6. 1: Comparison of the 2-DOF coupled BAW disk resonator sensing electrode schemes.

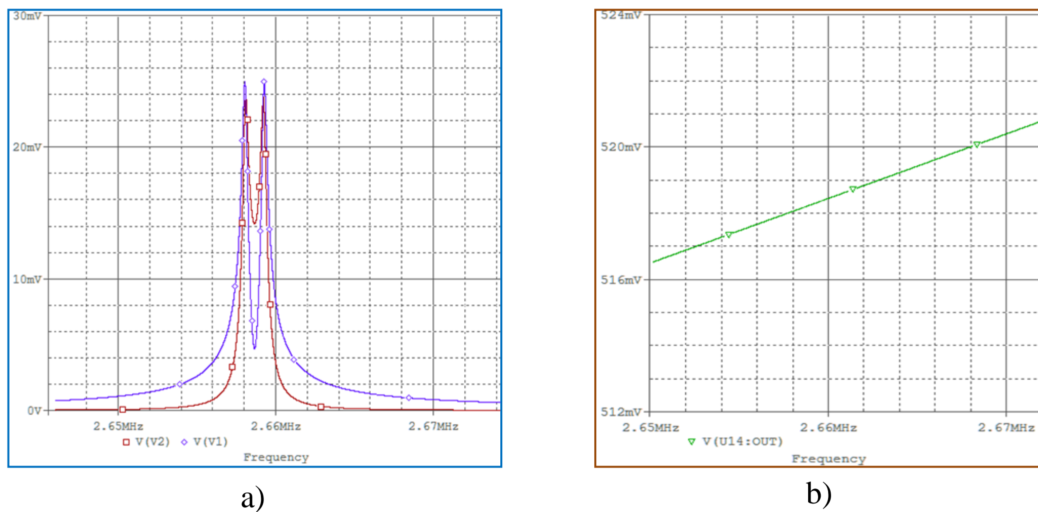

Figure 6. 6: RLC equivalent circuit model of a 750um radius 2-DOF coupled BAW disk resonator. a) Absence of parasitic feedthrough capacitance. b) Presence of parasitic feedthrough capacitance.

The parasitic feedthrough capacitance results in a feedthrough current, which increases with frequency. The magnitude of the feedthrough current far exceeds the effective motional current generated by the 2-DOF coupled BAW disk resonator. Consequently, the external data acquisition facility cannot measure anything but the dominant feedthrough current signal. Therefore, a parasitic feedthrough cancellation method [104] is adopted. As shown in Figure 6.7, two feedthrough cancellation techniques are employed.

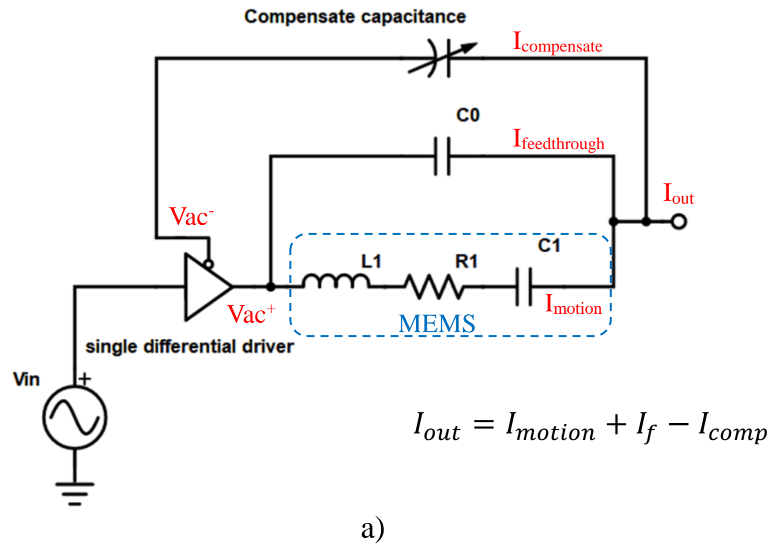

a)

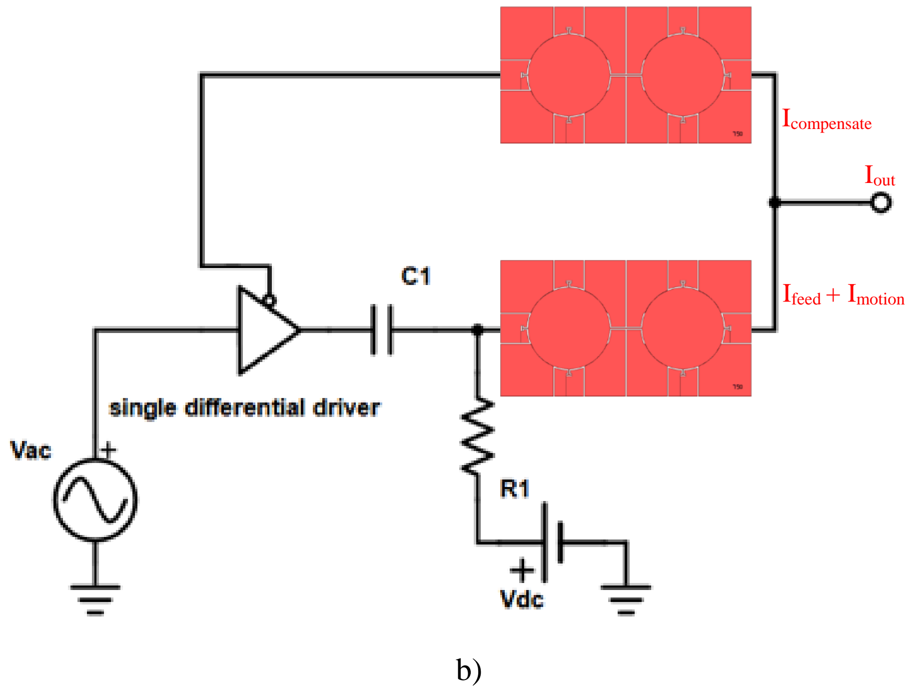

b)

Figure 6. 7: Feedthrough cancellation method. a) Tunable capacitance compensation technique. b) Dummy MEMS compensation technique.

Both techniques utilize an inversed current at a similar level to the feedthrough current; hence, they cancel each other out at the output junction. Figure 6.8 demonstrates the 2-DOF coupled BAW disk resonator measurement platform, which consists two precise tunable capacitances as the feedthrough compensation.

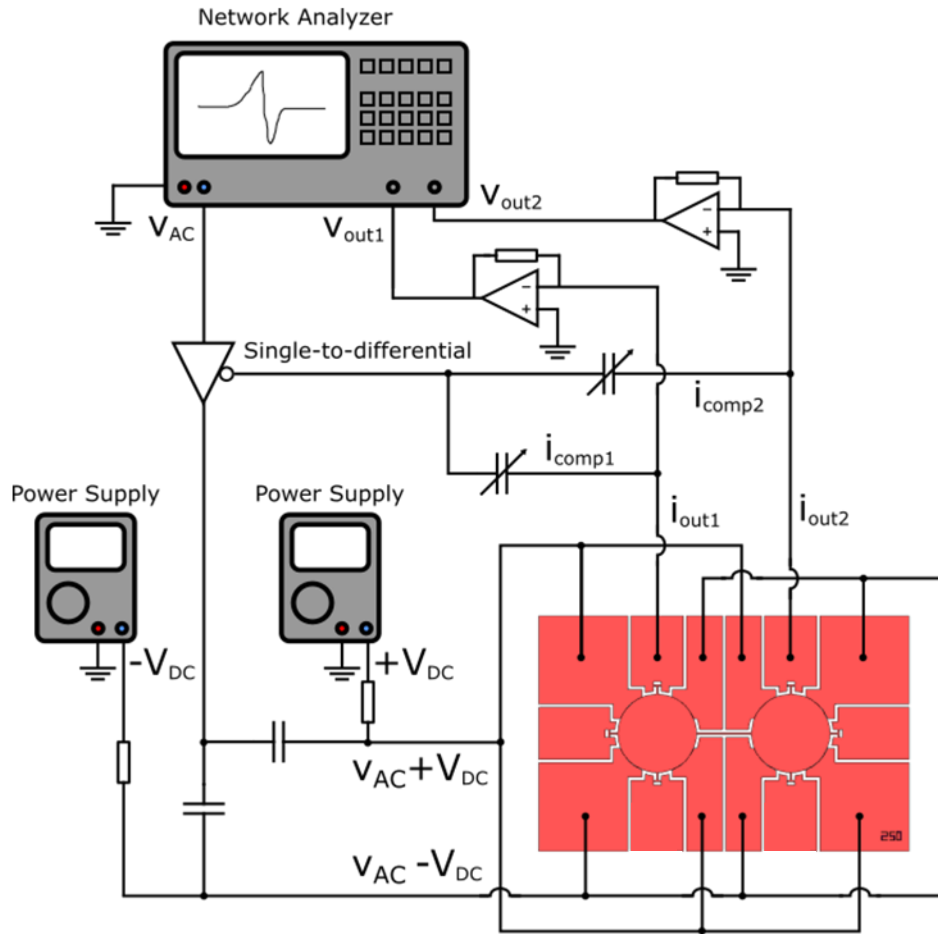

Figure 6. 8: 2-DOF coupled BAW disk resonator measurement platform.

By exploiting a 1-port capacitive measurement setup, the coupled disk resonator is excited electrostatically via the combination of DC and AC actuation voltages. A particular vibration mode (in-phase or out-of-phase) is selectively actuated by assigning the positive and negative DC voltage onto different electrodes pairs. The variable compensation capacitors are placed in parallel with each disk resonator, where the AC actuation voltage is passed through a single-to-differential driver, producing two out-of-phase AC voltages. Subsequently, the two out-of-phase AC voltages are fed to actuation electrodes and the compensation branches. Since the resulting tunable compensation currents (i_{comp1} and i_{comp2}) and the effective motional currents from the 2-DOF coupled BAW disk resonator (i_{out1} and i_{out2}) are opposite, they cancel each other out at the sense node. By carefully tuning the value of each variable capacitance, the feedthrough currents can eventually be eliminated, allowing the measurement of the

effective motional signals.

The interface circuit was fabricated on a PCB, and all the electronic components were standard SMDs. The prototype PCB had a dimension of $60 \times 50 \text{ mm}^2$. Details are presented in Figure 6.9.

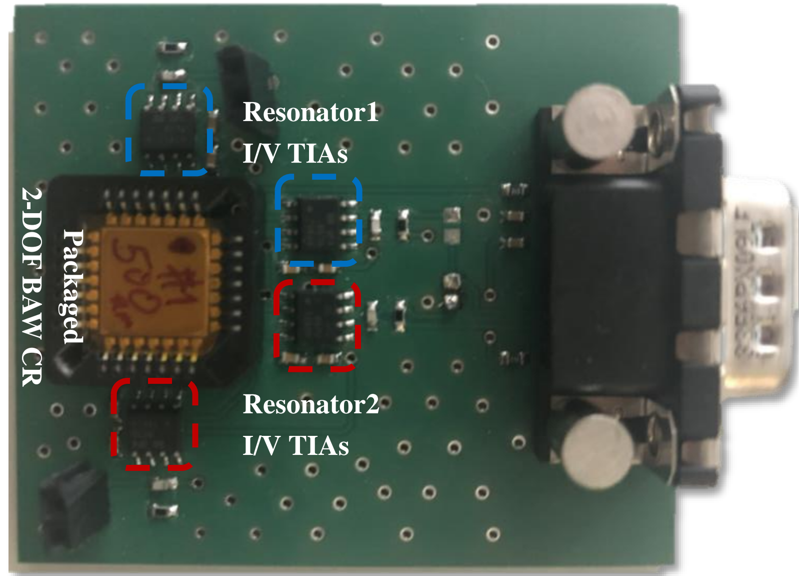

Figure 6. 9: Fabricated PCB interface circuit for a 2-DOF mode localized coupled BAW disk resonator.

As well as the PCB design based on variable capacitance compensation, two additional layout designs exploiting dummy MEMS device compensation and a tunable current source are included in the appendix.

6.3 Experiment Materials for Mass Sensing Characterizations

To characterize the mass sensitivity of multi-DOF coupled resonators – in particular, the 3-DOF weakly coupled resonator, the QCM mass senor, the 3-DOF coupled resonator stiffness sensor hybrid system, and the 2-DOF coupled BAW disk resonator – consecutive mass perturbations are added to target proof mass surfaces. However, unlike the stiffness perturbations, which can be easily manipulated via electrostatic forces, the implementation of mass perturbations is more complex. As the

comparison summarized in Table 6.2, properties of mass and stiffness perturbations are listed.

	Control	***Accurate***	***Simplicity***	***Reversibility***	***Reproducibility***
Mass perturbations					
Stiffness perturbations					

Table 6. 2: Comparison of mass/stiffness perturbation features in terms of feasibilities.

Indeed, the stiffness perturbation process is more flexible: the magnitude of the stiffness perturbation can be tuned by adjusting the potential difference (DC voltages) across the parallel plate structures. The accuracy of the stiffness perturbation depends on the minimum step of the voltage source, while the MEMS device can return to its initial state by shutting down the stiffness perturbation voltage source. In contrast, the mass perturbation process requires physical substances; for instance, the depositing of a uniform thin layer of a certain material. External facilities are required for depositions [105] or dispensations [57], and both procedures are time consuming. The accuracy of mass perturbation relies on the minimum mass and the possibility of immobilization on the proof mass surface.

In contrast to adding external mass, removing a portion of mass from the MEMS device proof mass is another approach to mass perturbation [106]. In this case, an expensive focused ion beam facility is required. Generally, adding or subtracting masses is permanent, resulting in the disposal of MEMS devices. This is a crucial problem for the characterization of prototype MEMS devices, considering the fabrication cost and yield rate.

In view of the difficulty in mass perturbation characterizations, the author has proposed a novel idea, which exploits magnetic nanoparticles as mass perturbations to create a reversible, relatively simple, and cost-effective mass characterization method.

In principle, such a novel approach could be adopted by any MEMS mass sensor, meaning that it is a universal solution for mass perturbation characterizations [107, 108].

Magnetic nanoparticles are artificial particles that possess a sphere-like structure and a typical diameter ranging from 1 nm to 1 μm. Such nanoparticles can be controlled by an external magnetic field. The magnetic materials commonly used for forming the core structure are cobalt, nickel, manganese, and iron [109]. Although the original purpose of magnetic nanoparticles was for biological assays, magnetic materials cannot interact with biological molecules directly; specifically, they are not able to handle strong covalent bonds to allow the bonding of functionalization. Thus, an additional chemical component is needed; namely, an outer layer of silica. A basic structural diagram of magnetic nanoparticles is shown in Figure 6. 10.

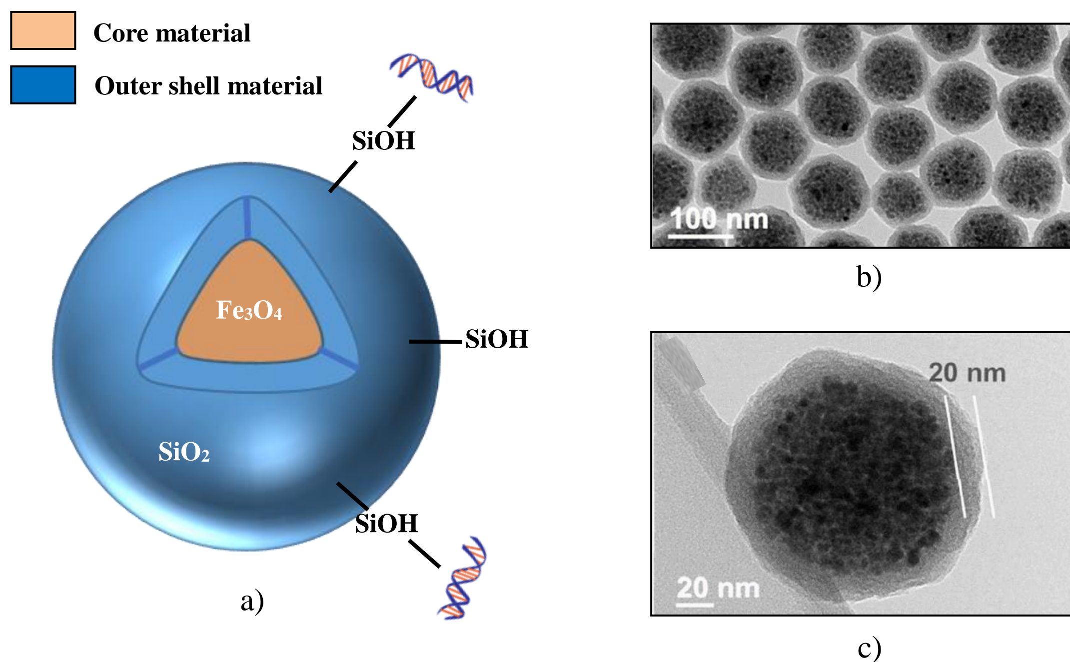

Figure 6. 10: Magnetic nanoparticles. a) Structure diagram. b) TEM image of magnetic nanoparticles cluster [110]. c) TEM image of a single magnetic nanoparticle [110].

Other possibilities for the outer shell materials and their functional groups exist; their use depends on the biological sensing tasks. In MEMS multi-DOF coupled resonator mass perturbation characterizations, basic magnetic nanoparticles comprised of iron core and a silicon dioxide outer shell are employed. The magnetic nanoparticles

were commercially available from Innosep Biosciences. Three batches with different diameters were purchased: 1 µm, 5 µm, and 10 µm. All the magnetic nanoparticles were stored in a liquid environment (de-ionized water or oil) and distributed in carrier bottles with a concentration of 10 mg/ml. The batches are shown in Figure 6.11.

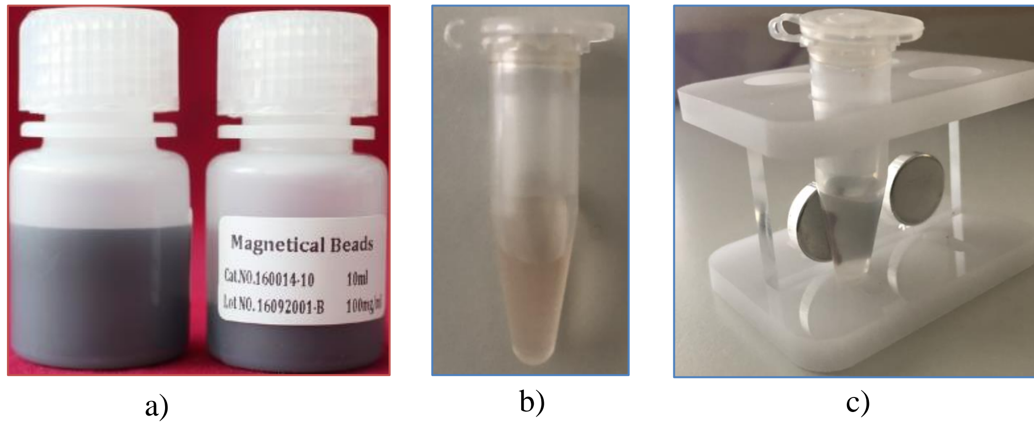

Figure 6. 11: Commercialized magnetic nanoparticles. a) Original production with a given concentration and volume. b) Diluted magnetic nanoparticles floating in an Eppendorf tube. c) Magnetic shelf.

6.3.1 Preparations of Magnetic Nanoparticles

Before dispensing the magnetic nanoparticles onto multi-DOF coupled resonators, a pre-treatment step is essential. Unwanted carrier liquid should be removed quickly after dispensing; otherwise, both the magnetic nanoparticles and the carrier liquid are counted as added mass, which would result in inaccurate characterizations. To accelerate this process, a 70% ethanol solution is used for the carrier liquid. Another important step is dilution, as the original concentration of magnetic nanoparticles far exceeds the desired amount. Basically, magnetic nanoparticles with net weight of 1 ng to 1 µg are used as mass perturbations. Figure 6.12 details the pre-treatment procedure, which comprised of magnetic nanoparticles transportation, separation of carrier liquid, dilution, and relocation.

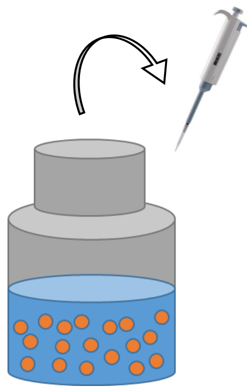

a)

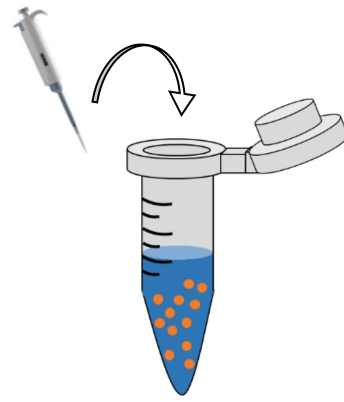

b)

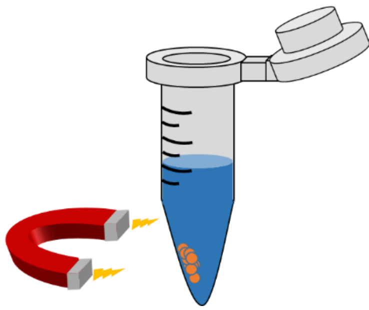

c)

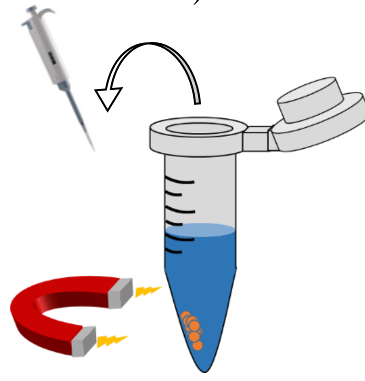

d)

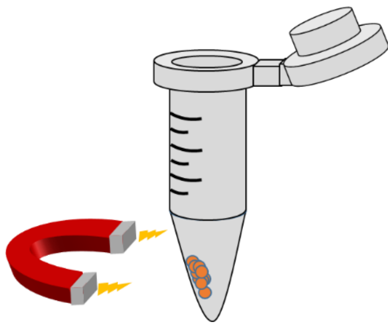

e)

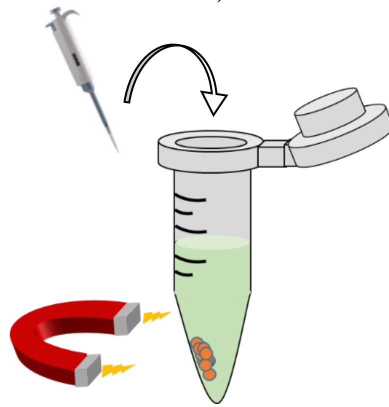

f)

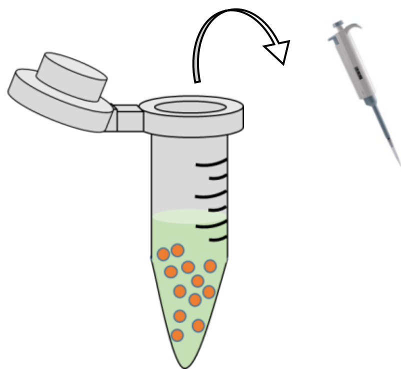

g)

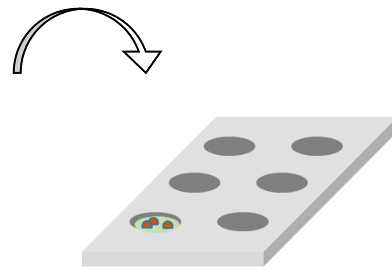

h)

Figure 6. 12: Magnetic nanoparticles pre-treatment. a) Transporting the magnetic nanoparticles from original container. b) Eppendorf tube temporary storage. c) Using magnet to attract floating nanoparticles. d) Separation of carrier liquid. e) Fully remove the liquid, only solid nanoparticle clusters exist. f) Reinjecting 70% ethanol. g) Shaking the Eppendorf tube to make the nanoparticles evenly distributed in 70% ethanol solution. h) Taking the desired quantity of diluted nanoparticle solution, relocating in a shallow well plate, preparing to be dispensed.

As the flow diagrams illustrated in Figure 6.12, an operating protocol of pre-treatment is compiled accordingly:

(1) Calculating the desired mass perturbation value. According to the concentration of original production, computing the transported nanoparticles mass value in terms of the volume of pipette (equation 6.1). Computing the diluted concentration, in terms of the transported masses and the volume of 70% ethanol solution (equation 6.2). Again, computing the relocated nanoparticles mass value, in terms of the volume of pipette and diluted concentration (equation 6.3).

$$M_{trans} = C_{origin} \times V_{tip1} \tag{6.1}$$

$$C_{diluted} = M_{trans}/V_{ethanol} \tag{6.2}$$

$$M_{relocation} = C_{diluted} \times V_{tip2} \tag{6.3}$$

$$M_{perb} = C_{diluted} \times V_{dispenser} \tag{6.4}$$

(2) Shaking the original container until nanoparticles evenly floating in the solution. Setting up a pipette with proper volume and installing appropriate tip, carefully sucking out nanoparticle solution from the original container.
(3) Injecting the transported nanoparticle solution into an Eppendorf tube.
(4) Placing a magnet at one side of the Eppendorf tube, hold it until nanoparticles are gathered as cluster.
(5) Reinstalling a clean pipette tip and configuring the volume to the same value as transportation step or a relative larger value.

(6) Carefully sucking out the carrier liquid in the Eppendorf tube while maintaining the gathered solid nanoparticles untouched.
(7) Reinstalling a clean pipette tip and configuring the volume to dilution required value.
(8) Loading up the 70% ethanol solution and injecting into the Eppendorf tube, check the volume scale on the Eppendorf tube, make sure the nanoparticle solution is correctly diluted
(9) Reinstalling a clean pipette tip and configuring the volume to relocation required value.
(10) Shaking the Eppendorf tube until nanoparticles evenly floating in the solution.
(11) Carefully sucking out the diluted nanoparticle solution, then distributing the diluted solution into one or several wells of the designed shallow well plate.
(12) Sending the shallow well plate to Microdispenser (Microplotter), preparing to dispense nanoparticles onto MEMS devices.

6.3.2 Reversibility of Magnetic Nanoparticles as Mass Perturbations

After the characterizations of mass sensitivity for multi-DOF coupled resonators, a reversal procedure can be performed so that tested MEMS devices can be reused. By utilizing the intrinsic magnetic affinity, the dispensed nanoparticles can be withdrawn from the proof mass of MEMS devices. This greatly improves the effective usage of each multi-DOF coupled resonator device and provides an economical solution for testing the mass sensitivity of MEMS devices. The reversibility is consisted of the following steps:

(1) Overhanging the packaged multi-DOF coupled resonator device, the dispensed side is facing down.
(2) Preparing 70% ethanol solution and filling into a Beaker cup.
(3) Slowly and steadily moving the hanged device, approaching the liquid surface of the 70% ethanol solution.
(4) Holding a magnet close to the liquid contact surface, ensure the dispensed side is

well contacted to the liquid solution but not fully immerse in it.

(5) Slightly shaking the hanged device, repeating several times until visually no nanoparticles attached.

(6) Overhanging the device for 45 minutes, ensure the humid of the contacted surface are entirely evaporated.

(7) Transferring the packaged device to oven dryer, running a 30 minutes comprehensive dry program.

(8) Testing the packaged device, checking the physical structure integrity under microscope and implementing a test run.

A detailed procedure of removing magnetic nanoparticles is represented in Figure 6.13.

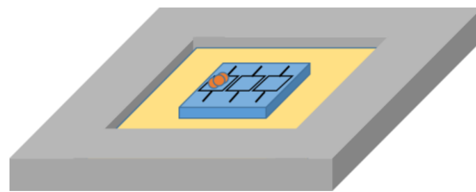

a)

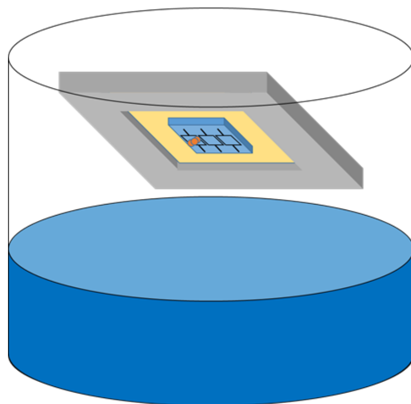

b)

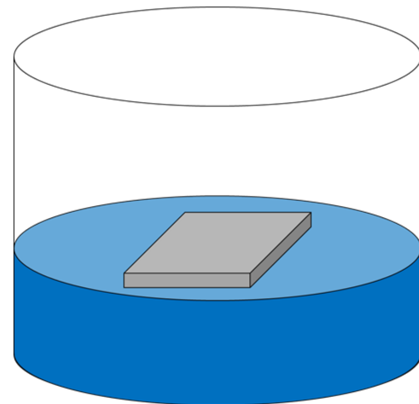

c)

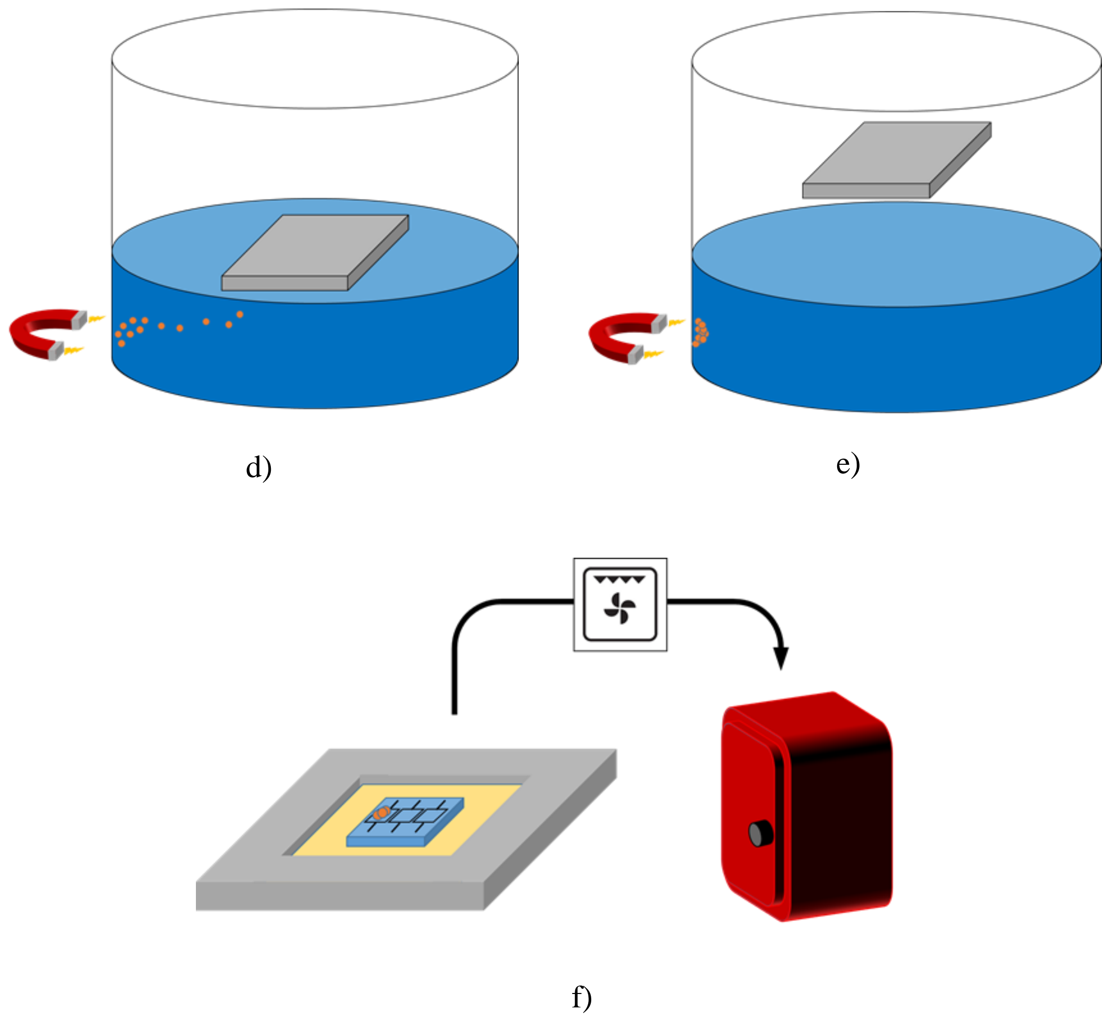

Figure 6. 13: Magnetic nanoparticles removal. a) Dispensed magnetic nanoparticles on packaged multi-DOF coupled resonator device. b) Flip-over the packaged device and approaching the liquid surface. c) Dispensed surface contacts the liquid. d) Using a magnet to attract the dispensed nanoparticles. e) Waiting humid evaporation. f) Oven dryer program.

6.3.3 Dispensing of Magnetic Nanoparticles

SonoPlot GIX Microplotter was used to dispense a small droplet (~20 nl) of diluted magnetic nanoparticles solution on one resonator in the multi-DOF coupled resonator system. The microplotter system consisted of a precise movement platform (x–y direction), a z-direction high-resolution positioning capillary tube, and a controller console. An ultrasonic pumping mechanism was used, which allowed an accurate and quick depositing process. Figure 6.14 details the procedure of dispensing nanoparticles.

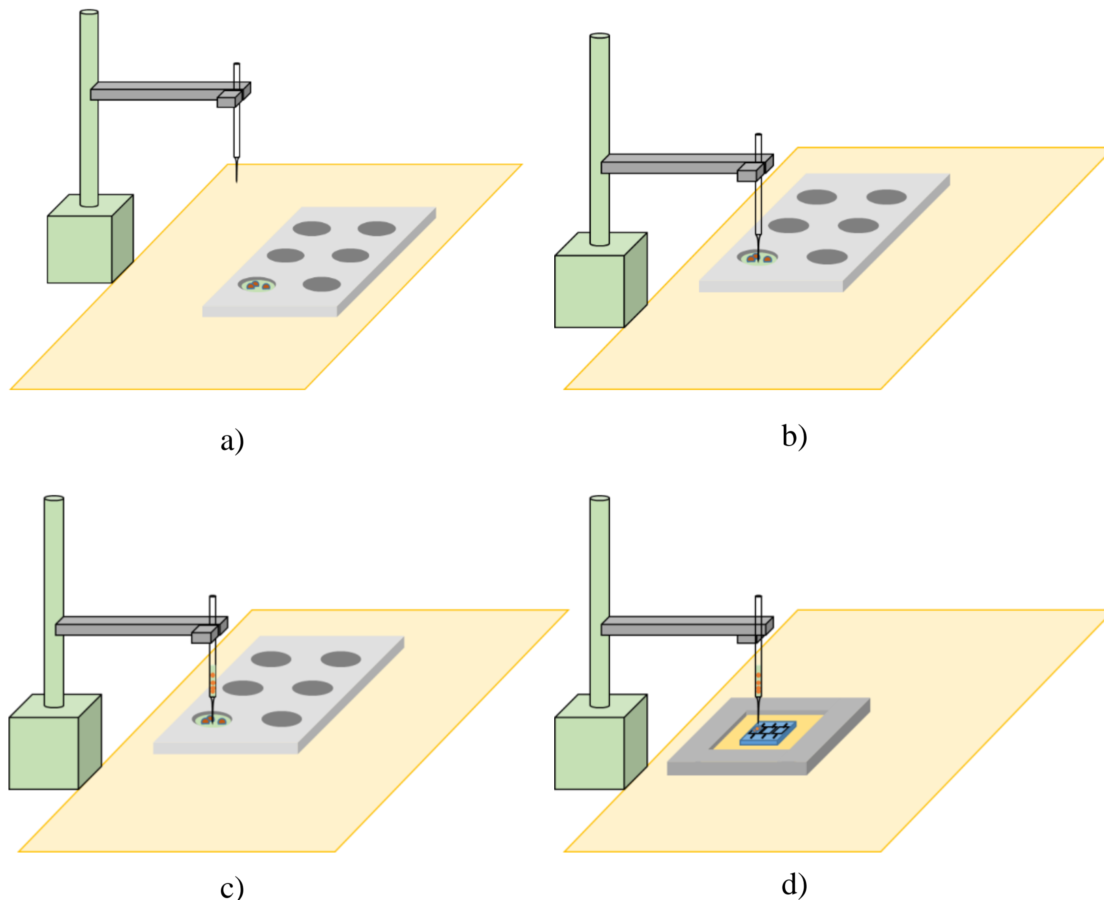

Figure 6. 14: Dispensing of magnetic nanoparticles. a) Calibration of positioning system. b) Set-up the coordinates to the filled well. c) Loading-up magnetic nanoparticle solution in the capillary. d) Depositing magnetic nanoparticle solution onto resonator proof mass surface.

In Figure 6.15 a), the method to calculate the dispensed weight of nanoparticles is illustrated. Figure 6.15 b) shows the actual Microplotter system.

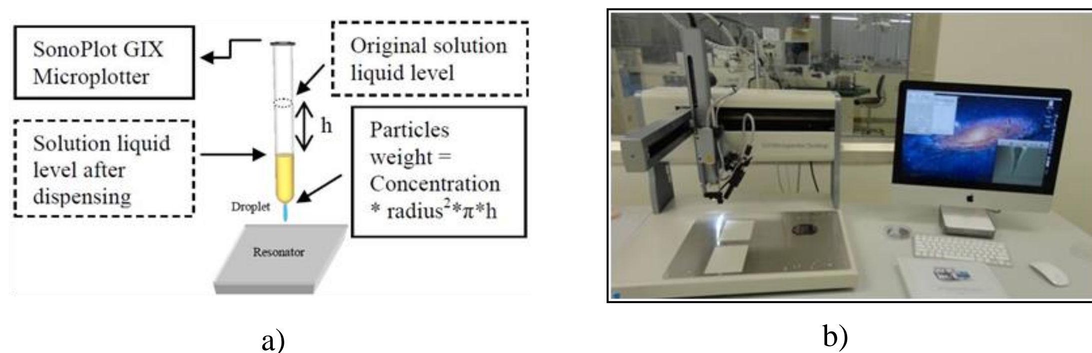

Figure 6. 15: Microdispenser system. a) Computation of dispensed weight of magnetic nanoparticles, where h is the change of liquid level. b) SonoPlot GIX Microplotter system.

6.4 Surface Functionalization of Multi-DOF Mode Localized Coupled Resonators

In the last two decades, biosensor technology has rapidly and widely evolved. Both assay- and device-based biosensors are used to analyze biological molecules, mainly antigens and antibodies, enzymes, DNA, and cells. The principal mechanism in a device-based biosensor is the transduction of a specific biological component that has a strong binding affinity with the target analyte. However, electronic devices such as MEMS sensors are silicon-based, and silicon is not capable of intrinsic adhesion or interaction with biological components. Hence, silicon surface modifications are indispensable; specifically, functionalization.

To capture the desired bioresponses on the surface of a MEMS device – for instance, antibody and antigen binding reactions – the counterpart of the analyte requires an area to dock. Biomolecules can be immobilized on the functionalized silicon surface using a hydrophobic or electrostatic approach. Furthermore, functionalization that exploits chemical reactions possesses enhanced stability. Table 6.3 [111] provides an overview of different strategies for functionalization on silicon-based surfaces.

Surface Material	***Modification***	***Binding Mechanism***	***Formed Film***
SiO_x	Silanization	Covalent	Monolayer
SiO_x	Esterification	Covalent	Monolayer
SiO_x	Phosphorization	Covalent	Monolayer
SiO_x	Layer-by-layer	Electrostatic	Multilayer
SiO_x	Liquid membrane	Electrostatic	Bilayer
$Si-H$	Hydrosilylation	Covalent	Monolayer

Table 6. 3: Strategies of silicon surface functionalization.

Considering the feasibility and applicability [112] of functionalization for multi-DOF coupled resonator devices, the chemical-reaction–based silanization process was selected. Briefly, silanization offers a coupling medium that enhances the stability of

the binding between silicon-based material and biological compounds. To be more specific, silanization utilizes hydroxyl groups to form a functional linkage. The self-assembled layers of organosilane are obtained by forming a siloxane network [113], which is suitable for bio-MEMS development.

The chemical reaction of silanization is divided into four steps: the silicon substrate is hydrolyzed; the silanol group forms siloxane linkages; hydrogen bonds are formed with hydroxide bonding; and covalent bonds are formed on the silicon surface. Table 6.4 summarizes a number of silanization reagents for silicon surface functionalization [111], which are correlated with the sensor types and target analyte.

Sensor applications	***Silanization reagent***	***Target analyte***	***Affinity counter part***
Biosensors	APTES	Poly-T/poly-A 15-mer DNA	15-mer ss-DNA
	APTES	Streptavdin	Biotin
	APTES & GA	Estrogen response elements	Estrogen receptors
	APTES & GA	PSA	Anti-PSA
	APTES & GA	Glucose	Glucose oxidase
	APTES & GA	CRP	Anti-CRP
	APDMES	Complementary DNA	16-mer ss-DNA
	APMS	PSA	Monoclonal antibodies
	APMS	Influenza	Antibodies
	APMS	ATP	Tyrosine kinase
pH sensors	APTES	H^+	
Gas sensors	APTES	TNT	

Table 6. 4: Silicon surface silanization. Colored sections indicate the possibility to be adopted for multi-DOF coupled resonators as biosensors.

As can be seen from the table above, (3-aminopropyl) triethoxysilane (APTES) as a silanization reagent can be adopted for a variety of bio-chemical sensors. Several studies [114-117] have provided reliable results that show APTES is an effective surface modification agent. For example, it has been used in silicon nanowire devices [118], silicon nanochannel glucose sensors [119], and silicon BAW resonators for biotin-streptavidin binding detections [120]. The APTES agent offers functional groups for aldehyde, carboxylic acid, and epoxy [111], and consequently enhances the

immobilization properties of biological molecules.

To extend the range of applications and improve the performance of the APTES-treated silicon surface, glutaraldehyde (GA) is used to coat an aldehyde-terminated layer. This approach increases the potential for additional reactions, including the interaction with amine groups, proteins, and enzymes [118]. A flow diagram of the APTES and GA linker process for silicon surface modification is shown in Figure 6.16.

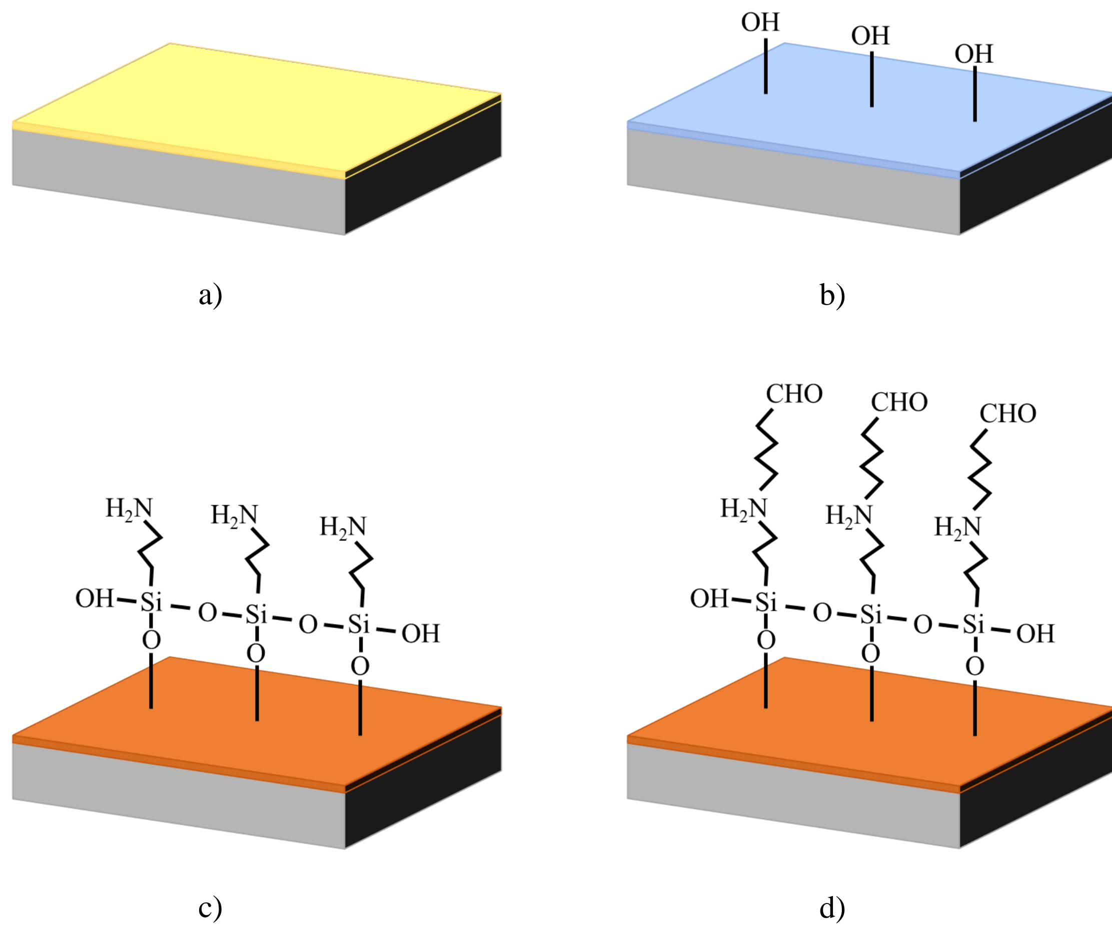

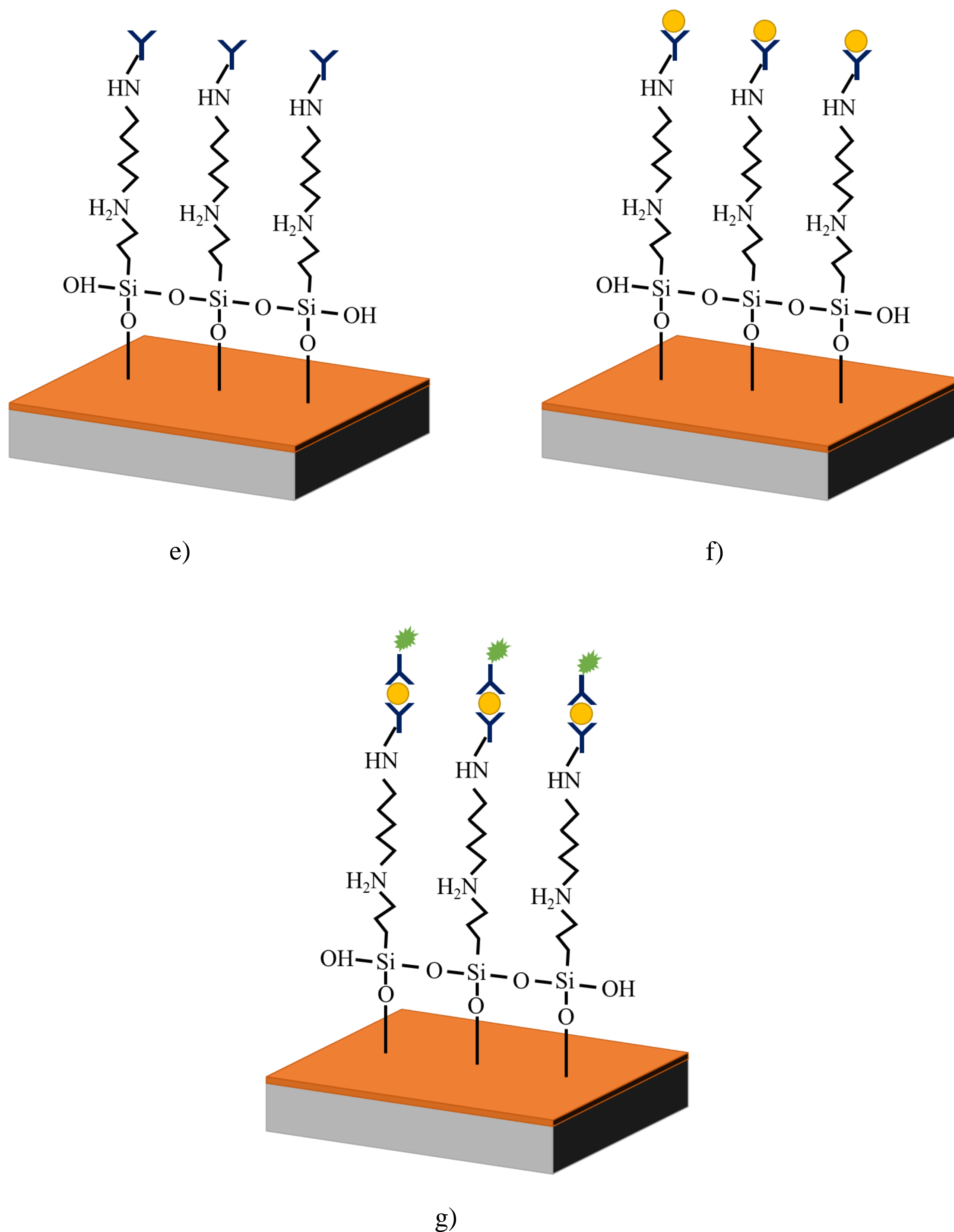

Figure 6. 16: Flow diagram of APTES & GA treatment for silicon surface functionalization. a) Original silicon surface (SiO_2 layer) cleaning via oxygen plasma or piranha solution. b) Hydroxyl groups are formed up after cleaning. c) 2% v/v APTES solution treatment, silane layer is formed. d) GA linker solution treatment. e) Functionalized silicon surface immobilizing bioreceptor (counterpart) of target analyte, here for example, specific antibodies. f) Adding sample solution, target analyte, here is antigen, are binding with antibodies. g) Additional sandwich assay procedure, using fluorescence labelled antibodies to confirm the antigen/antibody binding.

This is a universal functionalization process for silicon-based devices. Multi-DOF mode localized coupled resonators can utilize the APTES and GA treatment for biosensing applications. Once the target analyte successfully binds with the immobilized bioreceptor (counterpart), the effective mass value of the sensing resonator proof mass is altered. Hence, the induced mass perturbations can be determined by using the mode localization mechanism, the transduced signals are carried to the interface circuit, and they can finally be monitored on external facilities.

The APTES and GA reagents are commercially available from Sigma-Aldrich. The required chemical productions for the functionalization process are listed in Table 6.5.

Production Name	***Specifications***
Phosphate buffer saline (PBS)	pH 7.4, sodium chloride (70.3%), disodiumhydrogenorthophosphate (12.3%), and potassium chloride (17.4%)
Piranha solution	3:1; H_2SO_4/H_2O_2
De-ionized (DI) water	/
APTES	2% (v/v) APTES solution
GA	2.5% (v/v) Glutaraldehyde
Anhydrous toluene	Anhydrous, 99.8%
Borate buffer saline	Sodium chloride (85.7%), borate monosodium salt (9.3%) and boric acid (5%)

Table 6. 5: Chemical productions used for silicon surface functionalization.

A protocol of APTES & GA silanization based process for silicon surface functionalization is organized:

1) Pre-clean the sensing surface of the multi-DOF coupled resonator. The sensing surface is kept in piranha droplets for 15 minutes. Then the surface is rinsed with DI water couple of times, after that the device is required to dry under a stream of nitrogen gas for 20 minutes. Or oxygen plasma treatment for 10 min at 80 sccm, 150 mT, 225W RF. Then the sensing surface is rinsed with DI water couple of times and dried under a stream of nitrogen gas for 20 minutes.

2) Moving the device to oven dryer at 110 °C for ~1 hour to ensure the moisture on the surface is removed.

4) Preparing APTES solution in pre-heated anhydrous toluene (100–120 °C). Then depositing certain volume of the prepared 2% (v/v) APTES onto sensing surface.

5) Washing the APTES modified sensing surface with PBS and then keeping the surface to react with 2.5% (v/v) GA solution for 30 minutes at room temperature.

6) Dispensing the capture antibodies (bioreceptor) solution onto the functionalized sensing surface for immobilization. During the immobilizing progress, 1% Tween20 shall be introduced. The immobilization is performed at room temperature for 15 minutes to form a stable antibody layer. Generally, the capture antibody solution has a concentration of 0.1 mg/ml.

7) Adding target analyte onto the functionalized resonator sensing surface to bind with the immobilized selective antibodies. The sensing surface is treated with the target analyte for 10~30 minutes to ensure the antibody/antigen binding interaction.

6.5 Chapter Summary

This chapter described the interface circuit designs for multi-DOF mode localized coupled resonators. The motional current pick-up circuit and the corresponding experimental design and measurement platform for the 3-DOF electrostatic coupled resonator were discussed. Subsequently, a high speed peak detector circuit design was introduced, which achieved the mass to stiffness sensing transduction in the QCM/3-DOF coupled resonator hybrid system.

Next, the interface circuit for the 2-DOF coupled BAW disk resonator was illustrated, including different methods of feedthrough signal compensation. The experiment materials that were used for the multi-DOF coupled resonator mass sensitivity characterizations were shown, and a magnetic nanoparticle preparation protocol was proposed. Finally, this chapter explained the silicon surface functionalization processes, and covalent bond based on chemical silanization was selected as the major functionalization process.

Chapter 7

Experiments

7.1 Experiments

7.1.1 A Mass Sensor Based on 3-DOF Mode Localized Coupled Resonator under Atmospheric Pressure

A solution containing 10 um diameter magnetic nanoparticles with a concentration of 5mg/ml was added on resonator1. Magnetic nanoparticles were used as mass perturbation material due to their low cost, easy handling, and simple removal method to achieve reversibility. The added mass was controlled through the concentration of the nanoparticles in the solution (details of magnetic nanoparitcle preparation are introduced in chapter 6). The magnetic nanoparticles comprised a magnetic core and were covered with a SiO2 shell. Originally, the magnetic nanoparticles were stored in deionized water or oil. For the purpose of mass sensing, a rapidly evaporating solution was necessary. Accordingly, the carrier solution of magnetic nanoparticles was altered to 70% ethanol solution.

First, the concentration of magnetic nanoparticles was diluted to 2mg/ml with an Eppendorf tube. Next, a SonoPlot GIX Microplotter was used to dispense a small droplet (~20nL) of diluted magnetic nanoparticles solution on resonator1.

After the carrier solution (70% ethanol) evaporated, the solid magnetic nanoparticles were firmly attached to the resonator surface and accordingly a change of effective resonator mass was achieved. Figure 7.1 shows the dispensing process and

magnetic nanoparticles on resonator1, respectively. After deposition, the 3-DOF coupled resonator chip, with a mass perturbation on resonator1, was tested with the interface circuit measuring the motional current of resonators1 and 3. The corresponding system frequency response was captured by a Lock-in amplifier (Anfatec eLockIn204/2).The resonance frequency shift, amplitude change and resonance amplitude ratio were acquired and calibrated with the data obtained from the unperturbed system.

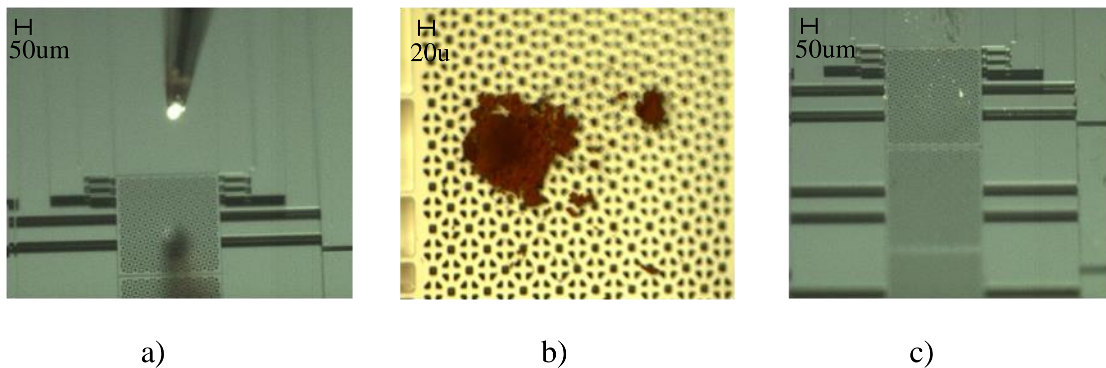

Figure 7. 1: a) Microplotter capillary tip above resonator1 of 3-DOF coupled resonator chip. b) Magnetic nanoparticles attached to resonator1. c) Magnetic nanoparticles had been washed away.

The frequency responses of the 3-DOF coupled resonator system for three mass perturbations are shown in Figure 7.2 a) & b). The added mass perturbations were computed according to the method depicted in equation 6.1 to 6.4 and Figure 6.15. The three consecutive added masses were 180ng, 265ng and 390ng, respectively. Moreover, the theoretical frequency responses of both reasontor1 and resonator3 were obtained by MATLAB simulations and are illustrated in Figure 7.2 c) & d).

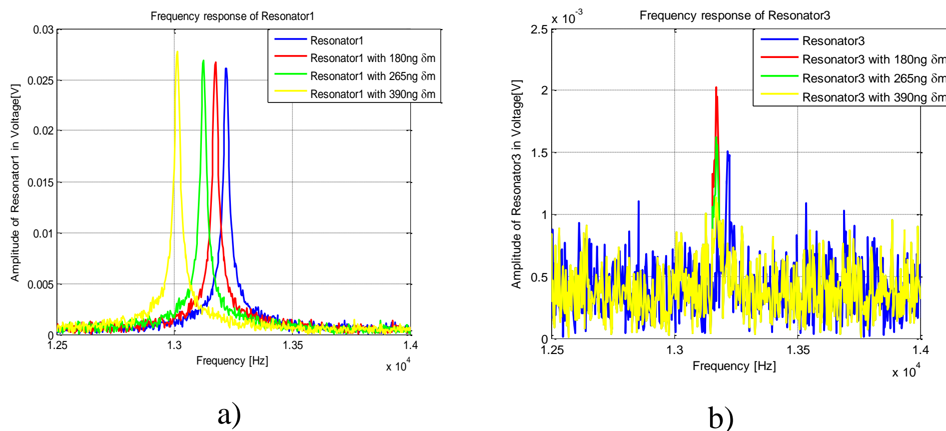

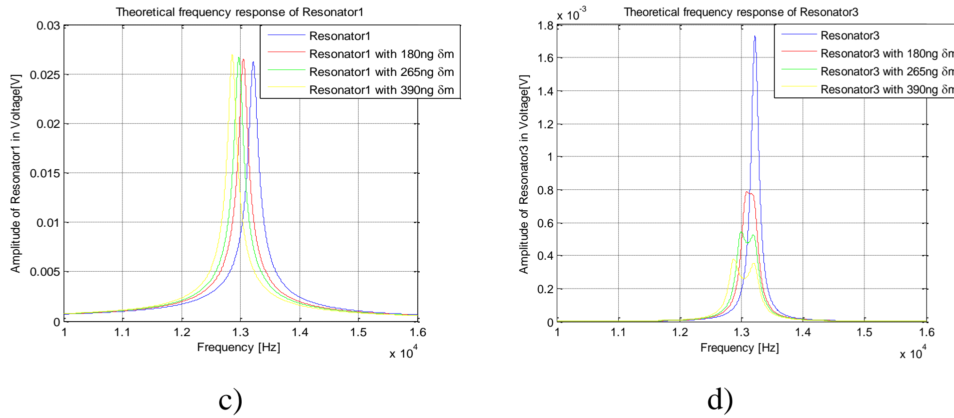

c) d)

Figure 7. 2: Frequency response of 3-DOF coupled resonator system after three consecutive mass perturbations. a) Frequency response of resonator1. b) Frequency response of resonator3. c) Simulated frequency response of resonator1. d) Simulated frequency response of resonator3.

According to extracted experimental data, the total noise value was $\bar{V}noise_{rms} = 402\mu V$. The total noise includes a variety of noise sources: mechanical noise due to the air damping, phase noise, thermal noise due to the interface circuit and environmental noise. Theoretically, simulation models without noise would give infinite resolution and sensitivity. However, by including a more realistic total noise value into the MATLAB simulation model, the maximum system resolution could be extracted with respect to the total noise floor. Using this methodology, the minimum detectable mass value for 3-DOF mode localized resonator operating at atmospheric pressure was 1.7ng. This is mainly due to the relatively high air damping and thus low Q-factor.

The unperturbed 3-DOF coupled resonator system response in comparison with the magnetic particles removed by rinsing are shown in Figure 7.3 a) & b), respectively. After the rinsing step, the relative error in comparison with the unperturbed case was less than 1%.

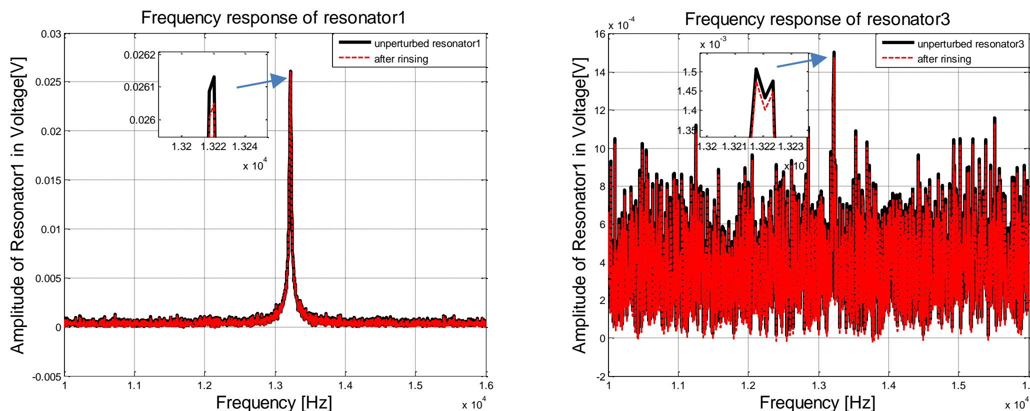

a) b)

Figure 7. 3: Frequency response of 3-DOF coupled resonator system. a) Frequency response of Resonator1without perturbation/after rinsing. b) Frequency response of Resonator3 without perturbation/ after rinsing.

The corresponding resonance frequency shift, amplitude change and the change of resonance amplitude ratio versus normalized mass perturbation are presented in Figure 7.4. The amplitude change is the deviation in resonator amplitude compared to the unperturbed amplitude at the unperturbed resonance frequency, whereas amplitude ratio is the ratio of vibration amplitudes of resonators1 and 3 at resonance. Also, a comparison with a theoretical model is included. As can be seen from Figure 7.4, the variations between theoretical amplitude ratio and measured data are larger than for frequency shift and amplitude change. The main reason is the influence of the damping, as the system is operating in air; with the observed low Q factor of approximately 8, the mode aliasing effect as discussed in chapter 2 & 3 occurs. Another explanation is fabrication tolerances; the unsymmetrical structure of the proof masses will induce inherent mode localization even without external perturbations. To improve the measurements, two approaches can be used: Firstly, put the system into a vacuum environment. However this method makes experiments cumbersome as a vacuum chamber is required and furthermore, it loses the potential of the resonator chip to be used as a biosensor if it only operates in vacuum. Secondly, an extra calibration electrode could be integrated into the 3-DOF coupled resonator system. By providing a controllable DC voltage to the calibration electrode, an electrostatic force can be generated. This electrostatic force can be used for compensating the inherent mode localization caused by fabrication tolerances. The second approach will be the main approach of improving the 3-DOF coupled resonator as a mass sensor in future work.

The mass sensitivity of the 3-DOF coupled resonator with output metric using the change of the resonance amplitude ratio, the resonance amplitude change and the resonance frequency shift can be computed by using equation 7.1, 7.2 and 7.3 respectively, where $\mathrm{AR_0}$ is the unperturbed amplitude ratio, $\mathrm{A_0}$ is the unperturbed resonance amplitude and $\mathrm{F_0}$ is the unperturbed resonance frequency.

$$S_{AR}^{3-DOF} = \left| \frac{\partial(amplitude\ ratio)/AR_0}{\partial\left(\frac{\Delta M}{M}\right)} \right| \tag{7.1}$$

$$S_{AC}^{3-DOF} = \left| \frac{\partial(resonance\ amplitude)/A_0}{\partial\left(\frac{\Delta M}{M}\right)} \right| \tag{7.2}$$

$$S_{FS}^{3-DOF} = \left| \frac{\partial(resonance\ frequency)/F_0}{\partial\left(\frac{\Delta M}{M}\right)} \right| \tag{7.3}$$

The calculated mass sensitivities of each output metric are summarized in Table 7.1. The comparison is based on the percentage of variations in three different output metrics with respect to the same percentage of mass changes. It can be seen that the change of the resonance amplitude ratio yields a sensitivity around two times larger than amplitude change and around two orders of magnitude larger than frequency shift.

Criteria	**Value**
Frequency Shift	0.27
Amplitude Ratio	25.31
Amplitude Change	17.29

Table 7. 1: Calculated mass sensitivity.

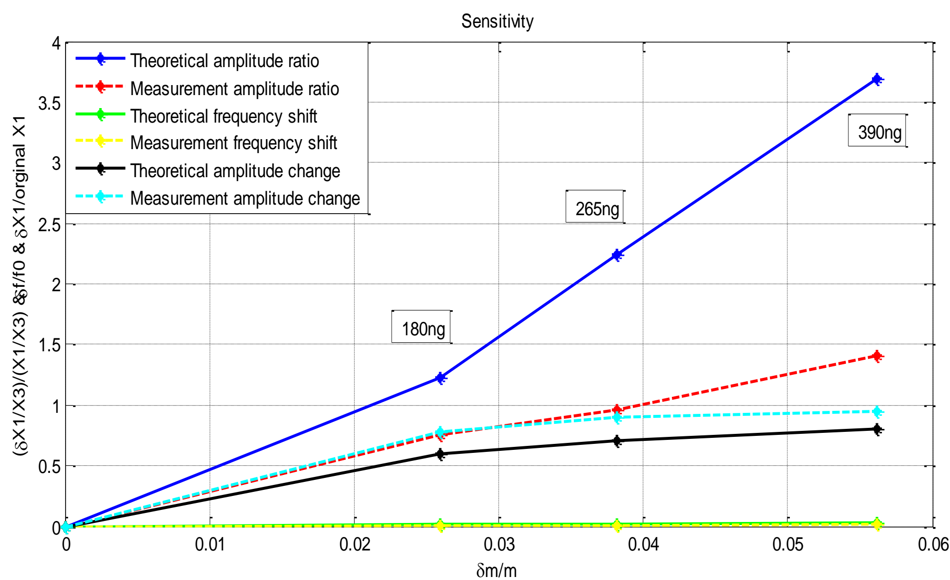

Figure 7. 4: Theoretical (simulated) and experimental sensitivities of 3-DOF coupled

resonator system.

It is expected that three different output metrics considered here also differ in system resolution, linearity and dynamic range. As discussed in section 2 the MATLAB model was used to derive the minimum detectable mass based on a total noise floor, whose value was obtained from extracted experimental data. However, to compare the dynamic range, resolution and linearity of using frequency shift, amplitude change and amplitude ratio as output metrics, a comprehensive noise analysis has to be performed. The coupling and cross-correlation of the various noise sources mechanism such as Brownian noise, phase noise, electronic interface noise, extrinsic noise and phase to amplitude noise coupling are still a subject of debate. This is outside the scope of this work. Recent publications discuss noise, resolution, sensitivity and linearity in mode localized coupled resonator systems in more detail [121, 122]. The results are encouraging and can be used as a starting point for further investigations of the 3-DOF mode localized coupled resonator as mass sensor. Finally, table 7.2 summarizes types of existing MEMS resonant mass sensors (resonant frequency shift as output metric), which can be used as contrasts for the proposed 3-DOF coupled resonator in this research topic.

Sensor Type	***Operation Environment***	***Resonant Frequency***	***Sensitivity*** $(\Delta f/\Delta M)$	***Reference***
Cantilever	Vacuum	45.9 KHz	0.43 Hz/pg	[123]
Cantilever Array	Vacuum	73-75 KHz	Not reported	[63]
FBAR	Vacuum	2.3 GHz	6 MHz/fg	[124]
BAW DRP	Air	3.145 MHz	34 Hz/ng	[125]
QCM	Air	5 MHz	56.6 Hz/ug	[126]
3-DOF CR	Air	13.3 KHz	0.8 Hz/ng	Presented in this work

Table 7. 2: A summary of MEMS resonant mass sensors. It is needed to be concerned, the mass sensitivities in the table are based on resonant frequency shift. Mode localization metric (AR) had been proved theoretically and experimentally, which

improved the normalized sensitivity for orders of magnitudes compared with resonant frequency shift. Hence the 3-DOF coupled resonator that exploits mode localization effect can yield higher sensitivity and possess common mode rejection ability.

With a novel reversible method to add nanoparticles as mass perturbations, this work characterized the mass sensitivity of a 3-DoF mode localized electrostatic coupled resonator operating under atmospheric pressure. As can be observed from Figure 11, the reusability of MEMS coupled resonator sensor after mass sensing operations is clearly demonstrated. Nanoparticles as mass perturbation to characterize the MEMS mass sensors is an effective and cost-effective technique, accordingly, it can contribute to the development MEMS mass resonant sensor developments in general. The mass sensitivity of a novel 3-DOF mode localized coupled resonator sensor is successfully obtained via a reversible nanoparticle depositions method. It demonstrates that the change of the resonance amplitude ratio as output metric yields higher sensitivity in comparison with amplitude change and frequency shift.

This work constitutes an important step towards realizing a high sensitivity biosensor for concentration measurement using a mode localized sensor operating in air.

7.1.2 A Novel QCM Mass Sensing System Incorporated with a 3-DOF Mode Localized Coupled Resonator Stiffness Sensor

A quartz crystal microbalance (QCM) comprised of an AT-cut quartz crystal slice is studied, which is deposited with conductive electrodes. Based on piezoelectric material properties, QCM serves as a sensor for mass variation detection ranging from ng to µg [127-129]. To characterize the QCM device, Sauerbrey's equation is used [130], in which the fundamental resonant frequency can be calculated by:

$$f_0 = \sqrt{\frac{u_q}{4\rho_q t_q^2}} \tag{7.4}$$

where u_q is the shear modulus of quartz, with an assigned value of $2.947 \times$

$10^{11}\ gcm^{-1}s^{-2}$, ρ_q is the density of quartz, with a value of 2.648 gcm^{-3}, t_q is the crystal thickness.

Further, Sauerbery's equation also determines the relationship between the mass loading (mass perturbation), resonant frequency and shifted frequency, as expressed:

$$\Delta f = -\frac{2\Delta m {f_0}^2}{A\sqrt{u_q \rho_q}} \tag{7.5}$$

where A is the area under piezoelectric effects, usually it is defined by the size of deposited metal electrodes. The equation 7.5 can be rewritten in a simplified form, with a parameter $C_f = 2{f_0}^2/\sqrt{u_q \rho_q}$ which correlates to the intrinsic property of the quartz, the shifted resonant frequency in response to mass perturbation hence can be expressed:

$$\Delta f = -\frac{C_f}{A} \times \Delta m \tag{7.6}$$

Benefiting from the acoustic resonator features, QCM devices are able to maintain thousands of Q-factor when operating in air [131]. Even in heavily damped environment such as liquid, QCM devices can still possess reasonable Q-factor values [132, 133] which allow the sensing mechanism to implement. Besides the favorable Q-factor in damped cases, QCM devices are robust and less complex in structure, as well as the capability of batch fabrications. These advantages make QCM an attractive sensor technology, particularly for biosensing applications. Generally, QCM devices utilize three sensing schemes: the resonant frequency shifts measurements, the impedance measurements (QCM-I) and dissipation measurements (QCM-D). Each scheme offers distinct features for different biosensing tasks.

The 3-DOF mode localized coupled resonator, on the other hand, has already demonstrated the superior ability in terms of sensitivity, common mode rejection and adaptability for both mass and stiffness sensing applications. Although the potential of the 3-DOF coupled resonator as biosensor has already been proved, the defect of such device operating under heavily damped environment is inevitable. A low Q-factor of

the 3-DOF coupled resonator will result in loss of SNR, sensitivity and more critically, disturb the system vibration behavior that eventually lead to mode aliasing. A simulation model is carried out to illustrate the 3-DOF coupled resonator responses in vacuum, air and liquid respectively, as shown in Figure 7.5.

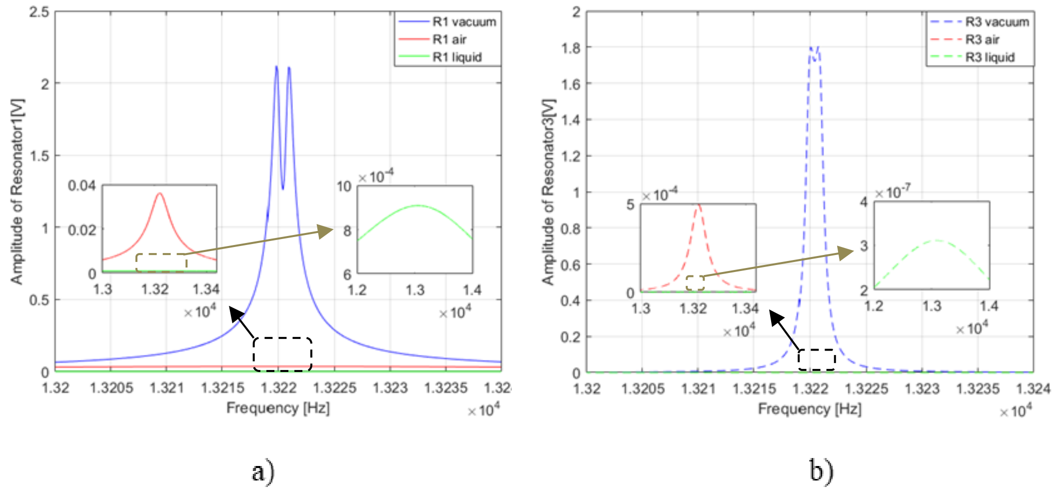

Figure 7. 5: Simulation model of a 3-DOF coupled resonator operating in three different environments: a) Responses of resonator 1. b) Responses of resonator 2.

It is can be observed, mode aliasing phenomenon occurred in both air and liquid environments. Even though the damping coefficient in air is relatively large and the vibration modes overlapped, the system sensing mechanism is still valid. This had been proved by simulation models in chapter 4.2.2 and once again, had been verified by the experiments of the 3-DOF coupled resonator under atmospheric pressure, as introduced in section 7.1.1. On the contrary, the attenuated amplitudes in liquid condition are beyond measurable. A conclusion can be drawn accordingly: the 3-DOF coupled resonator has best performance in vacuum and it can be used in air for specific sensing tasks for instance, biosensing applications. Unfortunately, such 3-DOF coupled resonator is not suitable for liquid contact measurements.

The emergence of QCM/3-DOF coupled resonator hybrid system could bring cross benefits for both sensing platforms. To counter the damping influences in 3-DOF coupled resonator, the QCM is used as the forehead of the hybrid system, since QCM is capable of handle sensing tasks in air or in liquid. As for the performance of QCM itself, mode localization sensing mechanism can be exploited via the 3-DOF coupled

resonator, consequently enhances the whole system sensitivity. To realize such hybrid system, the most important section is the signal conversion stage. More specific, a dedicate component is essential to establish connections between the output of the QCM and the input of the 3-DOF coupled resonator. Fundamentally, the 3-DOF coupled resonator is operating in vacuum condition to optimize its functionality, while having the stiffness perturbation port connected with the output of the QCM. However, to attain accurate and stable stiffness measurements from the 3-DOF coupled resonator, the stiffness perturbations should be induced by electrostatic forces. Thus, the output AC signals from the QCM are converted to DC form and then delivered to the stiffness perturbation port of the 3-DOF coupled resonator to generate electrostatic forces.

As presented in chapter 6.1.2, a high speed peak detector is employed to achieve a proper AC to DC conversion. High speed operational amplifiers, Schottky diode and Zener diode constitute the high speed peak detector unit. After integrating electronic components onto the prototype board, testing experiments of the peak detector circuit are carried out.

The QCM mass sensor is commercially available from thinkSRS, having a resonant frequency of 5 MHz. This QCM has both front and back side electrodes made of Chromium/Gold (Cr/Au), where the quartz crystal has an AT angle of cut. The dimension parameters are listed in Table 7.3.

Parameters	***Values***
Front electrode diameter	12.8 mm
Back electrode diameter	6.4 mm
Quartz diameter	25.4 mm
Front route length	6.3 mm
Front route width	2.6 mm
Wrap over electrode width	14.5mm
Back route width	1.5 mm

Table 7. 3: 5 MHz QCM device parameter values.

The schematic of the QCM device is demonstrated in Figure 7.6.

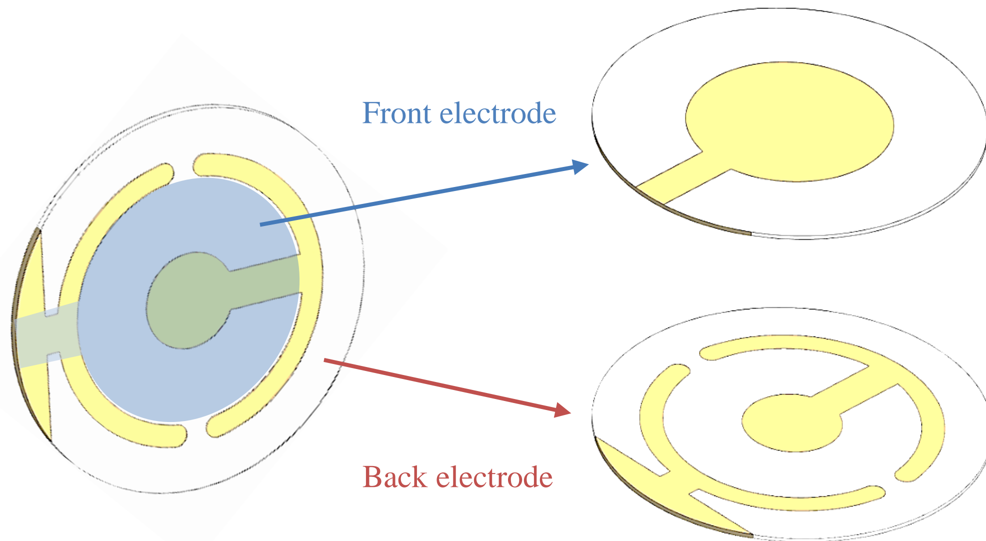

Figure 7. 6: Schematic of a QCM device has a resonant frequency of 5MHz, AT-cut and wrapped over electrodes

Firstly, a 5 MHz QCM device verification experiment is commenced, as shown in Figure 7.7.

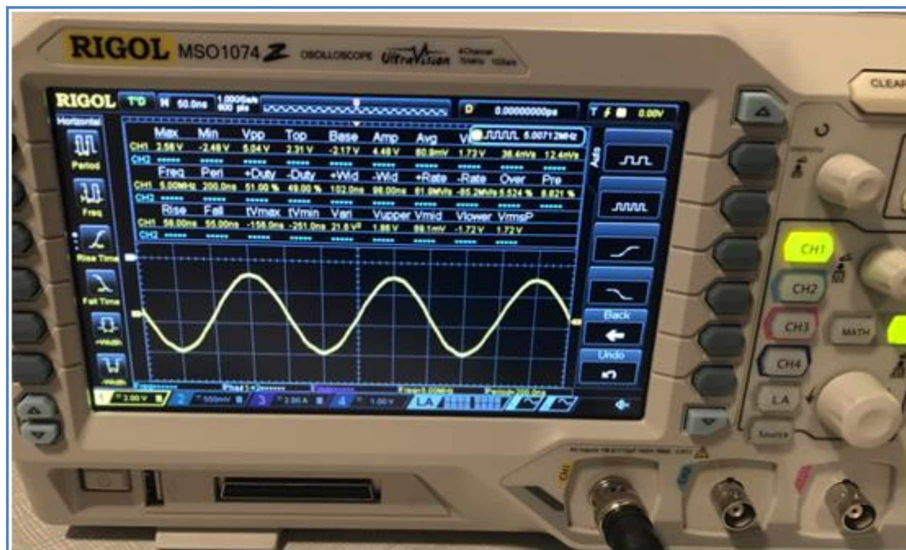

Figure 7. 7: Oscilloscope captured signal of an unperturbed QCM device, the QCM device has a resonant frequency of 5 MHz.

The peak detector circuit is then connected to the QCM, as can be seen in Figure 7.8, the original AC output signal is converted to DC signal as desired.

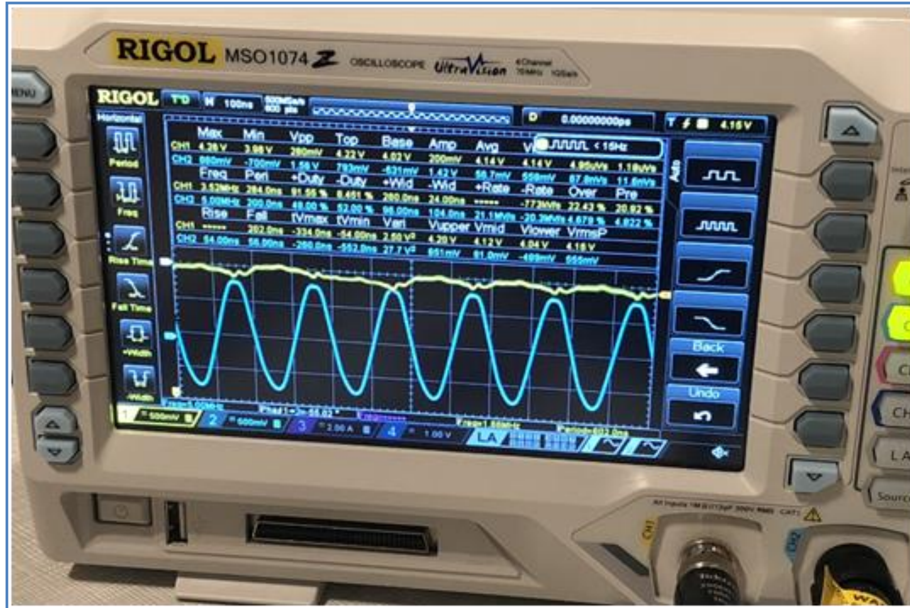

Figure 7. 8: Oscilloscope captured signal of an unperturbed QCM device connected with a high speed peak detector.

The system diagram is shown in Figure 7.9. A solution containing 1 μm diameter magnetic nanoparticles with a concentration of 10 mg/ml was used to be added onto the QCM. First, the concentration of the magnetic nanoparticles was diluted to 0.6 mg/ml with an Eppendorf tube. Next, a pipette with 2 μL volume was used for consecutive dispensing the diluted nanoparticles solution onto the QCM. Figure 7.10 shows the 3D printed QCM holder and dispensed magnetic nanoparticles on QCM, respectively.

Subsequently, the output signals from the QCM (with/without nanoparticles) were processed by a peak detector circuit, which was directly connected to the stiffness perturbation port (effectively a capacitor) of the fabricated 3-DOF coupled resonator. Henceforth, the generated electrostatic force altered the effective stiffness of resonator 3, introducing a perturbation. The 3-DOF coupled resonator was integrated with an interface circuit measuring the motional currents of resonators 1 and 3. The corresponding system frequency responses were captured by a lock-in amplifier (Anfatec eLockIn204/2). The resonance frequency shift, amplitude change and resonance amplitude ratio were acquired and compared with data obtained from a simulation model. Nanoparticles were consecutively added five times for sensitivity characterization. After the experimental procedure, the attached magnetic nanoparticles

on QCM could be easily removed using 70% ethanol and tissue paper. This allowed reversibility of the experiment.

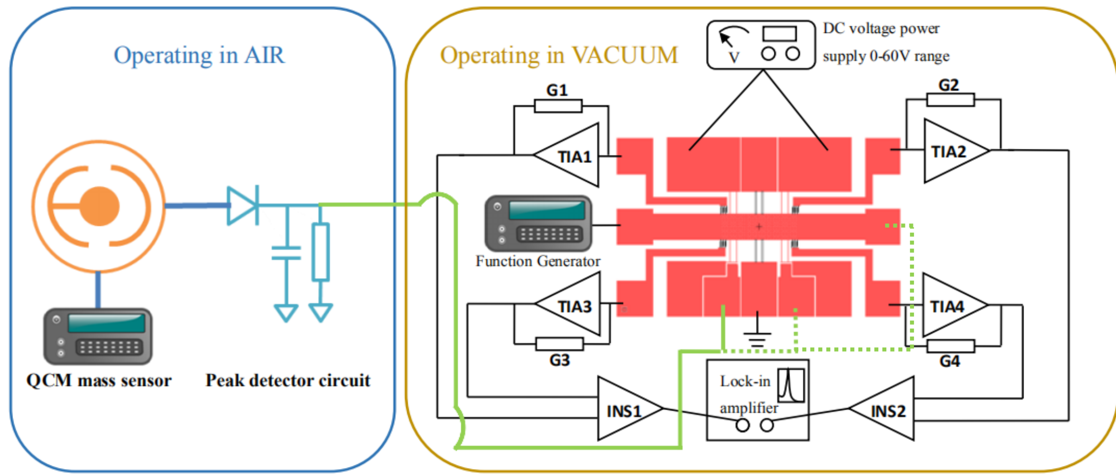

Figure 7. 9: QCM incorporated with a 3-DOF coupled resonator sensing system.

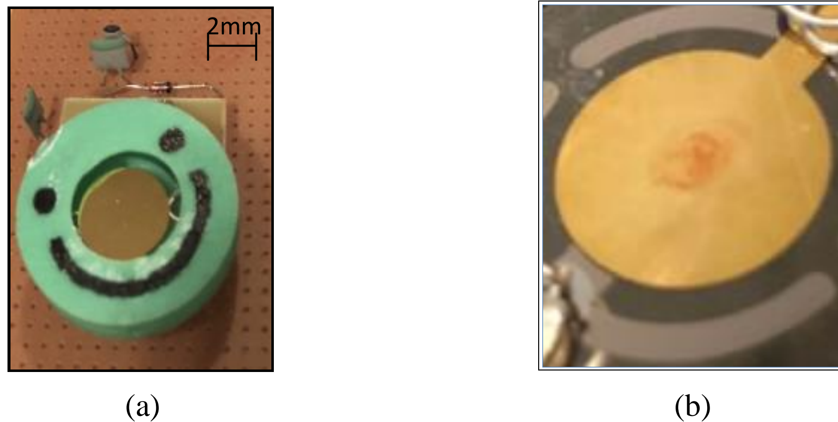

(a) (b)

Figure 7. 10: (a) QCM holder platform, (b) Dispensed magnetic nanoparticles on QCM.

The system frequency responses of the simulated model and measured experimental data of the 3-DOF coupled resonator system for adding mass five times on the QCM (1.2 μg to 6 μg with 1.2 μg steps) are shown in Figures 7.11 & 7.12. The corresponding resonance frequency shift, amplitude change and the change of resonance amplitude ratio are presented in Figure 7.13. Also, a comparison with the theoretical model is included. It can be seen that the change of the resonance amplitude ratio yields a sensitivity around three times larger than amplitude change and around 2 orders of magnitude larger than frequency shift.

In addition, a system level sensitivity comparison is established, which comprised

of the sensitivity of the QCM device and the sensitivity of the hybrid system. The sensitivity of the QCM based on the resonant frequency shifts as a function of added masses (QCM device only), the sensitivity of the hybrid system on the other hand, based on the amplitude changes and/or amplitude ratio changes of the 3-DOF coupled resonator as a function of the added masses on the QCM. The comparison is illustrated in Figure 7.14.

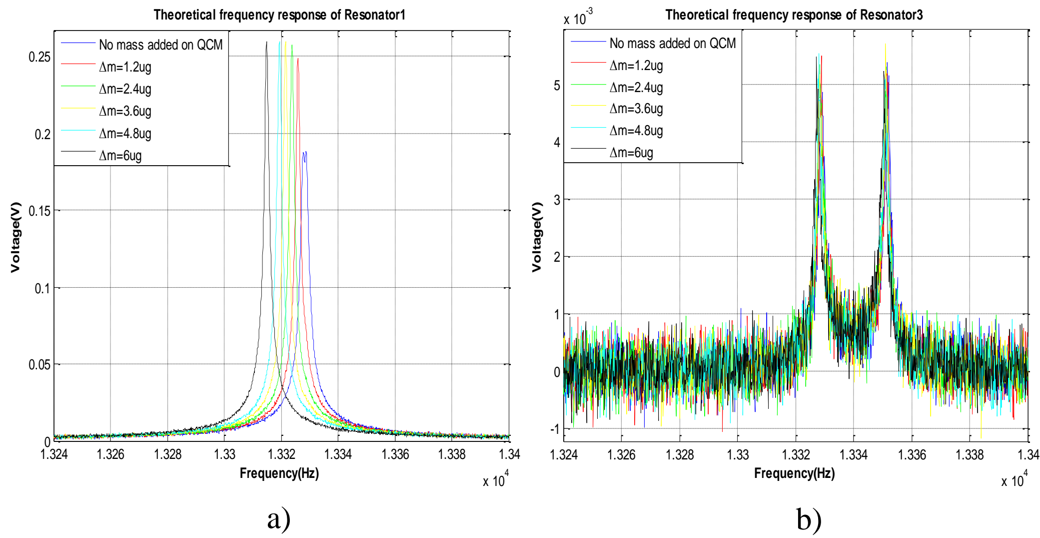

Figure 7. 11: Simulation for the frequency response of QCM incorporated with 3-DOF coupled resonator mass sensing system. a) Resonator1. b) Resonator3.

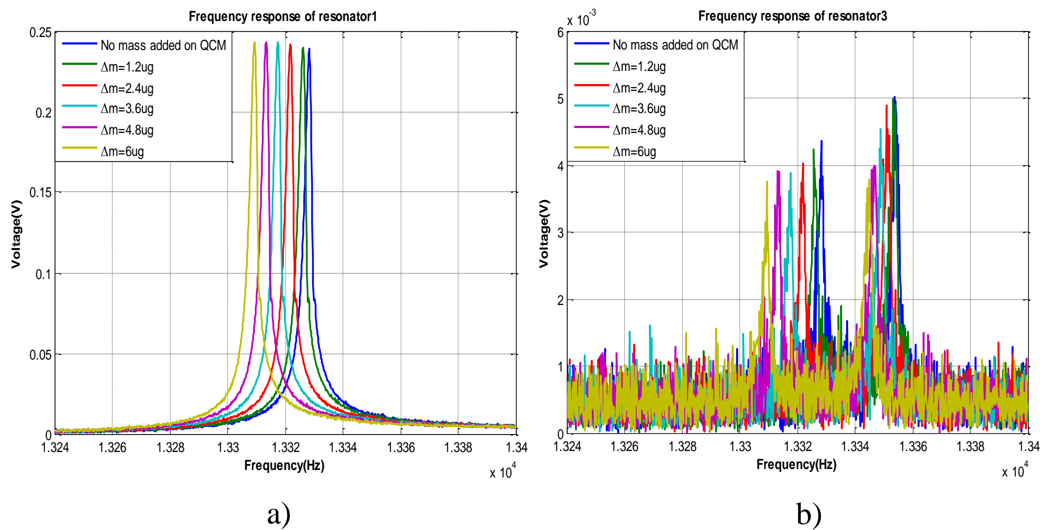

Figure 7. 12: The measured frequency response of 3-DOF coupled resonator system. (a) Resonator1. (b) Resonator3.

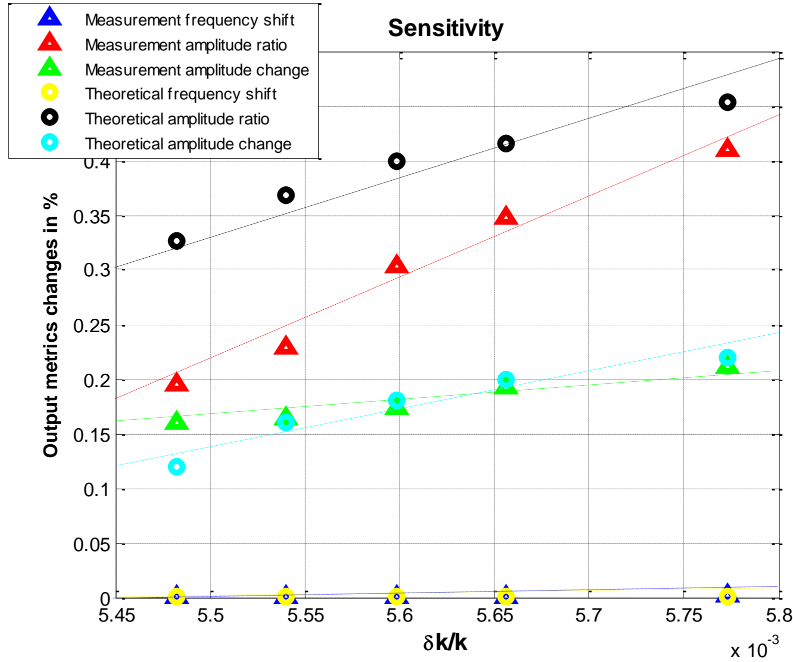

Figure 7. 13: Theoretical and experimental sensitivities of QCM incorporated with 3-DOF coupled resonator mass sensing system.

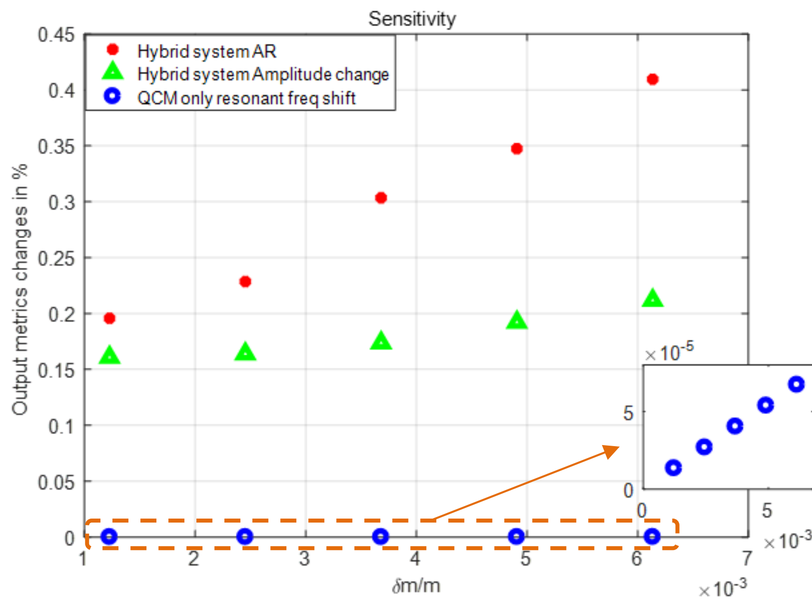

Figure 7. 14: System sensitivity comparison.

It is can be seen, the mode localization sensing schemes (amplitude ratio and amplitude change) in the hybrid system yield higher sensitivity compared with resonant frequency shift in the QCM mass sensor. This is a first proof that the hybrid system can not only overcome the dilemma of damped environment for mode localized coupled resonator, but also significantly improved the system sensitivity. Table 7.3 summarizes

the system normalized sensitives.

Type	Hybrid amplitude ratio changes	Hybrid amplitude changes	QCM resonant frequency shifts
Nor.S	35.6	15	0.011
Multiple	2.4		1364

Table 7. 4: Hybrid system and conventional QCM mass sensor sensitivity comparison.

In this work a novel hybrid mass sensing system is proposed. A QCM mass sensor is incorporated with a 3-DOF mode localized weakly coupled resonator stiffness sensor, which demonstrated a mass to stiffness sensing mechanism. A reversible method to add nanoparticles as mass perturbations on QCM is also introduced. Future effort of this work will constitute an important step towards a biochemical sensor that can exploit the advantages of mode localized coupled resonator but works directly in contact with a liquid.

7.1.3 Investigations of a 3-DOF Mode Localized Coupled Resonator under Small Stiffness Perturbations

Discussions about the best sensing metric for multi-DOF coupled resonator devices are ongoing. By exploiting the mode localization mechanism, superior sensitivity can be achieved in terms of eigenvector shifts and vibration amplitude ratio. However, the conclusion that the amplitude ratio is the dominating metric remains arguable, especially considering the aspect of sensor resolution. For example, Pandit et al. utilized a close-loop configuration to characterize a 2-DOF coupled double-ended tuning fork (DETF) resonator [134]. They performed a stability analysis of the output metrics based on resonant frequency shift and amplitude ratio. The results showed that the amplitude ratio as an output metric yields greater sensitivity and resolution for long term measurements, owing to the inherent common mode rejection ability of the mode localization mechanism. However, the resonant frequency shift as an output metric performed better for short term measurements (small integration time). Additionally, it possesses a better noise floor than amplitude ratio in the same time period.

Juillard et al. investigated the resolution limits for both open-loop and close-loop configurations of a 2-DOF coupled resonator [135]. The mode localization mechanism has been analytically studied, and an alternative mechanism called mutually injection-locked oscillators (MILOS) has been proposed. The research explored sensitivity in terms of resonant frequency shift, phase difference, and amplitude ratio; it also compared the resolution of different output metrics. The results showed that within a proper range for the multiplication value of the coupling strength and Q-factor, the phase difference yields greater sensitivity and resolution, making it the preferred output metric. Amplitude ratio, on the other hand, was shown not to be a superior output metric in some cases. As the conclusion states, under certain conditions, mode localized coupled resonator sensors may exploit phase difference or frequency shifts as output metric as a better compromise between the system sensitivity and resolution. On the other hand, the amplitude ratio still possesses its intrinsic merit, namely, the superior common mode rejection.

To investigate the resolution of the 3-DOF coupled resonator, a realistic noise floor has to be extracted first. Noise sources include mechanical noise from the 3-DOF coupled resonator, electrical noise (thermal noise) from the interface circuit, and environmental noise. A reliable total noise floor is obtained by capturing the baseline signal from a fully set-up experimental platform without the excitation of the 3-DOF coupled resonator, as illustrated in Figure 7.15.

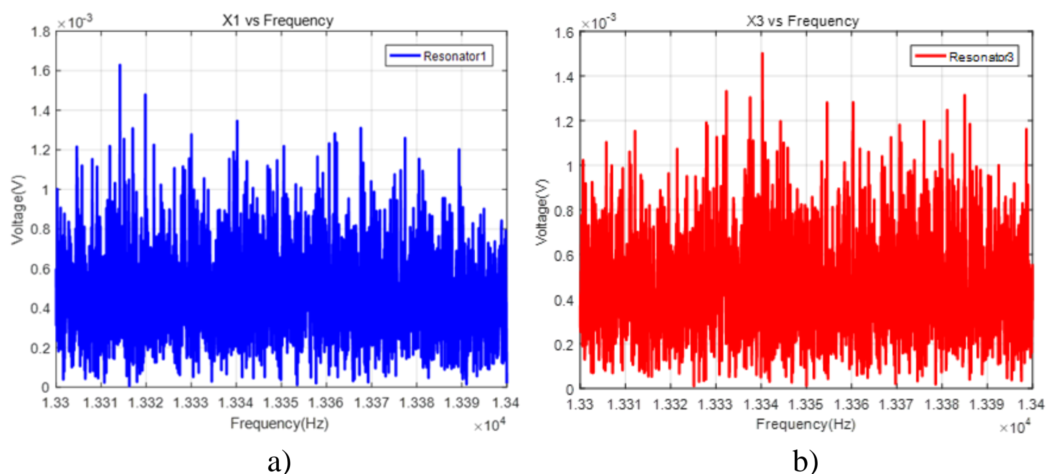

Figure 7. 15: Extracted noise floor of the 3-DOF coupled resonator. a) Resonator 1. b) Resonator 3.

The extracted noise floor can be used to compute the mean value (0.46 mV) and standard deviation (0.24 mV) of the total noise in the operation bandwidth of the device. A further computation can be made using equation 7.7, which offers a total noise equivalent stiffness perturbation (-2.47×10^{-5} N/m). This stiffness perturbation is then entered into the simulation to verify the system response, as shown in Figure 7.16. Ideally, this is the minimum detectable stiffness perturbation for a realistic 3-DOF coupled resonator sensor system, which defines the sensor resolution.

$$\Delta k_{perb} = -\frac{C_0}{d^2}\left[(V_{cp} + \Delta V_{perb})^2 - {V_{cp}}^2\right] \tag{7.7}$$

where C_0 is the nominal capacitance in the stiffness perturbation port (formed by a parallel plate structure between the proof mass and its adjacent electrode); d is the gap between the perturbation port; V_{cp} is the DC coupling voltage, in this case 35 V; and ΔV_{perb} is the injected DC perturbation voltage.

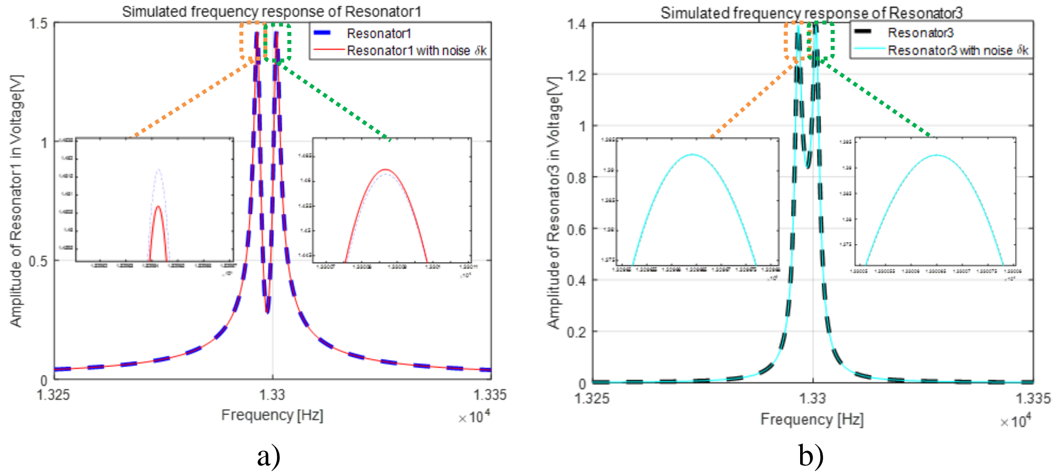

Figure 7. 16: Simulated 3-DOF coupled resonator responses with noise equivalent stiffness perturbation. a) Resonator1. b) Resonator3.

However, such a small stiffness perturbation is difficult to obtain in laboratory facilities. The general stiffness perturbation experiments were conducted using a commercialized 0–30 volt DC power source. To explore the resolution limit under laboratory conditions, stiffness perturbation experiments were carried out utilizing the DC power source with a minimum step value of 0.02 V. All experiments were

completed in vacuum (~8.8×10^{-6}mbar). The results are shown in Figure 7.17. As described in the theoretical analysis in chapter 3.1.1 and figure 3.2, out-of-phase vibration mode responses to negative stiffness perturbations yield a sensitive and linear behavior; hence, only out-of-phase mode related regions are captured.

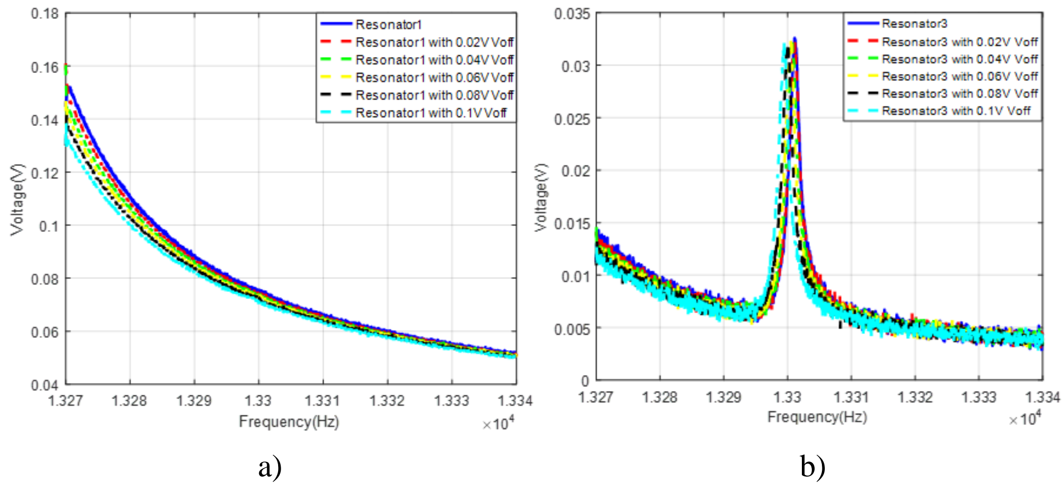

Figure 7. 17: Small stiffness perturbation experiments with DC perturbation voltage from 0.02V to 0.1V. a) Resonator1. b) Resonator3.

As can be seen from Figure 7.17, there are no apparent signal peaks in the data obtained from resonator 1 under consecutive stiffness perturbations. The main reason is fabrication tolerance or mismatching between the symmetrical resonator structures, which results in an initial unwanted system perturbation. However, the experiments presume the peak signal of resonator 1 still exists at the same peak frequency as in resonator 3, which is around 13,300 Hz. To capture accurate vibration amplitudes and resonant frequencies, a curve fitting technique is adopted to process the obtained signal data. This technique can eliminate the noise components by mathematical algorithms and, hence, discriminate between the entangled signals. Figure 7.18 depicts the curve-fitted signals.

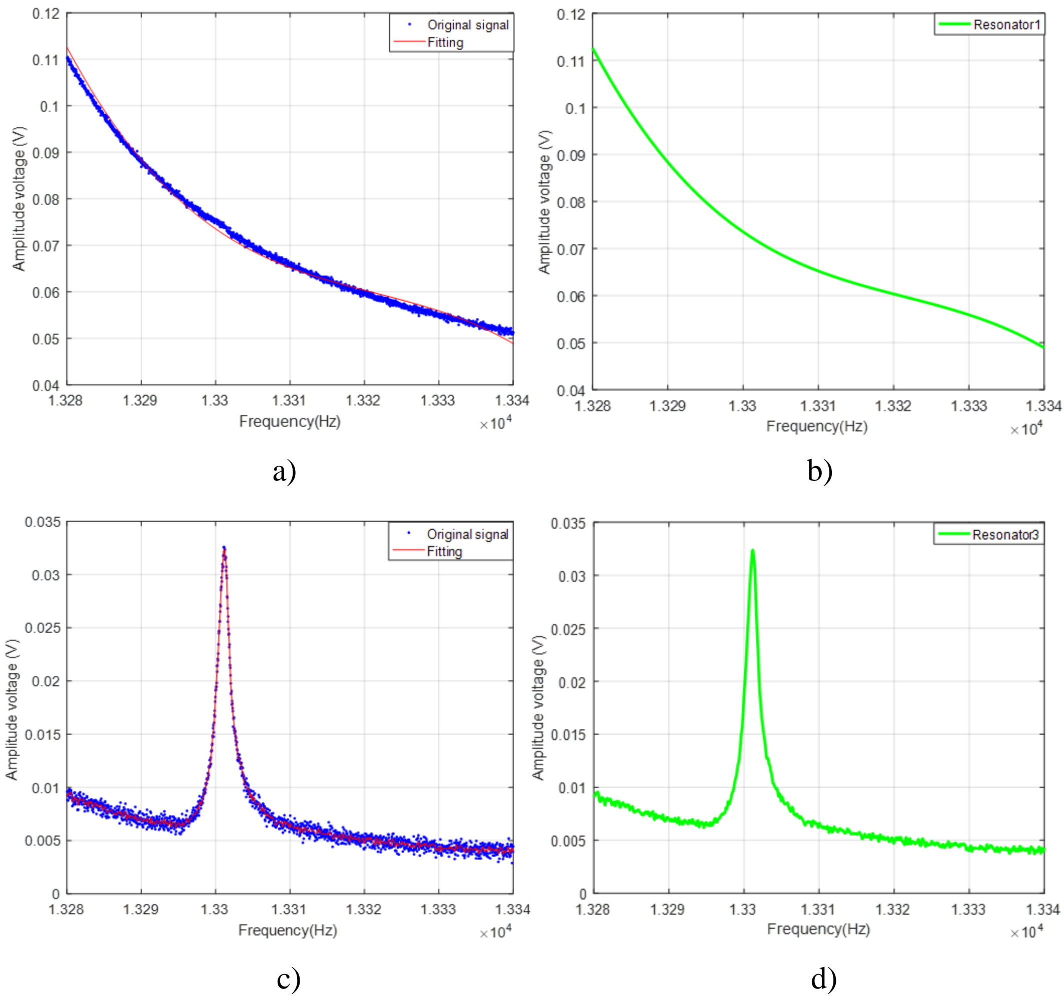

Figure 7. 18: Curve fitting technique for small stiffness perturbation experiments: a) Original data of resonator1 and polynomial fitting. b) Fitted curve of resonator1. c) Original data of resonator3 and polynomial fitting. d) Fitted curve of resonator3.

The same curve-fitting technique is applied to the data of the consecutive small stiffness perturbations. After the curve fitting procedure, the accurate out-of-phase mode frequencies, vibration amplitudes for resonator 1 and resonator 3, and their changed values due to small stiffness perturbations are obtained. Subsequently, the sensitivity in terms of resonant frequency shift and the amplitude ratio can be computed. A further comparison is performed to investigate the output metrics under the condition of small stiffness perturbations, as shown in Figure 7.19.

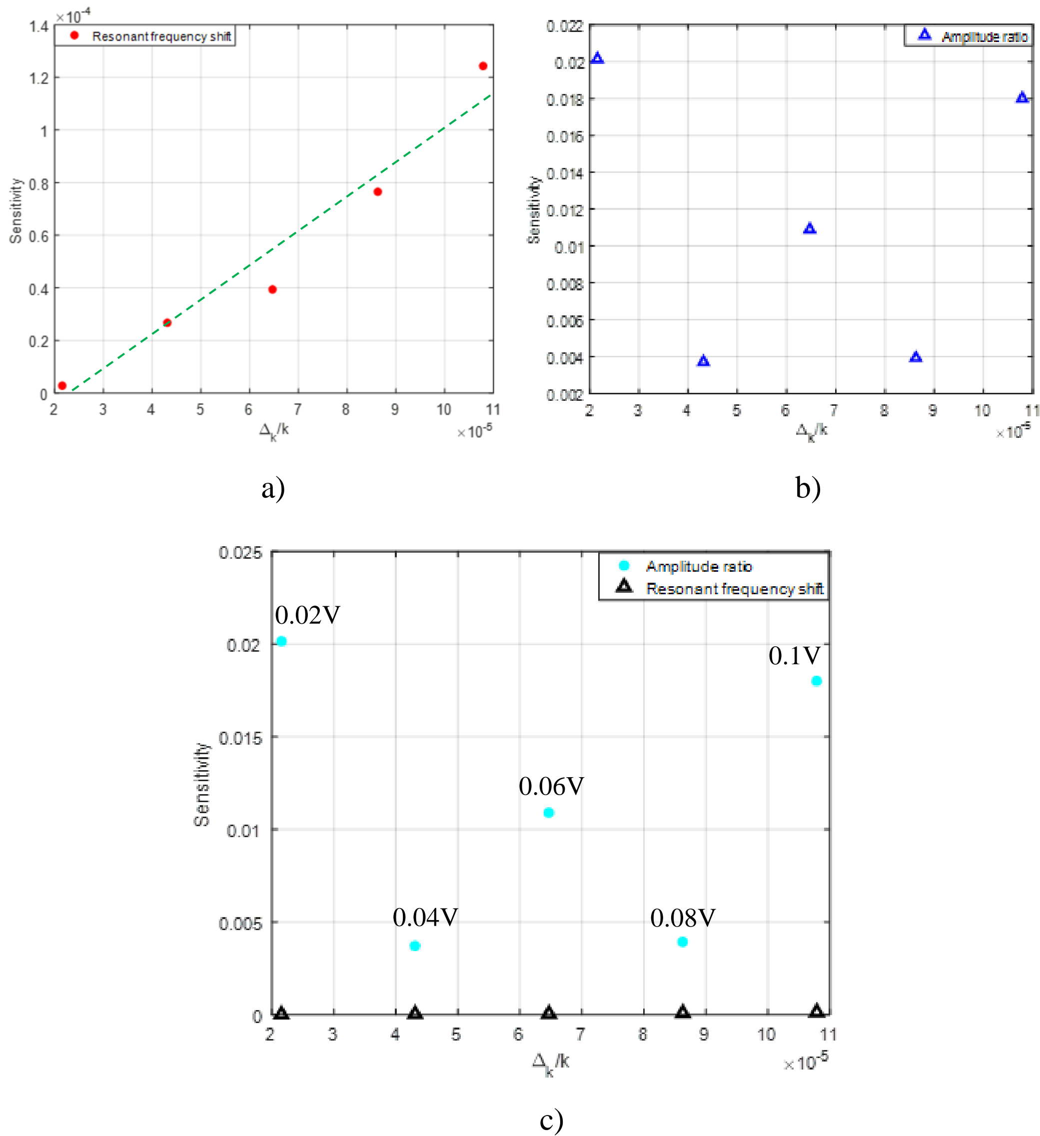

Figure 7. 19: Output metrics of 3-DOF coupled resonator with small stiffness perturbations. a) Resonant frequency shift. b) Amplitude ratio. c) Comparison of the two output metrics.

The resonant frequency shift demonstrated a linear behavior, whereas the amplitude ratio was distorted. Within the limitations of laboratory conditions, 0.02 V is the minimum DC voltage that could be achieved from the power source. Even in such conditions, resonant frequency shift as an output metric is functional but the amplitude ratio is invalid. Although the normalized sensitivity level of the amplitude ratio is higher than the resonant frequency, the resolution of the resonant frequency is superior. To verify the system functionality, experiments based on relatively large stiffness perturbations were carried out.

A short summary of these findings can be provided. Compared with amplitude ratio, resonant frequency shift as a function of small stiffness perturbations possesses superior linearity and stability and results in better limit of detection and resolution. The experiments were completed below a perturbation voltage of 0.1 V, with a step value of 0.02 V. It has been experimentally shown that amplitude ratio is not a preferred output metric to handle stiffness perturbations smaller than 0.0054 N/m (0.1 Vperb). In contrast, resonant frequency shift as an output metric can attain a minimum detection level of 0.0011 N/m (0.02 Vperb), as well as a better linear response and stability.

Nevertheless, it is not correct to assert that the resonant frequency shift has greater performance in terms of resolution. To be more specific, it is not correct to conclude that the enhancements of sensitivity achieved by the mode localization mechanism are less effective under the restriction of resolution. Firstly, the small stiffness perturbations were created by a DC power source that utilized its minimum step value. It could certainly have been affected by the instability of the power source itself; for example, transmission interferences and inaccuracy due to non-calibration. Secondly, the curve-fitting technique used in the experiments was not optimized. This technique might assist the data processing of the resonant frequency shift, but it causes errors for amplitude measurements. Thirdly, the fabrication tolerances and asymmetrical structures induced intrinsic perturbation that disturbed the vibration behavior, resulting in the absence of out-of-phase peak in resonator 1. This may have caused errors in computing the out-of-phase amplitude ratios. Finally, resonant frequency drifting due to temperature variations was mixed with resonant frequency shifts due to perturbations, thus yielding relatively better responses in comparison with the amplitude ratio, especially for small perturbations.

A further analysis based on the vibration amplitude changes was performed. The out-of-phase vibration amplitudes of resonator 3 were captured and computed as a function of normalized stiffness perturbations, as shown in Figure 7.20.

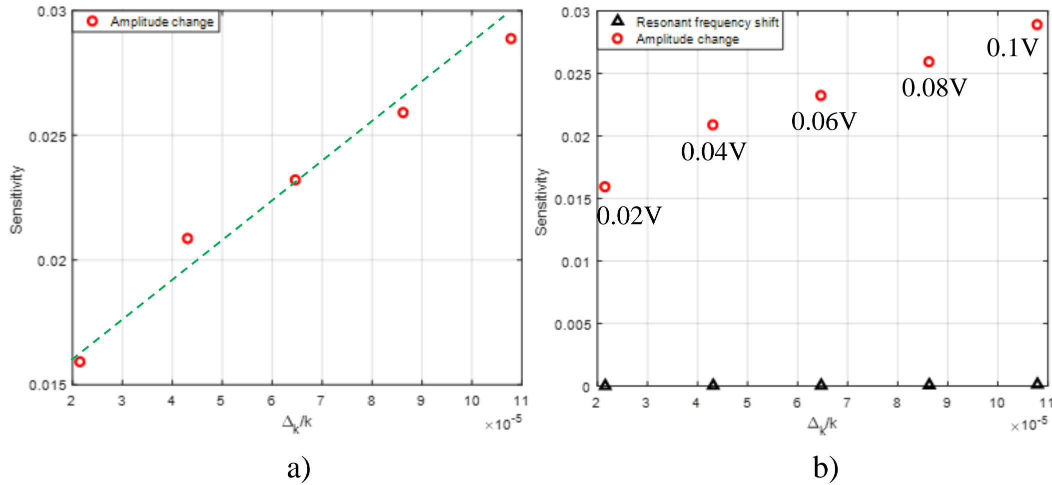

Figure 7. 20: Output metrics of 3-DOF coupled resonator with small stiffness perturbations. a) Vibration amplitude changes. b) Compared with resonant frequency shifts.

As Figure 7.20 shows, vibration amplitude change as an output metric yields greater sensitivity, around two orders of magnitude higher than that of resonant frequency shifts. Vibration amplitude changes also possess a linear response and comparable stability with resonant frequency shifts. It should be pointed out that the vibration amplitude change is another output metric based on the mode localization mechanism and is theoretically correlated with the eigenvector shifts.

Intuitively and theoretically, the mode localization mechanism (vibration amplitude changes and amplitude ratios) is superior to conventional resonant frequency shift. However, the amplitude ratio as an output metric depends on multiple factors, particularly the fabrication perfectibility and system integrality. The dependency scales with the quantity of stiffness perturbation, small perturbations requiring better conditions of the fabricated mode localized coupled resonator.

7.2 Chapter Summary

This chapter discussed three applications based on the 3-DOF mode localized coupled resonator: i) a 3-DOF mode localized coupled resonator as a mass sensor; ii) a QCM/3-DOF mode localized coupled resonator hybrid system for biosensing; and iii)

a 3-DOF mode localized coupled resonator under the condition of small stiffness perturbations. All experimental data were verified by theoretical calculations and simulations. It is experimentally shown that the 3-DOF mode localized coupled resonator has the potential to be employed as a mass or biosensor. Additionally, it can be used as a flexible platform that interacts with other MEMS components, and it can also serve as an extremely sensitive stiffness or force sensor.

Chapter 8

Future Works

8.1 3-DOF Mode Localized Weakly Coupled Resonator for Multi-Mass Detection

As discussed in chapter 3, the proposed 3-DOF coupled resonator can be employed as a stiffness change sensor or a mass change sensor. The perturbations (stiffness or mass) on resonator 1 or resonator 3 in the coupled system can be measured by exploiting the mode localization mechanism. To maximize the displacements of resonator 1 and resonator 3, the middle resonator in the 3-DOF coupled system was designed to be at least two times stiffer than the adjacent resonators.

All theoretical computations, simulations, and experiments for the 3-DOF coupled resonator were based on sensing the perturbations affecting resonator 1 or resonator 3 only. The author proposed a novel design of a 3-DOF coupled resonator, which utilizes two of the three resonators to accomplish multi-mass detection.

8.1.1 Theoretical Analysis

In terms of structure, some adjustments had to be made to the original 3-DOF coupled resonator, resulting in the use of three identical resonators; the middle resonator is no longer stiffer. Accordingly, the system equations of motion can be expressed as:

$$M\ddot{X}1(t) + b1\dot{X}1(t) + (K + Kc)X1(t) - KcX2(t) = F1\,(t) \qquad (8.63)$$

$$(M + \Delta M_2)\ddot{X}2(t) + b2\dot{X}2(t) + (K + 2Kc)X2(t) \\ -Kc(X1(t) + X3(t)) = F2(t) \tag{8.64}$$

$$(M + \Delta M_1)\ddot{X}3(t) + b3\dot{X}3(t) + (K + Kc)X3(t) - KcX2(t) = F3(t) \tag{8.65}$$

Two independent mass perturbations are applied on resonator 2 and resonator 3. The equations of motion can be re-written in a matrix form and hence can be solved using an eigenstates computation method. The damping coefficients b1, b2, and b3 are disregarded in the following equations, allowing the derivation of expressions for the vibration amplitudes, amplitude ratios, and mode frequencies of the multi-mass sensing system.

$$\lambda_n \begin{bmatrix} M & 0 & 0 \\ 0 & M + \Delta M_2 & 0 \\ 0 & 0 & M + \Delta M_1 \end{bmatrix} \begin{bmatrix} u_{\lambda_n 1} \\ u_{\lambda_n 2} \\ u_{\lambda_n 3} \end{bmatrix} \\ = \begin{bmatrix} K + Kc & -Kc & 0 \\ -Kc & K + 2Kc & -Kc \\ 0 & -Kc & K + Kc \end{bmatrix} \begin{bmatrix} u_{\lambda_n 1} \\ u_{\lambda_n 2} \\ u_{\lambda_n 3} \end{bmatrix} \tag{8.66}$$

The plotted mode frequencies as a function of mass perturbations (two independent mass perturbations) and the amplitude ratio versus the same mass perturbations are illustrated in Figure 8.1.

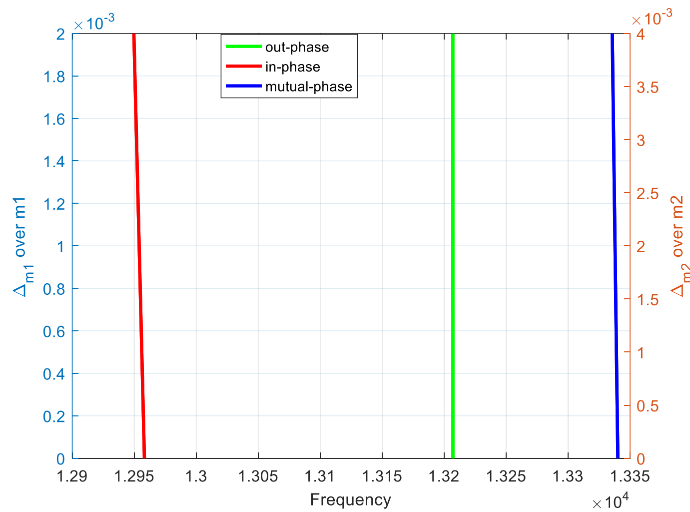

a)

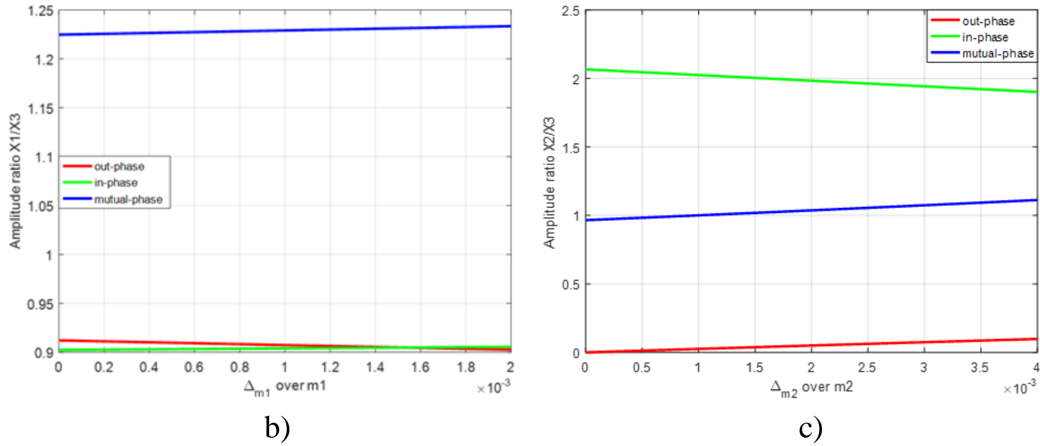

Figure 8. 1: Theoretical analysis of a 3-DOF mode localized coupled resonator for multi-mass detection. a) Mode frequencies versus two independent mass perturbations on resonator 2 and resonator 3 respectively. b) Amplitude ratio (resonator1/resonator3) versus mass perturbations of resonator3. c) Amplitude ratio (resonator2/resonator3) versus mass perturbations of resonator2.

The mutual-phase in the theoretical calculations represented the third vibration mode, in which each resonator vibrates out-of-phase with others.

8.1.2 Simulations

System responses of the 3-DOF coupled resonator for multi-mass detection can be simulated using the models from chapter 4. A first group of simulations are carried out to determine the system behavior under five consecutive mass perturbations (10 ng to 50 ng) of resonator 3, as shown in Figure 8.2.

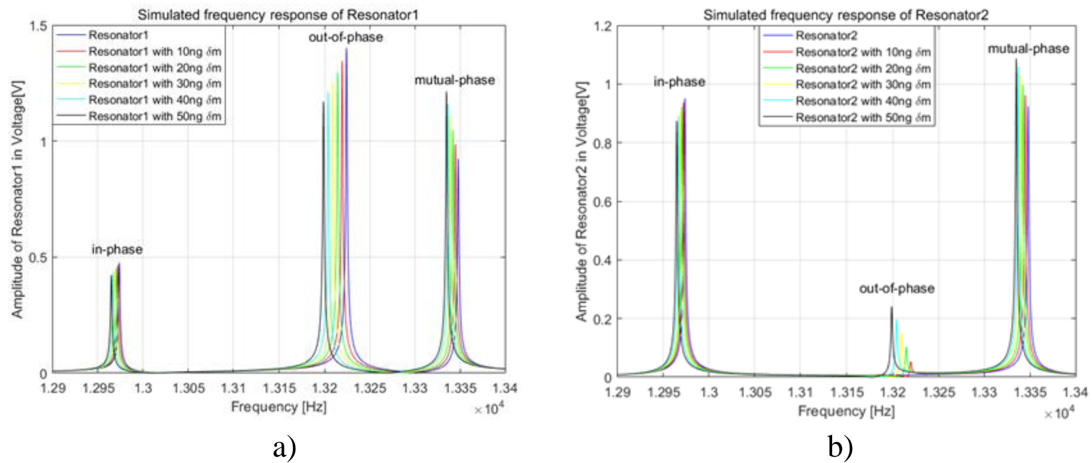

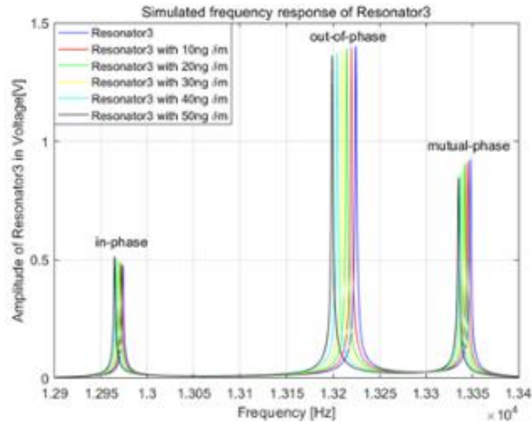

c)

The vibration amplitudes of all three resonators are obtained. Each resonator has three vibrational peaks denoting the corresponding vibration mode and the correlated mode frequency. The Amplitude ratios of resonator 1/resonator 3 & resonator 2/resonator 3 as a function of resonator3 mass perturbations hence can be computed.

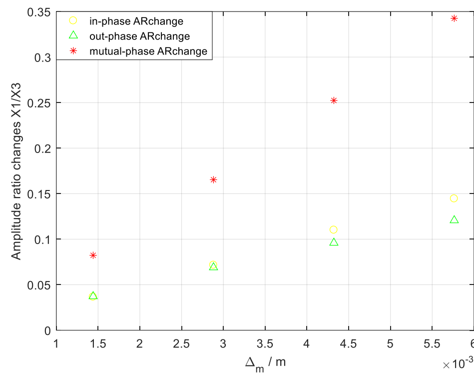

d)

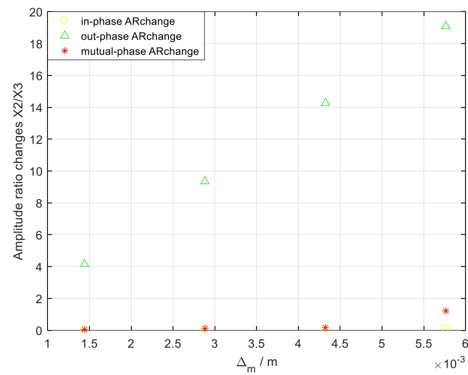

e)

Figure 8. 2: Simulated responses of multi-mass detection (only resonator3 has mass perturbations): a) Resonator1. b) Resonator2. c) Resonator3. d) Amplitude ratio change of resonator1/resonator3. e) Amplitude ratio change of resonator2/resonator3.

In what follows, resonator 2 has been subjected to five consecutive mass perturbations (20 ng to 100 ng, in 20 ng steps), and resonator 3 has concurrently been subjected to another five consecutive mass perturbations (10 ng to 50 ng, in 10 ng steps). The amplitude ratio changes are plotted and then compared with the previous resonator 3 mass perturbations case, as illustrated in Figure 8.3.

Evidently, the amplitude ratio changes in term of resonator 1/resonator 3 and resonator 2/resonator 3 both demonstrated value shifts in response to different mass perturbations on resonator 2. More specific, after the first group of perturbations on resonator 3, second group of perturbations on resonator 2 will alter the system behavior again.

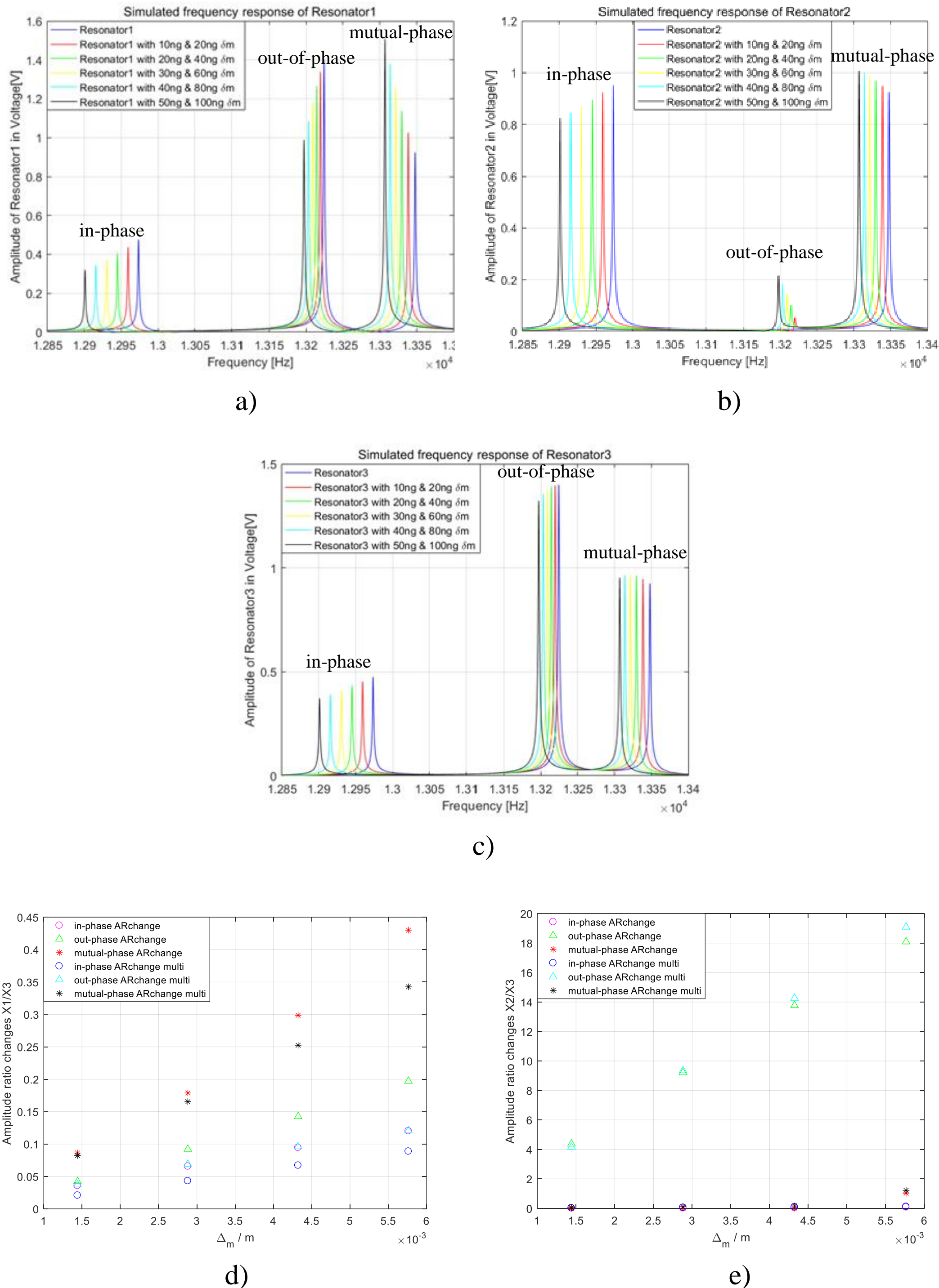

Figure 8. 3: Simulated responses of multi-mass detection (both resonator2 & resonator3 have independent mass perturbations): a) Resonator1. b) Resonator2. c) Resonator3. d) Amplitude ratio change of resonator1/resonator3. e) Amplitude ratio change of resonator2/resonator3. The label named multi indicates multi-mass perturbations.

It is intriguing to observe the tendency of amplitude ratio changes in terms of resonator 1 and resonator 3 and of resonator 2 and resonator 3. With mass perturbations on both resonator 2 and resonator 3, the amplitude ratio changes of resonator 1 and

resonator 3 for all vibration modes shifted to lower values. In contrast, the amplitude ratio changes of resonator 2 and resonator 3 for all vibration modes shifted to higher values. Figure 8.4 shows a COMSOL model of the vibration behavior of multi-mass perturbations.

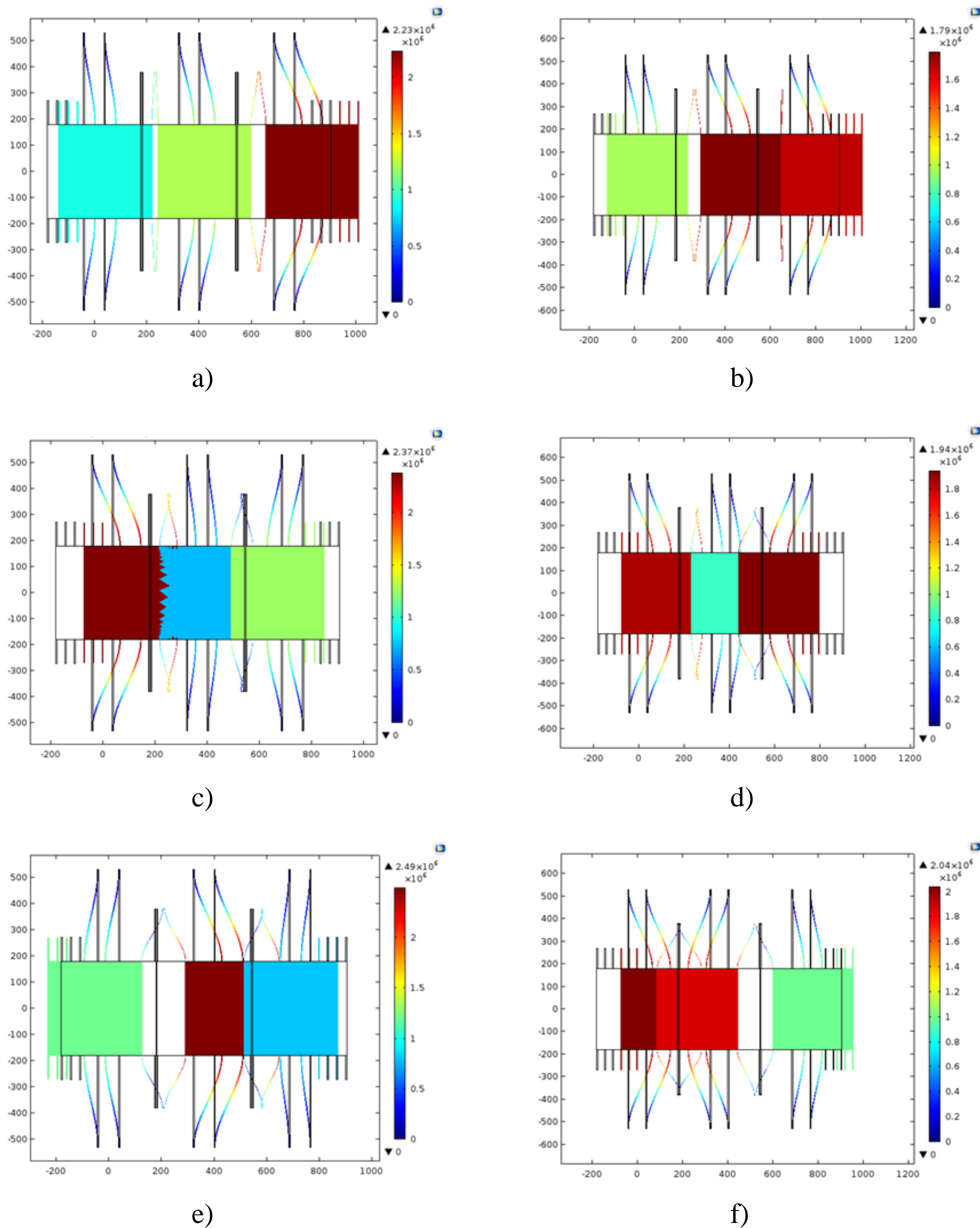

Figure 8. 4: COMSOL simulation of a 3-DOF coupled resonator for multi-mass detection. a), c), e) Only resonator3 has mass perturbation; b), d), f) Both resonator2 and resonator3 have mass perturbations.

All the simulations provided reliable evidence that the 3-DOF coupled resonator

can be employed as a multi-mass detection sensor. Qualitatively, the tendency of amplitude ratio changes can be used to determine whether there are mass perturbations on either resonator 2 or resonator 3. Quantitatively, the shifted values of amplitude ratio changes can be used to calculate the amount of added mass perturbations on resonator 2, resonator 3, or both.

Accordingly, such a 3-DOF coupled resonator multi-mass detection sensor can be further developed to handle multi-biomolecule sensing tasks. Figure 8.5 depicts a multi-analyte biosensor using the 3-DOF coupled resonator.

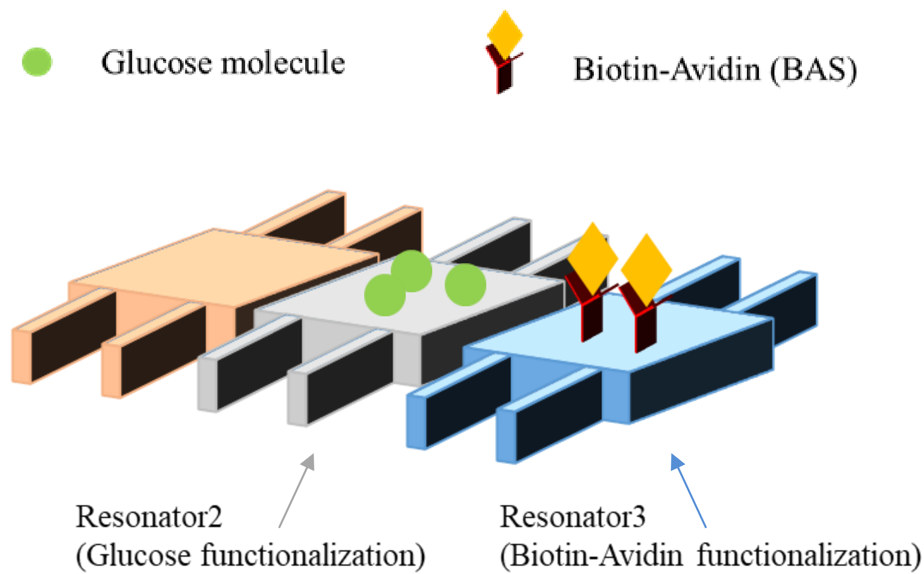

Figure 8. 5: 3-DOF coupled resonator as a multi-analyte biosensor.

Future research in this direction will constitute an important step towards developing a biosensor that can not only exploit the advantages of mode localized coupled resonators but also perform mixed-sample detections; for example, a multi-analyte blood test.

8.2 3-DOF Mode Localized Weakly Coupled Resonator with Embedded Micro-channel

Another possible approach to the design of 3-DOF mode localized coupled resonators is embedded micro-channels (EMC). Although this approach requires

adequate fabrication technology, it is certainly a feasible way of improving the original 3-DOF coupled resonator design (in particular, it could overcome the drawback of a damped environment). The embedded micro-channels approach has already been experimentally proved [136]. Figure 8.6 depicts a resonator with embedded micro-channels in the 3-DOF coupled resonator system.

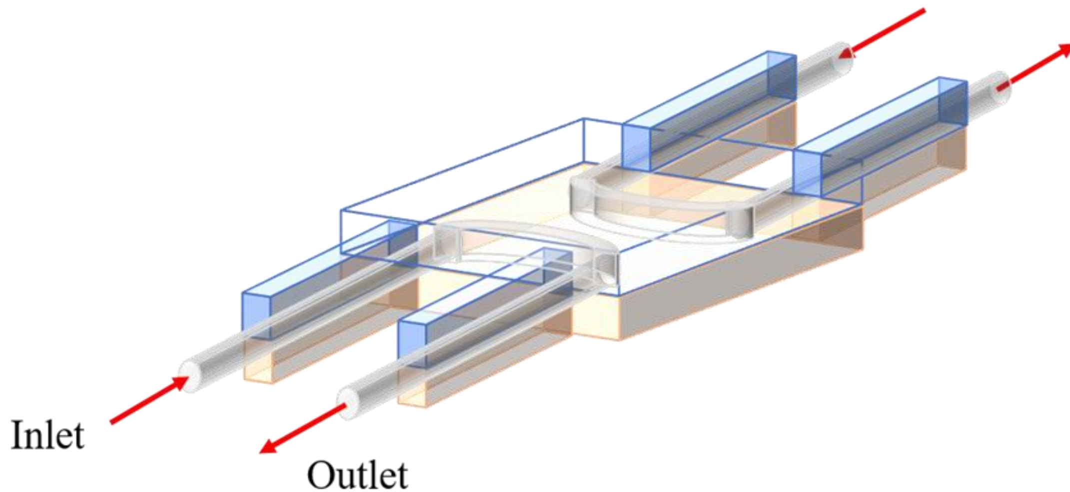

Figure 8. 6: A resonator with embedded micro-channels (EMC).

Two possible ways of designing of an EMC 3-DOF coupled resonator are proposed: i) grow mesoporous silica on the side walls of the micro-channels and exploit the mesoporous property to perform biochemical sensing; ii) utilize magnetic nanoparticles that flow in the micro-channels as a magnetic medium. In ii), when the device is exposed in a magnetic field, the magnetic nanoparticles are attracted by the external magnetic field and hence generate magnetic forces that perturb the coupled system. In summary, EMC technology can enhance the performance of 3-DOF mode localized coupled resonators as biochemical sensors or as physical sensors.

8.3 Research Questions and Future Directions

Although some possible areas for future works have been proposed in the aforementioned sections, research questions raised by present results can render valuable information and guide the future directions of this topic.

Firstly, all the experiments so far were based on open-loop configurations, where the frequency responses from coupled resonator system were extracted by exploiting Lock-in amplifier. The vibration amplitudes and corresponding mode frequencies were garnered via frequency sweep function in the Lock-in amplifier. This greatly extended the system operation time and caused a time consuming procedure to obtain the desired parameters. In practical, some applications require the sensor system to response the rapid changing perturbations, which is obviously an impact to the open-loop configuration. Consequently, a close loop system for the multi-DOF mode localized coupled resonators is demanded. In order to monitor the multi-DOF mode localized coupled resonator in real-time, efforts toward to capture the vibration amplitudes are necessary, rather than focusing on the resonance mode frequencies. An integrated algorithm to direct compute amplitude ratios could potentially benefit the performance of the close-loop system. In these circumstances, a proper designed self-oscillating electronic circuitry in combination with analogue and digital components is a feasible starting point.

Additionally, it could be an intriguing work to experimentally study the common mode rejection ability of the proposed multi-DOF coupled resonators. Especially, in some biosensing applications, humidity and temperature can potentially affect the results.

Ultimately, it will always be an interesting topic to explore the possibility of other materials for the MEMS sensors, such as graphene.

8.4 Chapter Summary

This chapter introduces two potential applications of the 3-DOF coupled resonator. The multi-mass detection application requires experimental verification. An additional fabrication process is needed to develop a modified 3-DOF coupled resonator with three identical resonators. The mass sensitivity characterization method that exploits magnetic nanoparticles can be adopted to subject resonator 2 and resonator 3 to two

independent mass perturbations. Future research will determine the practical application of multi-mass detection. The EMCs on the other hand, require more effort in fabrication as well as modifications in device structure and experiment designs.

Chapter 9

Conclusions

9.1 Research Contributions and Novelties

This research introduces the use of a novel 3-DOF electrostatic weakly coupled resonator as a mass sensor. Using mode localization, the system sensitivity has been improved by orders of magnitude over conventional resonant frequency-shift based sensors. In the mode localization scheme, eigenvector shift (correlated with vibration amplitude change) was used as one sensing metric that significantly improved the sensitivity. The amplitude ratio provided even greater sensitivity, as well as high common mode noise rejection.

The contributions of this research were divide into five sections. Firstly, the 3-DOF weakly coupled resonator was studied by mathematical computations. The eigenstate method was introduced to solve the system equations of motion, and hence obtain the vibration mode shapes and corresponding mode frequencies. General expressions of mode frequency, vibration amplitude, and amplitude ratio were all deduced. All expressions were also reformed either for stiffness perturbation or for mass perturbation. Normalized sensitivities as a function of stiffness and mass perturbations were derived accordingly.

Secondly, three different simulation models were established to verify the 3-DOF weakly coupled resonator behavior. A novel Simulink/MATLAB model offered an accurate, fast, and flexible system-level simulation for any proposed multi-DOF coupled resonator. Compared with the eigenstate method, the Simulink/MATLAB

model involved complex parameters such as the damping coefficient, non-linearity, and noise sources. Unlike COMSOL models or equivalent RLC circuit models, which depend on either mesh precisions or definitions of electronic components, the Simulink/MATLAB model was based on system transfer functions and was therefore more accurate.

Thirdly, several aspects of the system were investigated, such as mode aliasing, damping influences, and coupling strength. The 3-DOF coupled resonator as a mass sensor under atmospheric pressure was developed using the created simulation models. The simulation results showed that the 3-DOF coupled resonator was able to handle mass and biosensing tasks, whereas the damped environment (low Q-factor) resulted in a reduction of functionality.

Fourthly, in order to overcome the problems of the damped environment, two novel designs were proposed: a QCM mass sensor incorporated with a 3-DOF coupled resonator stiffness sensor, and a 2-DOF coupled BAW disk resonator. Both of the designs were studied theoretically and verified by different simulation methods.

Finally, a novel reversible and controllable mass perturbation technique was proposed. By adopting magnetic nanoparticles and a micro-plotter machine, consecutive mass perturbations were attained. The magnetic property of the nanoparticles was utilized to achieve reversible measurements. This technique is a universal solution that could be used in any MEMS mass sensor.

9.2 Practical Works

The 3-DOF coupled resonator and the 2-DOF coupled BAW resonator were fabricated by three different SOI based processes: two steps of release, dry release and a dicing-free technique, and a dicing-free technique that exploits a carrier wafer. The fabricated devices were firstly bonded and packaged, then mounted on designed PCBs. The experimental data were acquired via a lock-in amplifier, and further data processing was completed on a PC. Experiments in the vacuum environment were conducted under 8.8×10^{-6}mbar conditions.

The mass sensitivity characterization for the 3-DOF coupled resonator was carried out under atmospheric pressure. Magnetic nanoparticles were prepared and dispensed according to an organized operation protocol. The experiment results agreed well with those of the simulation model, and reversibility was demonstrated by removing the dispensed nanoparticles properly. Although the 3-DOF coupled resonator did not render the highest level of mass sensitivity in terms of resonant frequency shift, by exploiting mode localization it can still surpass most existing MEM mass sensors. This work constitutes an important step towards realizing a high-sensitivity biosensor for concentration measurement using a mode localized sensor operating in air.

The QCM/3-DOF coupled resonator hybrid system was tested by dispensing consecutive masses onto the QCM mass sensor. The added masses were realized by the deposition of magnetic nanoparticles. The AC output signals from the QCM were converted into DC voltages and then fed to the 3-DOF coupled resonator as electrostatic forces based stiffness perturbations. The QCM mass sensor operated in air, while the 3-DOF coupled resonator was placed in vacuum. The experiment results agreed well with those of the simulation models. Future work based on this research will constitute an important step towards a biochemical sensor that can exploit the advantages of a mode localized coupled resonator and yet work directly in contact with a liquid.

The detection limit of stiffness perturbations for the 3-DOF coupled resonator was investigated under laboratory conditions. Experiments demonstrated that resonant frequency shift exhibited better resolution than amplitude ratio for perturbation voltages smaller than 0.1 V. This was mainly due to the fabrication tolerance and asymmetrical structures. However, the conclusion was still open, particularly another mode localization metric: vibration amplitude change exhibited superiority in terms of resolution and sensitivity. Further research is needed to explore the resolution of different output metrics, and a comprehensive noise analysis is essential.

Appendix A

Interface Circuit PCB

To perform signal collection and processing, different interface circuit designs were included in this research topic. According to the sensing schemes and the configurations of the proposed multi-DOF coupled resonators, types of PCB layouts were developed. Since the principle of interface circuit design has already been introduced in chapter 6, this section covers the created PCB layouts, as exhibited in Figure A.1.

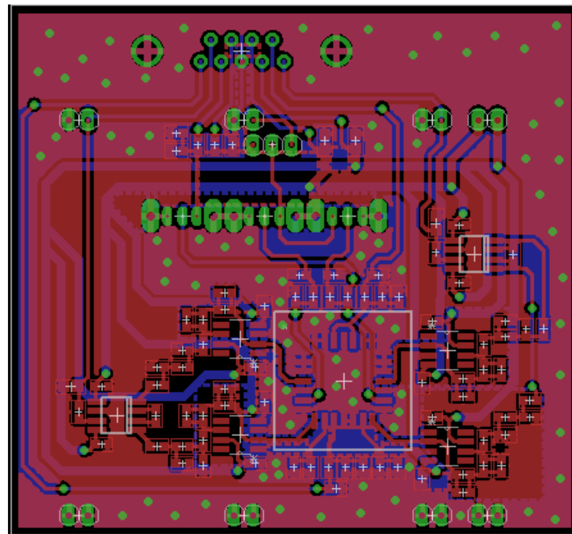

a)

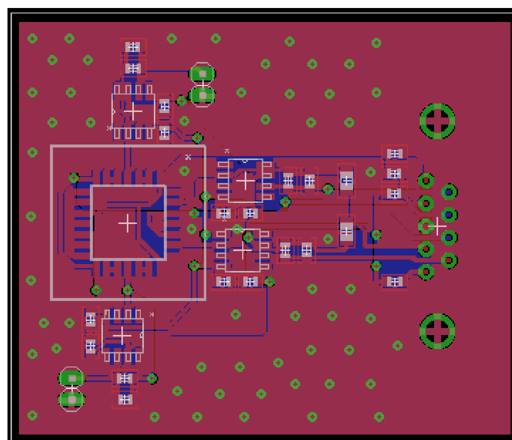

b)

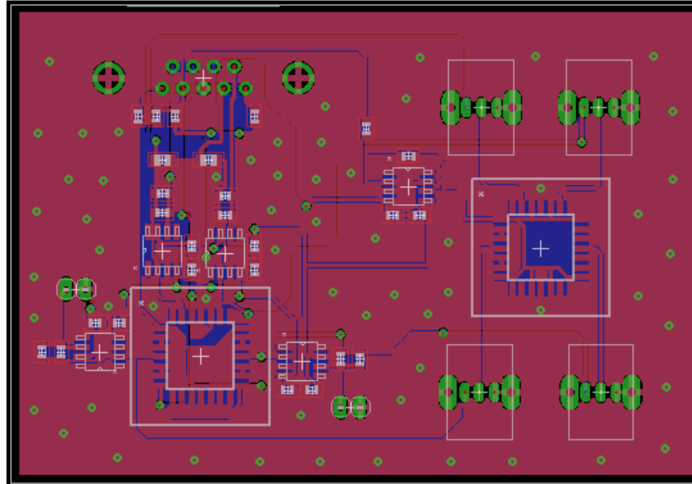

c)

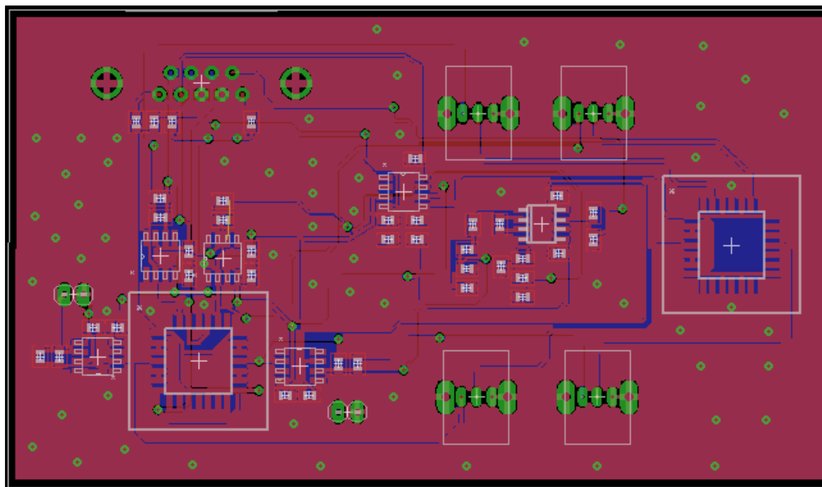

d)

Figure A. 1: PCB layouts of the multi-DOF coupled resonator interface circuits. a) PCB layout of the 3-DOF coupled resonator interface circuit. b) PCB layout of the 2-DOF BAW coupled resonator interface circuit that exploits variable capacitor for feedthrough compensation. c) PCB layout of the 2-DOF BAW coupled resonator interface circuit that exploits dummy MEMS for feedthrough compensation. d) PCB layout of the 2-DOF BAW coupled resonator interface circuit that exploits dummy MEMS & differential scheme for feedthrough compensation.

Appendix B

Bonding and Packaging

The fabricated multi-DOF coupled resonators were first glued in proper chip carriers, subsequently a TPT HB-16 semi-automatic wire bonder machine was employed to perform wire bonding tasks. The wire bonding materials and parameters are listed in Table B.1.

Parameter Names	*Parameter Values/Materials*
Glue	SMD
Wires	Aluminum 18 μm diameters
Type of welding	Wedge
Bonding mechanism	Thermo-ultrasonic
Operating mode	Manual

Table B. 1: Wire bonding materials and parameters.

Two types of chip carriers were adopted in this work: i) 28-pin Au plated J-lead carrier (SSM P/N CCJ02803) which were commercialized from Spectrum-Semiconductor Materials, inc. ii) Self designed 28-pin carrier. Bonding diagrams for different multi-DOF coupled resonator designs are demonstrated in Figure B.1.

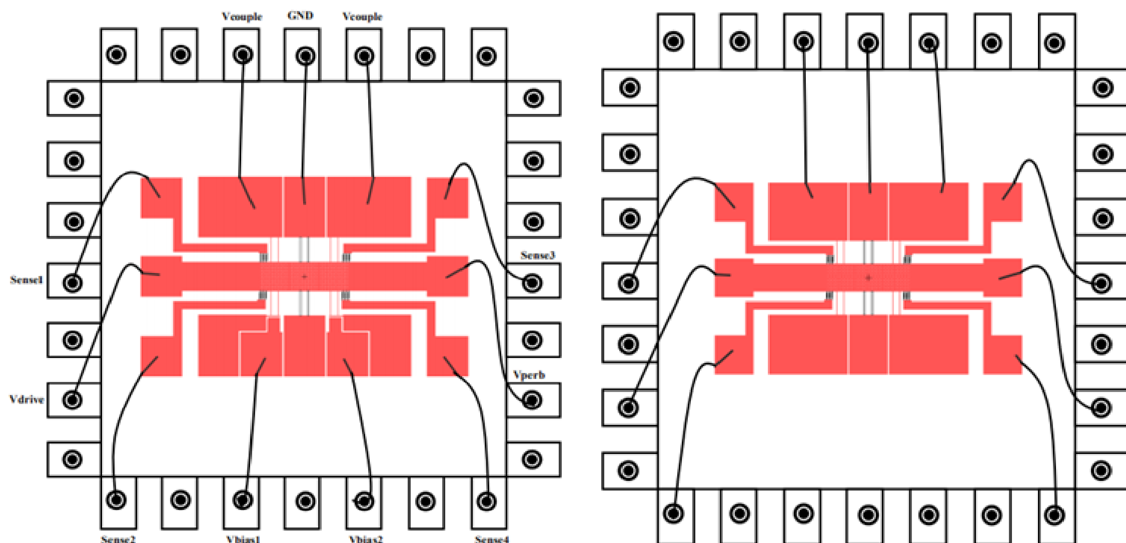

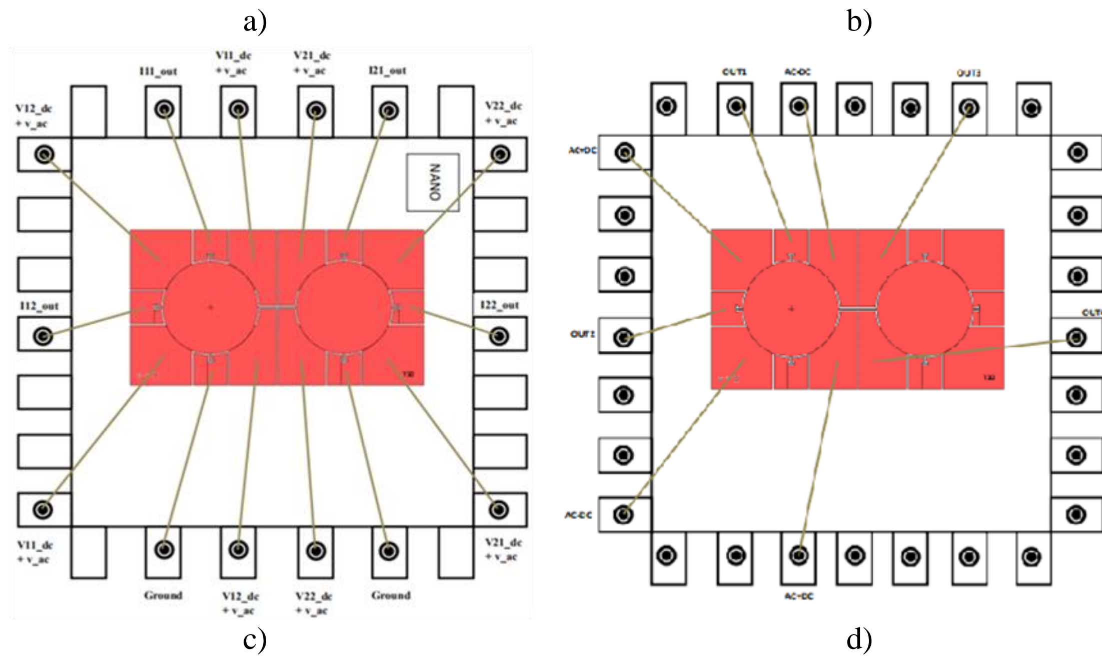

Figure B. 1: Wire bonding diagrams. a) 3-DOF coupled resonator with bias ports bonded. b) 3-DOF coupled resonator without bias port. c) 2-DOF coupled BAW resonator 2-ports differential sensing scheme. d) 2-DOF coupled BAW resonator 1-port sensing scheme.

The actual bonded coupled resonator chips are illustrated in Figure B.2.

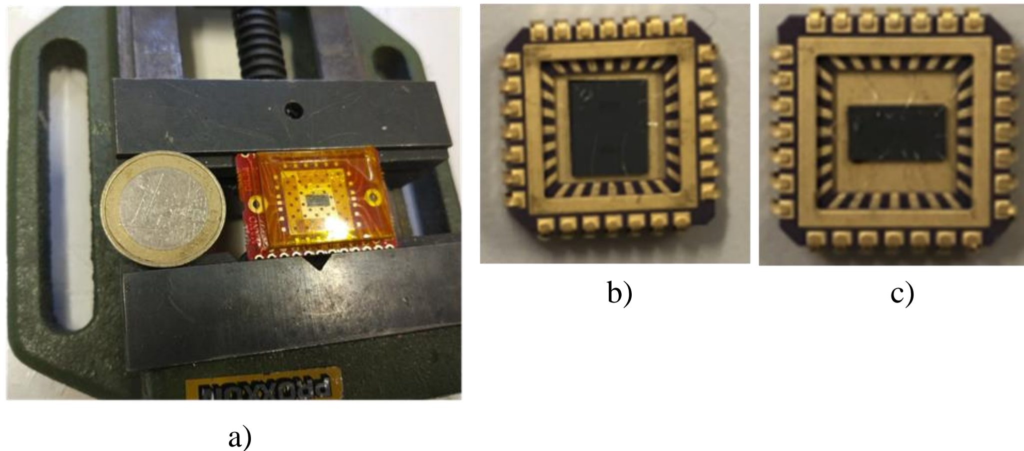

Figure B. 2: Actual bonded coupled resonator chips. a) DIY 28-pin carrier. b) 28-pin J-lead carrier, 3-DOF coupled resonator. c) 28-pin J-lead carrier, 2-DOF coupled BAW resonator.

Appendix C

Publication List

Journal Publications:

- **Y. Wang**, C. Zhao, C. Wang, D. Cerica, M. Baijot, Q. Xiao, et al., "A mass sensor based on 3-DOF mode localized coupled resonator under atmospheric pressure," Sensors and Actuators A: Physical, vol. 279, pp. 254-262, 2018.

- Q. Xiao, **Y. Wang**, S. Dricot, and M. Kraft, "Design and experiment of an electromagnetic levitation system for a micro mirror," Microsystem Technologies, pp. 1-10, 2019.

- D. Tsikritsis, H. Shi, **Y. Wang**, S. Velugotla, V. Sršeň, A. Elfick, et al., "Label-free biomarkers of human embryonic stem cell differentiation to hepatocytes," Cytometry Part A, vol. 89, pp. 575-584, 2016.

Conference Proceedings:

- **Y. Wang**, C. Wang, C. Zhao, H. Liu, D. Cerica, M. Baijot, et al., "A Novel Qcm Mass Sensing System Incorporated with A 3-Dof Mode Localized Coupled Resonator Stiffness Sensor," in 2019 20th International Conference on Solid-State Sensors, Actuators and Microsystems & Eurosensors XXXIII (TRANSDUCERS & EUROSENSORS XXXIII), 2019, pp. 1823-1826.

- **Y. Wang**, C. Zhao, C. Wang, D. Cerica, M. Baijot, V. Pachkawade, et al., "A Reversible Method to Characterize the Mass Sensitivity of a 3-Dof Mode Localized Coupled Resonator under Atmospheric Pressure," in Multidisciplinary Digital Publishing Institute Proceedings, 2017, p. 493.

- C. Wang, H. Liu, **Y. Wang**, X. Song, J. Bai, and M. Kraft, "Genetic algorithm for electro-mechanical co-optimization of a MEMS accelerometer comprising a mechanical motion pre-amplifier with a 2nd-order sigma delta modulator," in Proc. DTIP, 2019, pp. 1-4.

- C. Wang, H. Liu, X. Song, F. Chen, I. Zeimpekis, **Y. Wang**, et al., "Genetic

Algorithm for the Design of Freeform Geometries in a MEMS Accelerometer Comprising a Mechanical Motion Pre-Amplifier," in 2019 20th International Conference on Solid-State Sensors, Actuators and Microsystems & Eurosensors XXXIII (TRANSDUCERS & EUROSENSORS XXXIII), 2019, pp. 2099-2102.

References

[1] H. C. Nathanson, W. E. Newell, R. A. Wickstrom, and J. R. Davis, "The resonant gate transistor," *IEEE Transactions on Electron Devices,* vol. 14, pp. 117-133, 1967.

[2] K. E. Petersen, "Silicon as a mechanical material," *Proceedings of the IEEE,* vol. 70, pp. 420-457, 1982.

[3] B.-H. Kim, S.-I. Kim, J.-C. Lee, S.-J. Shin, and S.-J. Kim, "Dynamic characteristics of a piezoelectric driven inkjet printhead fabricated using MEMS technology," *Sensors and Actuators A: Physical,* vol. 173, pp. 244-253, 2012.

[4] P. F. Van Kessel, L. J. Hornbeck, R. E. Meier, and M. R. Douglass, "A MEMS-based projection display," *Proceedings of the IEEE,* vol. 86, pp. 1687-1704, 1998.

[5] L. J. Hornbeck, "Current status of the digital micromirror device (DMD) for projection television applications," in *Electron Devices Meeting, 1993. IEDM'93. Technical Digest., International*, 1993, pp. 381-384.

[6] C.-C. Nguyen, "Micromechanical resonators for oscillators and filters," in *Ultrasonics Symposium, 1995. Proceedings., 1995 IEEE*, 1995, pp. 489-499.

[7] P. Stephanou, G. Piazza, C. White, M. Wijesundara, and A. Pisano, "Mechanically coupled contour mode piezoelectric aluminum nitride MEMS filters," in *Micro Electro Mechanical Systems, 2006. MEMS 2006 Istanbul. 19th IEEE International Conference on*, 2006, pp. 906-909.

[8] J. E.-Y. Lee, B. Bahreyni, Y. Zhu, and A. A. Seshia, "A single-crystal-silicon bulk-acoustic-mode microresonator oscillator," *IEEE Electron Device Letters,* vol. 29, pp. 701-703, 2008.

[9] D. Peroulis, S. Pacheco, K. Sarabandi, and P. Katehi, "MEMS devices for high isolation switching and tunable filtering," in *Microwave Symposium Digest. 2000 IEEE MTT-S International*, 2000, pp. 1217-1220.

[10] M. A. Schmidt and R. T. Howe, "Silicon resonant microsensors," in *14th Automotive Materials Conference: Ceramic Engineering and Science Proceedings*, 1987, pp. 1019-1034.

[11] G. Binnig, C. F. Quate, and C. Gerber, "Atomic force microscope," *Physical review letters,* vol. 56, p. 930, 1986.

[12] A. N. Cleland and M. L. Roukes, "A nanometre-scale mechanical electrometer," *Nature,* vol. 392, pp. 160-162, 1998.

[13] B. Bahreyni and C. Shafai, "A resonant micromachined magnetic field sensor," *IEEE Sensors Journal,* vol. 7, pp. 1326-1334, 2007.

[14] H. Johari and F. Ayazi, "Capacitive bulk acoustic wave silicon disk gyroscopes,"

in *Electron Devices Meeting, 2006. IEDM'06. International*, 2006, pp. 1-4.

[15] D. Christensen, C. Ahn, V. Hong, E. Ng, Y. Yang, B. Lee*, et al.*, "Hermetically encapsulated differential resonant accelerometer," in *Solid-State Sensors, Actuators and Microsystems (TRANSDUCERS & EUROSENSORS XXVII), 2013 Transducers & Eurosensors XXVII: The 17th International Conference on*, 2013, pp. 606-609.

[16] X. Zou and A. Seshia, "Non-linear frequency noise modulation in a resonant MEMS accelerometer," *IEEE Sensors Journal,* 2017.

[17] F. Chen, X. Li, and M. Kraft, "Electromechanical Sigma–Delta Modulators ($\Sigma\Delta {\mathrm {M}} $) Force Feedback Interfaces for Capacitive MEMS Inertial Sensors: A Review," *IEEE Sensors Journal,* vol. 16, pp. 6476-6495, 2016.

[18] V. Qaradaghi, M. Mahdavi, V. Kumar, and S. Pourkamali, "Frequency output MEMS resonator on membrane pressure sensors," in *SENSORS, 2016 IEEE*, 2016, pp. 1-3.

[19] H. Zhang, M. S. Marma, S. K. Bahl, E. S. Kim, and C. E. McKenna, "Sequence specific label-free DNA sensing using film-bulk-acoustic-resonators," *IEEE Sensors Journal,* vol. 7, pp. 1587-1588, 2007.

[20] H.-S. Liao, K.-Y. Huang, and C.-S. Chang, "Cantilever-based mass sensor using high order resonances for liquid environment," in *Advanced Intelligent Mechatronics (AIM), 2011 IEEE/ASME International Conference on*, 2011, pp. 652-655.

[21] M. Spletzer, A. Raman, A. Q. Wu, X. Xu, and R. Reifenberger, "Ultrasensitive mass sensing using mode localization in coupled microcantilevers," *Applied Physics Letters,* vol. 88, p. 254102, 2006.

[22] P. S. Thakur, K. Sugano, T. Tsuchiya, and O. Tabata, "Study on Vibration-coupling Control of Out-of-plane Coupled Resonator for Anti-shock Tuning Fork Gyroscopes," *IEEJ Transactions on Sensors and Micromachines,* vol. 134, pp. 392-399, 2014.

[23] P. W. Anderson, "Absence of diffusion in certain random lattices," *Physical review,* vol. 109, p. 1492, 1958.

[24] C. Zhao, G. S. Wood, J. Xie, H. Chang, S. H. Pu, H. M. Chong*, et al.*, "A sensor for stiffness change sensing based on three weakly coupled resonators with enhanced sensitivity," in *Micro Electro Mechanical Systems (MEMS), 2015 28th IEEE International Conference on*, 2015, pp. 881-884.

[25] C. Zhao, M. H. Montaseri, G. S. Wood, S. H. Pu, A. A. Seshia, and M. Kraft, "A review on coupled MEMS resonators for sensing applications utilizing mode localization," *Sensors and Actuators A: Physical,* vol. 249, pp. 93-111, 2016.

[26] M. H. Montaseri, J. Xie, H. Chang, Z. Chao, G. Wood, and M. Kraft, "Atmospheric pressure mode localization coupled resonators force sensor," in *Solid-State Sensors, Actuators and Microsystems (TRANSDUCERS), 2015 Transducers-2015 18th International Conference on*, 2015, pp. 1183-1186.

[27] H. Kang, J. Yang, and H. Chang, "A mode-localized accelerometer based on four degree-of-freedom weakly coupled resonators," in *2018 IEEE Micro*

Electro Mechanical Systems (MEMS), 2018, pp. 960-963.
[28] P. Pai, F. Chowdhury, C. H. Mastrangelo, and M. Tabib-Azar, "MEMS-based hemispherical resonator gyroscopes," in *Sensors, 2012 IEEE*, 2012, pp. 1-4.
[29] Y. Hui, T. Nan, N. X. Sun, and M. Rinaldi, "High resolution magnetometer based on a high frequency magnetoelectric MEMS-CMOS oscillator," *Journal of Microelectromechanical Systems,* vol. 24, pp. 134-143, 2015.
[30] M. H. Hasan, F. M. Alsaleem, and H. M. Ouakad, "Novel threshold pressure sensors based on nonlinear dynamics of MEMS resonators," *Journal of Micromechanics and Microengineering,* vol. 28, p. 065007, 2018.
[31] S. Pallavi and A. A. Prince, "RF MEMS-based biosensor for pathogenic bacteria detection," *BioNanoScience,* vol. 3, pp. 321-328, 2013.
[32] W. C. Young and R. G. Budynas, *Roark's formulas for stress and strain* vol. 7: McGraw-Hill New York, 2002.
[33] V. Kaajakari, "Practical MEMS: Design of microsystems, accelerometers, gyroscopes, RF MEMS, optical MEMS, and microfluidic systems," *Las Vegas, NV: Small Gear Publishing,* 2009.
[34] T. Lalinský, E. Burian, M. Drzik, S. Hascik, Z. Mozolová, and J. Kuzmík, "Thermal actuation of a GaAs cantilever beam," *Journal of micromechanics and Microengineering,* vol. 10, p. 293, 2000.
[35] J. Verd, A. Uranga, G. Abadal, J. Teva, F. Torres, F. Pérez-Murano*, et al.*, "Monolithic mass sensor fabricated using a conventional technology with attogram resolution in air conditions," *Applied physics letters,* vol. 91, p. 013501, 2007.
[36] G. Meyer and N. Amer, "Novel optical approach to atomic force microscopy," *SPIE MILESTONE SERIES MS,* vol. 107, pp. 200-200, 1995.
[37] S. Dohn, R. Sandberg, W. Svendsen, and A. Boisen, "Enhanced functionality of cantilever based mass sensors using higher modes," *Applied Physics Letters,* vol. 86, p. 233501, 2005.
[38] N. Blanc, J. Brugger, N. De Rooij, and U. Dürig, "Scanning force microscopy in the dynamic mode using microfabricated capacitive sensors," *Journal of Vacuum Science & Technology B: Microelectronics and Nanometer Structures Processing, Measurement, and Phenomena,* vol. 14, pp. 901-905, 1996.
[39] S. Minne, S. Manalis, and C. Quate, "Parallel atomic force microscopy using cantilevers with integrated piezoresistive sensors and integrated piezoelectric actuators," *Applied Physics Letters,* vol. 67, pp. 3918-3920, 1995.
[40] B. L. Pruitt and T. W. Kenny, "Piezoresistive cantilevers and measurement system for characterizing low force electrical contacts," *Sensors and Actuators A: Physical,* vol. 104, pp. 68-77, 2003.
[41] M. Yang, X. Zhang, K. Vafai, and C. S. Ozkan, "High sensitivity piezoresistive cantilever design and optimization for analyte-receptor binding," *Journal of Micromechanics and Microengineering,* vol. 13, p. 864, 2003.
[42] K. A. Brown, B. H. Yang, and R. M. Westervelt, "Self-driving capacitive cantilevers for high-frequency atomic force microscopy," *Applied Physics Letters,* vol. 100, p. 053110, 2012.

[43] M. Dukic, J. D. Adams, and G. E. Fantner, "Piezoresistive AFM cantilevers surpassing standard optical beam deflection in low noise topography imaging," *Scientific reports,* vol. 5, p. 16393, 2015.

[44] N. Jalili and K. Laxminarayana, "A review of atomic force microscopy imaging systems: application to molecular metrology and biological sciences," *Mechatronics,* vol. 14, pp. 907-945, 2004.

[45] H.-J. Butt, B. Cappella, and M. Kappl, "Force measurements with the atomic force microscope: Technique, interpretation and applications," *Surface science reports,* vol. 59, pp. 1-152, 2005.

[46] R. Raiteri, M. Grattarola, H.-J. Butt, and P. Skládal, "Micromechanical cantilever-based biosensors," *Sensors and Actuators B: Chemical,* vol. 79, pp. 115-126, 2001.

[47] I.-H. Hwang and J.-H. Lee, "Self-actuating biosensor using a piezoelectric cantilever and its optimization," in *Journal of Physics: conference series*, 2006, p. 362.

[48] H. H. Johnny and Y. F. Li, "High sensitivity piezoresistive cantilever sensor for biomolecular detection," in *Journal of Physics: Conference Series*, 2006, p. 429.

[49] G. A. Campbell and R. Mutharasan, "Near real-time detection of Cryptosporidium parvum oocyst by IgM-functionalized piezoelectric-excited millimeter-sized cantilever biosensor," *Biosensors and Bioelectronics,* vol. 23, pp. 1039-1045, 2008.

[50] J. Xie, J. Yang, and J. Zhou, "Vibrational Energy Loss Analysis of a MEMS Disk Resonator Gyroscope," in *2018 IEEE/ASME International Conference on Advanced Intelligent Mechatronics (AIM)*, 2018, pp. 385-390.

[51] S. Kazmi, C. Salm, and J. Schmitz, "Mechanical resonators on CMOS for integrated passive band pass filters," in *Ultimate Integration on Silicon (ULIS), 2013 14th International Conference on*, 2013, pp. 193-196.

[52] J. Lopez, J. Verd, J. Teva, G. Murillo, J. Giner, F. Torres*, et al.*, "Integration of RF-MEMS resonators on submicrometric commercial CMOS technologies," *Journal of Micromechanics and Microengineering,* vol. 19, p. 015002, 2008.

[53] E. Algre, Z. Xiong, M. Faucher, B. Walter, L. Buchaillot, and B. Legrand, "MEMS ring resonators for laserless AFM with sub-nanoNewton force resolution," *Journal of Microelectromechanical Systems,* vol. 21, pp. 385-397, 2012.

[54] K. Tanaka, Y. Mochida, M. Sugimoto, K. Moriya, T. Hasegawa, K. Atsuchi*, et al.*, "A micromachined vibrating gyroscope," *Sensors and Actuators A: Physical,* vol. 50, pp. 111-115, 1995.

[55] Q. Li, D. Xiao, X. Zhou, Y. Xu, M. Zhuo, Z. Hou*, et al.*, "0.04 degree-per-hour MEMS disk resonator gyroscope with high-quality factor (510 k) and long decaying time constant (74.9 s)," *Microsystems & Nanoengineering,* vol. 4, 2018.

[56] H. Ding, W. Wang, B.-F. Ju, and J. Xie, "A MEMS resonant accelerometer with sensitivity enhancement and adjustment mechanisms," *Journal of Micromechanics and Microengineering,* vol. 27, p. 115010, 2017.

[57] K. Park, N. Kim, D. T. Morisette, N. Aluru, and R. Bashir, "Resonant MEMS mass sensors for measurement of microdroplet evaporation," *Journal of Microelectromechanical Systems,* vol. 21, pp. 702-711, 2012.
[58] A. Heidari, Y.-J. Yoon, W.-T. Park, P.-C. Su, J. Miao, J. T. M. Lin*, et al.*, "Biotin-streptavidin binding interactions of dielectric filled silicon bulk acoustic resonators for smart label-free biochemical sensor applications," *Sensors,* vol. 14, pp. 4585-4598, 2014.
[59] X. Huang, S. Li, J. Schultz, Q. Wang, and Q. Lin, "A capacitive MEMS viscometric sensor for affinity detection of glucose," *Journal of Microelectromechanical Systems,* vol. 18, pp. 1246-1254, 2009.
[60] B. E. DeMartini, J. F. Rhoads, M. A. Zielke, K. G. Owen, S. W. Shaw, and K. L. Turner, "A single input-single output coupled microresonator array for the detection and identification of multiple analytes," *Applied Physics Letters,* vol. 93, p. 054102, 2008.
[61] D. F. Wang, D. Zhou, S. Liu, and J. Hong, "Localized trio cantilevers for identifying different mass perturbations," *Microsystem Technologies,* pp. 1-11, 2018.
[62] A. Ashok, P. M. Kumar, S. S. Singh, P. Raju, P. Pal, and A. K. Pandey, "Achieving wideband micromechanical system using coupled non-uniform beams array," *Sensors and Actuators A: Physical,* vol. 273, pp. 12-18, 2018.
[63] M. Spletzer, A. Raman, H. Sumali, and J. P. Sullivan, "Highly sensitive mass detection and identification using vibration localization in coupled microcantilever arrays," *Applied Physics Letters,* vol. 92, p. 114102, 2008.
[64] H. Zhang, W. Yuan, B. Li, Y. Hao, M. Kraft, and H. Chang, "A novel resonant accelerometer based on mode localization of weakly coupled resonators," in *Solid-State Sensors, Actuators and Microsystems (TRANSDUCERS), 2015 Transducers-2015 18th International Conference on*, 2015, pp. 1073-1076.
[65] P. Pai, H. Pourzand, and M. Tabib-Azar, "Magnetically coupled resonators for rate integrating gyroscopes," in *SENSORS, 2014 IEEE*, 2014, pp. 1173-1176.
[66] M. Manav, G. Reynen, M. Sharma, E. Cretu, and A. Phani, "Ultrasensitive resonant MEMS transducers with tuneable coupling," *Journal of Micromechanics and Microengineering,* vol. 24, p. 055005, 2014.
[67] C. Pierre and E. Dowell, "Localization of vibrations by structural irregularity," *Journal of Sound and Vibration,* vol. 114, pp. 549-564, 1987.
[68] C. Hodges, "Confinement of vibration by structural irregularity," *Journal of sound and vibration,* vol. 82, pp. 411-424, 1982.
[69] A. W. Leissa, "On a curve veering aberration," *Zeitschrift für angewandte Mathematik und Physik ZAMP,* vol. 25, pp. 99-111, 1974.
[70] C. Pierre, "Mode localization and eigenvalue loci veering phenomena in disordered structures," *Journal of Sound and Vibration,* vol. 126, pp. 485-502, 1988.
[71] P. Thiruvenkatanathan, "Mode-localized sensing in micromechanical resonator arrays," University of Cambridge, 2011.
[72] P. Thiruvenkatanathan, J. Woodhouse, J. Yan, and A. A. Seshia, "Manipulating

vibration energy confinement in electrically coupled microelectromechanical resonator arrays," *Journal of microelectromechanical systems,* vol. 20, pp. 157-164, 2011.

[73] P. Thiruvenkatanathan, J. Yan, J. Woodhouse, and A. A. Seshia, "Enhancing parametric sensitivity in electrically coupled MEMS resonators," *Journal of Microelectromechanical Systems,* vol. 18, pp. 1077-1086, 2009.

[74] P. Thiruvenkatanathan, J. Yan, and A. A. Seshia, "Common mode rejection in electrically coupled MEMS resonators utilizing mode localization for sensor applications," in *Frequency Control Symposium, 2009 Joint with the 22nd European Frequency and Time Forum. IEEE International*, 2009, pp. 358-363.

[75] E. Gil-Santos, D. Ramos, A. Jana, M. Calleja, A. Raman, and J. Tamayo, "Mass sensing based on deterministic and stochastic responses of elastically coupled nanocantilevers," *Nano letters,* vol. 9, pp. 4122-4127, 2009.

[76] C. Zhao, G. Wood, J. Xie, H. Chang, S.-H. Pu, and M. Kraft, "Comparative study of different output metrics for a three weakly coupled resonator sensor," in *Solid-State Sensors, Actuators and Microsystems (TRANSDUCERS), 2015 Transducers-2015 18th International Conference on*, 2015, pp. 2196-2199.

[77] C. Zhao, G. S. Wood, J. Xie, H. Chang, S. H. Pu, and M. Kraft, "A force sensor based on three weakly coupled resonators with ultrahigh sensitivity," *Sensors and Actuators A: Physical,* vol. 232, pp. 151-162, 2015.

[78] Manav, "Vibration mode localization in coupled microelectromechanical resonators," University of British Columbia, 2014.

[79] C. Zhao, G. S. Wood, J. Xie, H. Chang, S. H. Pu, and M. Kraft, "A three degree-of-freedom weakly coupled resonator sensor with enhanced stiffness sensitivity," *Journal of Microelectromechanical Systems,* vol. 25, pp. 38-51, 2016.

[80] R. A. Brookhuis, T. S. Lammerink, and R. J. Wiegerink, "Differential capacitive sensing circuit for a multi-electrode capacitive force sensor," *Sensors and Actuators A: Physical,* vol. 234, pp. 168-179, 2015.

[81] Y. Bai, Y. Lu, P. Hu, G. Wang, J. Xu, T. Zeng*, et al.*, "Absolute position sensing based on a robust differential capacitive sensor with a grounded shield window," *Sensors,* vol. 16, p. 680, 2016.

[82] C. S. Lu and O. Lewis, "Investigation of film-thickness determination by oscillating quartz resonators with large mass load," *Journal of Applied Physics,* vol. 43, pp. 4385-4390, 1972.

[83] S. J. Martin, J. J. Spates, K. O. Wessendorf, T. W. Schneider, and R. J. Huber, "Resonator/oscillator response to liquid loading," *Analytical chemistry,* vol. 69, pp. 2050-2054, 1997.

[84] J.-Y. Lee, B. Bahreyni, Y. Zhu, and A. Seshia, "Ultrasensitive mass balance based on a bulk acoustic mode single-crystal silicon resonator," *Applied Physics Letters,* vol. 91, p. 234103, 2007.

[85] A. Heidari, Y.-J. Yoon, and H.-J. Choi, "Analysis and design of a high performance and low cost bio-mass sensor based on the radial contour mode disk resonator," *Microelectronic Engineering,* vol. 88, pp. 1730-1732, 2011.

[86] J. E. Lee, B. Bahreyni, and A. A. Seshia, "Thin film monitoring with silicon bulk acoustic resonators," in *SENSORS, 2008 IEEE*, 2008, pp. 581-584.

[87] A. Cagliani and Z. J. Davis, "Ultrasensitive bulk disk microresonator-based sensor for distributed mass sensing," *Journal of Micromechanics and Microengineering,* vol. 21, p. 045016, 2011.

[88] J.-Y. Lee and A. Seshia, "5.4-MHz single-crystal silicon wine glass mode disk resonator with quality factor of 2 million," *Sensors and Actuators A: Physical,* vol. 156, pp. 28-35, 2009.

[89] M. H. Zarifi and M. Daneshmand, "Bulk disc resonators radial and wineglass mode resonance characterization for mass sensing applications," *Microsystem Technologies,* vol. 22, pp. 1013-1020, 2016.

[90] J. R. Clark, W.-T. Hsu, and C.-C. Nguyen, "High-Q VHF micromechanical contour-mode disk resonators," in *International Electron Devices Meeting 2000. Technical Digest. IEDM (Cat. No. 00CH37138)*, 2000, pp. 493-496.

[91] M. A. Abdelmoneum, M. U. Demirci, and C.-C. Nguyen, "Stemless wine-glass-mode disk micromechanical resonators," in *The Sixteenth Annual International Conference on Micro Electro Mechanical Systems, 2003. MEMS-03 Kyoto. IEEE*, 2003, pp. 698-701.

[92] Z. Hao, S. Pourkamali, and F. Ayazi, "VHF single-crystal silicon elliptic bulk-mode capacitive disk resonators-part I: design and modeling," *Journal of Microelectromechanical Systems,* vol. 13, pp. 1043-1053, 2004.

[93] C. Cai, H. Zheng, M. Khan, and K. Hung, "Modeling of material damping properties in ANSYS," in *CADFEM Users' Meeting & ANSYS Conference*, 2002, pp. 9-11.

[94] J. Dong, D. Mukhopadhyay, and P. M. Ferreira, "Design, fabrication and testing of a silicon-on-insulator (SOI) MEMS parallel kinematics XY stage," *Journal of micromechanics and microengineering,* vol. 17, p. 1154, 2007.

[95] O. Raccurt, F. Tardif, F. A. d'Avitaya, and T. Vareine, "Influence of liquid surface tension on stiction of SOI MEMS," *Journal of Micromechanics and Microengineering,* vol. 14, p. 1083, 2004.

[96] B. Volland, H. Heerlein, I. Kostic, and I. Rangelow, "The application of secondary effects in high aspect ratio dry etching for the fabrication of MEMS," *Microelectronic engineering,* vol. 57, pp. 641-650, 2001.

[97] P. Docker, P. Kinnell, and M. Ward, "A dry single-step process for the manufacture of released MEMS structures," *Journal of Micromechanics and Microengineering,* vol. 13, p. 790, 2003.

[98] J. B. Xie, Y. C. Hao, H. L. Chang, and W. Z. Yuan, "Single mask selective release process for complex SOI MEMS device," in *Key Engineering Materials*, 2013, pp. 1116-1121.

[99] I. Sari, I. Zeimpekis, and M. Kraft, "A dicing free SOI process for MEMS devices," *Microelectronic Engineering,* vol. 95, pp. 121-129, 2012.

[100] Y. Hao, J. Xie, W. Yuan, and H. Chang, "Dicing-free SOI process based on wet release technology," *Micro & Nano Letters,* vol. 11, pp. 775-778, 2016.

[101] S. A. Bhave, D. Gao, R. Maboudian, and R. T. Howe, "Fully-differential poly-

SiC Lame mode resonator and checkerboard filter," in *18th IEEE International Conference on Micro Electro Mechanical Systems, 2005. MEMS 2005.*, 2005, pp. 223-226.
[102] A.-H. Lin, J.-Y. Lee, J. Yan, and A. Seshia, "Methods for enhanced electrical transduction and characterization of micromechanical resonators," *Sensors and Actuators A: Physical,* vol. 158, pp. 263-272, 2010.
[103] C. Tu, H. Zhu, Y. Xu, and J. E.-Y. Lee, "Differential-capacitive-input and differential-piezoresistive-output enhanced transduction of a silicon bulk-mode microelectromechanical resonator," *Sensors and Actuators A: Physical,* vol. 210, pp. 41-50, 2014.
[104] J.-Y. Lee and A. Seshia, "Parasitic feedthrough cancellation techniques for enhanced electrical characterization of electrostatic microresonators," *Sensors and Actuators A: Physical,* vol. 156, pp. 36-42, 2009.
[105] I.-B. Baek, S. Byun, B. K. Lee, J.-H. Ryu, Y. Kim, Y. S. Yoon*, et al.*, "Attogram mass sensing based on silicon microbeam resonators," *Scientific reports,* vol. 7, p. 46660, 2017.
[106] G. S. Wood, C. Zhao, S. H. Pu, S. A. Boden, I. Sari, and M. Kraft, "Mass sensor utilising the mode-localisation effect in an electrostatically-coupled MEMS resonator pair fabricated using an SOI process," *Microelectronic Engineering,* vol. 159, pp. 169-173, 2016.
[107] Y. Wang, C. Zhao, C. Wang, D. Cerica, M. Baijot, V. Pachkawade*, et al.*, "A Reversible Method to Characterize the Mass Sensitivity of a 3-Dof Mode Localized Coupled Resonator under Atmospheric Pressure," in *Multidisciplinary Digital Publishing Institute Proceedings*, 2017, p. 493.
[108] Y. Wang, C. Zhao, C. Wang, D. Cerica, M. Baijot, Q. Xiao*, et al.*, "A mass sensor based on 3-DOF mode localized coupled resonator under atmospheric pressure," *Sensors and Actuators A: Physical,* vol. 279, pp. 254-262, 2018.
[109] B. I. Kharisov, H. R. Dias, O. V. Kharissova, A. Vázquez, Y. Pena, and I. Gomez, "Solubilization, dispersion and stabilization of magnetic nanoparticles in water and non-aqueous solvents: recent trends," *RSC Advances,* vol. 4, pp. 45354-45381, 2014.
[110] S. Kralj and D. Makovec, "Magnetic assembly of superparamagnetic iron oxide nanoparticle clusters into nanochains and nanobundles," *ACS nano,* vol. 9, pp. 9700-9707, 2015.
[111] L. C. de Smet, D. Ullien, M. Mescher, and E. J. Sudhölter, "Organic surface modification of silicon nanowire-based sensor devices," in *Nanowires-Implementations and Applications*, ed: IntechOpen, 2011.
[112] X. G. Zhang, *Electrochemistry of Silicon and its Oxide*: Springer Science & Business Media, 2007.
[113] N. S. K. Gunda, M. Singh, L. Norman, K. Kaur, and S. K. Mitra, "Optimization and characterization of biomolecule immobilization on silicon substrates using (3-aminopropyl) triethoxysilane (APTES) and glutaraldehyde linker," *Applied Surface Science,* vol. 305, pp. 522-530, 2014.
[114] Q. Weiping, X. Bin, W. Lei, W. Chunxiao, Y. Danfeng, Y. Fang*, et al.*,

"Controlled site-directed assembly of antibodies by their oligosaccharide moieties onto APTES derivatized surfaces," *Journal of colloid and interface science,* vol. 214, pp. 16-19, 1999.

[115] A. Maria Chong and X. Zhao, "Functionalization of SBA-15 with APTES and characterization of functionalized materials," *The Journal of Physical Chemistry B,* vol. 107, pp. 12650-12657, 2003.

[116] S.-H. Choi and B.-m. Z. Newby, "Suppress polystyrene thin film dewetting by modifying substrate surface with aminopropyltriethoxysilane," *Surface science,* vol. 600, pp. 1391-1404, 2006.

[117] J. Landoulsi, M. J. Genet, K. El Kirat, C. Richard, S. Pulvin, and P. G. Rouxhet, "Silanization with APTES for controlling the interactions between stainless steel and biocomponents: reality vs expectation," in *Biomaterials-Physics and Chemistry*, ed: IntechOpen, 2011.

[118] Y. Cui and C. M. Lieber, "Functional nanoscale electronic devices assembled using silicon nanowire building blocks," *science,* vol. 291, pp. 851-853, 2001.

[119] X. Wang, Y. Chen, K. A. Gibney, S. Erramilli, and P. Mohanty, "Silicon-based nanochannel glucose sensor," *Applied Physics Letters,* vol. 92, p. 013903, 2008.

[120] A. Heidari, Y.-J. Yoon, W.-T. Park, P.-C. Su, J. Miao, J. Lin*, et al.*, "Biotin-streptavidin binding interactions of dielectric filled silicon bulk acoustic resonators for smart label-free biochemical sensor applications," *Sensors,* vol. 14, pp. 4585-4598, 2014.

[121] C. Zhao, G. Sobreviela, M. Pandit, S. Du, X. Zou, and A. Seshia, "Experimental observation of noise reduction in weakly coupled nonlinear MEMS resonators," *Journal of Microelectromechanical Systems,* vol. 26, pp. 1196-1203, 2017.

[122] C. Zhao, M. Pandit, G. Sobreviela, A. Mustafazade, S. Du, X. Zou*, et al.*, "On the noise optimization of resonant MEMS sensors utilizing vibration mode localization," *Applied Physics Letters,* vol. 112, p. 194103, 2018.

[123] X. Li, H. Yu, X. Gan, X. Xia, P. Xu, J. Li*, et al.*, "Integrated MEMS/NEMS resonant cantilevers for ultrasensitive biological detection," *Journal of Sensors,* vol. 2009, 2009.

[124] H. Campanella, A. Uranga, A. Romano-Rodriguez, J. Montserrat, G. Abadal, N. Barniol*, et al.*, "Localized-mass detection based on thin-film bulk acoustic wave resonators (FBAR): Area and mass location aspects," *Sensors and Actuators A: Physical,* vol. 142, pp. 322-328, 2008.

[125] A. T.-H. Lin, J. Yan, and A. A. Seshia, "Electrically addressed dual resonator sensing platform for biochemical detection," *Journal of Microelectromechanical Systems,* vol. 21, pp. 34-43, 2011.

[126] O. G. Andrusyak, M. Bubelnik, J. Mares, T. McGovern, and C. W. Siders, "Single-pulse and burst-mode ablation of gold films measured by quartz crystal microbalance," in *Laser-Induced Damage in Optical Materials: 2004*, 2005, pp. 61-72.

[127] C. R. Kirkendall and J. W. Kwon, "Liquid damping isolation on quartz crystal microbalance for effective preservation of high quality factor and sensitivity in liquid," in *SENSORS, 2009 IEEE*, 2009, pp. 607-610.

[128] S. Beißner, J.-W. Thies, C. Bechthold, P. Kuhn, B. Thürmann, S. Dübel*, et al.*, "Low-cost, in-liquid measuring system using a novel compact oscillation circuit and quartz-crystal microbalances (QCMs) as a versatile biosensor platform," *Journal of Sensors and Sensor Systems,* vol. 6, pp. 341-350, 2017.

[129] X. Huang, Q. Bai, J. Hu, and D. Hou, "A practical model of quartz crystal microbalance in actual applications," *Sensors,* vol. 17, p. 1785, 2017.

[130] G. Sauerbrey, "Verwendung von Schwingquarzen zur Wägung dünner Schichten und zur Mikrowägung," *Zeitschrift für physik,* vol. 155, pp. 206-222, 1959.

[131] T. Lederer, B. P. Stehrer, S. Bauer, B. Jakoby, and W. Hilber, "Utilizing a high fundamental frequency quartz crystal resonator as a biosensor in a digital microfluidic platform," *Sensors and Actuators A: Physical,* vol. 172, pp. 161-168, 2011.

[132] M. Rodahl, F. Höök, A. Krozer, P. Brzezinski, and B. Kasemo, "Quartz crystal microbalance setup for frequency and Q-factor measurements in gaseous and liquid environments," *Review of Scientific Instruments,* vol. 66, pp. 3924-3930, 1995.

[133] M. Rodahl, F. Höök, and B. Kasemo, "QCM operation in liquids: an explanation of measured variations in frequency and Q factor with liquid conductivity," *Analytical Chemistry,* vol. 68, pp. 2219-2227, 1996.

[134] M. Pandit, C. Zhao, G. Sobreviela, A. Mustafazade, S. Du, X. Zou*, et al.*, "Closed-loop characterization of noise and stability in a mode-localized resonant MEMS sensor," *IEEE transactions on ultrasonics, ferroelectrics, and frequency control,* vol. 66, pp. 170-180, 2018.

[135] J. Juillard, P. Prache, P. M. Ferreira, and N. Barniol, "Impact of output metric on the resolution of mode-localized MEMS resonant sensors," in *2017 Joint Conference of the European Frequency and Time Forum and IEEE International Frequency Control Symposium (EFTF/IFCS)*, 2017, pp. 506-509.

[136] Y. Bao, S. Cai, H. Yu, T. Xu, P. Xu, and X. Li, "Resonant-gravimetric particle sensors with air-filtering cantilever fabricated in low-cost non-SOI silicon," in *2018 IEEE Micro Electro Mechanical Systems (MEMS)*, 2018, pp. 908-911.